



Universiteit
Leiden
The Netherlands

Squaramide-based supramolecular polymers : from self-assembly to in vivo application

Saez Talens, V.

Citation

Saez Talens, V. (2018, December 10). *Squaramide-based supramolecular polymers : from self-assembly to in vivo application*. Retrieved from <https://hdl.handle.net/1887/67527>

Version: Not Applicable (or Unknown)

License: [Licence agreement concerning inclusion of doctoral thesis in the Institutional Repository of the University of Leiden](#)

Downloaded from: <https://hdl.handle.net/1887/67527>

Note: To cite this publication please use the final published version (if applicable).

Cover Page



Universiteit Leiden



The handle <http://hdl.handle.net/1887/67527> holds various files of this Leiden University dissertation.

Author: Saez, Talens V.

Title: Squaramide-based supramolecular polymers : from self-assembly to in vivo application

Issue Date: 2018-12-10

Squaramide-based supramolecular polymers: from self-assembly to *in vivo* application

PROEFSCHRIFT

Ter verkrijging van
de graad van Doctor aan de Universiteit Leiden,
op gezag van Rector Magnificus prof. mr. C. J. J. M. Stolker
volgens het besluit van het College voor Promoties
te verdedigen op maandag 10 december 2018
klokke 13:45 uur

door

Victorio Saez Talens

Geboren op 6 September 1990 te Carcaixent, País Valencià, Spain

Promotor: Prof. dr. A. Kros

Copromotor: Dr. R. E. Kieltyka

Overige leden:

Prof. dr. H.S. Overkleeft (voorzitter), Faculty of Science, LIC

Prof. dr. M.H.M. Noteborn (secretaris), Faculty of Science, LIC

Prof. dr. I.K. Voets, Eindhoven University of Technology

Prof. dr. G. Fernández, University of Münster

Dr. S.A. Bonnet, Faculty of Science, LIC

Doctoral Thesis, Leiden University, 2018

Cover Design: Elena Pérez Gallent

Printed by Ridderprint BV

ISBN: 978-94-6375-185-8

dedicat a la meva família

i amics

Table of Contents

Chapter 1	7
Introduction	
Chapter 2	35
Aromatic gain in a supramolecular polymer	
Chapter 3	73
A self-assembly mode “tug-of-war” in squaramide-based supramolecular polymers driven by aromaticity-modulated hydrogen bonding	
Chapter 4	155
Morphological transitions of a squaramide-based supramolecular polymer nanoparticle in water by modulating its monomer structure	
Chapter 5	197
Biodistribution of squaramide-based supramolecular polymer nanoparticles in zebrafish embryos	
Chapter 6	239
Summary and perspectives	
Samenvatting	245
Curriculum Vitae	249
List of publications	252

CHAPTER 1

Introduction

1.1 Hierarchical self-assembly in Nature: inspiration for the design of supramolecular polymers

In Nature, specific and reversible non-covalent forces between biomolecules drive the self-assembly of ordered and functional biological materials.¹ Self-assembled structures, such as DNA, proteins, cell membranes and viruses, are responsible to transport of genetic information, perform a wide range of functions such as DNA replication (performed by proteins) or protection of the intracellular content from its surroundings (cell membrane). Central to all of these materials is that the organization of these biomolecules is triggered by non-covalent forces such as hydrogen-bonding, aromatic interactions, van der Waals, electrostatic or hydrophobic effects, which are individually weak, but can be collectively strong.²⁻⁴

One example of self-assembly in Nature is the formation of filamentous structures such as amyloids or actin filaments. Amyloids are a class of filamentous supramolecular biopolymers, well-known for their presence in neurodegenerative diseases.⁵ These fibrils are typically composed of polypeptides self-assembled in a perpendicular orientation to the fiber. The polypeptides interact primarily *via* multiple hydrogen-bonds between the amide groups that are adjacent to each other into the backbone, synergistically with other non-covalent interactions, such as ionic, van der Waals and hydrophobic interactions (Figures 1.1a and 1.1b).^{6,7} A nucleation-elongation mechanism is behind the growth of these filamentous structures through the transition from micelles to fibrils by polymerization of proteins at the fibril ends.⁸

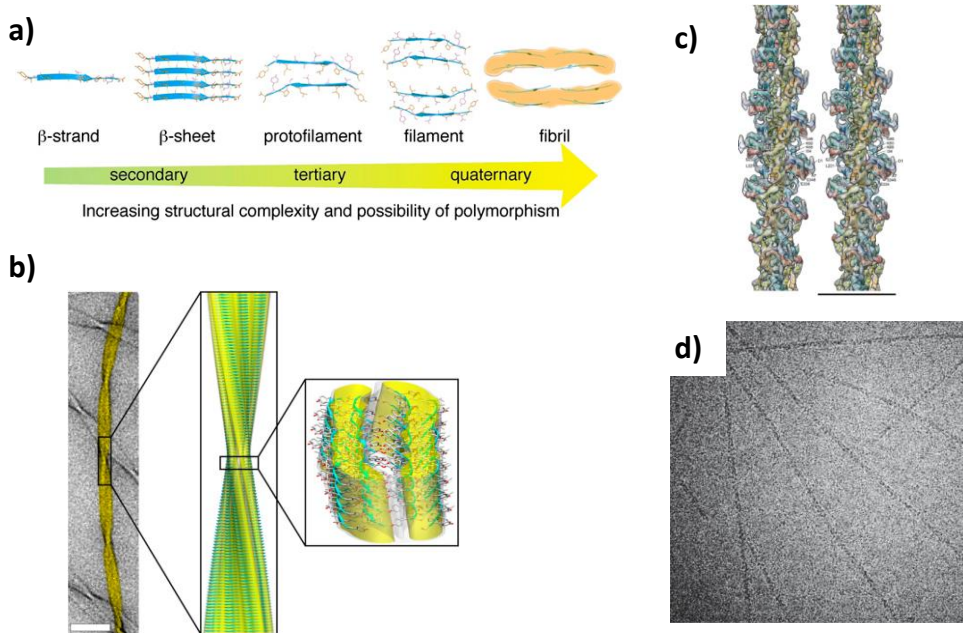


Figure 1.1. a) Hierarchical self-assembly of amyloids. b) Atomic-resolution of the reconstructed amyloid fibril structure (*Center*). TEM image of an amyloid fibril (*left*), scale bar = 50 nm. (*Right*) β -sheets depicted in a ribbon illustration. (Atoms of oxygen in red, carbon in gray, and nitrogen in blue). Figure adapted from reference 7. c) Three-dimensional density map of F-actin (scale bar 100 Å). d) cryo-TEM picture of F-actin filaments. Figure adapted from reference 11.

Actin filaments are another type of biological supramolecular polymer found in eukaryotic cells, namely in their cytoskeleton that is responsible for their architecture and motion. Actin is a 42 kDa globular protein that self-assembles through hydrophobic units and salt bridges in various locations into a helical ribbon structure⁹ (Figures 1.1c and 1.1d).^{10,11} Similar to amyloid fibrils, these structures self-assemble by a cooperative mechanism, starting from a peptide trimer.¹²

1.2 Non-covalent interactions employed in the design of supramolecular systems in water

Hydrophobic effects

The hydrophobic effect arises from the poor solvation of hydrophobic molecules.¹³ If a solute is introduced into water, the water molecules would need to rearrange their ice-like structure, which is energetically unfavorable. Consequently, this forces their aggregation, increasing the entropy as a consequence of releasing water into the bulk.¹⁴

Hydrogen bonding

Hydrogen bonds involve a hydrogen atom covalently linked to another electronegative atom (such as F, O or N) which it is attracted to another highly electronegative atom in close proximity (D-H...A).¹⁵ These special dipole-dipole interactions can be classified according to their nature,^{16,17} geometry or strength, with the latter criteria being the most common. Based on their strength,¹⁸ they can be further sub-divided into strong interactions (60-120 kJ mol⁻¹), in which the hydrogen atom is located in the middle of the donor and acceptor atoms and has a comparable character to covalent bonds; moderate strength (16-60 kJ mol⁻¹), which are formed by neutral donor and acceptor groups *via* electron lone pairs; and finally weak hydrogen-bond interactions (<12 kJ mol⁻¹) that can be of high relevance in crystal structures where they can be at close range in large numbers.¹⁹ However, an important consideration when applying them in the design of supramolecular monomers is the attractive or repulsive interactions between neighboring groups within the molecular recognition units, otherwise known as secondary interactions. The partial charges located on the neighboring heteroatoms can either decrease or increase the monomer binding strength by 8-12 kJ/mol per interaction.

The perceived hydrogen-bonding strength of a solute molecule is often lower in water because of the surrounding solvent which can compete with these interactions. Hence, to facilitate monomer self-assembly hydrogen-bonding interactions are often inserted within the hydrophobic pocket of the monomer to shield them from water in the design process. For example, ureas^{20,21} or carboxamides²² are common units used as hydrogen-bonding motifs in

combination with hydrophobic effects to trigger the formation of water-based supramolecular polymers.

Aromatic interactions

Aromatic interactions can take place between unsaturated cyclic compounds. Two arrangements of these interactions are possible: edge-to-face or face-to-face.¹⁹ Edge-to-face aromatic interactions, which are more energetically more favourable based on the interaction of their π -electron clouds, are responsible for the typical herringbone packing observed in crystal structures.¹⁹ On the other hand, face-to-face aromatic interactions, such as the stacking of nucleobases of DNA are postulated to be behind its stability.¹⁹

Other non-covalent interactions

As important as the previous interactions, the next two interactions are also valuable in the construction of supramolecular polymers. *Hydrophilic interactions*, namely the interactions of polar groups with water molecules are important for self-assembly of amphiphiles. Both polar and charged groups increase water solubility, and when combined with hydrophobic groups can facilitate their nanoscale phase segregation.²³ A second interaction that can play an important effect on self-assembly are *van der Waals* forces that arises from the polarization of an electron cloud by a nearby nucleus. This interaction is a weak non-directional electrostatic interaction that can be broken down into dispersion (London) and exchange-repulsion terms.¹⁹

Among the various non-covalent forces being involved in the process of self-assembly, the aforementioned ones are the most common interactions employed in the organic supramolecular polymer toolbox.

1.3 Supramolecular polymers

Lehn, Cram and Pedersen pioneered the field of supramolecular chemistry with their fundamental work on host-guest chemistry in the 1960s being awarded the Nobel Prize in 1987. At the beginning of the 90's, Lehn and Fouquey developed a system consisting of a complementary triple hydrogen bonding motif between uracil and 2,6-diacylaminopyridine.^{24,25} They linked together two molecular recognition units using tartaric acid as a crosslinker. When the resulting compounds were mixed in an equimolar ratio, a liquid-crystalline material was obtained that consisted of supramolecular chains composed of the monomer. This early example initiated the growth of the supramolecular polymer field and ever since a plethora of other polymers were published, where monomer building blocks are capable of self-organizing into well-defined structures.

1.3.1 Growth mechanisms in supramolecular polymers

The growth mechanism of supramolecular polymers is evaluated based on the response to temperature or concentration variation.²⁶ The dependency on these two factors is governed by the reversibility of the non-covalent forces, which upon rising the concentration or diminishing the temperature results in the enhancement of the degree of polymerization (DP). Thus, the three major growth mechanisms for this polymerization process are²⁷: isodesmic, ring-chain and cooperative.

In the isodesmic mechanism, a constant decrease in the free energy upon addition of monomers to the pre-formed polymer occurs due to an identical equilibrium constant (K_a) for the addition of each monomer to the growing polymer chain. The degree of polymerization (DP) is directly related to the value of the equilibrium constant with temperature and concentration having a great influence on the polydispersity of the resulting polymers (Figure 1.2a).²⁶ The ring-chain supramolecular polymerization mechanism involves a flexible, bifunctional monomer that is in equilibrium with the formation of a linear aggregate array and its cyclic counterpart (Figure 1.2b) throughout the polymerization. The cooperative (nucleation-elongation) growth mechanism is a two-stage polymerization process involving a nucleation and elongation phase. These steps are characterized by two equilibrium constants, one for nucleation (K_n) and a second one for the elongation of the polymer (K_e) once a nucleus of a certain DP is formed that is larger than K_a with both stages showing isodesmic growth.

Elongation is triggered below a critical temperature or above a critical concentration (Figure 1.2c). Moreover, a second scenario can be also possible, where oligomerization of the monomers is initially favoured over polymerization, and thus $K_n > K_e$. This phenomenon is known as anticooperative growth results in the formation of discrete objects with low dispersity.^{28,29}

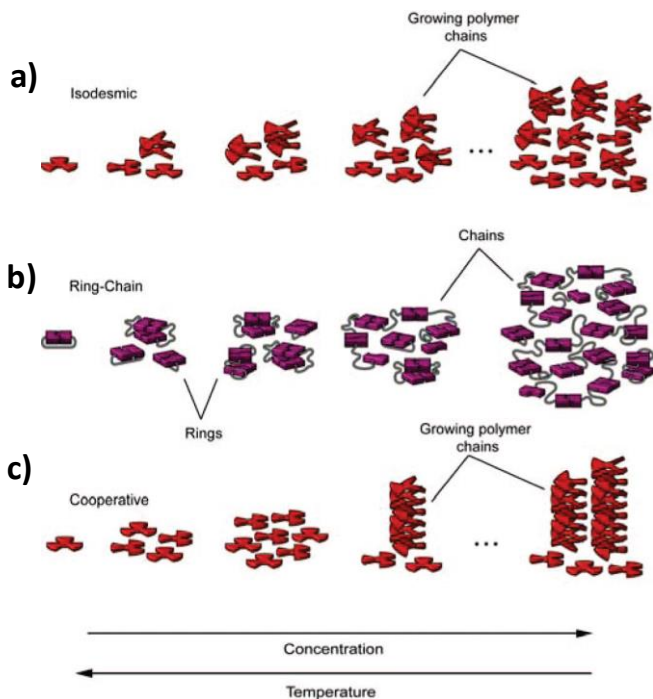


Figure 1.2. Cartoon showing the assembly and/or disassembly as an effect of concentration and/or temperature of (a) isodesmic, (b) ring-chain and (c) cooperative supramolecular polymerization. Figure adapted from reference 27.

1.4 Supramolecular polymerization in aqueous solution

Understanding the interplay of the various non-covalent forces used to construct supramolecular polymers is vital to understand how this process occurs and the resultant polymer architectures formed. Water, the medium used by nature, affords self-assembled structures with a high degree of complexity, robustness and adaptability.³⁰⁻³² The combination of hydrophobic effects together with one or more other non-covalent forces in a synergistic manner is the means to design supramolecular polymers resulting in robust polymers in polar media.³⁷ However, due to the strong nature of hydrophobic interactions in water kinetic trapping of such self-assemblies can be expected with various structures from the same building block and pathway dependency.^{33,34}

1.4.1 Representative examples of monomers used for supramolecular polymerization in water

Single-chain amphiphiles

Amphiphilic or amphipathic compounds consist of a hydrophilic and a hydrophobic domain. For example, the Stupp group has developed supramolecular polymers based on peptide amphiphiles to yield long unidimensional cylindrical objects on the micron scale in aqueous media.³⁵ The monomeric building block is composed of an aliphatic tail connected to a hydrophilic peptide segment. Bioactive epitopes can be introduced in the hydrophilic domain to mimic biochemical or biophysical attributes of the natural extracellular matrix for tissue engineering and regenerative medicine applications.³⁶ Rybtchinski and co-workers exploited hydrophobic effects of aromatic cores to drive self-assembly in water. In a recent work, they studied the supramolecular polymerization mechanism of two perylene diimide (PDI) amphiphile motifs, functionalized either with an aliphatic chain or a perfluorooctyl chain (Figure 1.3a).³⁷ They measured the length of both PDI-based supramolecular polymers under the same sample preparation conditions, giving as a result a fiber length of two orders of magnitude longer for the fluorinated derivatives when compared with the purely aliphatic compounds, mostly attributed to the association constant of the fluorinated analogues (10^{15} M^{-1}), being three times larger than the aliphatic derivatives. In addition, the aggregation mechanism of the fluorinated PDI was studied in mixtures of different ratios of water/THF. Remarkably, it was observed that these structures self-

assembled *via* a cooperative mechanism when the ratio water/THF was 60/40, or higher in THF content. On the other hand, this mechanism was found to be isodesmic when the ratio was changed to a content 70/30, or lower in THF content. The authors stated that the hydrophobicity of the aliphatic tail is highly influenced by the large surface of the fluorine atoms, and they highlighted that the cooperative mechanism was a specific result due to the rigidity conferred by the fluorinated chain. These observations opened a new possibility for the design of supramolecular polymers.

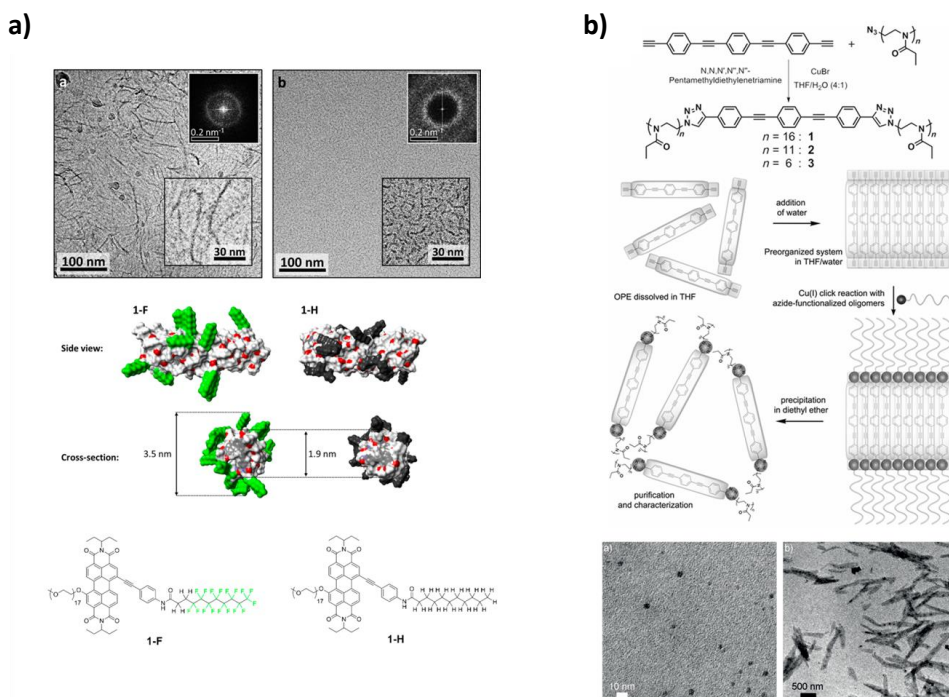


Figure 1.3. (a) Perylenelediimide (PDI) derivatives with hydrogenated (**1-H**) and fluorinated (**1-F**) aliphatic chains (structures represented at the bottom) and their fibrillar self-assembly as followed by cryoTEM in a mixture of 65:35 water/THF (v/v). Figure adapted from reference 37. (b) Synthesis of OPE-PeTO_x bolaamphiphiles with three different hydrophilic side chain lengths (*top*) and TEM pictures (*bottom*) of self-assembled monomer **1** (*left*) and **3** (*right*) in water. Figure adapted from reference 40.

Chapter 1

Bolaamphiphiles

Bolaamphiphiles contain a hydrophobic domain and two water soluble moieties at opposite ends of their core.^{38,39} They are more water soluble in comparison to amphiphiles, which translates into a higher critical aggregation concentration and a lower critical aggregation number. Upon self-assembly, these monomers can form a wide range of morphologies including disks, vesicles, spheres and fibers.³⁹ For example, Fernández and co-workers developed oligo phenyleneethynylene-based bolaamphiphiles substituted with two hydrophilic poly(2-ethyl-2-oxazoline) (PEtOx) of different lengths (Figure 1.3b). These self-assembled structures are triggered by a combination of π - π interactions and hydrophobic effects with the growth mechanism of the polymers being highly influenced by the length of their hydrophilic side chains. While the monomers with a PEtOx chain with 6 repeat units show nucleation-elongation or cooperative growth, the ones containing 16 units show isodesmic growth.⁴⁰ Sijbesma and co-workers developed a bolaamphiphilic structure with two urea motifs in the aliphatic core and two hydrophilic poly(ethylene glycol) side chains (Figure 1.4a). The hydrogen bonding between the monomers through the urea moieties in combination with the hydrophobic/hydrophilic ratio of the bolaamphiphile, triggered the formation of one-dimensional rod-like structures in water. Recently, these motifs have been exploited to prepare strain stiffening hydrogels when fixed through an topochemical polymerization within the fiber.⁴¹⁻⁴⁴ Bouteiller and co-workers reported another bis-urea based supramolecular polymer that is able to self-assemble in water, aprotic and non-polar solvents (Figure 1.4b). In this report, it was found that the driving force of the supramolecular polymerization depends on the solvent, but in all cases long, rigid filamentous structures are formed.⁴⁵ This amphiphile structure will be used and studied in this thesis as the main building block to drive the formation of supramolecular polymers.

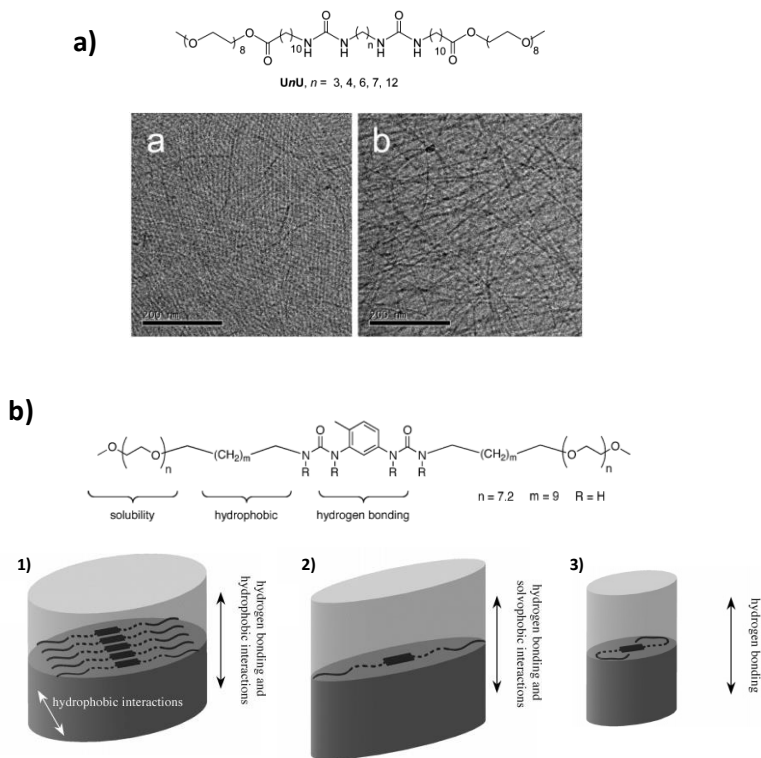


Figure 1.4. (a) Bis-urea based bolaamphiphiles developed by Sijbesma and co-workers with aliphatic spacers of various lengths (*top*). CryoTEM pictures (*bottom*) at 1 wt% of the rod-like structures for U4U (a) and U7U (b), adapted from reference 44. (b) Molecular structure of bis-urea bolaamphiphile introduced by Bouteiller and co-workers (*top*) and schematic representation of the filaments upon self-assembly in water (1), acetonitrile (2) and toluene (3), adapted from reference 45.

Chapter 1

C₃-symmetric amphiphiles

C_3 -symmetric monomers with a disc-shaped conformation that consist of a rigid core and solubilizing chains on the periphery represent another well-known class of monomers forming supramolecular polymer architectures. As an illustrative example, the group of van Esch and Eelkema has studied and exploited the formation of a low molecular weight hydrogelator-based on trishydrazone units (Figure 1.5a).⁴⁶⁻⁴⁸ They were able to control the mechanical properties and microstructure of the resulting materials through catalysis using a reaction-coupled system. The formation of the gelator was done *in situ* by reacting cyclohexane trishydrazide building block **1** with three molecules of aldehyde **2** (Figure 1.5a). By using either acid or nucleophilic aniline catalysis, hydrogels can be formed under ambient conditions on the order of minutes. Additionally, Meijer and co-workers have exploited the use of 1,3,5-benzentricarboxamides (BTA) for the formation of supramolecular polymers in numerous studies with a recent focus in aqueous solutions.⁴⁹⁻⁵² In order to promote the solubility of these structures in aqueous media, tetraethylene glycol is conjugated to the periphery of the BTA structure, and by a combination of hydrophobic, aromatic interactions and hydrogen-bonding, self-assembly takes place. Recent studies have proposed the use of this aggregate as a platform for intracellular drug delivery (Figure 1.5b).⁵²

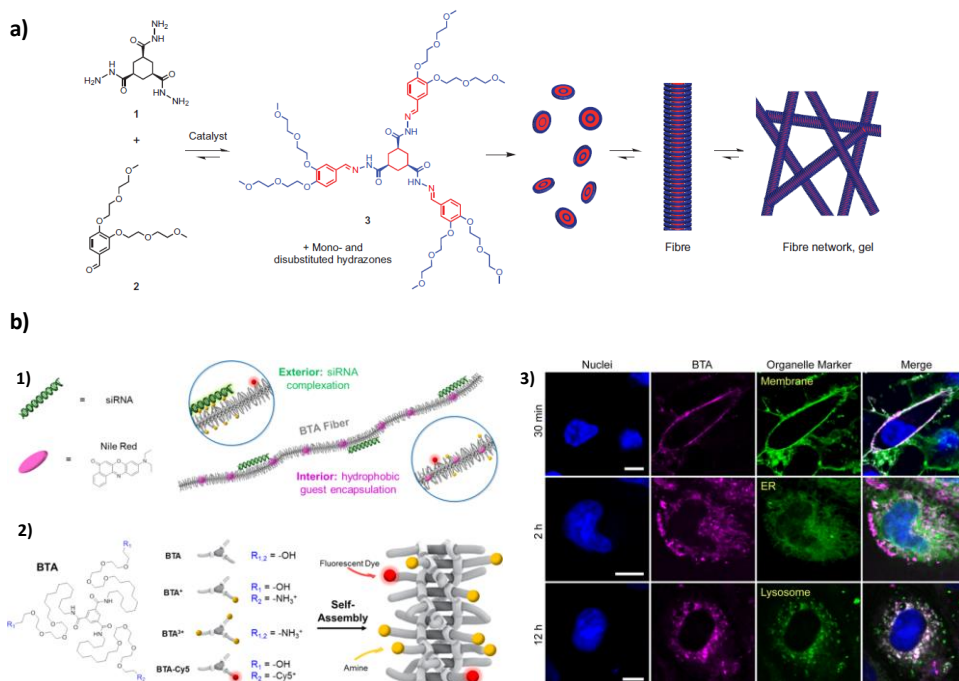


Figure 1.5. (a) Hydrogel formation proposed by van Esch and co-workers. Trishydrazone hydrogelator **3** synthesized by a reaction of **1** and **2** and triggers fiber formation, trapping the surrounding solvent to form a gel. Image adapted from reference 48. (b) Intracellular siRNA delivery using BTA supramolecular polymers. (1) Nile red (hydrophobic fluorescent molecule) is trapped in the lipophilic core, while siRNA condenses on the exterior of the fiber by electrostatic interactions. (2) Self-assembly *via* co-assembly of the BTA-based monomers. (3) Cellular internalization of BTA polymers. Imaging of HK-2 cells over several hours, which were incubated with cationic and dye labelled BTA aggregates. Scale bars 10 μ M. Image adapted from reference 52.

Host-guest complexes

Supramolecular polymers based on the host-guest complexation of monomers in water compose another class in the field. Macrocyclic hosts such as cyclodextrins, cucurbiturils, or calixarenes are commonly used blocks to obtain host-guest mediated supramolecular polymers, together with their complementary guest molecules.⁵³⁻⁵⁵ An example is the work of Harada and co-workers on cyclodextrin-guest complexes.^{56,57} In one system, they coupled a guest *t*-Bu-cinnamoyl to the edge of a host α -cyclodextrin to trigger the formation of chiral supramolecular polymers by insertion of the *t*-butyl aliphatic moiety in the hydrophobic pocket of the cyclodextrin, resulting in a degree of polymerization of approximately 15

monomers from a single monomer (Figure 1.6a).⁵⁸ By a similar approach, a cyclodextrin-based co-polymer was developed based on the selective binding of different guests by α -CD and β -CD coupled to guest molecules adamantane and *t*-Boc cinnamoyl using two different building blocks to form an alternating copolymer. (Figure 1.6b).⁵⁹

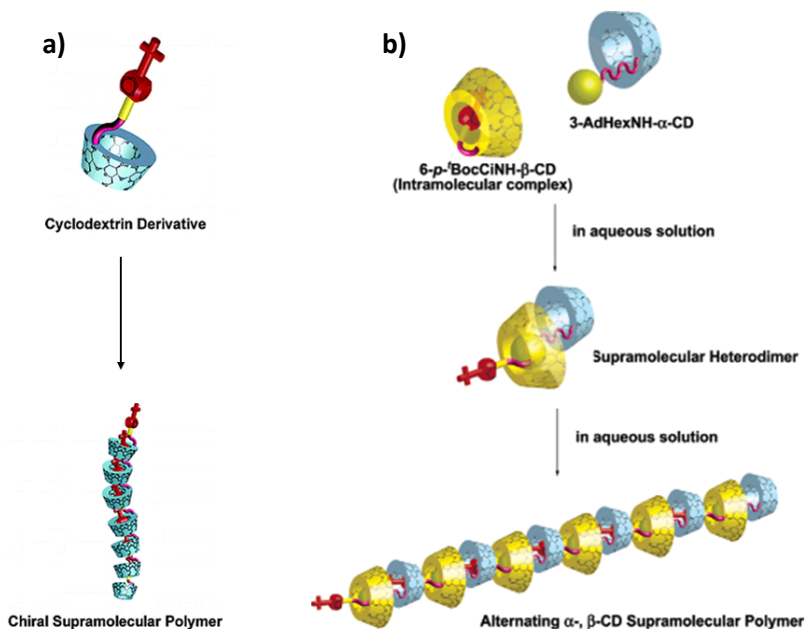


Figure 1.6. (a) Cyclodextrin-based chiral supramolecular polymers consisting of repeating units of *t*-Bu-cinnamoyl (guest) linked to the edge of α -cyclodextrin (host). (b) α -cyclodextrin-adamantane and β -cyclodextrin-*t*-Bu-cinnamoyl building blocks forming a co-polymer of approximately 30 monomers long. Images adapted from reference 58 (a) and 59 (b).

1.4.2 Biomaterials based on supramolecular polymers

The supramolecular polymer materials used in the biomaterials field can be subdivided into two major designs: the first one corresponds to the one-dimensional, shape persistent objects (Figure 1.7, top box) consisting of stacked motifs, while the second group corresponds to polymeric precursors with molecular recognition motifs that form networked structures. Because of their unique properties that include responsiveness, modularity, and tuneability, in comparison to their covalent counterparts there is growing recognition of their applicability in this area with several promising *in vitro* and *in vivo* studies.^{60–64} As drug delivery platforms,^{65,66} supramolecular materials are envisaged to promote the

solubilization of insoluble drugs, small hydrophobic molecules or proteins, while providing a platform to control the circulation time and release within the body. For instance, supramolecular polymers based on peptide amphiphiles have been employed as drug carriers for the encapsulation of poorly soluble drugs, such as camptothecin, with the inhibition of tumor growth in a mouse model.⁶⁷ Another area of interest concerns the engineering of 3D cell microenvironments, in which the development of artificial extracellular matrices with tunable mechanics, bioactivity and materials is sought after for applications in the fields of tissue engineering⁶⁸ and regenerative medicine.^{63,69} Typically, these matrices are prepared with bioactive peptides or proteins to provide cell-specific cues.⁷⁰⁻⁷² These soft supramolecular materials can be employed to support and deliver cells by their encapsulation and have been therefore explored for reconstituting aspects of functional tissues,⁷³ delivery of cells⁷⁴ or repair of native tissues.⁷⁵

Chapter 1

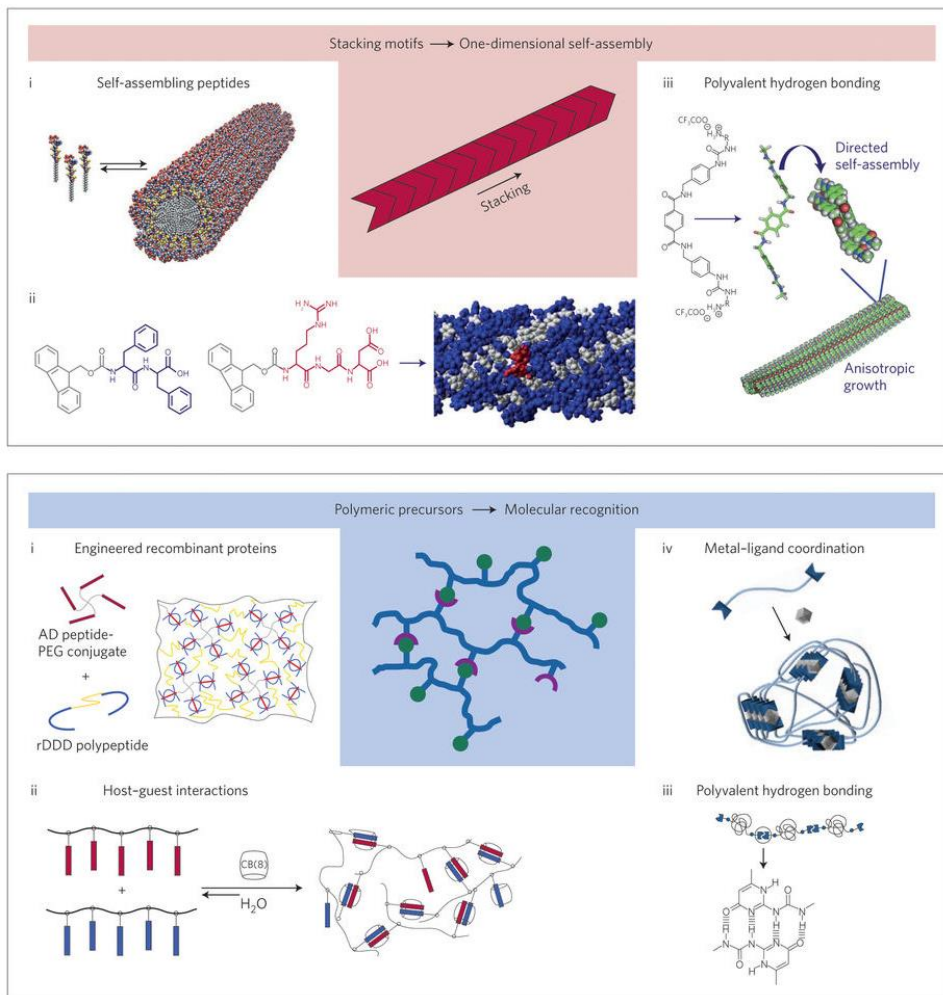


Figure 1.7. (Top) Examples of one-dimensional self-assemblies based on stacking motifs. (Bottom) Crosslinked polymeric blocks or extended polymer chains by molecular recognition motifs. Figure adapted from reference 64.

1.5 Squaramides

Squaramides consist of a cyclobutenedione ring with two N-H donor groups opposite two carbonyls (Figure 1.8).⁷⁶⁻⁷⁸ Squaramides present a rigid and planar ring system that is stabilized by the sp^2 -hybridized nitrogens, with the potential for the nitrogen lone pairs to be conjugated with the π -system of the cyclobutenedione ring system. Their partial aromatic character (Hückel's Rule, $4n + 2$, $n = 0$) can be enhanced upon complexation of ions at either side of the ring by hydrogen bond formation.^{79,80} Frontera and co-workers computed the aromatic character of the squaramide ring with respect to ion binding according to energetic, magnetic and electronic criteria (see sub-section 1.4). They observed the NICS values became more negative upon complexation (NICS (0.6) = -6.3 ppm for the isolated squaramide ring, -7.6 ppm for N-H hydrogen bond formation with carboxylates, -8.1 ppm for C=O bond formation with ammonium, and -8.7 ppm when both sides are engaged with the aforementioned ions) suggesting that the increase in aromaticity facilitates exceedingly high H-bond acceptor and donor characters (as a reference, a fully aromatic system (i.e. benzene) has a NICS (0.6) value of -10.1 ppm).

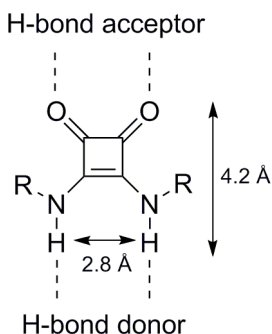


Figure 1.8. Molecular structure of the squaramide synthon.

Squaramides have been applied to mimic the anion transport behavior of complex proteins through ion channels across lipid bilayers as demonstrated by Gale and co-workers⁸¹⁻⁸³ Moreover, they have been extensively explored in the ion receptor field in various presentations including macrocyclic compounds and polymers showing improved ion selectivity and affinity. Squaramide ion transporters show a better anion-transport activity compared against analogous transporters based on ureas and thioureas. The association constant (K_a) of a

family of analogous molecules consisting of these three motifs was calculated by $^1\text{H-NMR}$ spectroscopic studies using Bu_4NCl salts in $\text{DMSO-d}_6/0.5\%$ water.⁸¹ The K_a measured for squaramides with these ions was on the order of $260\text{-}643\text{ M}^{-1}$, while the urea motifs were on the order of $31\text{-}88\text{ M}^{-1}$ and the thiourea on the order of $15\text{-}43\text{ M}^{-1}$ (this range of values is due to the substituents used for the design of the anion transporter). These results are relevant in this area, showing that squaramides are ideal candidates for anion transport activities, with improved properties compared to their urea and thiourea analogues, without increasing significantly the hydrophobicity. Squaramides are also being increasingly explored as scaffolds for new therapies.^{84,85} Clinical candidates such as Perzinfotel or Navarixin, both consisting of a double substituted squaramide moieties, have been studied for the treatment of strokes and chronic obstructive pulmonary disease, respectively. Squaramides have also been applied in the area of organocatalysis due to their capacity to act as more effective hydrogen-bond donors relative to the currently existing thiourea or urea scaffolds. Squaramide-based organocatalysts have been used to carry out organic transformations such as Michael additions⁸⁶, Friedel-Craft reactions⁸⁷, 1-4 additions of malonates to nitroolefins⁸⁸ or addition of 1,3-dicarbonyls to acyl phosphonate compounds⁸⁹. These are just few examples of the extensive applications squaramides have in the area of catalysis. Finally, squaramides have been applied in the bioconjugation field due to their stability to hydrolysis in aqueous medium, with special attention on the formation of glycoconjugates. Yan and co-workers used the squaramide motif to link carbohydrate conjugates based on lactoside and dinucleotide in water, showing the potential of these units as linkers.⁹⁰ Rotger and co-workers designed a peptidomimetic structure with a N-methylated squaramide, by a conventional solid-phase peptide synthesis. This hybrid was found to fold in water, and due to its dynamic properties, the authors stated that this motif could be used to design bioactive peptidomimetic molecules.⁹¹

1.6 Aromaticity

Aromaticity is a core concept in organic chemistry, but it is challenging to define because of its multidimensional character. This concept is used to describe the unusual properties of a group of cyclic and unsaturated planar organic molecules relative to their acyclic analogues.⁹²⁻⁹⁵ Some of these properties are: (1) increased molecular stability, (2) intermediate bond lengths in between single and double bonds, (3) preference for substitution to addition with retention of the π -electron

arrangement, and (4) induction of π -electron ring currents when the systems are exposed to external magnetic fields, translating into specific and characteristic values of $^1\text{H-NMR}$ chemical shifts that are downfield compared to non-aromatic compounds.⁹⁶ Qualitatively, cyclic unsaturated compounds are classified as aromatic according when they satisfy Hückel's rule, which states that cyclic (and planar) π -electron systems with $(4n + 2)$ π -electrons are more stable than those containing $4n$ π -electrons. Because aromaticity cannot be quantified easily, this concept is probed computationally. Computational methods that tackle the various criteria such as nucleus-independent chemical shift (NICS) (magnetic),^{97,98} harmonic oscillator model of aromaticity (HOMA) or harmonic oscillator model of electron delocalization (HOMED) (geometric)⁹⁶ and aromatic stabilization energies (ASE) or block-localized wave functions (BLW) (energetic) can be employed.⁹⁴ These computational methods are applied in chapters 2 and 3.

Aromaticity has been used to explain the high efficiency of a number of organic reactions such as in the Cope rearrangement and [1,5]-shifts.⁹⁹ Recently, the effect of aromaticity on the hydrogen-bonding interaction has started to be explored.^{100–103} Schleyer, Wu and co-workers showed computationally that the hydrogen-bonding strength can be affected by the aromatic character of heterocyclic rings upon dimerization.¹⁰¹ They compared 2-pyridinone dimers against 2-hydroxypyridine dimers. Upon dimerization of 2-pyridinone, the NICS index shifted from -10.6 ppm (monomer) to -13.4 ppm (dimer), suggesting an increase in $4n+2$ π -electron delocalization or aromatic character of the ring with a 45% increase of the interaction energy, compared to its acyclic analogue (Figures 1.9a and 1.9b). On the other hand, the dimerization of 2-hydroxypyridine showed the opposite effect. A NICS value of -24.2 ppm was estimated for the single monomer while the dimer displayed a NICS value of -21.4 ppm, suggesting a loss of its aromatic sextet character upon hydrogen bonding being weakened relative to their acyclic analogues. Hence, the computed dimerization energy of 2-hydroxypyridine decreased by 21% compared with its acyclic analogue dimer (Figure 1.9c and 1.9d). By similar methods, Wu, Fernández and co-workers showed that the aromatic character of 4-pyridone can be increased through the π -polarization of the oligomers by hydrogen-bonding, resulting in an increase in strength of the hydrogen bond interactions.¹⁰²

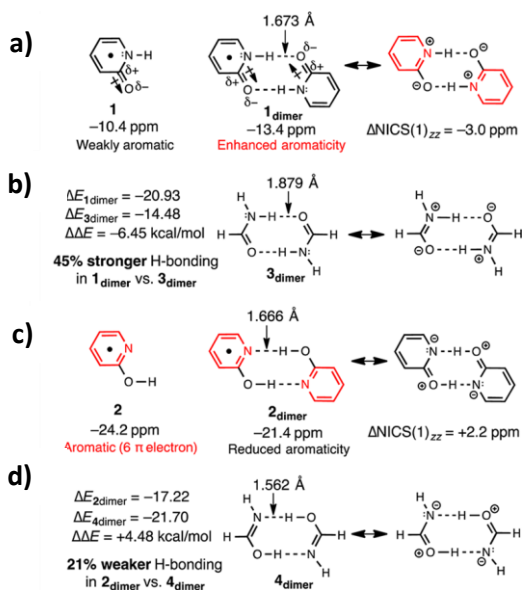


Figure 1.9. NICS, hydrogen-bond lengths and dimerization energies of (a) 2-pyridinone, (b) formamide, (c) 2-hydroxypyridine and (d) hydroxyimine dimers. Figure adapted from reference 101.

1.7. Aim and outline

The development of synthetic supramolecular polymers in aqueous media and their potential for use as biomaterials has garnered much attention over the last few years. The examples disclosed in this introductory chapter are characterized by a broad diversity in molecular design, which is necessary to explore the supramolecular material playing field. However, self-assembled biomaterials and understanding the contribution of the non-covalent interactions involved in their self-assembly still remains challenging. When water is involved in the self-assembly process, hydrophobicity is often employed as the major driving force, with other directional non-covalent forces being used to promote their one-dimensional aggregation. Hydrogen bonding takes the lead here in terms of directionality compared to other non-covalent bonding forces and is often included in the monomer design.

In this thesis, I aim to develop and study a robust and adaptable scaffold for supramolecular polymer self-assembly in water. For this purpose, I rely on the use of squaramides to provide directional interactions in order to drive the formation of one-dimensional aggregates through self-assembly. The interplay of hydrogen-bonding and aromaticity in the monomer self-assembly process is explored in the

squaramide unit, by examining the consequence of aromatic gain on this process. Additionally, by systematic modification of the monomer structure, a library of supramolecular structures with different morphologies is developed and their use as future drug nanovehicles is studied in an *in vivo* model involving zebrafish embryos.

In **chapter 2**, I explore the potential for synergy between hydrogen-bonding and aromaticity in the squaramide unit upon its supramolecular polymerization in water. The synthesis and design of a squaramide-based bolaamphiphile is reported. Experimentally, the morphological aspect of the resulting aggregates is explored by a combination of microscopic (cryo-TEM) and scattering techniques (DLS and SAXS). At the molecular level, spectroscopic techniques reveal the influence of the self-assembly on the geometric (FTIR) and electronic (UV-Vis) properties of the squaramide synthons. Finally, by a combination of computational methods (NICS, HOMA and ASE), I explore the consequence of a gain in aromatic character on the self-assembly of the squaramide-based bolaamphiphiles.

In **chapter 3**, the concept of aromaticity-modulated non-covalent interactions in squaramides is further explored. The oxosquaramides presented in chapter 2 are thionated. Following a similar strategy, the size and shape of the self-assembled aggregates is studied by microscopy (cryo-TEM) and scattering (DLS and SAXS) in water. The changes at the molecular level upon self-assembly on the electronic and geometric properties are investigated by UV-Vis and FTIR spectroscopy, while changes to the aromatic character of both ring systems were compared computationally. Whereas oxosquaramides self-assemble in a head-to-tail hydrogen-bonding stacked configuration, and both increase their aromatic character upon self-assembly.

In **chapter 4**, a library of systematically modified squaramide-based bolaamphiphiles is examined for their capacity to self-assemble into various morphologies. Aggregate morphologies from spheres to fibers are achieved by simply modifying the monomer structure, namely their hydrophilic and hydrophobic domains. Spectroscopic (UV-Vis and IR) and microscopy (cryo-TEM and SAXS) studies are pursued to further understand the self-assembly of such aggregates at various length scales. Control over their morphology opens the door for their use as supramolecular polymer nanoparticles for drug delivery.

Chapter 1

In **chapter 5**, the distribution and circulation behavior of spherical, rod and fibrillar squaramide-based supramolecular structures in a zebrafish embryo *in vivo* model is explored. First, I report the synthesis of a cyanine-labeled reporter molecule, which is further used for fluorescent labelling the various squaramide-based bolaamphiphile structures. The co-assembly of the monomers is followed by cryo-TEM and zeta potential, while the dynamics and exchange kinetics of the three different co-assembled squaramide-based supramolecular structures are investigated by fluorescence spectroscopy through FRET in water. Finally, the tracking of the aggregates *in vivo* is achieved in a zebrafish embryo model by confocal microscopy, showing distinct distribution and clearance of the various structures through a change in shape. Additionally, I examine the potential for macrophage uptake of the nanoparticle morphologies.

1.8 References

- (1) Whitesides, G.; Mathias, J.; Seto, C. *Science* **1991**, *254* (5036), 1312.
- (2) Mendes, A. C.; Baran, E. T.; Reis, R. L.; Azevedo, H. S. *Wiley Interdiscip. Rev. Nanomedicine Nanobiotechnology* **2013**, *5* (6), 582.
- (3) Liu, Z.; Qiao, J.; Niu, Z.; Wang, Q. *Chem. Soc. Rev.* **2012**, *41* (18), 6178.
- (4) Li, H.; LaBean, T. H.; Leong, K. W. *Interface Focus* **2011**, *1* (5), 702.
- (5) King, J.; Haase-Pettingell, C.; Gossard, D. *Am. Sci.* **2002**, *90* (5), 445.
- (6) Fändrich, M. *Cell. Mol. Life Sci.* **2007**, *64* (16), 2066.
- (7) Fitzpatrick, A. W. P. *Proc Natl Acad Sci U S A* **2013**, *5590* (4), 5468.
- (8) Wetzel, R. *Acc. Chem. Res.* **2006**, *39* (9), 671.
- (9) Pollard, T. D.; Cooper, J. A. *Science* **2009**, *326* (5957), 1208.
- (10) Holmes, K. C.; Popp, D.; Gebhard, W.; Kabsch, W. *Nature*. 1990, 44–49.
- (11) Fujii, T.; Iwane, A. H.; Yanagida, T.; Namba, K. *Nature* **2010**, *467* (7316), 724.
- (12) Oosawa, F.; Kasai, M. *J. Mol. Biol.* **1962**, *4* (1), 10.
- (13) Southall, N. T.; Dill, K. A.; Haymet, A. D. J. *J. Phys. Chem.* **2002**, *106* (3), 521.
- (14) Chandler, D. *Nature* **2002**, *417* (30), 491.
- (15) Wilson, A. J. *Soft Matter* **2007**, *3* (4), 409.

- (16) Gilli, P.; Gilli, G. *J. Mol. Struct.* **2010**, *972*, 2.
- (17) Gilli, P.; Bertolasi, V.; Ferretti, V.; Gilli, G. *J. Am. Chem. Soc.* **2000**, *122* (42), 10405.
- (18) Laurence, C.; Berthelot, M. *Perspect. Drug Discov. Des.* **2000**, *18*, 39.
- (19) Steed, Jonathan W.; Atwood, J. L. *Supramolecular Chemistry*, Second ed.; Wiley, Ed.; 2009.
- (20) Bellot, M.; Bouteiller, L. *Langmuir* **2008**, *24* (24), 14176.
- (21) Lortie, F.; Boileau, S.; Bouteiller, L.; Chassenieux, C.; Demé, B.; Ducouret, G.; Jalabert, M.; Lauprêtre, F.; Terech, P. *Langmuir* **2002**, *18* (19), 7218.
- (22) Cantekin, S.; Greef, F. A. De; Palmans, A. R. A. *Chem Soc Rev* **2012**, *41*, 6125.
- (23) Israelachvili, J. N. *Intermolecular and Surface Forces*, 3rd ed.; Academic Press: Amsterdam, 2011.
- (24) Lehn, J. -M. *Angew. Chemie Int. Ed. English* **1990**, *29* (11), 1304.
- (25) Fouquey, C.; Lehn, J. -M.; Levelut, A. -M. *Adv. Mater.* **1990**, *2* (5), 254.
- (26) Smulders, M. M. J.; Nieuwenhuizen, M. M. L.; De Greef, T. F. A.; Van Der Schoot, P.; Schenning, A. P. H. J.; Meijer, E. W. *Chem. Eur. J.* **2010**, *16* (1), 362.
- (27) De Greef, F. A., Smulders, M. J., Wolffs, M., Schenning, A. P. H. J., Sijbesma, R.P., Meijers, E. W. *Chem. Rev.* **2009**, *109* (11), 5687.
- (28) Zhao, D.; Moore, J. S. *Org. Biomol. Chem.* **2003**, *1* (20), 3471.
- (29) Rest, C.; Kandaneli, R.; Fernández, G. *Chem. Soc. Rev.* **2015**, *44* (8), 2543.
- (30) Rybtchinski, B. *ACS Nano* **2011**, *5* (9), 6791.
- (31) Krieg, E.; Bastings, M. M. C.; Besenius, P.; Rybtchinski, B. *Chem. Rev.* **2016**, *16*, 2414.
- (32) Krieg, E.; Rybtchinski, B. *Chem. Eur. J.* **2011**, *17* (33), 9016.
- (33) Brocorens, P.; Linares, M.; Guyard-Duhayon, C.; Guillot, R.; Andrioletti, B.; Suhr, D.; Isare, B.; Lazzaroni, R.; Bouteiller, L. *J. Phys. Chem. B* **2013**, *117* (17), 5379.
- (34) Tantakitti, F.; Boekhoven, J.; Wang, X.; Kazantsev, R. V.; Yu, T.; Li, J.; Zhuang, E.; Zandi, R.; Ortony, J. H.; Newcomb, C. J.; Palmer, L. C.; Shekhawat, G. S.; de la Cruz, M. O.; Schatz, G. C.; Stupp, S. I. *Nat. Mater.* **2016**, *15* (4), 469.
- (35) Hartgerink, J. D. *Science* **2001**, *294* (5547), 1684.
- (36) Silva, G. A. *Science* **2004**, *303* (5662), 1352.

Chapter 1

- (37) Krieg, E.; Weissman, H.; Shimoni, E.; Baris, A.; Rybtchinski, B. *J. Am. Chem. Soc.* **2014**, *136* (26), 9443.
- (38) Fuhrhop, J. H.; Wang, T. *Chem. Rev.* **2004**, *104*, 2901.
- (39) Nuraje, N.; Bai, H.; Su, K. *Prog. Polym. Sci.* **2013**, *38* (2), 302.
- (40) Rudolph, T.; Kumar Allampally, N.; Fernández, G.; Schacher, F. H. *Chem. Eur. J.* **2014**, *20* (43), 13871.
- (41) Chebotareva, N.; Bomans, P. H. H.; Frederik, P. M.; Sommerdijk, N. J. M.; Sijbesma, R. P. *Chem. Commun.* **2005**, No. 39, 4967.
- (42) Pal, A.; Voudouris, P.; Koenigs, M. M. E.; Besenius, P.; Wyss, H. M.; Degirmenci, V.; Sijbesma, R. P. *Soft Matter* **2014**, *10* (7), 952.
- (43) Fernandez-Castano Romera, M.; Lafleur, R. P. M.; Guibert, C.; Voets, I. K.; Storm, C.; Sijbesma, R. P. *Angew. Chemie - Int. Ed.* **2017**, 8771.
- (44) Pal, A.; Karthikeyan, S.; Sijbesma, R. *J. Am. Chem. Soc.* **2010**, *132* (23), 7842.
- (45) Obert, E.; Bellot, M.; Bouteiller, L.; Andrioletti, F.; Lehen-Ferrenbach, C.; Boué, F. *J. Am. Chem. Soc.* **2007**, *129* (50), 15601.
- (46) Eelkema, R.; van Esch, J. H. *Org. Biomol. Chem.* **2014**, 6292.
- (47) Boekhoven, J.; Poolman, J. M.; Maity, C.; Li, F.; van der Mee, L.; Minkenberg, C. B.; Mendes, E.; van Esch, J. H.; Eelkema, R. *Nat Chem* **2013**, *5* (5), 433.
- (48) Boekhoven, J.; Brizard, A. M.; Van Rijn, P.; Stuart, M. C. A.; Eelkema, R.; Van Esch, J. H. *Angew. Chemie - Int. Ed.* **2011**, *50* (51), 12285.
- (49) Leenders, C. M. A.; Albertazzi, L.; Mes, T.; Koenigs, M. M. E.; Palmans, A. R. A.; Meijer, E. W. *Chem. Commun.* **2013**, 49 (19), 1963.
- (50) Leenders, C. M. A.; Baker, M. B.; Pijpers, I. A. B.; Lafleur, R. P. M.; Albertazzi, L.; Palmans, A. R. A.; Meijer, E. W. *Soft Matter* **2016**, *12* (11), 2887.
- (51) Albertazzi, L.; Hofstad, R. W. Van Der; Meijer, E. W. *Science* **2014**, *491* (6183), 10.
- (52) Bakker, M. H.; Lee, C. C.; Meijer, E. W.; Dankers, P. Y. W.; Albertazzi, L. *ACS Nano* **2016**, *10* (2), 1845.
- (53) Dong, S.; Zheng, B.; Wang, F.; Huang, F. *Acc. Chem. Res.* **2014**, *47* (7), 1982.
- (54) Ni, X. L.; Chen, S.; Yang, Y.; Tao, Z. *J. Am. Chem. Soc.* **2016**, *138* (19), 6177.
- (55) Wang, L.; Li, L. L.; Fan, Y. S.; Wang, H. *Adv. Mater.* **2013**, *25* (28), 3888.

- (56) Harada, A.; Takashima, Y.; Nakahata, M. *Acc. Chem. Res.* **2014**, *47* (7), 2128.
- (57) Harada, A.; Hashidzume, A.; Takashima, Y. *Adv. Polym. Sci.* **2006**, *201* (1), 1.
- (58) Miyauchi, M.; Takashima, Y.; Yamaguchi, H.; Harada, A. *J. Am. Chem. Soc.* **2005**, *127* (9), 2984.
- (59) Miyauchi, M.; Harada, A. *J. Am. Chem. Soc.* **2004**, *126* (37), 11418.
- (60) Stupp, S. I. *Nano Lett.* **2010**, *10* (12), 4783.
- (61) Shoichet, M. S. *Macromolecules* **2010**, *43* (2), 581.
- (62) Drury, J. L.; Mooney, D. J. *Biomaterials* **2003**, *24* (24), 4337.
- (63) Boekhoven, J.; Stupp, S. I. *Adv. Mater.* **2014**, *26* (11), 1642.
- (64) Webber, M. J.; Appel, E. A.; Meijer, E. W.; Langer, R. *Nat. Mater.* **2015**, *15* (1), 13.
- (65) Rajangam, K.; Behanna, H. A.; Hui, M. J.; Han, X.; Hulvat, J. F.; Lomasney, J. W.; Stupp, S. I. *Nano Lett.* **2006**, *6* (9), 2086.
- (66) Zhang, P.; Cheetham, A. G.; Lin, Y. A.; Cui, H. *ACS Nano* **2013**, *7* (7), 5965.
- (67) Soukasene, S.; Toft, D. J.; Moyer, T. J.; Lu, H.; Lee, H.; Standley, S. M.; Cryns, V. L.; Stupp, S. I. *ACS Nano* **2011**, *5* (11), 9113.
- (68) Soranno, D. E.; Lu, H. D.; Weber, H. M.; Rai, R.; Burdick, J. A. *J. Biomed. Mater. Res. - Part A* **2014**, *102* (7), 2173.
- (69) Stupp, S. I. *Mrs Bull.* **2005**, *30* (7), 546.
- (70) Parisi-Amon, A.; Mulyasasmita, W.; Chung, C.; Heilshorn, S. C. *Adv. Healthc. Mater.* **2013**, *2* (3), 428.
- (71) Mulyasasmita, W.; Cai, L.; Dewi, R. E.; Jha, A.; Ullmann, S. D.; Luong, R. H.; Huang, N. F.; Heilshorn, S. C. *J. Control. Release* **2014**, *191*, 71.
- (72) Storrie, H.; Guler, M. O.; Abu-Amara, S. N.; Volberg, T.; Rao, M.; Geiger, B.; Stupp, S. I. *Biomaterials* **2007**, *28* (31), 4608.
- (73) Dankers, P. Y. W.; Boomker, J. M.; Huizinga-van der Vlag, A.; Wisse, E.; Appel, W. P. J.; Smedts, F. M. M.; Harmsen, M. C.; Bosman, A. W.; Meijer, W.; van Luyn, M. J. A. *Biomaterials* **2011**, *32* (3), 723.
- (74) Padin-Iruega, M. E.; Misao, Y.; Davis, M. E.; Segers, V. F. M.; Esposito, G.; Tokunou, T.; Urbanek, K.; Hosoda, T.; Rota, M.; Anversa, P.; Leri, A.; Lee, R. T.; Kajstura, J. *Circulation* **2009**, *120* (10), 876.

Chapter 1

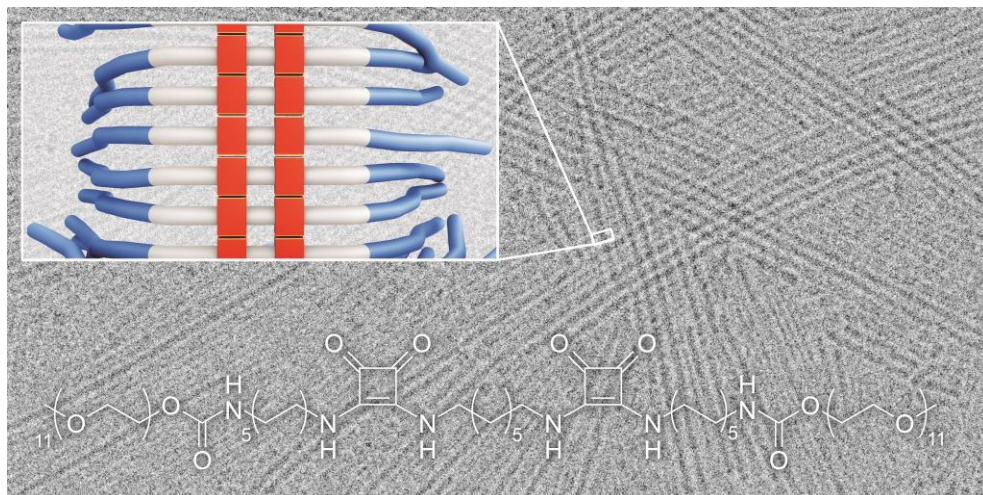
- (75) Ellis-Behnke, R. G.; Liang, Y.-X.; You, S.-W.; Tay, D. K. C.; Zhang, S.; So, K.-F.; Schneider, G. E. *Proc. Natl. Acad. Sci. U. S. A.* **2006**, *103* (13), 5054.
- (76) Alemán, J.; Parra, A.; Jiang, H.; Jørgensen, K. A. *Chem. Eur. J.* **2011**, *17* (25), 6890.
- (77) Ian Storer, R.; Aciro, C.; Jones, L. H. *Chem. Soc. Rev.* **2011**, *40* (5), 2330.
- (78) Wurm, F. R.; Klok, H.-A. *Chem. Soc. Rev.* **2013**, *42* (42), 8179.
- (79) Quiñonero, D.; Garau, C.; Frontera, A.; Ballester, P.; Costa, A.; Deyà, P. M. *Chemistry* **2002**, *8* (2), 433.
- (80) Quiñonero, D.; Frontera, A.; Ballester, P.; Deyà, P. M. *Tetrahedron Lett.* **2000**, *41* (12), 2001.
- (81) Busschaert, N.; Kirby, I. L.; Young, S.; Coles, S. J.; Horton, P. N.; Light, M. E.; Gale, P. A. *Angew. Chemie - Int. Ed.* **2012**, *51* (18), 4426.
- (82) Edwards, S. J.; Valkenier, H.; Busschaert, N.; Gale, P. A.; Davis, A. P. *Angew. Chemie - Int. Ed.* **2015**, *54* (15), 4592.
- (83) Busschaert, N.; Park, S.-H.; Baek, K.-H.; Choi, Y. P.; Park, J.; Howe, E. N. W.; Hiscock, J. R.; Karagiannidis, L. E.; Marques, I.; Félix, V.; Namkung, W.; Sessler, J. L.; Gale, P. A.; Shin, I. *Nat. Chem.* **2017**, *9*, 1.
- (84) Olmo, F.; Rotger, C.; Ramírez-Macías, I.; Martínez, L.; Marín, C.; Carreras, L.; Urbanová, K.; Vega, M.; Chaves-Lemaun, G.; Sampedro, A.; Rosales, M. J.; Sánchez-Moreno, M.; Costa, A. *J. Med. Chem.* **2014**, *57* (3), 987.
- (85) Ribeiro, C. J. A.; Espadinha, M.; Machado, M.; Gut, J.; Gonçalves, L. M.; Rosenthal, P. J.; Prudêncio, M.; Moreira, R.; Santos, M. M. M. *Bioorganic Med. Chem.* **2016**, *24* (8), 1786.
- (86) Yang, K. S.; Nibbs, A. E.; Türkmen, Y. E.; Rawal, V. H. *J. Am. Chem. Soc.* **2013**, *135* (43), 16050.
- (87) Zhu, Y.; Malerich, J. P.; Rawal, V. H. *Angew. Chemie - Int. Ed.* **2010**, *49* (1), 153.
- (88) Okino T.; Hoashi Y. and Takemoto Y. *J. Am. Chem. Soc.*, **2003**, *125*, 12672–12673.
- (89) Jiang H.; Paixao M. W.; Monge D. and Jørgensen K. A. *J. Am. Chem. Soc.*, **2010**, *132*, 2775–2783.
- (90) Yan H.; Aguilar A. L. and Zhao Y. *Bioorg. Med. Chem. Lett.*, **2007**, *17*, 6535–6538.
- (91) Martínez L.; Martorell G.; Sampedro A.; Ballester P.; Costa A. and Rotger C. *Org. Lett.*, **2015**, *17* (12), 2980–2983.
- (92) Karabiyik, H.; Sevinçek, R.; Karabiyik, H. *J. Mol. Struct.* **2014**, *1064* (1), 135.

- (93) Watson, K.; Park, S.; Im, J.; Nguyen, S. T.; *Ca. J. Am. Chem. Soc.* **2001**, *123* (17), 5592.
- (94) Cyrański, M. K.; Krygowski, T. M.; Katritzky, A. R.; Schleyer, P. V. R. *J. Org. Chem.* **2002**, *67* (4), 1333.
- (95) Krygowski, T. M.; Szatyłowicz, H.; Stasyuk, O. A.; Dominikowska, J.; Palusiak, M. *Chem. Rev.* **2014**, *114* (12), 6383.
- (96) Krygowski, T. M.; Cyrański, M. K. *Chem. Rev.* **2001**, *101* (5), 1385.
- (97) Chen, Z.; Wannere, C. S.; Corminboeuf, C.; Puchta, R.; Schleyer, P. von R. *Chem. Rev.* **2005**, *105* (10), 3842.
- (98) Schleyer, P. von R.; Maerker, C.; Dransfeld, A.; Jiao, H.; Hommes, N. J. R. van E. *J. Am. Chem. Soc.* **1996**, *118* (26), 6317.
- (99) Babinski, D. J.; Bao, X.; El Arba, M.; Chen, B.; Hrovat, D. A.; Borden, W. T.; Frantz, D. E. *J. Am. Chem. Soc.* **2012**, *134* (39), 16139.
- (100) Kakeshpour, T.; Wu, J. I.; Jackson, J. E. *J. Am. Chem. Soc.* **2016**, *138* (10), 3427.
- (101) Wu, J. I.; Jackson, J. E.; Schleyer, P. V. R. *J. Am. Chem. Soc.* **2014**, *136* (39), 13526.
- (102) Anand, M.; Fernández, I.; Schaefer, H. F.; Wu, J. I. *J. Comput. Chem.* **2016**, *37* (1), 59.
- (103) Schleyer, P. V. R.; Wu, J. I.; Cossío, F. P.; Fernández, I. *Chem. Soc. Rev.* **2014**, *43* (14), 4909.

Chapter 1

CHAPTER 2

Aromatic gain in a supramolecular polymer



This chapter was published as an original research paper: Victorio Saez Talens, Pablo Englebienne, Thuat T. Trinh, Willem E. M. Noteborn, Ilja K. Voets, Roxanne E. Kieltyka, *Angew. Chem., Int. Ed.* **2015**, *54*, 10502-10506

2.1 Abstract

The synergy of aromatic gain and hydrogen bonding in a supramolecular polymer is explored. Partially aromatic bis-squaramide bolaamphiphiles were designed to self-assemble through a combination of hydrophobic, hydrogen-bonding, and aromatic effects into stiff, high-aspect-ratio fibers. UV and IR spectroscopy show electron delocalization and geometric changes within the squaramide ring indicative of strong hydrogen bonding and aromatic gain of the monomer units. The aromatic contribution to the interaction energy was further supported computationally by nucleus-independent chemical shift (NICS) and harmonic oscillator model of aromaticity (HOMA) indices, demonstrating greater aromatic character upon polymerization: at least 30% in a pentamer. The aromatic gain–hydrogen bonding synergy results in a significant increase in thermodynamic stability and a striking difference in aggregate morphology of the bis(squaramide) bolaamphiphile compared to isosteres that cannot engage in this effect.

2.2 Introduction

Aromatic gain is considered to be a thermodynamic driving force in several organic reactions. In aromatic substitutions, Bergman cyclizations, aromatic Cope rearrangements, [1,5]H sigmatropic shifts and [4+2] cyclizations, among others, the restoration of aromaticity helps to explain their exergonic character and increased efficiency.¹⁻⁶ In supramolecular polymers,⁷⁻¹⁷ where monomers are held together by non-covalent interactions resulting in higher-order aggregates with various topologies, the concept of aromatic gain in the construction of such systems is unexplored.

Aromaticity has captivated chemists since its introduction as a concept 150 years ago by Kekulé.¹⁸ In contrast to other chemical concepts, such as electronegativity or van der Waals radii, aromaticity is not a direct physical observable and its exact definition is the subject of much debate.¹⁹⁻²² Classically, cyclic π -conjugated compounds are aromatic when they show differences in geometric, energetic, and magnetic criteria relative to their acyclic analogues.²³⁻²⁵ In recent years, computational methods such as nucleus-independent chemical shift (NICS),^{24,26} harmonic oscillator model of aromaticity (HOMA),²⁷ and aromatic stabilization energies (ASE),²⁵ have grown in use to describe aromaticity. In the case of NICS, excellent correlation has been reported with experimental nuclear magnetic resonance data as well as other descriptors of aromaticity,¹⁹ thus opening the door to predict the aromaticity of new compounds and structures *a priori*. Very recently, NICS calculations demonstrated reciprocal hydrogen-bonding–aromaticity relationships that can have important consequences on the strength of hydrogen-bonding interactions.²⁸

Squaramides,^{29,30} which are composed of two NH hydrogen-bond donors opposite two carbonyl hydrogen-bond acceptors on a conformationally rigid cyclobutene ring, are predicted to show partial aromatic character.^{29,30} This character arises from the delocalization of the nitrogen lone pair into the cyclobutenedione ring system (Hückel's rule: $(4n + 2) \pi$ electrons, $n = 0$).³¹ In the solid state, catemers of disubstituted squaramides arranged in a head-to-tail motif have been reported³² and they may benefit from strong resonance-assisted hydrogen bonding (RAHB) interactions similar to squaric acids.³³ Applications of the squaramide unit have been found in medicinal chemistry, catalysis, and anion recognition.³⁴⁻³⁶ The capacity of squaramides to form strong hydrogen bonds that simultaneously

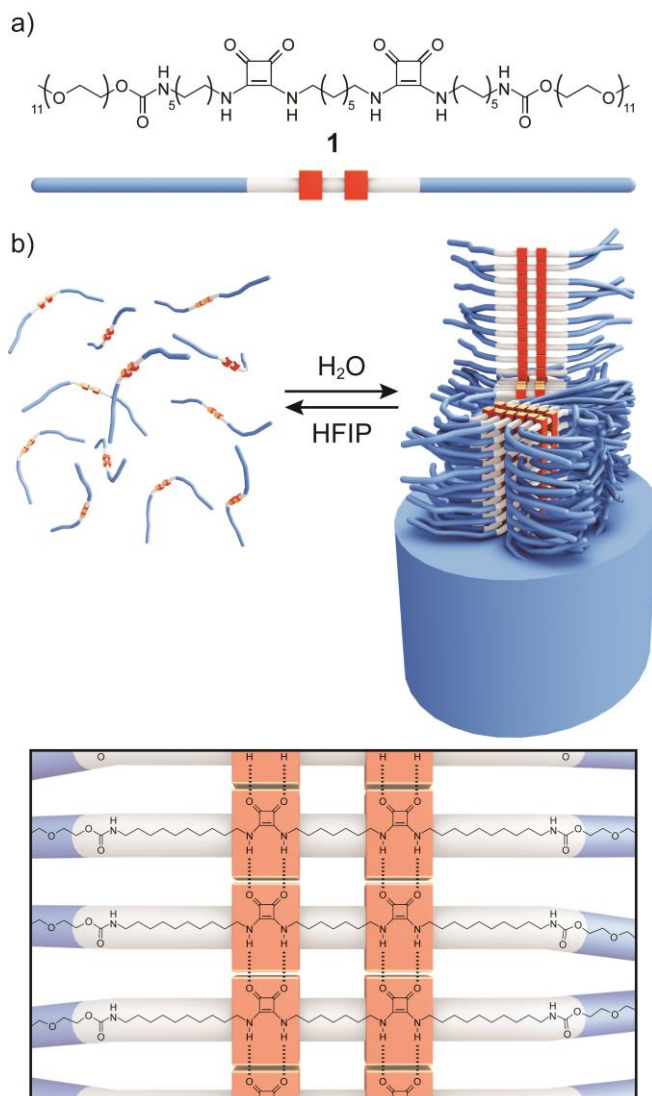


Figure 2.1. (a) Structure of the squaramide-based bolaamphiphile **1**. (b) Self-assembly of **1** into fibrillar structures, and depolymerization by hexafluoroisopropanol (HFIP). Within the fibrillar structure, hydrogen bonds are proposed to occur parallel to the fiber axis while π -interactions between squaramide bolaamphiphiles occur in the lateral direction, as depicted. (Bottom) Proposed hydrogen-bonding interactions between squaramide monomers.

influence their aromatic character is highly appealing to guide the formation of increasingly stable supramolecular polymers. Herein, I incorporate the squaramide synthon into a bolaamphiphilic construct that self-assembles into stiff fibers in water, and I explore the coupling of hydrogen-bonding and aromatic gain using experiment and computation.

2.3 Results and discussion

Compound **1** consists of two oligo(ethylene glycol) methyl ether chains opposite a central hydrophobic core with two embedded squaramide units (Figure 2.1). ^1H NMR spectra of **1** in D_2O were suggestive of strong aggregation that is resistant to thermal denaturation up to $65\text{ }^\circ\text{C}$ (Figure S2.1). Only ^1H NMR spectra recorded in CDCl_3 or HFIP- d_2 were well-resolved and suggestive of various degrees of depolymerization.

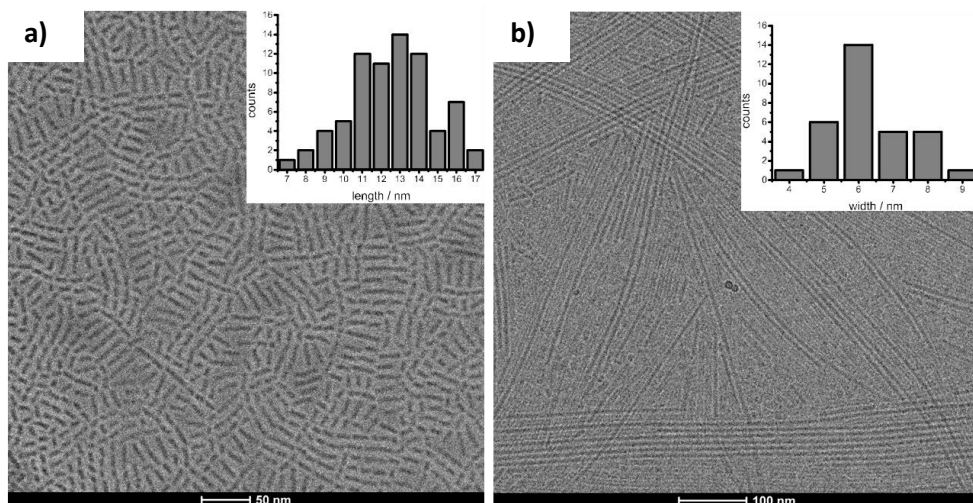


Figure 2.2. Cryo-TEM images of **1** in aqueous solution (1 wt%) after sonication: (a) $t=0$, and (b) $t=2$ weeks. Inset: Histograms of length (a) and width (b).

The effect of the squaramide synthon on the self-assembly of **1** in water was evaluated by cryo-transmission electron microscopy (cryo-TEM) and atomic force microscopy (AFM). Cryo-TEM images of **1** (1 wt%) displayed stiff, micrometer-long fibrils with a uniform diameter. Short, rod-like structures on the order of 12.6 ± 2.4 nm in length were found upon sonication (Figure 2.2a) and slowly progressed into micrometer-long fibers. Fibers of **1** were 6.4 ± 1.2 nm in diameter, on par with the length of the hydrophobic region of the bolaamphiphile (Figure 2.2b). By small-angle X-ray scattering measurements (SAXS, Figures 2.3, S2.3 and S2.4), a

cross-sectional radius (r_{cs}) of 3.5 nm and a cross-sectional mass per unit length (M_L) of 2.5×10^{20} – 6.0×10^{20} g nm⁻¹ was determined for fibers of **1**, indicating that approximately 10–30 squaramide bolaamphiphiles per nm can be found along the fiber axis. These results suggest that hydrogen bonds parallel to the fiber axis drive the formation of highly anisotropic fibers, meanwhile the combination of hydrophobic and π -interactions between squaramide moieties facilitate the assembly of several bolaamphiphiles in the lateral direction (Figure 2.1). To better understand the consequence of self-assembly on the squaramide synthon, spectroscopy at the molecular level was pursued. UV-Vis spectroscopy of **1** in water showed maxima at 255 and 329 nm, and a shoulder around 310 nm at the various concentrations tested (Figure S2.5). Disruption of the polymerized

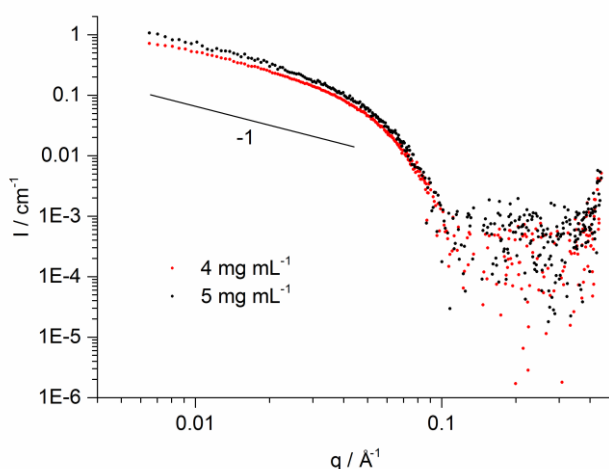


Figure 2.3. Small-angle X-ray scattering profiles of squaramide fibers collected at concentrations of 4 and 5 mg mL⁻¹.

state was achieved using both temperature (Figure 2.4a) and various solvents (Figure 2.4b). More specifically, hexafluoroisopropanol (HFIP), a potent hydrogen bond disruptor, promoted depolymerization resulting in the gradual loss of the red-shifted hydrogen-bonded squaramide N-H proton-donor π - π^* bands (329 nm) and the blue-shifted C=O proton-acceptor n - π^* bands (255 nm), concomitant with the growth of the non-hydrogen bonded monomer band (310 nm) (Figure 2.5).³⁷ These experimental trends are in agreement with TD-DFT calculations (Table S2.2), where two superimposed absorption bands of similar intensity corresponding to the HOMO–LUMO and HOMO–(LUMO+1) transitions are predicted for the monomer; in oligomers, the high wavelength band is

progressively red-shifted while the other appears blue-shifted. Self-assembly of **1** through strong hydrogen bonding interactions results in increased orbital overlap between squaramide units and further electron delocalization within the individual squaramide rings, enabling aromatic gain to occur (see supporting information chapter 2).

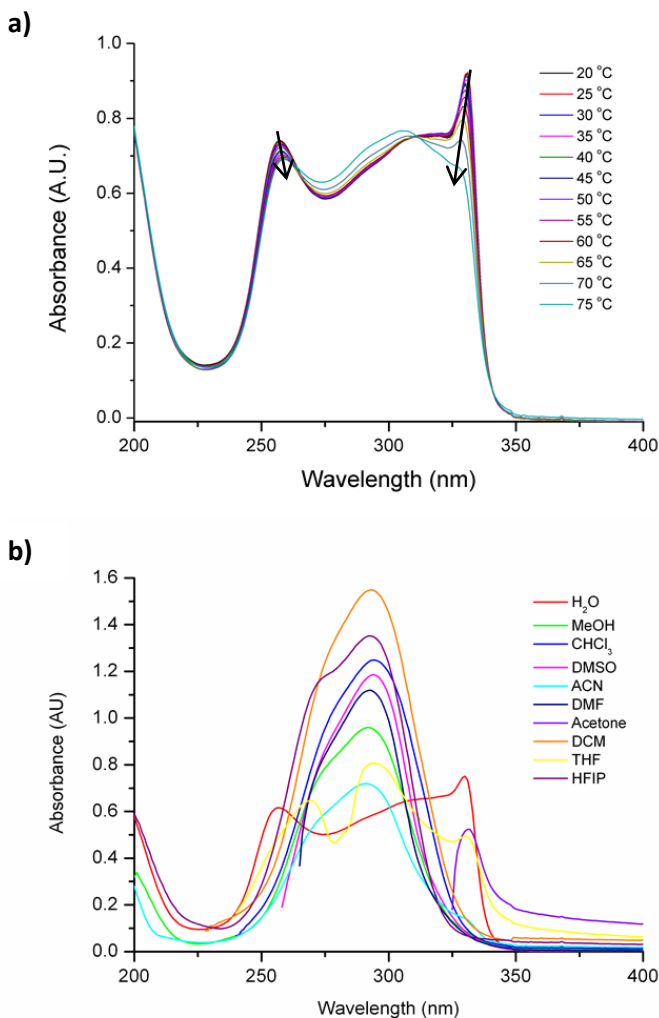


Figure 2.4. (a) Temperature-dependent UV-Vis spectra of **1** (0.029 mM) from 20 to 75 °C. (b) UV-Vis spectra of **1** (0.029 mM) in various solvents at room temperature.

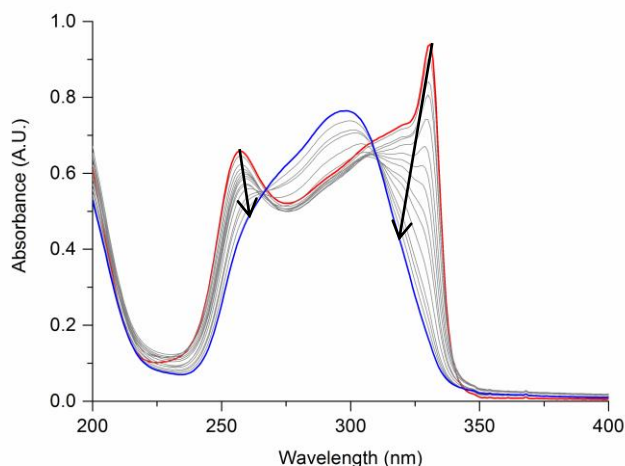


Figure 2.5. UV-Vis spectrum of **1** in water (0.029 mM) as a function of HFIP concentration (red line before HFIP titration, blue line after HFIP titration with 5 v/v%).

Geometric changes to the squaramides upon self-assembly were examined by IR spectroscopy. Solutions of **1** (2 wt%) in D₂O were measured at room temperature. Above the amide I region, a small broad band at 1796 cm⁻¹, consistent with squaramide ring breathing, was found experimentally (Figure 2.6) and confirmed by modeling (Table S2.3). In the amide I region, asymmetric and symmetric C=O stretches (1687, 1676, and 1642 cm⁻¹) of the squaramide and carbamate moieties were recorded. Strong hydrogen bonding of the squaramide units was observed through the N-H stretch at 3162 cm⁻¹ (inset in Figure 2.6). In HFIP-d₂, the blue-shifting of several bands such as the ring breathing (13 cm⁻¹) and symmetric C=O stretch (14 cm⁻¹) modes were observed and suggestive of depolymerization. Owing to lack of transparency of HFIP-d₂ in the N-H region, an approximation for free N-H stretch (3452 cm⁻¹) was made for **1** in CDCl₃ (Figure 2.7) The experimental data correlated well with *ab initio* calculations. These results revealed that bond lengths in the squaramide are systematically altered as a function of oligomer length (Figure 2.8a): double bonds become longer, whereas single bonds shorten, resulting in a ring with less bond length alternation. With these bond lengths, it was computed HOMA values of -0.015 and 0.516 for the isolated monomer and the central monomer in a pentamer, respectively, while a value of one is defined for aromatic compounds. Experiments point to strong

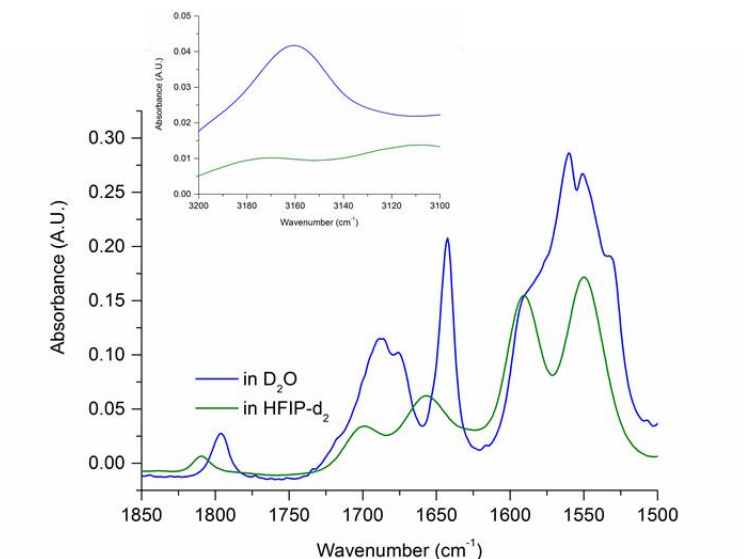


Figure 2.6. IR spectrum of **1** recorded in the amide I region and amide II in D₂O and [D₂]HFIP. Inset: N-H and C-H stretch region.

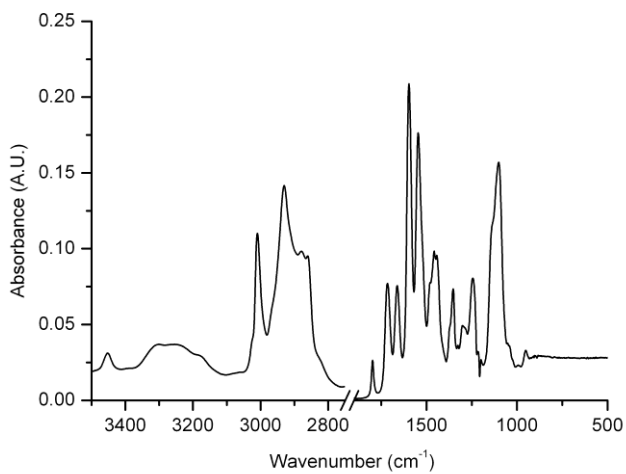


Figure 2.7. Infrared spectrum of **1** (2 wt%) in CHCl₃.

hydrogen bonding and computed geometric considerations demonstrate an increase in aromatic character within the squaramide unit due to supramolecular polymerization.

NICS-scan profiles,³⁸ a measurement of the magnetic shielding above and at the center of the ring, were computed on an axis passing through the center of the squaramide ring for monomers to pentamers to quantify the aromatic character upon oligomerization (NICS and NICS-scan profiles were computed by positioning

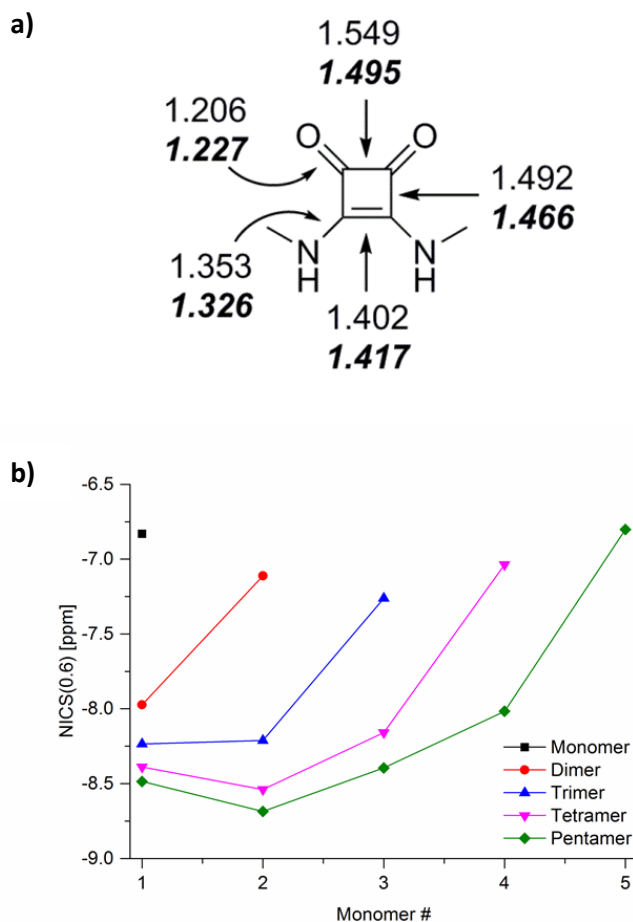


Figure 2.8. (a) Geometric changes (computed at the M06-2X/6-311+G(d,p) level of theory) in N-methyl squaramide between an isolated monomer (normal text) and the central monomer in a pentamer (in bold italics). (b) NICS values at a point 0.6 Å from the ring plane for an isolated monomer and each monomer in oligomers of length 2–5 (GIAO-M06-2X/6-311+G(d,p)).

a ghost atom at the center of the squaramide ring ranging from between 0 and 5 Å above it, see figure S2.10 with the NICS-scans for dimers, trimers, tetramers and pentamers). The profiles for the individual squaramide units were negative overall and exhibited a minimum around 0.6 Å, consistent with an aromatic ring. Upon increasing oligomer length, the NICS values became more negative without a change in the shape of the curves, suggestive of increased aromaticity. In particular, the change in NICS at 0.6 Å from the ring plane (Figure 2.8b) when going from a monomer (-6.8) to the central monomer of a pentamer (-8.4), is in line with previous reports.³⁹ Additionally, the aromatic stabilization energy accounts for at least 30% of the total interaction energy in a squaramide pentamer (-85.6 kJ mol⁻¹ out of - 271.7 kJmol⁻¹ including BSSE correction) using a heterodimer of vinylogous amides that cannot exhibit aromaticity as a reference (Table S.2.8 and S2.9).

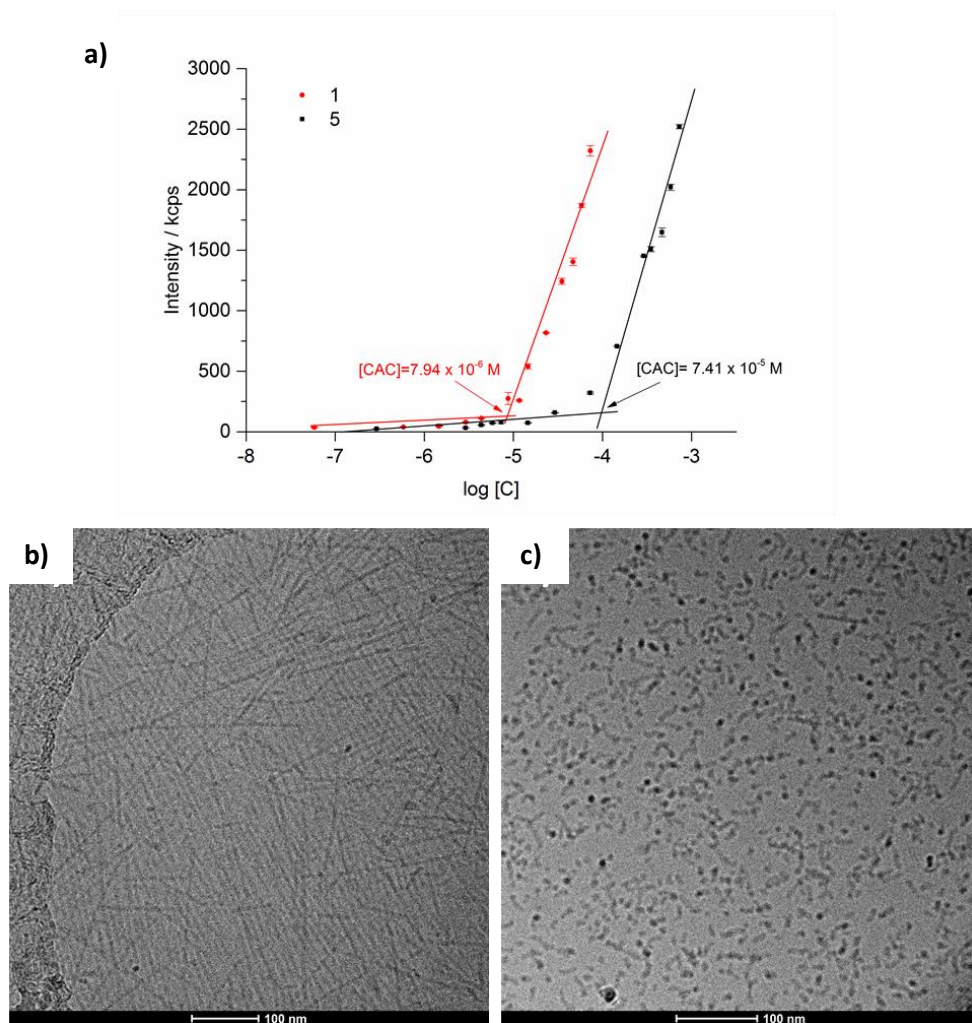


Figure 2.9. (a) Scattered intensity (1000 s^{-1}) as a function of concentration, $\log[C]$, of **1** and **5** using static light scattering (SLS) experiments to determine the critical aggregation concentration (CAC). Representative cryo-TEM images: the image (b) belongs to **1** and the image (c) to **5**, showing fibrils in the case of **1** and worm-like or spherical aggregates in the case of **5**.

I further investigated the thermodynamic consequence of aromatic gain experimentally by measuring the critical aggregation concentration (CAC) using static light scattering (SLS). An order of magnitude lower CAC, corresponding to a free energy difference $\Delta\Delta G_{\text{agg}} = -5.25 \text{ kJ mol}^{-1}$, was obtained for molecule **1** ($7.94 \times 10^{-6} \text{ M}$) in comparison to urea-based analogue **5** ($7.41 \times 10^{-5} \text{ M}$; see the supporting information section 2.6.15) (Figure 2.9a). These results are further supported by DFT calculations, where the interaction energy computed per hydrogen bond of

urea oligomers was found to be smaller (-23.9 vs. -35.6 kJ mol⁻¹ for pentamers) and does not increase as steeply with oligomer length (+18% vs. +30%). Intriguingly, a striking difference in the fiber morphology was found above the CAC of both molecules. Whereas **1** consistently formed long and stiff micron-sized fibers (Figure 2.9b), short worm-like or spherical aggregates were obtained for **5** (Figure 2.9c). Given the similarity of the hydrophilic and hydrophobic blocks, these results suggest that the coupling of aromatic gain and hydrogen-bonding in addition to the structural rigidity of the squaramide units act collectively to lower the critical aggregation concentration and propagate the formation of high-aspect-ratio fibers in water.

2.4 Conclusions

I found that the capacity of squaramides to couple hydrogen bonding and aromaticity facilitates the formation of robust supramolecular polymers. The gain in aromatic character upon assembly is demonstrated through bond length equalization, decreased NICS values, high aromatic stabilization (ASE) values, and increased thermodynamic stability of the resultant aggregates. These changes are in accordance with the geometric, magnetic, and energetic criteria used to describe aromaticity. Moreover, the aromatic gain is a significant component of the total interaction energy of squaramide-based supramolecular polymers, explaining the observed increase in thermodynamic stability relative to the monomers and to their urea counterparts. In summary, this self-tuning behavior between hydrogen bonding and aromaticity within the squaramide ring system cannot be achieved by other simple ditopic synthons, such as ureas or amides, commonly used to construct supramolecular polymers. Therefore, I anticipate that the information gained here can enrich the palette of hydrogen-bonding monomers used for supramolecular polymer assembly by implementing aromaticity as a design consideration.

2.5 References

- (1) Alabugin, I. V.; Manoharan, M. *J. Am. Chem. Soc.* **2003**, *125* (15), 4495–4509.
- (2) Babinski, D. J.; Bao, X.; El Arba, M.; Chen, B.; Hrovat, D. A.; Borden, W. T.; Frantz, D. E. *J. Am. Chem. Soc.* **2012**, *134* (39), 16139–16142.
- (3) Manoharan, M.; De Proft, F.; Geerlings, P. *J. Org. Chem.* **2000**, *65* (19), 6132–6137.

Chapter 2

- (4) Bernasconi, C. F.; Ragains, M. L.; Bhattacharya, S. *J. Am. Chem. Soc.* **2003**, *125* (40), 12328–12336.
- (5) Bekele, T.; Shah, M. H.; Wolfer, J.; Abraham, C. J.; Weatherwax, A.; Lectka, T. *J. Am. Chem. Soc.* **2006**, *128* (6), 1810–1811.
- (6) Manaa, M. R.; Sprehn, D. W.; Ichord, H. A. *J. Am. Chem. Soc.* **2002**, *124* (47), 13990–13991.
- (7) De Greef, T. F. a; Smulders, M. M. J.; Wolffs, M.; Schenning, A. P. H. J.; Sijbesma, R. P.; Meijer, E. W. *Chem. Rev.* **2009**, *109* (11), 5687–5754.
- (8) Aida, T.; Meijer, E. W.; Stupp, S. I. *Science* **2012**, *335* (6070), 813–817.
- (9) Chebotareva, N.; Bomans, P. H. H.; Frederik, P. M.; Sommerdijk, N. a J. M.; Sijbesma, R. P. *Chem. Commun.* **2005**, No. 39, 4967–4969.
- (10) Leenders, C. M. A.; Albertazzi, L.; Mes, T.; Koenigs, M. M. E.; Palmans, A. R. A.; Meijer, E. W. *Chem. Commun.* **2013**, *49* (19), 1963–1965.
- (11) Hartgerink, J. D. *Science* **2001**, *294* (5547), 1684–1688.
- (12) Obert, E.; Bellot, M.; Bouteiller, L.; Andrioletti, F.; Lehen-Ferrenbach, C.; Boué, F. *J. Am. Chem. Soc.* **2007**, *129* (50), 15601–15605.
- (13) Rybtchinski, B. *ACS Nano* **2011**, *5* (9), 6791–6818.
- (14) Borzsonyi, G.; Beingessner, R. L.; Yamazaki, T.; Cho, J. Y.; Myles, A. J.; Malac, M.; Egerton, R.; Kawasaki, M.; Ishizuka, K.; Kovalenko, A.; Fenniri, H. *J. Am. Chem. Soc.* **2010**, *132* (43), 15136–15139.
- (15) Görl, D.; Zhang, X.; Würthner, F. *Angew. Chemie - Int. Ed.* **2012**, *51* (26), 6328–6348.
- (16) Van Esch, J.; Kellogg, R. M.; Feringa, B. L. *Tetrahedron Lett.* **1997**, *38* (2), 281–284.
- (17) van Esch, J.; De Feyter, S.; Kellogg, R. M.; De Schryver, F.; Feringa, B. L. *Chem. Eur. J.* **1997**, *3* (8), 1238–1243.
- (18) Kekulé, A. *Bull. Soc. Chem. Fr.* **1865**, *3*, 98.
- (19) Cyrański, M. K.; Krygowski, T. M.; Katritzky, A. R.; Schleyer, P. V. R. *J. Org. Chem.* **2002**, *67* (4), 1333–1338.
- (20) Baldrige, K. K.; Siegel, J. S. *J. Phys. Org. Chem.* **2004**, *17* (9), 740–742.

- (21) Gomila, R. M.; Quiñonero, D.; Rotger, C.; Garau, C.; Frontera, A.; Ballester, P.; Costa, A.; Deyà, P. M. *Org. Lett.* **2002**, *4* (3), 399–401.
- (22) Katritzky, A. R.; Karelson, M.; Sild, S.; Krygowski, T. M.; Jug, K. *J. Org. Chem.* **1998**, *63* (15), 5228–5231.
- (23) Krygowski, T. M.; Szatyłowicz, H.; Stasyuk, O. A.; Dominikowska, J.; Palusiak, M. *Chem. Rev.* **2014**, *114* (12), 6383–6422.
- (24) Chen, Z.; Wannere, C. S.; Corminboeuf, C.; Puchta, R.; Schleyer, P. von R. *Chem. Rev.* **2005**, *105* (10), 3842–3888.
- (25) Cyrański, M. K. *Chem. Rev.* **2005**, *105* (10), 3773–3811.
- (26) Schleyer, P. V. R.; Maerker, C.; Dransfeld, A.; Jiao, H.; Van Eikema Hommes, N. J. R. *J. Am. Chem. Soc.* **1996**, *118* (26), 6317–6318.
- (27) Krygowski, T. M. *J. Chem. Inf. Comput. Sci.* **1993**, *33* (1), 70–78.
- (28) Wu, J. I.; Jackson, J. E.; Schleyer, P. V. R. *J. Am. Chem. Soc.* **2014**, *136* (39), 13526–13529.
- (29) Wurm, F. R.; Klok, H.-A. *Chem. Soc. Rev.* **2013**, *42* (42), 8179–8574.
- (30) Ian Storer, R.; Aciro, C.; Jones, L. H. *Chem. Soc. Rev.* **2011**, *40* (5), 2330–2346.
- (31) Rotger, M. C.; Piña, M. N.; Frontera, A.; Martorell, G.; Ballester, P.; Deyà, P. M.; Costa, A. *J. Org. Chem.* **2004**, *69* (7), 2302–2308.
- (32) Prohens, R.; Portell, A.; Puigjaner, C.; Barbas, R.; Alcobé, X.; Font-Bardia, M.; Tomàs, S. *CrystEngComm* **2012**, *14* (18), 5745.
- (33) Gilli, G.; Bertolasi, V.; Gilli, P.; Ferretti, V. *Acta Crystallogr. Sect. B Struct. Sci.* **2001**, *57* (6), 859–865.
- (34) Busschaert, N.; Kirby, I. L.; Young, S.; Coles, S. J.; Horton, P. N.; Light, M. E.; Gale, P. A. *Angew. Chemie - Int. Ed.* **2012**, *51* (18), 4426–4430.
- (35) Rostami, A.; Guérin, G.; Taylor, M. S. *Macromolecules* **2013**, *46* (16), 6439–6450.
- (36) Ambrosi, G.; Formica, M.; Fusi, V.; Giorgi, L.; Guerri, A.; Micheloni, M.; Paoli, P.; Pontellini, R.; Rossi, P. *Chem. Eur. J.* **2007**, *13* (2), 702–712.
- (37) Sobczyk, L.; Grabowski, S. J.; Krygowski, T. M. *Chem. Rev.* **2005**, *105* (10),

Chapter 2

- 3513–3560.
- (38) Stanger, A. J. *Org. Chem.* **2006**, *71* (3), 883–893.
- (39) Quiñonero, D.; Prohens, R.; Garau, C.; Frontera, A.; Ballester, P.; Costa, A.; Deyà, P. M. *Chem. Phys. Lett.* **2002**, *351* (1–2), 115–120.
- (40) Horcas, I.; Fernández, R.; Gómez-Rodríguez, J. M.; Colchero, J.; Gómez-Herrero, J.; Baro, A. M. *Rev. Sci. Instrum.* **2007**, *78* (1).
- (41) Scalmani, G.; Frisch, M. J.; Mennucci, B.; Tomasi, J.; Cammi, R.; Barone, V. J. *Chem. Phys.* **2006**, *124* (9).
- (42) Marenich, A. V.; Cramer, C. J.; Truhlar, D. G. *J. Phys. Chem. B.* **2009**, *113*, 6378–6396.
- (43) M. F. et. al. *Gaussian 09, Revis. B. 01, Gaussian, Inc., Wallingford, CT.* **2010**.
- (44) Yan Zhao; Donald G. Truhlar. **2008**, *41* (2), 157–167.
- (45) Simon, S.; Duran, M.; Dannenberg, J. J. *J. Chem. Phys.* **1996**, *105* (24), 11024–11031.

2.6 Supporting Information

2.6.1 Materials

All solvents and reagents were obtained from commercial suppliers and were used without further purification. O-methyl-undecaethylene glycol was obtained from Polypure. Deuterated dimethylsulfoxide and chloroform were purchased from Euriso-top. Palladium on matrix activated carbon, triethylsilane and all other commercial grade reagents and chemicals were bought from Sigma Aldrich and used as received. Water was deionized before use.

2.6.2 General methods

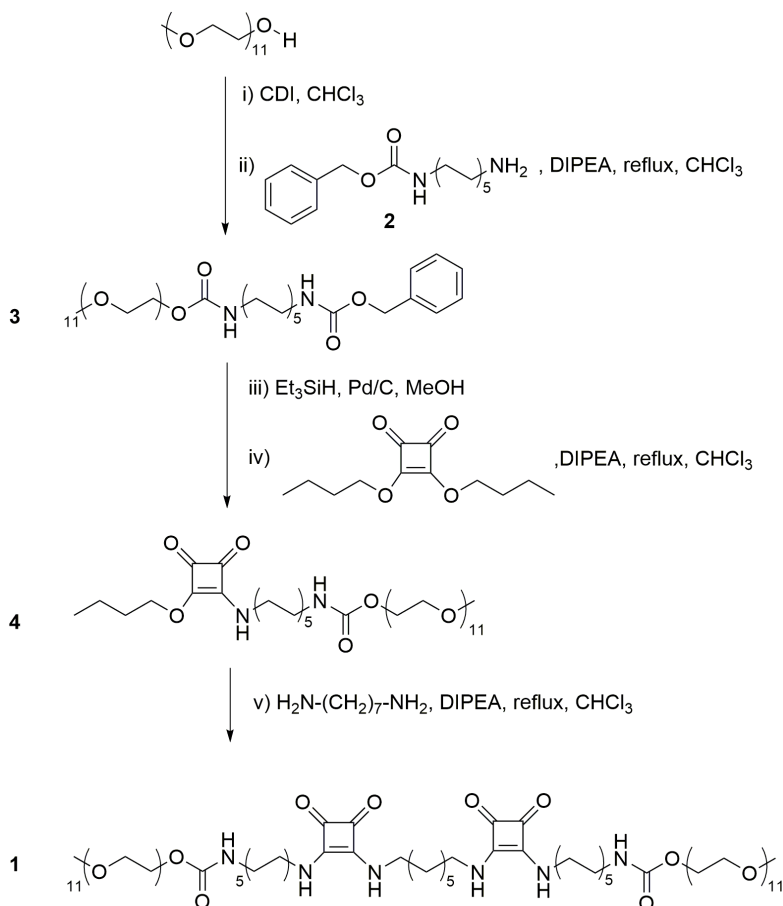
The bis-squaramide and bisurea bolaamphiphiles were purified using a Grace Reveleris X1 flash chromatography system equipped with a C18 column. ^1H NMR and ^{13}C NMR spectra were acquired on a Bruker DMX-400 (400 MHz) operating at 400 MHz for ^1H NMR and 100 MHz for ^{13}C NMR at 298K. LC-MS analysis was performed on a Finnigan Surveyor HPLC system equipped with a Gemini C18 50 \times 4.60 mm column (UV detection at 200-600 nm), coupled to a Finnigan LCQ Advantage Max mass spectrometer with ESI. The mobile phase was a gradient of 10-90% of $\text{H}_2\text{O}-\text{CH}_3\text{CN}$ with 0.1% trifluoroacetic acid over 13.5 minutes. MALDI-TOF-MS (Matrix-assisted laser desorption ionization–time-of-flight) spectra were recorded on a Bruker microflex LRF mass spectrometer in reflection positive-ion mode using α -cyano-4-hydroxycinnamic acid as a matrix on a ground steel target plate. AFM images were collected on a Veeco Multimode AFM with a Nanoscope IIIa controller device at ambient temperature in tapping mode. Silicon cantilever tips were used for image acquisition (OMCL-AC240TS-R3, 50-90 kHz, 0.6-3.5 N/m from Olympus). The scanning speed was at a line frequency of 1.0 Hz, and the original images were made at a resolution of 512 \times 512 pixels. Cryogenic TEM samples were applied to a Quantifoil R2/2 holey carbon film and freeze-plunged into liquid ethane in a FEI Vitrobot Mark IV. The grids were imaged in a FEI Titan Krios at 300 KV using a Falcon Direct Detector (Netherlands Centre for Nanoscopy (NeCN)) or an FEI F20 at 200 kEV using a Gatan Ultrascan camera (Leids Universitair Medisch Centrum (LUMC)). Small angle X-ray scattering measurements were performed on a SAXSLAB GANESHA 300 XL SAXS system equipped with a GeniX 3D Cu Ultra Low Divergence micro focus sealed tube source producing X-rays with a wavelength $\lambda = 1.54 \text{ \AA}$ at a flux of 1×10^8 ph/s and a Pilatus 300K silicon pixel detector with 487 \times 619 pixels of $172 \mu\text{m}^2$ in size placed at two sample-to-detector distances of 713 and 1513 mm respectively to access a

Chapter 2

q -range of $0.006 \leq q \leq 0.44 \text{ \AA}^{-1}$ with $q = 4 \pi/\lambda(\sin\theta/2)$. Silver behenate was used for calibration of the beam centre and the q range. Samples were contained at room temperature in 2 mm quartz capillaries (Hilgenberg GmbH, Germany). The two-dimensional SAXS patterns were brought to an absolute intensity scale using the calibrated detector response function, known sample-to-detector distance, measured incident and transmitted beam intensities, and azimuthally averaged to obtain one dimensional SAXS profiles. The scattering curves of the self-assembled fibers were obtained by subtraction of the scattering contribution of the solvent and quartz cell. The small angle X-ray scattering profiles were analyzed using the software package SasView (<http://www.sasview.org/>). Absorption spectra were obtained on a Cary 300 UV-Vis spectrophotometer. All measurements were carried out using a quartz cuvette with a 1 cm path length. Transmission FTIR spectra were measured using a Bio-Rad Excalibur spectrometer equipped with a nitrogen cooled MCT detector. Static light scattering (SLS) measurements were performed using a Malvern Zetasizer Nano ZS ZEN3500. The laser wavelength was 633 nm and the scattering angle was 173° .

2.6.3 Synthetic routes

Synthesis of 1



Scheme S2.1. Synthetic route to obtain 1.

Synthesis of compound 2:

N-(benzyloxycarbonyloxy)succinimide (2.89 g, 11.60 mmol) was dissolved in 150 mL chloroform and added dropwise over 1 hour to a cooled (0°C), stirring solution of 1,10-diaminodecane (9.98 g, 58.00 mmol) dissolved in 150 mL chloroform. The reaction was allowed to reach room temperature and continued to stir for 18 hours. The solution was then concentrated by evaporation, ethyl acetate was added and the mixture washed 3x with water. The aqueous layers were discarded and the ethyl acetate layer was washed 3x with 1 M HCl. A white precipitate

formed in the organic layer, which was collected by filtration and washed with ethyl acetate to yield the product as a white crystalline solid.

Yield: 2.38 g, 67.1 % $^1\text{H-NMR}$ (δ_{H} [ppm], DMSO- d_6 , 400 MHz): 7.90 (br s, 3H), 7.41-7.25 (m, 5H), 5.02 (s, 2H), 3.02-2.95 (m, 2H), 2.79-2.72 (m, 2H), 1.57-1.50 (m, 2H), 1.42-1.26 (m, 14H). $^{13}\text{C-NMR}$ (δ_{C} [ppm], DMSO- d_6 , 100 MHz): 156.03, 137.29, 128.29, 127.68, 127.64, 65.01, 40.13, 38.73, 29.35, 28.82, 28.72, 28.64, 28.46, 26.92, 26.18, 25.76.

Synthesis of compound 3:

O-methyl-undecaethylene glycol (0.60 g, 1.16 mmol) was activated with 1,1'-carbonyldiimidazole (0.75 g, 4.64 mmol) in 25 mL chloroform for 2 hours at room temperature (LC-MS: $t=4.14$ min, m/z : 611.27 [M+H] $^+$). Subsequently, **2** (0.43 g, 1.40 mmol) and DIPEA (0.404 mL, 2.32 mmol) were added to the reaction mixture and refluxed overnight. The product was purified by flash column chromatography using a 10-90% CH₃CN/H₂O gradient over 25 minutes on a C18 silica column. The product was concentrated by evaporation and lyophilized overnight to obtain a white solid.

Yield: 0.7 g, 68.7 % $^1\text{H-NMR}$ (δ_{H} [ppm], CDCl₃, 400 MHz): 7.38-7.34 (m, 5H), 5.12 (s, 2H), 4.24-4.22 (m, 2H), 3.71-3.56 (m, 42H), 3.40 (s, 3H), 3.21-3.15 (m, 4H), 1.52-1.48 (m, 4H), 1.32-1.27 (m, 12H). $^{13}\text{C-NMR}$ (δ_{C} [ppm], CDCl₃, 100 MHz): 156.41, 136.71, 128.52, 128.12, 128.08, 71.93, 70.59, 70.51, 69.73, 66.60, 63.90, 59.04, 41.10, 29.94, 29.41, 29.20, 26.71, 26.69. LC-MS: $t = 7.64$ min, m/z : 849.20 [M+H] $^+$. MALDI-TOF-MS: m/z calc: 849.07; found: 871.426 [M+Na] $^+$, 887.384 [M+K] $^+$.

Synthesis of compound 4:

Compound **3** (0.20 g, 0.24 mmol) was dissolved in 5 mL methanol and Pd/C (2.5 mg, 0.024 mmol) was added. The solution was briefly degassed with argon, prior to the dropwise addition of triethylsilane (0.38 mL, 2.40 mmol). The addition of triethylsilane resulted in an effervescent solution and once complete, the solution was filtered over Celite to remove the remaining Pd/C. The filtrate was concentrated by evaporation and a gentle stream of air. The dried product was redissolved in 25 mL chloroform and 3,4-dibutoxy-3-cyclobutene-1,2-dione (67 μL , 0.31 mmol) and DIPEA (31 μL , 0.24 mmol) were added to the reaction mixture. The reaction mixture was stirred and refluxed overnight and purified by flash

column chromatography using a gradient of 10-90% CH₃CN/H₂O over 25 minutes on a C18 silica column. The product was concentrated by evaporation and lyophilized overnight to obtain compound **4** as white solid.

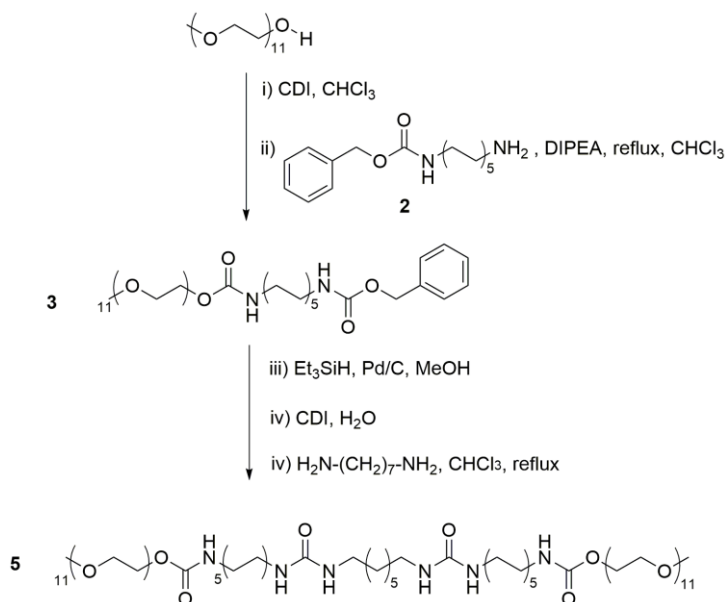
Yield: 168.6 mg, 81.0 % ¹H-NMR (δ_H[ppm], CDCl₃, 400 MHz): 6.34 (br s, 1H), 4.96 (br s, 1H), 4.79-4.74 (m, 2H), 4.25-4.22 (m, 2H), 3.72-3.41 (m, 47H), 3.20-3.15 (m, 2H), 1.84-1.79 (m, 2H), 1.66-1.30 (m, 18H), 1.00 (s, 3H). ¹³C-NMR (δ_C[ppm], CDCl₃, 100 MHz): 177.16, 172.53, 156.70, 73.32, 71.90, 70.53, 70.46, 69.64, 63.78, 58.99, 44.85, 41.01, 32.03, 30.69, 29.92, 29.37, 29.18, 29.08, 26.68, 26.35, 18.66, 13.70. LC-MS: t=7.28 min, *m/z*: 867.40 [M+H]⁺. MALDI-TOF-MS: *m/z* calc: 867.08; found: 889.481 [M+Na]⁺, 905.479 [M+K]⁺.

Synthesis of compound 1:

Compound **4** (160.0 mg, 0.19 mmol) was dissolved in 25 mL chloroform with DIPEA (50 μL, 0.38 mmol) and 1,7-heptanediamine (14 μL, 0.10 mmol) were added and refluxed overnight. The product was purified by flash column chromatography using a gradient of 10-90% CH₃CN/H₂O over 25 minutes on a C18 silica column. The product was concentrated down by evaporation and lyophilized overnight to obtain a white solid.

Yield: 100.3 mg, 62.8 % ¹H-NMR (δ_H[ppm], CDCl₃, 400 MHz): 4.24-4.22 (m, 4H), 3.71-3.56 (m, 84H), 3.40 (s, 6H), 3.18-3.15 (m, 4H), 3.01-2.82 (m, 8H), 1.68-1.64 (m, 8H), 1.51-1.29 (m, 34H). ¹³C-NMR (δ_C[ppm], CDCl₃, 100 MHz): 184.30, 168.40, 136.24, 71.99, 70.63, 70.59, 69.74, 64.12, 59.12, 45.09, 43.99, 41.09, 30.90, 30.43, 29.96, 29.85, 29.47, 29.26, 29.00, 28.74, 28.33, 26.76, 26.44, 25.19. LC-MS: t = 6.97 min, *m/z*: 1715.73 [M+H]⁺. MALDI-TOF-MS: *m/z* calc: 1716.16; found: 1716.306 [M+H]⁺, 1738.167 [M+Na]⁺, 1754.129 [M+K]⁺.

Synthesis of 5



Scheme S2.2 Synthetic route of 5.

Synthesis of compound 5:

Compound **3** (0.41 g, 0.48 mmol) was dissolved in 10 mL methanol and Pd/C (5.00 mg, 0.048 mmol) was added. The solution was degassed with argon and triethylsilane was added dropwise (0.70 mL, 4.8 mmol). The addition of triethylsilane resulted in an effervescent solution and once finished, the solution was filtered over Celite. The filtrate was concentrated by evaporation and dried by a gentle stream of air. The dried product was redissolved in 10 mL of water and stirred at 0 °C. Initially, 1,1'-carbonyldiimidazole (86 mg, 0.53 mmol) was added to the reaction mixture at 0 °C. After 30 min, another identical aliquot of 1,1'-carbonyldiimidazole was added. The reaction mixture was stirred at 0 °C for another 30 minutes and progress of the reaction was followed by the appearance of the product peak by LC-MS ($t=5.50$ min, m/z : 809.40 [M+H]⁺). Once CDI activation of the free amine was achieved, the solution was lyophilized and redissolved in CHCl₃. Aliquots of 1,7-heptanediamine (7.27 μL, 0.048 mmol at a time) were added to the solution gradually until the reaction mixture showed full conversion to **5** by LCMS. The product was purified by flash column chromatography on a C18 silica column using a gradient of 10-90% CH₃CN/H₂O

over 40 minutes. The product was concentrated by evaporation and lyophilized overnight to obtain compound **5** as a white solid.

Yield: 183 mg, 23.7 % $^1\text{H-NMR}$ (δ_{H} [ppm], CDCl_3 , 400 MHz): 4.25-4.22 (m, 4H), 3.73-3.57 (m, 84H), 3.41 (s, 6H), 3.21-3.16 (m, 12H), 1.58-1.45 (m, 12H), 1.41-1.26 (m, 30H). $^{13}\text{C-NMR}$ (δ_{C} [ppm], CDCl_3 , 100 MHz): 158.90, 156.59, 72.01, 70.64, 69.79, 63.88, 59.14, 41.10, 40.47, 39.91, 30.41, 29.97, 29.78, 29.43, 29.39, 29.32, 29.21, 28.02, 26.94, 26.71, 26.12. LC-MS: $t = 7.34$ min, m/z : 1611.87 $[\text{M}+\text{H}]^+$. MALDI-TOF-MS: m/z calc: 1612.08; found: 1612.338 $[\text{M}+\text{H}]^+$, 1634.286 $[\text{M}+\text{Na}]^+$, 1650.253 $[\text{M}+\text{K}]^+$.

2.6.4 Lower critical solution temperature

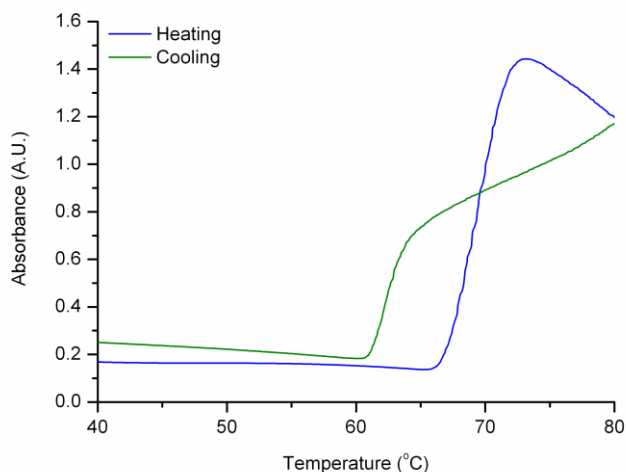


Figure S2.1. LCST determination of **1** in water (2.33 mM) by UV-vis spectroscopy. The optical density was recorded as a function of temperature at 450 nm, where the molecules do not absorb light. The large increase in optical density above 68 °C represents the LCST for **1**.

2.6.5 Cryogenic-Transmission Electron Microscopy (cryo-TEM)

Cryogenic TEM samples were prepared by applying 3 μL sample of **1** (5.82 mM) and **5** (6.21 mM) in water to a glow-discharged Quantifoil R2/2 holey carbon film, blotting excess liquid off for 1 second and plunge-freezing it into liquid ethane using a FEI Vitrobot Mark IV. The grids were imaged in a FEI Titan Krios at 300 KV using a Falcon Direct Electron Detector (Netherlands Centre for Electron Nanoscopy, NeCEN) (sample **1**) or a FEI Tecnai F20 at 200 kEV using a Gatan UltraScan camera (Leids Universitair Medisch Centrum (LUMC)) (sample **5**) at between -2 and -5 micron under focus.

2.6.6 Atomic force microscopy (AFM)

A stock solution of **1** (6 mM) was diluted to 12 μM in water, and drop-casted (25 μL) on freshly cleaved mica. The samples were dried overnight at room temperature. The obtained data were processed using the WSxM software (Nanotec Electronica).⁴⁰

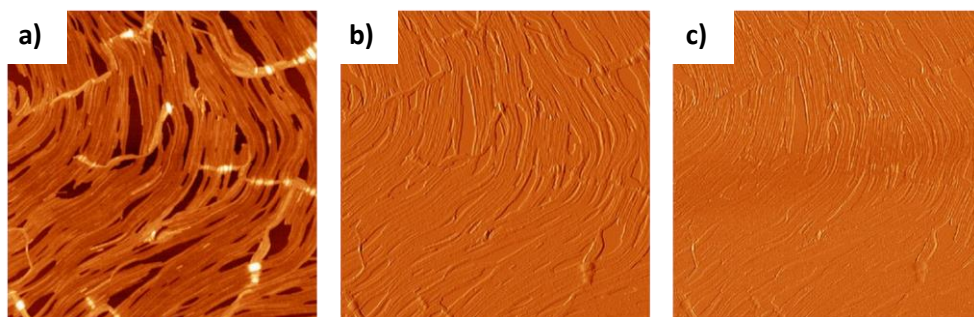


Figure S2.2. AFM height (a), amplitude (b) and phase (c) images of **1**, deposited on mica 1 hour after dissolution (3 x 3 μm scale).

2.6.7 Small-angle X-ray scattering (SAXS)

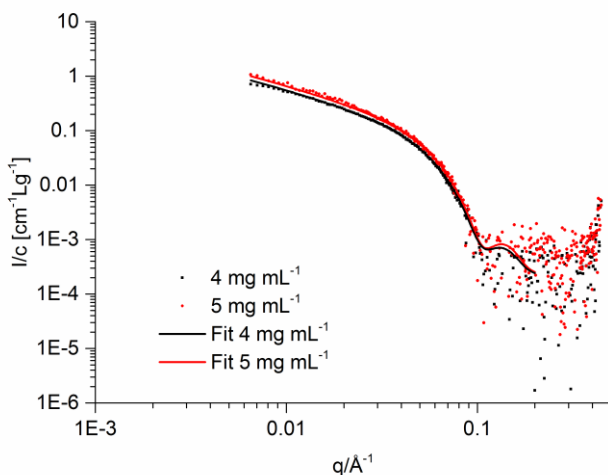


Figure S2.3: Small angle X-ray profiles of squaramide fibers **1** collected at a concentration of 4 and 5 mg mL^{-1} normalized by weight concentration (i.e., the symbols correspond to experimental data (I/c vs. q)).

Small angle X-ray scattering (SAXS) experiments were performed to probe the structure of the self-assembled squaramide fibers in water at room temperature. The SAXS profiles of the 4 and 5 mg mL^{-1} sample are given in Figure S2.3. In the low- q regime the scattering profiles decay with a powerlaw slope of unity, which is characteristic for scattering profiles of 1D objects with a length beyond the resolution of the experiment ($\sim \pi/q_{\text{min}} = 48 \text{ nm}$). Upon normalization to 1 mg mL^{-1} the SAXS profiles taken at 4 and 5 mg mL^{-1} nearly superpose, which means that interfiber interactions are insignificant at the length scales probed. A Casassa–Holtzer plot of the same data is given in Figure S2.4.

The experimental data can be readily modeled using a form factor developed for homogeneous cylinders (lines represent fit to experimental data in Figure S2.3). Several other, more elaborate form factors were also tested, including those of core-shell, and flexible homogeneous cylinders. Since these more complex models do not significantly improve the goodness of fit, only the results of the simplest form factor are presented. Since the length L of the fibers is beyond the experimental resolution we fix L at an arbitrary value of 200 nm. We also fix $\rho_{\text{solvent}} = 9.37 \times 10^6 \text{ \AA}^{-2}$. From the modeling of the SAXS data, we obtain values for the

Chapter 2

radius of the fibers, r_{cs} , and their electron length density, ρ_{cyl} . For the 4 and 5 mg/mL samples, we obtain $\langle r_{cs} \rangle = 3.5$ nm, and $\rho_{cyl} = 10.4 \times 10^6 \text{ \AA}^{-2}$, respectively.

To extract the cross-sectional mass per unit length, M_L , from the scattering profiles we use:

$$\frac{d\Sigma(q)}{d\Omega} = I(q) = \frac{\pi}{q} I_{cs}(q)$$

$$M_L = \frac{I_{cs}(0)}{c\Delta\rho_M^2}$$

with the electron length density difference per mass, $\Delta\rho_M$, and the height of the Holtzer plateau, l_{cs} as indicated by the dash-dotted lines in Figure S2.4. Computation of $\Delta\rho_M$ from the squaramide composition $C_{53}H_{93}N_5O_{30}$ and the measured specific volume, $v = 0.83 \text{ cm}^3 \text{ g}^{-1}$ gives $\Delta\rho_M = 1.29 \times 10^{10} \text{ cm g}^{-1}$, which is comparable to the value obtained from the form factor fit, which gives $\Delta\rho_M = 0.87 \times 10^{10} \text{ cm g}^{-1}$. Using these values we obtain $M_L = 2.5 - 6.0 \times 10^{20} \text{ g nm}^{-1}$, which corresponds to 10 – 30 squaramide bolaamphiphiles per nm.

Table S2.1. Structural parameters extracted from the SAXS profiles of the squaramide bolaamphiphiles

		Holtzer		Computation			Form factor		
1	v	$qI(q)/c^3$	$l_{cs} = qI(q)/\pi$	$\Delta\rho_M^2$	M_L	SQ/L	$\Delta\rho_M^2$	M_L	SQ/L
[wt%]	$\text{cm}^3 \text{ g}^{-1}$	$\text{cm}^2 \text{ Lg}^{-1}$	cm^2	$10^{10} \text{ cm g}^{-1}$	$10^{20} \text{ g nm}^{-1}$	nm^{-1}	$10^{10} \text{ cm g}^{-1}$	$10^{20} \text{ g nm}^{-1}$	nm^{-1}
0.4%	0.83	1.29×10^5	1.64×10^5	1.68	2.45	11.5	0.74	5.51	25.9
0.5%	0.83	1.39×10^5	2.22×10^5	1.68	2.65	12.5	0.74	5.96	28.0

^aTaken from Holtzer plateau at $0.0065 \leq q \leq 0.0164 \text{ \AA}^{-1}$

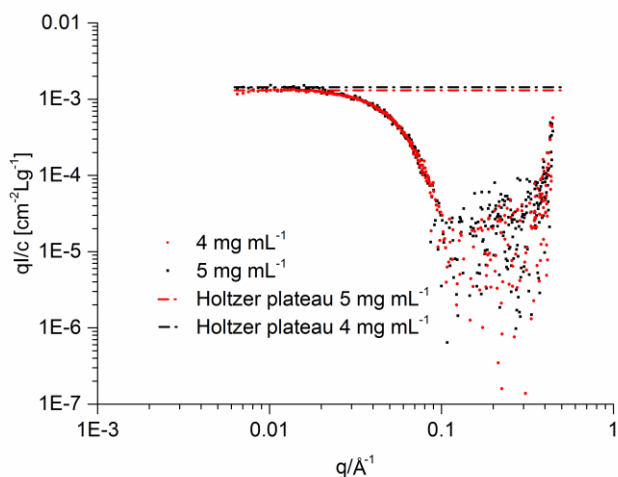


Figure S2.4: Casassa–Holtzer plot of the scattering profiles in Figure S2.3. The Holtzer plateaus ($0.0065 \leq q \leq 0.0164 \text{ \AA}^{-1}$) are indicated by dash-dotted red and black lines.

2.6.8 UV-Vis spectroscopy

Serial dilutions of a stock solution of **1** (5.82 mM) were performed in water. A UV-Vis spectrum for each sample was recorded from $400\text{--}200 \text{ nm}$. Two peaks were observed for **1** at 255 and 329 nm and a shoulder at 310 nm .

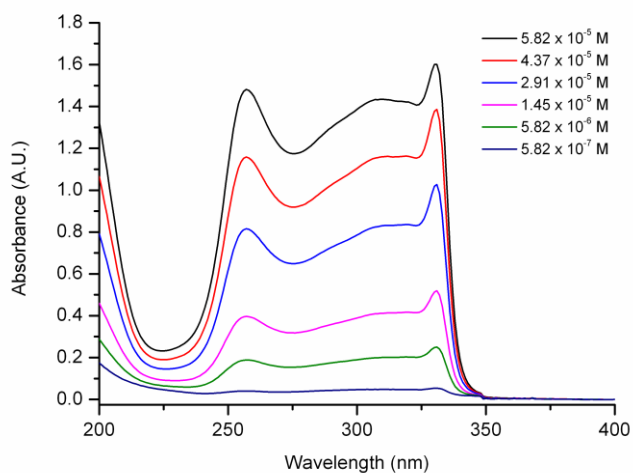


Figure S2.5.1. Concentration-dependent UV-Vis spectra of **1** (absorbance vs wavelength).

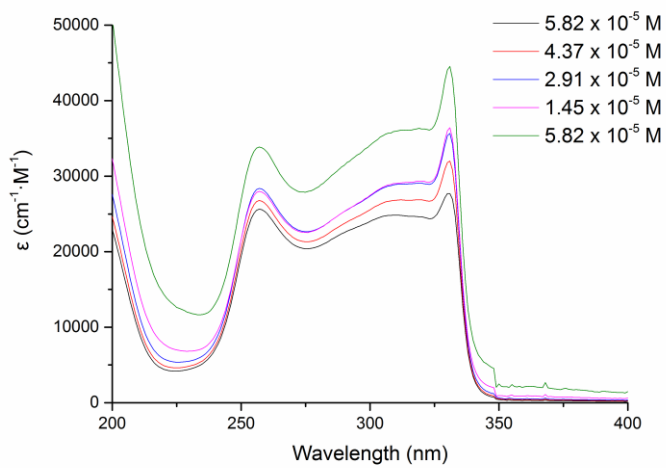


Figure S2.5.2. Concentration-dependent UV-Vis spectra of **1** (ϵ vs wavelength).

2.6.9 TD-DFT calculations

The time-dependent DFT (TD-DFT) method⁴¹ was used to compute UV-Vis absorption spectra for a squaramide monomer up to a pentamer. The M06-2X/6-31+G(d,p) level of theory was used, which significantly reduces the computational cost, but still yields a spectrum comparable with M06-2X/6-311+G(d,p) (a test was performed with the dimer structure). We employed a continuum model of water of type SMD⁴² to describe the effect of solvation.

Table S2.2. Major absorption bands for squaramide monomers (n=1) and oligomers (n=2-5).

n	λ	Strength
1	266.75	0.3555
	263.98	0.4299
2	271.85	0.8728
	261.16	0.7281
3	274.43	1.4391
	258.25	0.5650
4	276.07	2.0098
	257.79	1.3904
5	277.18	2.5755
	257.57	1.3952

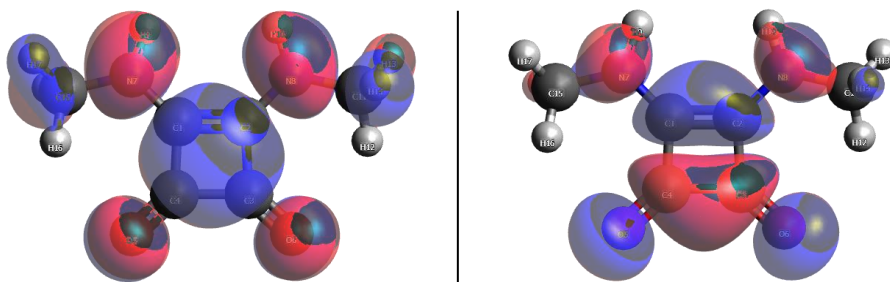


Figure S2.6. Frontier molecular orbitals of the squaramide monomer computed at the M06-2X/6-31+G(d,p) level of theory. Left: HOMO; right: LUMO.

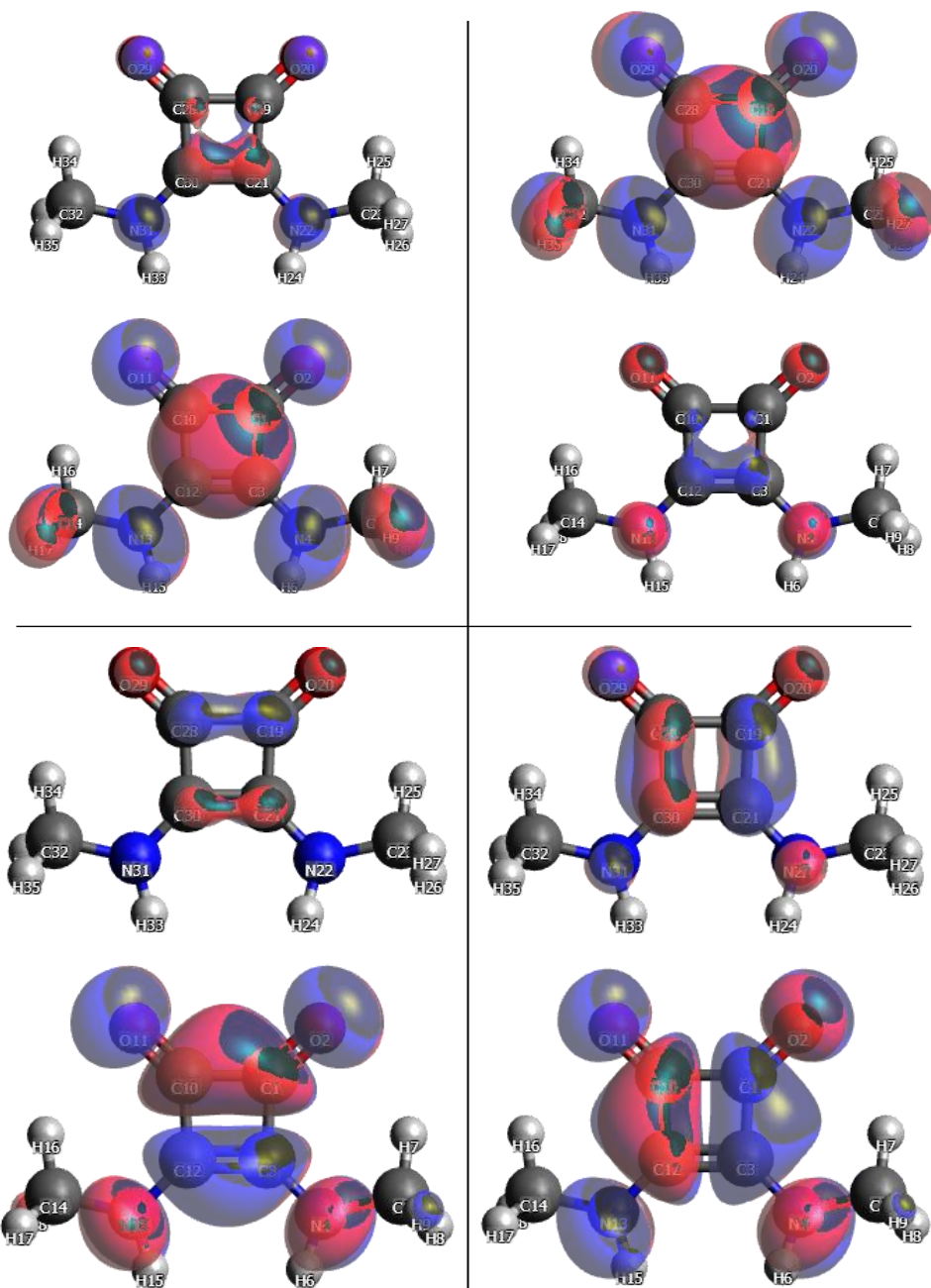


Figure S2.7. Frontier molecular orbitals of the squaramide dimer computed at the M06-2X/6-31+G(d,p) level of theory. Top left: HOMO-1; top right: HOMO; bottom left: LUMO; bottom right: LUMO+1.

2.6.10 Fourier transform infrared (FTIR)

Samples of **1** were dissolved in D₂O, HFIP-d₂ or CHCl₃ to provide a final concentration of 11.7 mM. Measurements in liquid phase were performed in a CaF₂ cell for liquid samples at room temperature. Liquid samples were measured after the addition of the solvent to the solid.

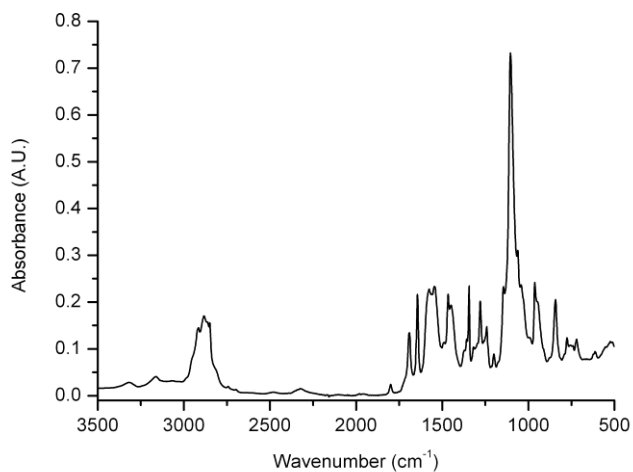


Figure S2.8. Infrared spectrum of **1** in the solid state. Solid FTIR was recorded in ATR mode.

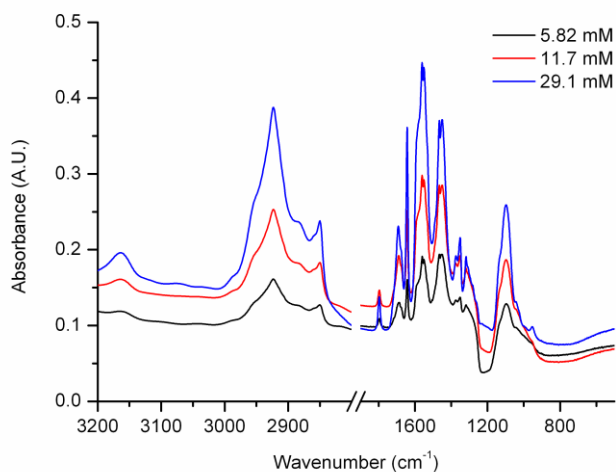


Figure S2.9. Infrared spectrum of **1** (5.82 mM, 11.7 mM, 29.1 mM) in water.

2.6.11 Infrared spectra predictions

A frequency calculation was performed to verify that structures were at a minimum of energy and to obtain vibrational spectroscopy predictions at the same theory level of geometry optimization. The zero point energy correction was also included in our calculations.

Table S2.3. Infrared spectra assignment (wavenumbers in cm^{-1}) of vibrational modes in the 1500-2000 cm^{-1} region for squaramide monomer (1) and oligomers (2-5), computed from structures optimized at the M06-2X/6-311+G(d,p) level of theory.

Mode	1	2	3	4	5
C=O sym	1719	1696	1678	1666	1661
C=O antisym	1849	1817	1783	1774	1762
Ring breathing	1919	1916	1909	1909	1908

2.6.12 DFT optimization and geometries

DFT calculations were performed with the Gaussian 09 suite of programs.⁴³ The M06-2X hybrid functional was selected for its good performance in taking into account non-covalent interactions, such as hydrogen bonds and π -interactions.⁴⁴ A monomer of N,N'-dimethylsquaramide was built and optimized at the M06-2X/6-311+G(d,p) level of theory, and subsequently oligomers from dimers to pentamers were optimized at the same level. Bond lengths were measured for each of the squaramide units in monomer and oligomers, and the HOMA index was computed as:

$$HOMA = 1 - \frac{98.89}{4} \sum (r_i - 1.397)^2$$

Table S2.4. Bond lengths for squaramide monomer (n=1) and oligomers (n=2-5). # is the monomer number in the oligomer (#1 always has non-hydrogen bonded NH, #n has non-hydrogen bonded C=O). HOMA was computed with equation shown above.

<i>n</i>	#	C(O)- C(N)	C(O)- C(O)	C(N)- C(N)	C=O	C-N	HOMA
1	1	1.492	1.549	1.402	1.206	1.353	-0.015
2	1	1.472	1.512	1.400	1.210	1.336	0.393
2	2	1.477	1.525	1.396	1.207	1.339	0.277
3	1	1.471	1.508	1.405	1.218	1.335	0.424
3	2	1.469	1.504	1.411	1.223	1.330	0.459
3	3	1.477	1.522	1.401	1.216	1.338	0.301
5	1	1.470	1.505	1.407	1.220	1.334	0.445
5	2	1.466	1.497	1.416	1.226	1.327	0.508
5	3	1.466	1.495	1.417	1.227	1.326	0.516
5	4	1.467	1.499	1.415	1.225	1.328	0.489
5	5	1.476	1.520	1.402	1.217	1.337	0.314

2.6.13 Nucleus-independent chemical shift (NICS) calculations

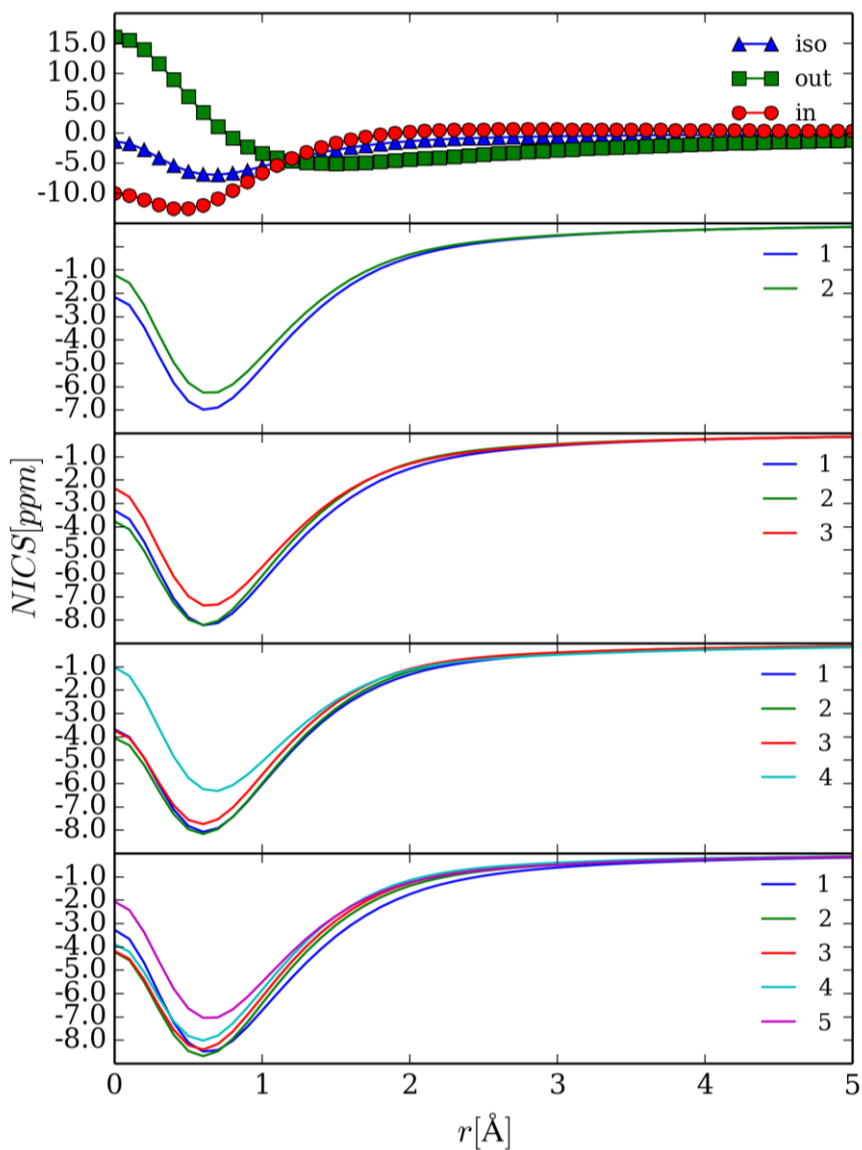


Figure S2.10. NICS-scan profiles for squaramide monomer and oligomers ($n=2-5$). For the monomer, the isotropic shielding as well as the individual out-of- and in-plane contributions are displayed. For the oligomers, only the isotropic shielding is shown, and the markers are hidden for clarity; the lines are meant as a guide for the eye.

Table S2.5. NICS(0), computed on the plane of the squaramide ring. *n* is the number of monomers in the oligomer, and # is the monomer number in the oligomer (#1 always has non-hydrogen bonded NHs, #*n* has non-hydrogen bonded C=Os).

<i>n</i>	Monomer #				
	1	2	3	4	5
1	-1.34				
2	-3.17	-2.04			
3	-3.31	-3.77	-2.23		
4	-3.33	-4.12	-3.88	-2.03	
5	-3.27	-4.22	-4.17	-3.88	-1.79

Table S2.6. NICS(0.6), computed 0.6 Å from the plane of the squaramide ring on an axis perpendicular to it. Idem Table S2.5.

<i>n</i>	Monomer #				
	1	2	3	4	5
1	-6.83				
2	-7.97	-7.11			
3	-8.24	-8.21	-7.26		
4	-8.39	-8.54	-8.16	-7.04	
5	-8.49	-8.69	-8.40	-8.02	-6.80

Table S2.7. NICS(1), computed 1.0 Å from the plane of the squaramide ring on an axis perpendicular to it. Idem Table S2.5.

<i>n</i>	Monomer #				
	1	2	3	4	5
1	-5.54				
2	-6.17	-5.64			
3	-6.39	-6.10	-5.67		
4	-6.58	-6.33	-5.99	-5.52	
5	-6.73	-6.43	-6.14	-5.85	-5.38

2.6.14 Interaction energies

The total interaction energy for each oligomer ($n=2-5$) was computed as

$$\Delta E(n\text{-mer}) = E(n\text{-mer}) - nE(\text{monomer})$$

Table S2.8. Interaction energies (ΔE) corrected for Basis Set Superposition Error (ΔBSSE) for an isolated squaramide or urea ($n=1$) and oligomers ($n=2-5$); n_{Hbond} is the number of hydrogen bonds in the corresponding oligomer.

n	n_{Hbond}	Squaramide			Urea		
		ΔE	ΔBSSE	$\Delta E/n_{\text{Hbond}}$	ΔE	ΔBSSE	$\Delta E/n_{\text{Hbond}}$
1	0	0.0	0.0	0.0	0.0	0.0	0.0
2	2	-51.7	3.2	-25.8	-38.4	2.0	-20.2
3	4	-120.3	6.0	-30.1	-84.4	3.9	-22.1
4	6	-194.4	9.5	-32.4	-134.5	6.2	-23.4
5	8	-271.7	12.8	-34.0	-182.6	8.4	-23.9

To calculate the contribution of the aromatic stabilization to the interaction energy in squaramide oligomers, we computed the interaction energy of systems analogous to squaramide that can form the same hydrogen bond pattern but cannot exhibit aromatic stabilization, heterodimers **5** and **6** (see Figure S2.11). The former is a minimal system that generates the same arrangement of hydrogen bonds as present in a squaramide dimer, while the latter exhibits a di(vinyligous amide) pattern. The structure of the complex was optimized at the M06-2X/6-311+G(d,p) level of theory, and the interaction energy was calculated by subtracting the energy of the individual isolated molecules. The interaction energy was corrected for Basis Set Superposition Error by single point counterpoise method;⁴⁵ the BSSE value represented 4-6% of the total interaction energy. The contribution of the aromatic stabilization was calculated as the difference between the interaction energy of the oligomer and the interaction energy of the non-aromatic heterodimer times the number of bonds between monomers in the oligomer (i.e., $n-1$) (see Table S2.9):

$$E^{aro}(n\text{-mer}) = \Delta E(n\text{-mer}) - (n-1)\Delta E(\text{nonaromatic})$$

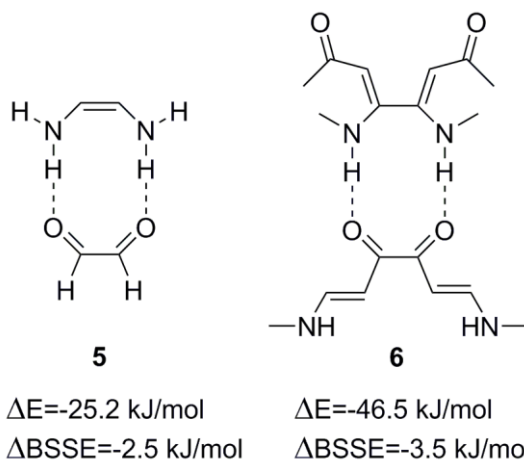


Figure S2.11. Reference non-aromatic systems for the calculation of the aromatic stabilization energy in a squaramide dimer. ΔE is the interaction energy corrected for BSSE (ΔBSSE).

Table S2.9. Interaction energy (ΔE), aromatic stabilization energy (E_{aro}) and percentage of the total interaction energy of the oligomers E_{aro} accounts for compared to heterodimers **5** and **6**.

<i>n</i>	ΔE	5		6	
		E_{aro}	$E_{\text{aro}}/\Delta E$	E_{aro}	$E_{\text{aro}}/\Delta E$
2	-51.7	-26.5	51%	-5.2	10%
3	-120.3	-69.8	58%	-27.2	23%
4	-194.4	-118.8	61%	-54.9	28%
5	-271.7	-170.8	63%	-85.6	32%

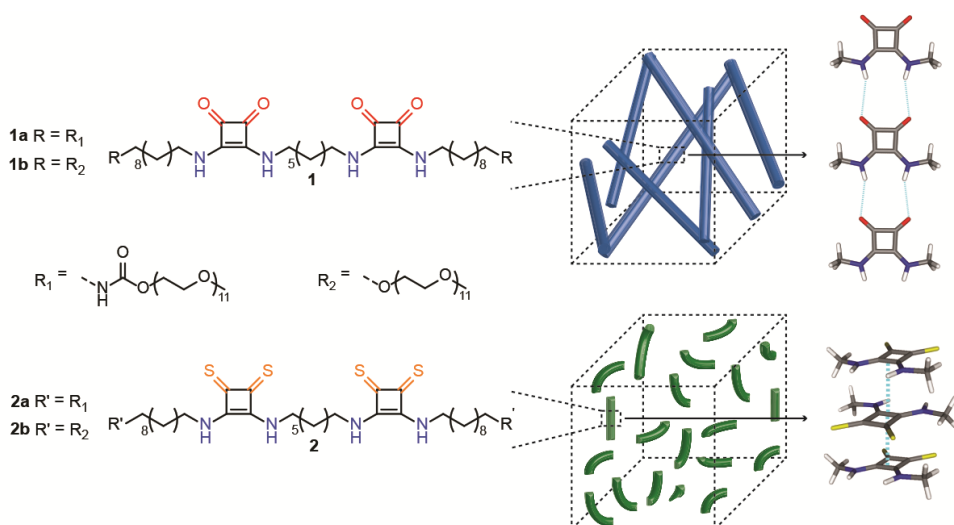
2.6.15 Critical aggregation concentration

The CAC was determined by static light scattering through serial dilutions of the self-assemblies of **1** and **5**. Individual stock solutions of **1** and **5** of the same concentration (2.91 mM), were prepared by dissolving each of the compounds in Milli-Q water and leaving to stand overnight. A dilution series was prepared in a range from 0.29 mM to 2.91 mM and their respective scattered light intensities measured in a polystyrene cuvette at room temperature. The measurements were recorded in triplicate. The CAC value was obtained from the intersection between the lines drawn to the points representing the aggregated and non-aggregated species. Subsequently, Gibbs free energy for molecules **1** and **5** were calculated from the experimentally determined CAC values using the equation $\Delta G = RT \ln(\text{CAC})$.

Chapter 2

CHAPTER 3

A self-assembly mode “Tug-of-war” in squaramide-based supramolecular polymers driven by aromaticity-modulated hydrogen bonding



This chapter was prepared as an original research paper: Victorio Saez Talens, Mahsa Boraghi, Raisa Rudge, Chia-Hua Wu, Thuat T. Trinh, Pablo Englebienne, Ilja K. Voets, Judy I. Wu, Roxanne E. Kieltyka

3.1 Abstract

Despite a growing understanding of the factors driving monomer self-assembly to form supramolecular polymers, the effect of aromaticity gain in hydrogen-bonding cyclic π -conjugated synthons is overlooked. Herein, I demonstrate the interplay of aromaticity gain and hydrogen bonding on “switching” the self-assembly modes of squaramide-based bolaamphiphiles. Surprisingly, O \rightarrow S substitution in squaramide synthons resulted in supramolecular polymers with increased fiber flexibility and lower degrees of polymerization. Computation and experimental studies suggest that both oxo- and thiosquaramide bolaamphiphiles self-assemble through hydrogen-bonding interactions, but into drastically different arrangements: “head-to-tail” versus “stacked”, respectively. Computed energetic and magnetic criteria of aromaticity reveal that both modes of self-assembly increase the aromatic character of the squaramide synthons, giving rise to stronger intermolecular hydrogen bonding interactions in the resultant supramolecular polymer structures. These examples illustrate the effects of aromaticity gain in cyclic π -conjugated synthons on supramolecular polymerization, and suggest that aromaticity-modulated hydrogen bonding (AMHB) should be considered in monomer design.

3.2 Introduction

Supramolecular polymers have a dynamic character that endows them with unique properties, such as responsiveness and self-healing,¹⁻⁴ leading to numerous potential applications in biomedical materials, adhesives, inks or personal care products.⁵⁻⁷ To gain access to such materials, the monomers are engineered to engage in various non-covalent interactions including hydrogen-bonding,⁸⁻¹⁰ aromatic interactions, solvophobicity and van der Waals, that drive their self-assembly into hierarchical architectures through stacking or molecular recognition of polymeric precursors.¹¹⁻²⁰ The growing number of synthesized monomers has contributed significantly to the development of general design rules to facilitate monomer self-assembly in organic solvents and water. However, to further guide their rational design, it is necessary to understand factors that influence the strength of noncovalent interactions either within or between monomers. Here, I demonstrate the impact of the combination of hydrogen bonding and aromaticity gain on the mode of monomer self-assembly in a supramolecular polymer.

Aromaticity, with its near 150-year old history starting with Kekulé, continues to fascinate chemists with its peculiar energetic, geometric, and spectroscopic manifestations in molecules. Nevertheless, Wu, Jackson and co-workers demonstrated computationally²¹⁻²³ and experimentally²⁴ that aromaticity can also significantly influence the strengths of *intermolecular* hydrogen bonding interactions beyond the traditional electrostatic-based view of hydrogen bonding through a reciprocal aromaticity-modulated hydrogen bonding (AMHB) relationship. These authors demonstrated that hydrogen bonding interactions that increase cyclic $4n + 2$ π -electron delocalization (i.e., increase aromaticity) in heterocycles can be strengthened, while those that decrease cyclic $4n + 2$ π -electron delocalization (decreased aromaticity) are weakened.^{21,22,24} Such effects are especially pronounced when hydrogen-bonded assemblies of cyclic π -conjugated motifs are considered, as the effects of aromaticity gain in each of the synthon rings can add up to an astonishing overall aromatization of the self-assembled system.²³ Concurrently, the Kielyka group reported the self-assembly of a novel squaramide-based bolaamphiphile that takes

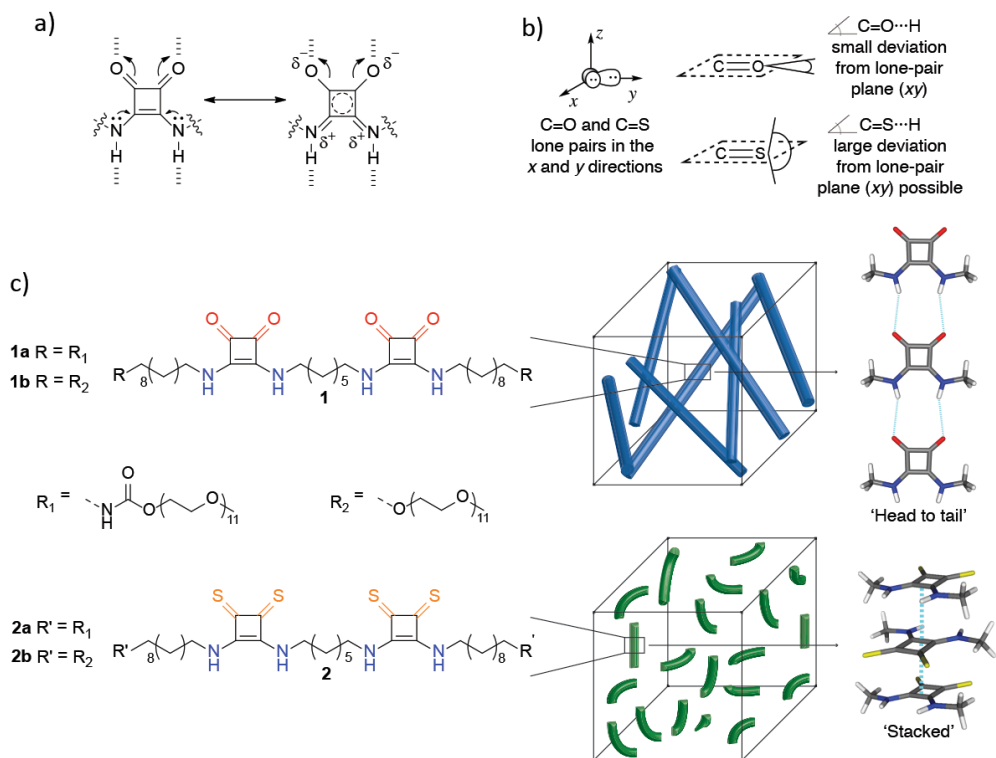


Figure 3.1. (a) Aromaticity-modulated hydrogen bonding (AMHB) in oxosquaramide; the resonance form on the right shows increased cyclic 2π -electron delocalization in the four membered ring. (b) Carbonyls ($\text{C}=\text{O}$) typically form hydrogen bonds with small deviations from the lone-pair (xy) plane, but thiocarbonyls ($\text{C}=\text{S}$) can form hydrogen bonds with $\text{C}=\text{S}\cdots\text{H}$ angles of close to 90° . As a result, $\text{C}=\text{O}$ and $\text{C}=\text{S}$ containing synthons are expected to promote drastically different self-assembly modes. (c) Structures of the oxosquaramide (**1a** and **1b**) and thiosquaramide (**2a** and **2b**) bolaamphiphiles under study. **1a** and **1b** self-assemble into rigid fibers (*top*), while **2a** and **2b** self-assemble into short flexible rod-like structures (*bottom*). This disparity is attributed to the “head-to-tail” self-assembly of the oxosquaramides versus “stacked” self-assembly of the thiosquaramides.

advantage of aromaticity gain to form robust supramolecular polymers in water.²⁵ Squaramides²⁶⁻³⁰ are ditopic hydrogen-bonding synthons that can self-associate through two hydrogen bond acceptors ($\text{C}=\text{O}$ groups) and two hydrogen bond donors ($\text{N}-\text{H}$ groups) directly opposite one another on a cyclobutenedione ring. Upon hydrogen bonding at both ends simultaneously, the two $\text{C}=\text{O}$ π -bonds and the two N lone pairs become

polarized to give increased cyclic 2π -electron delocalization ($4n + 2$, $n = 0$) in the four membered ring (Figure 3.1a). Evidence based on experiment and computations revealed that such aromaticity-hydrogen bonding coupling effects intensify with the head-to-tail polymerization of squaramide-based bolaamphiphiles, further reinforcing these interactions.²⁵

Inspired by these results, we performed an O→S exchange of the carbonyl moieties to examine the self-assembly and the aromatic gain on the interaction of thiosquaramide-based bolaamphiphiles relative to the oxosquaramide counterparts. Thiosquaramides, with their demonstrated greater acidity and lipophilicity compared to oxosquaramides,³¹ can potentially self-assemble in very different ways due to the unique supramolecular interactions enabled by the two thiocarbonyls. Thiocarbonyls are typically considered to be weaker hydrogen bond acceptors compared to carbonyls,³² but can engage in effective S⋯ π interactions as well as less directional hydrogen bonding interactions with potentially more than one donor due to the more polarizable nature of the S lone-pairs.^{33,34} Studies based on a survey of carbonyl and thiocarbonyl containing structures in the Cambridge Structural Database (CSD),³⁵ for example, have shown that C=O⋯H interactions generally exhibit small deviations (0 to 20°) from the lone-pair plane (i.e., the plane defined by the two sets of O lone-pairs, see *xy* plane in Figure 3.1b, top), while C=S⋯H interactions can deviate significantly from the lone-pair plane, displaying close to 90° lone-pair plane⋯H angles (Figure 3.1b, bottom). For this reason, C=S-containing synthons may give rise to drastically different modes of self-assembly compared to analogous C=O-containing synthons in the solution phase. Here, we show indeed that, upon O→S exchange, **1** and **2** self-assemble through intermolecular hydrogen-bonding into supramolecular polymers with surprisingly different morphologies: oxosquaramides **1** self-assemble “head-to-tail”, while thiosquaramides **2** “stack” on top of each other as a result of intermolecular hydrogen bonding at a C=S⋯H angle close to 90° (see illustration based on computed results of self-assembled N-methyl-oxosquaramides (**1'**) and N-methyl-thiosquaramides (**2'**) in Figure 3.1c). In this paper, we perform computations and experiments to examine the interplay between

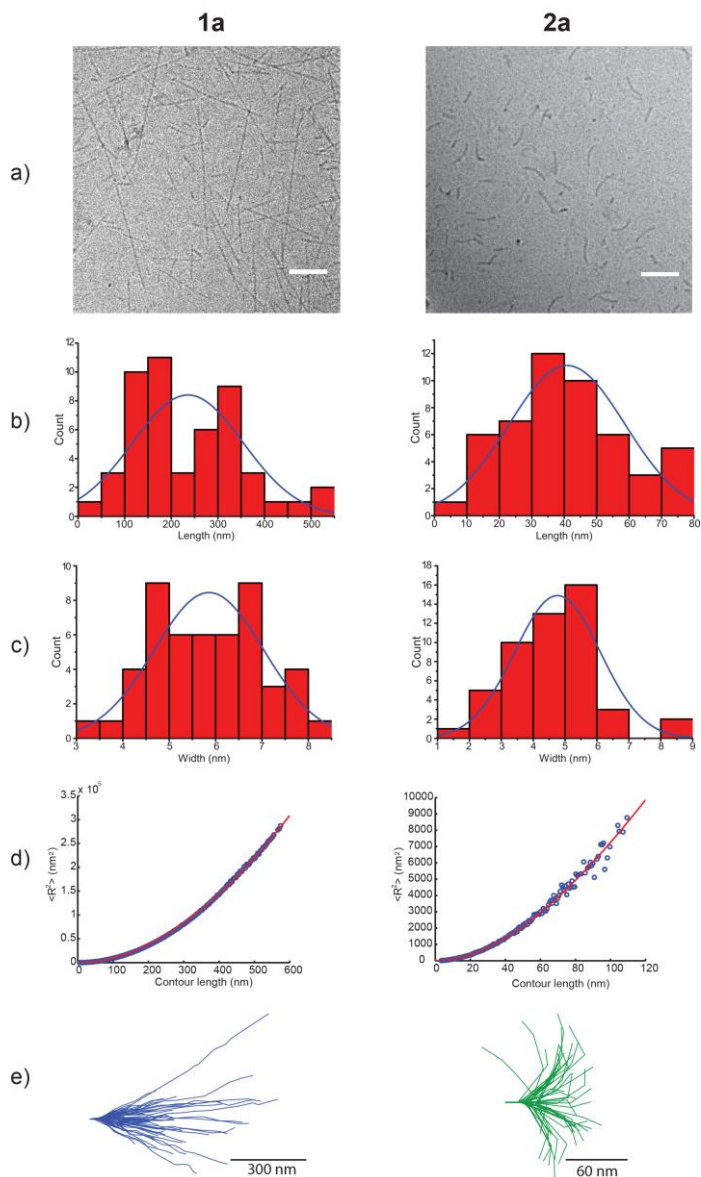


Figure 3.2. (a) Cryo-TEM images of **1a** (left) and **2a** (right) in aqueous solution (580 μM) after overnight equilibration. Scale bar: 100 nm. (b) Histograms of length distributions of **1a** (left) and **2a** (right) ($N = 50$, with average lengths of 235 ± 118 nm for **1a**, and 41 ± 18 nm for **2a**). (c) Histograms of width distributions of **1a** (left) and **2a** (right) ($N = 50$, with average widths of 5.8 ± 1.2 nm for **1a**, and 4.8 ± 1.3 nm for **2a**) (d) End-to-end distance plots (R^2) as function of contour length for **1a** (left) and **2a** (right), respectively, determined by cryo-TEM (blue open circles). Least-square fits are shown as red lines. (e) Fiber contours of **1a** (left) and **2a** (right) analyzed from cryo-TEM images, where initial tangents were aligned (contour lengths of 252 ± 116 nm for **1a** and 77 ± 17 nm for **2a**).

intermolecular hydrogen bonding geometries and aromaticity gain in synthons on the self-assembly mode “tug-of-war” of oxo- and thio-squaramide bolaamphiphiles. Despite the different hydrogen bonding arrangements of oxo- versus thio- squaramide synthons, computations suggest that both modes of self-assembly enhance the aromatic character of the squaramides, leading to stronger intermolecular interactions between the monomers, and increased structural rigidity in the respective supramolecular polymers.

3.3 Results and discussion

Synthesis and characterization of squaramide-based bolaamphiphiles. The molecular design of the squaramide-based bolaamphiphiles **1** and **2** consists of two squaramide synthons embedded within a hydrophobic core consisting of alkyl chains and surrounded by oligo(ethylene glycol)s to drive their nanophase segregation and one-dimensional self-assembly in water (see Figure 3.1c). In the original design of **1a**,²⁵ activation of the poly(ethylene glycol) by 1,1-carbonyldiimidazole was used for coupling to the hydrophobic spacer because of its synthetic facility, but to eliminate any effects imparted by the formed carbamate on the self-assembly an identical molecule bearing an ether between these domains was also synthesized and compared. The non-carbamate derivative **1b** was prepared by an alternate synthetic protocol (Scheme S3.1 and SI), giving moderate yields after reverse phase column chromatography. Thio-analogues **2a** and **2b** were prepared by reacting **1a** and **1b**, respectively, with pentathiodiphosphorus(V) acid-P,P'-bis(pyridinium betaine) in acetonitrile at room temperature to exclusively thionate the carbonyl groups of the squaramide moieties (Scheme S3.2);³⁶ reverse-phase column chromatography provided good yield for this step (89% **2a**, 72% **2b**). Carbon-13 nuclear magnetic resonance (¹³C-NMR) showed a downfield shift of $\Delta\delta \approx 20$ ppm of the C=S of the thiosquaramide compared to the C=O signal and a $\Delta\delta \approx 2-4$ ppm of the C=C of the cyclobutadione ring. The identity and purity of the proposed compounds were confirmed by a combination of techniques, including ¹H-NMR, ¹³C-NMR, LC-MS and ATR-FTIR (see Figure S3.1 and S3.2).

Monomer 2 forms shorter and more flexible supramolecular polymers than 1 in water. Cryogenic transmission electron microscopy (cryo-TEM) and small-angle X-ray scattering (SAXS) experiments probed the morphology and internal structure of the squaramide-based supramolecular polymers in water, showing surprisingly different aggregate morphologies and were thus suggestive of a distinct mode of self-assembly for the oxosquaramides and thiosquaramides in their respective fibers. Both **1a** and **1b** resulted in high-aspect-ratio fibers with lengths of 235 ± 118 and 246 ± 176 nm, respectively (Figures 3.2a, 3.2b, S3.6 and S3.7). In contrast, the thionated **2a** and **2b** were five to ten times shorter, displaying rod-like structures with lengths of 41 ± 18 and 24 ± 27 nm, respectively (Figure 3.2a, 3.2b, S3.6 and S3.7). The oxosquaramide supramolecular polymers (**1a**: 5.8 ± 1.2 nm, **1b**: 5.7 ± 1.2 nm) were also slightly thicker than the thiosquaramide derivatives (**2a**: 4.8 ± 1.3 nm and **2b**: 3.9 ± 1.1 nm) (Figure 3.2c and S3.7). Overall, by comparison of the molecules with and without the peripheral carbamates by cryo-TEM, these results suggest that the squaramide synthons are largely responsible for the observed self-assembled structures.

Statistical analyses of the cryo-TEM images with respect to the shape fluctuations of the supramolecular polymer structures suggest that **1a** forms long, rigid high-aspect ratio fibers, while **2a** forms short, flexible rod-like structures. Tracking of the contour lengths of the fibrillar assemblies using the Easyworm software³⁷ provided values of 252 ± 116 nm for **1a** and 77 ± 17 nm for **2a** (Figure 3.2d-e). Fig. 3.2d displays the mean square end-to-end distance $\langle R^2 \rangle$ plots as a function of contour length for the fiber (**1a**) and rod-like (**2a**) structures, respectively. The persistence length (P_l), which quantifies the stiffness of a semi-flexible polymer,³⁸ was determined from the $\langle R^2 \rangle$ by applying the worm-like chain model (WLC) (see supporting information, section 3.6.5).³⁷ Supramolecular polymers of **1a** displayed much larger P_l values (581 ± 76 nm)³⁷ compared to those of **2a** (47 ± 4 nm), and was thus suggestive of distinct mechanical properties for the oxo- versus thiosquaramide analogues. From P_l , the bending rigidity of the assembly of **1a** ($(2.4 \pm 0.3) \times 10^{-27}$ N·m²) was determined to be around 10-fold greater relative to that of **2a** ($(1.9 \pm 0.2) \times 10^{-28}$ N·m²).

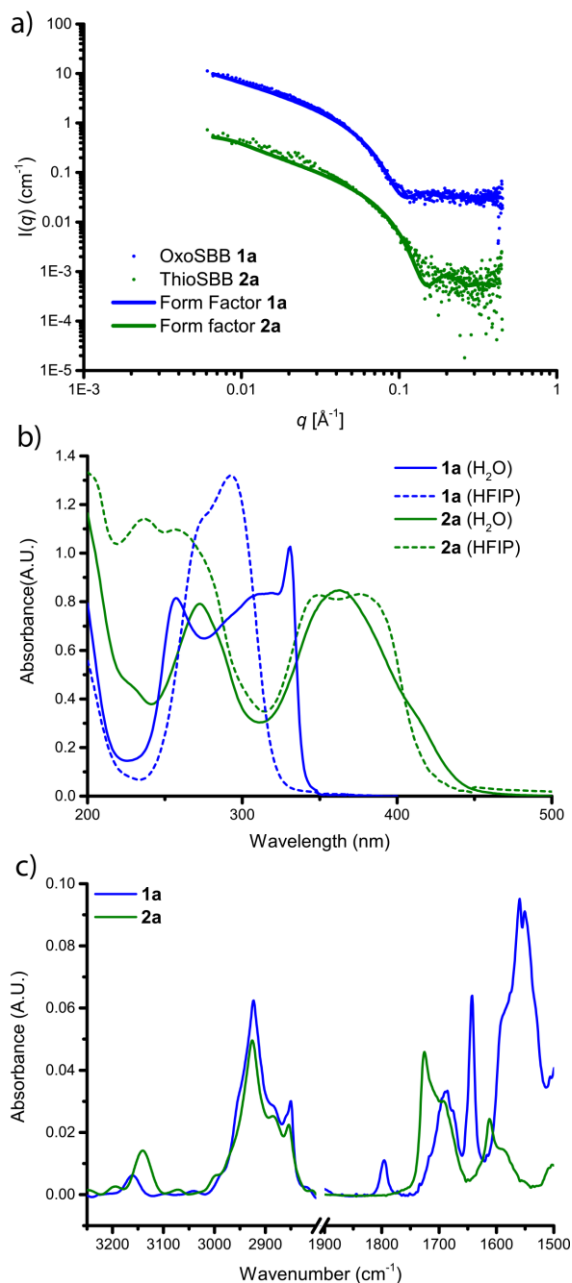


Figure 3.3. (a) Experimental SAXS profiles of **1a** and **2a** (5 mg mL⁻¹). The curves are modeled with a form factor for homogeneous and flexible homogeneous cylinders for **1a** and **2a**, respectively. The blue curve is shifted vertically by multiplying with a factor of 10 to enable visualization of the two profiles. (b) UV-Vis spectrum of **1a** and **2a** in water and HFIP (30 μM). (c) IR spectrum recorded in the N-H region, amide I region and amide II in D₂O for both **1a** and **2a** (5.8 mM).

SAXS profiles provided further insight into the morphologies of the oxo- versus thiosquaramide-based supramolecular polymers. We previously found that self-assemblies of **1a** showed profiles with a q^{-1} slope in the low q regime (Figure 3.3a, blue line) characteristic of fiber-like objects.²⁵ The data was modelled with a form factor for homogeneous cylinders, yielding a cross-sectional radius (r_{cs}) of ~ 3.4 nm. From this data, the cross-sectional mass per unit length (M_L) of **1a** was determined (Table S3.1) yielding a comparable number of bolaamphiphiles within the cross-section as reported earlier by our group.²⁵ Supramolecular polymers of **2a** also displayed a q^{-1} slope at in the same region (Figure 3.3a, green line), but were better modelled with a form factor for flexible homogenous cylinders, resulting in an r_{cs} (~ 2.3 nm) on par with cryo-TEM images. From the M_L of **2a**, approximately 10-14 bolaamphiphiles per nm (see supporting information, section 3.6.6) were determined within the fiber cross-section. SAXS measurements of **1b** (q^{-1} slope) showed similar scattering profiles to **1a** with the carbamate moiety, whereas **2b** (Figure S3.8) displayed a significantly lower q -slope, indicating the coexistence of two morphologies. Consequently, the morphological differences and monomer packing found within the cross-section of **1** versus **2** clearly suggest that the mode of monomer self-assembly is different for the oxo- and thiosquaramide analogues.

Self-assembled monomers 1 and 2 show distinct spectroscopic signatures in water. Spectroscopic measurements, namely UV-Vis and IR, were used to shed light into the effect of self-assembly on the squaramide synthon and the self-assembly of the squaramide monomers at a molecular level. The UV-Vis spectrum of **1a** in water presents two absorption maxima at 255 nm and 329 nm, corresponding to the monomers self-assembled into a supramolecular polymer, and a broad band between these maxima belonging to the depolymerized fraction (Figure 3.3b, solid blue line). When **1a** is dissolved in hexafluoroisopropanol (HFIP), a low dielectric solvent known to effectively disrupt hydrogen bonds,³⁹⁻⁴¹ the two maxima start to coalesce, superimposing with the monomer band (Figure 3.3b, dotted blue line). Similar trends were observed for monomer **1b** in both conditions (Figure S3.11). UV-Vis spectra for the thiosquaramide analogs display the

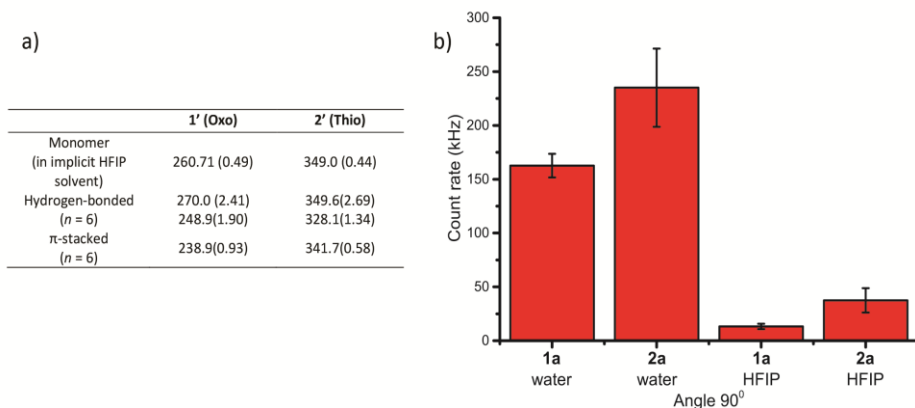


Figure 3.4. (a) Table with computed UV-Vis absorptions (λ , in nm) for the monomers, “head-to-tail” hexamers, and “stacked” hexamers of **1'** and **2'** in implicit solvation in a low dielectric solvent at IEF-PCM-M06-2X/6-311+G(d,p). Only transitions with oscillator strengths > 0.35 are listed (see values in parenthesis). (b) Scattered intensity (kHz) of samples of **1a** and **2a** in water and HFIP at the same concentration (580 μ M).

opposite trend in water, with **2a** showing bands with maxima at 363 nm and 272 nm (Figure 3.3b, solid green line); both are red-shifted in comparison to **1a**. Upon dissolving monomers of **2a** in HFIP, both bands at 272 and 363 nm are split into two peaks each at 258 and 237 nm, and 349 and 377 nm (Figure 3.3b, green dotted line), respectively. Similar trends in the UV-Vis spectra were observed for **2b** in both conditions (Figure S3.12).

To better understand the origin of the spectral differences in the two monomers in water and HFIP, TD-DFT computations were executed for models of N-methyl-oxosquaramide (**1'**) and N-methyl-thiosquaramide (**2'**) probing two potential aggregation modes for each: “head-to-tail” and “stacked.” UV absorption peaks in the 250 to 400 nm region were computed for the isolated monomers and self-assembled hexamers of **1'** and **2'** in implicit solvation at a low dielectric constant ($\epsilon < 20$, see supporting information, section 3.6.8) at IEF-PCM-M06-2X/6-311+G(d,p) to model **1** and **2** in their polymerized and depolymerized states (see table in Figure 3.4). Computed UV spectra revealed that when **1'** self-assembles in a “head-to-tail” mode, two coalescing peaks for the monomer at 259.1 and 258.7 nm, corresponding to the HOMO \rightarrow LUMO and HOMO \rightarrow LUMO+1 transitions respectively, become largely separate in the hexamer at 274.2

and 254.5 nm. These results are consistent with the experimentally obtained UV-Vis spectra for **1a** and **1b** in water (Figure 3.3b, blue solid line) and HFIP (Figure 3.3b, blue dotted line). On the other hand, when **2'** self-assembles in a “stacked” mode, the two peaks for the monomer at 347.4 and 336.1 nm, corresponding to the HOMO → LUMO and HOMO → LUMO+1 transitions respectively, coalesce upon oligomerization into peaks at 342.9 and 340.1 nm. These results are consistent with the experimentally obtained UV-Vis spectra for **2a** and **2b** in water (Figure 3.3b, green solid line) and HFIP (Figure 3.3b, green dotted line). For comparison, the computed UV results of the alternate self-assembly modes, i.e., “stacked” for **1'** and “head-to-tail” for **2'**, did not correlate with the experimentally observed trends (see data in Figure 3.4a). Hence, distinct UV-Vis spectra recorded for **1** and **2** are connected to their unique self-assembly modes that enable polarization of the squaramide motif.

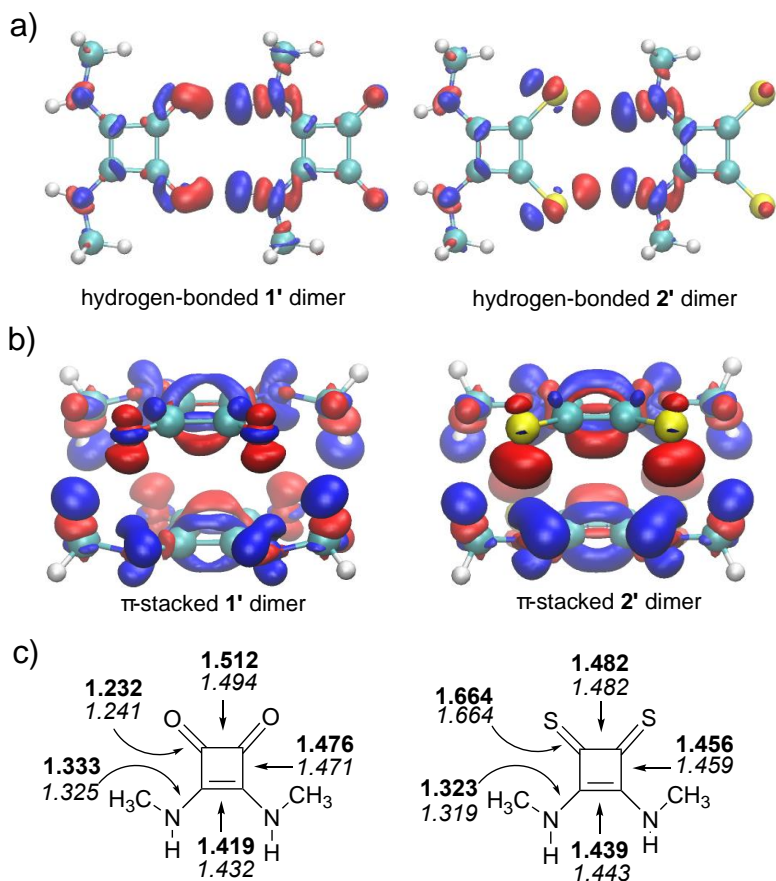


Figure 3.5. Computed electron density difference (EDD) maps for the (a) “head-to-tail” **1'** and **2'** dimers (note larger lobes on **1'**), and (b) “stacked” **1'** and **2'** dimers (note larger lobes on **2'**). Blue indicates electron density loss, red indicates electron density gain. (c) Computed geometries in implicit solvation for the isolated monomers of **1'** and **2'** (bond distances in Å, values in bold font), the “head-to-tail” hexamer of **1'** (left, averaged bond distances for each of the monomeric units, values in italics font), and the “stacked” hexamer of **2'** (right, averaged bond distances for each of the monomeric units, values in italics font).

Static light scattering (SLS) measurements of monomers **1a** and **2a** (Figure 3.4b) were performed in order to support their respective polymerization in water and depolymerization in HFIP solution. Scattered light intensities of supramolecular polymers of **1a** and **2a** indicated the presence of large objects in solution. When **1a** and **2a** were dissolved in HFIP, a 10-fold decrease in scattering intensity was recorded, consistent with the

depolymerization of the squaramide-based supramolecular polymers through solvation of the bolaamphiphiles and simultaneous disruption of hydrogen-bonding.

To confirm the role of hydrogen bonding in the self-assembly of the oxo- and thiosquaramides, infrared spectra were obtained for **1** and **2** in both D₂O and HFIP-d₂. In D₂O, **1a** showed asymmetric and symmetric C=O stretches at 1642, 1687, and 1676 cm⁻¹ for the squaramide and carbamate moieties, N–H stretches at 3162 cm⁻¹, and a small broad ring breathing band at 1796 cm⁻¹ (Figure 3.3c, blue). When **1a** was dissolved in HFIP-d₂, the C=O and ring breathing bands were shifted to higher wavenumbers by 10–15 cm⁻¹, with the latter indicative of greater ring bond length alternation in the squaramide moieties upon depolymerization; the N–H bands were not visible due to their likely overlap with stretches in the O–H region. For **2a**, C=O stretches at 1687 and 1676 cm⁻¹ were recorded for the carbamate moieties and an intense ring-breathing peak at 1726 cm⁻¹ (Figure 3.3c, green). The C=S stretches were expected to appear at the fingerprint region due to the heavier sulfur atom in the C=S bond comparison to the C=O, but could not be assigned due to their overlap with other bands of higher intensity. Additionally, compared to **1a**, the N–H stretches of **2a** were red-shifted to 3142 cm⁻¹ and of increased in intensity. When **2a** was dissolved in HFIP-d₂, the intense ring-breathing band was shifted towards lower wavenumbers by close to 20 cm⁻¹, and is consistent with shifts in the computed ring breathing frequencies for the **2'** monomer (at 1757 cm⁻¹) versus “stacked” **2'** hexamer (at 1774 cm⁻¹). In HFIP-d₂, the shift of the thiosquaramide N–H stretch confirmed disruption of the hydrogen-bond interaction between the monomers. Similar trends were observed for **1b** and **2b** (as well as **1a** and **2a**) in bulk and in solution (see Figure S3.1-5), respectively, except additional vibrations were recorded for the carbamate moieties. Key features of the IR spectra agreed with the computed IR vibrational modes of **1'** and **2'** as well as their self-assembled hexamers in implicit solvation at a low dielectric constant (see general methods and Tables S3.6 and S3.7). The solution-phase IR results suggest that both **1** and **2** engage in hydrogen bonding upon self-assembly, but the self-assembled **1** displays more significant ring bond length equalization than **2**.

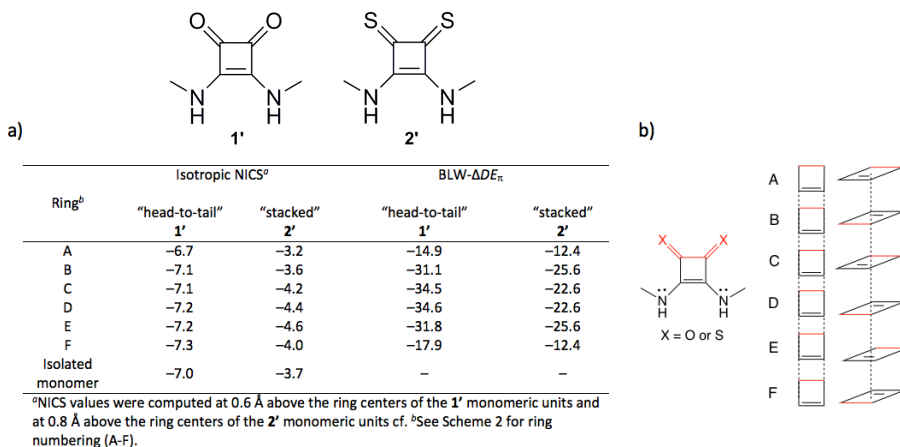


Figure 3.6. (a) Table with the computed isotropic NICS values (in ppm) and BLW- ΔDE_{π} values (in kcal/mol) for each of the monomer rings in the “head-to-tail” 1' hexamer and “stacked” 2' hexamer. More negative NICS values indicate greater aromaticity gain in the monomers upon self-assembly. All BLW- ΔDE_{π} values were computed at B3LYP/6-31G(d); more negative ΔDE_{π} values indicate greater cyclic π -electron delocalization gain in the monomers upon self-assembly. (b) Rings A to F in the “head-to-tail” and “stacked” hexamers of 1' and 2'.

Computational studies of aromaticity gain in oxo- and thioamidine supramolecular polymers. Density Functional Theory (DFT) computations of model “head-to-tail” and “stacked” hexamers of 1' and 2' were carried out to examine the competition between the different self-assembly modes. Single point energy calculations at the IEF-PCM-M06-2X/6-311+G(d,p) level (see supporting information, section 3.6.8) reveal a more negative averaged hydrogen bonding interaction energy (ΔE_{HB}) for the “head-to-tail” 1' hexamer (−10.77 kcal/mol) compared to that of the “stacked” 1' hexamer (−8.73 kcal/mol), indicating that the “head-to-tail” mode is favoured for 1' in water. Conversely, the computed averaged ΔE_{HB} for the “head-to-tail” 2' hexamer (−9.00 kcal/mol) was significantly lower relative to that of the “stacked” 2' hexamer (−12.99 kcal/mol), suggesting a dominant stacking mode for 2' in water. Accordingly, computed electron density difference (EDD) maps for the “head-to-tail” vs. “stacked” dimers of 1' and 2' show that C=O's form effective hydrogen bonding interactions with N–H's in the O lone-pair plane, but C=S's form stronger interactions with the N–H's at roughly 90° angles to the S lone-pair plane. As shown in Figure 3.5a, EDD maps for the “head-to-tail” 1' and 2' dimers show increased electron

density at the O/S's (indicated in red, electron density gain) and decreased electron density at the amine H's (indicated in blue, electron density loss); as expected by the stronger hydrogen bond acceptor ability of C=O, the "head-to-tail" **1'** dimer displays greater electron density change. In Figure 3.5b, EDD maps of the "stacked" **1'** and **2'** dimers also show increased electron density at the O/S's (in red) and decreased electron density at the general N–H region (in blue), suggestive of attractive noncovalent interactions between the stacks. The much greater electron density change for the "stacked" **2'** dimer is consistent with the ability of C=S to engage in less directional hydrogen bonding interactions.^{33,34} These findings further support that differences in the physical properties and spectroscopic features of the supramolecular polymers of **1** versus **2** likely arise from their preferred self-assembly modes.

Computed geometries for the monomers and hexamers of **1'** and **2'** at the IEF-PCM-B3LYP-D3/6-31+G(d) level show that the ring bonds of **1'** (Figure 3.5c, left, values in bold font) become more bond length equalized (i.e., increased aromatic character) upon self-assembly in the "head-to-tail" **1'** hexamer (values in italics font); all of the single bonds shorten (by 0.005 to 0.018 Å) and the double bonds lengthen (by 0.009 to 0.013 Å). In contrast, the ring bonds of **2'** (Figure 3.5c, right, values in bold font) are altered to a lesser degree upon self-assembly in the "stacked" **2'** hexamer (values in italics font); the two C–N bonds shorten (by 0.004 Å) and the ring C=C bond lengthens (by 0.004 Å), but the C–C and C=S bonds exhibit little to no change (a zero to 0.003 Å change). Harmonic Oscillator Model of Electron Delocalization (HOMED) analyses⁴² confirm these observations, showing increased HOMED values when **1'** (0.329, HOMED value for isolated monomer) self-assembles into the "head-to-tail" **1'** hexamer (0.383, averaged HOMED values for six monomer units), while those of **2'** (0.447, isolated monomer) and the "stacked" **2'** hexamer (0.445, average for six monomer units) stay close. HOMED values range from 0 (non-aromatic) to 1 (fully aromatic compounds) and measure the degree of ring bond equalization in molecules as a criterion for aromaticity (see supporting information, section 3.6.10). These geometric features agree with the IR spectra of **1(a/b)** and **2(a/b)** in the solution phase, which suggest that the

geometries of oxo- and thiosquaramides change in opposite ways upon monomer self-assembly.

Computations based on the magnetic and energetic criteria of aromaticity revealed significant aromaticity gain in both the “head-to-tail” self-assembled monomers of **1'** and the “stacked” monomers of **2'**. Isotropic nucleus independent chemical shifts (NICS)^{43,44} were computed at 0.6 Å above each of the “head-to-tail” **1'** ring centers, and at 0.8 Å above each of the “stacked” **2'** ring centers (due to the more diffuse orbitals of the S atoms) to quantify the magnetic effects of aromaticity gain. As shown in the table in Figure 3.6, the computed isotropic NICS for both **1'** (NICS(0.6) = –7.0 ppm) and **2'** (NICS(0.8) = –3.7 ppm) become more negative in the “head-to-tail” **1'** hexamer (NICS(0.6) = –6.7 to –7.3 ppm) and “stacked” **2'** hexamer (NICS(0.8) = –3.2 to –4.6 ppm), documenting aromaticity gain in both monomers upon self-assembly.

Block-localized wavefunction (BLW) analyses⁴⁵ quantified the energetic effects of aromaticity gain in the “head-to-tail” hexamer of **1'** and the “stacked” hexamer of **2'** (see supporting information, section 3.6.10). The BLW method, the simplest variant of valence bond calculations, measures π -electron delocalization energies (DE_π) in molecules by comparing the energy of the fully delocalized wavefunction (Ψ_{deloc}) of a molecule to that of its hypothetical π -electron localized wavefunction (Ψ_{loc}) in which all π -electron delocalization effects are “turned off”: $DE_\pi = \Psi_{\text{deloc}} - \Psi_{\text{loc}}$ (i.e., a more negative DE_π value indicates more π -electron delocalization in a molecule). The computed DE_π difference between the isolated monomers (e.g., **1'** and **2'**) versus “head-to-tail” or “stacked” monomers provides a measure of the extra gain in π -electron delocalization in monomers upon self-assembly; $\Delta DE_\pi = DE_\pi$ (“head-to-tail” or “stacked” monomer) – DE_π (monomer) (i.e., a more negative ΔDE_π value indicates more π -conjugation gain upon “head-to-tail” hydrogen-bonding or “stacked” hydrogen-bonding of the monomer). For cyclic π -conjugated monomers, like **1'** and **2'**, large negative ΔDE_π values suggest enhanced aromatic character in the self-assembled monomer (see supporting information, section 3.6.10 and Figure 3.6a). Remarkably, the computed ΔDE_π values for each of the monomers in

the “head-to-tail” **1'** hexamer (averaged $\Delta DE_{\pi} = -27.5$ kcal/mol) and the “stacked” **2'** hexamer (averaged $\Delta DE_{\pi} = -20.6$ kcal/mol) are substantial, and suggest significant aromaticity gain upon self-assembly through hydrogen bonding (Table S3.2 for more details). These computations suggest that in low dielectric environments, such as in the hydrophobic core of a supramolecular polymer, aromaticity gain can be considered as an important driving force when combined with hydrogen-bonding to direct the self-assembly of supramolecular polymers.

3.4 Conclusions

Here I demonstrate that oxosquaramide and thiosquaramide monomers self-assemble into surprisingly different fibrillar morphologies in water: oxosquaramide-based bolaamphiphiles form long, rigid fibrillar architectures, while the thio-analogues form short, flexible rod-like structures. Evidence based on spectroscopic measurements and computational analyses revealed that oxosquaramides self-assemble into a “head-to-tail” arrangement by aligning their hydrogen bond donors (N–H’s) and acceptors (C=O’s) along the squaramide ring plane, while thiosquaramides prefer antiparallel “stacked” configurations in which the N–H’s of each unit are stacked above and below the C=S’s of an adjacent layer and interact through C=S \cdots H hydrogen bonding with a close to 90° C=S \cdots H angle, suggesting that the hydrogen bond in the oxosquaramides have a preferential alignment parallel to the fiber axes, while thiosquaramides might not benefit of this alignment resulting in a decrease of the length and stiffness of the aggregate. Based on IR measurements, the self-assembled oxosquaramides displayed distinct bond length equalization, whereas ring bond distances of the self-assembled thiosquaramides were altered to a lesser degree. However, computations revealed that polarization of both monomers in the “head-to-tail” and “stacked” self-assembly modes occurs through hydrogen bonding, thereby increasing the aromatic character of both squaramide synthons. These findings further suggest that changes in the aromatic characters of hydrogen-bonding synthons can be used to “fine-tune” the intermolecular interactions between monomers, with potent effects on their mode of supramolecular polymerization. I emphasize that beside the often-used checklist for

controlling hydrogen bonding interactions,⁸⁻¹⁰ *aromaticity gain* also should be considered in the molecular designs of self-assembling monomers for supramolecular polymers, and more broadly in supramolecular chemistry.

3.5 References

- (1) Aida, T., Meijer, E. W. & Stupp, S. I. *Science*, **2012**, 335 (6070), 813–817.
- (2) Appel, E. A., del Barrio, J., Loh, X. J. & Scherman, O. A. *Chem. Soc. Rev.*, **2012**, 41 (18), 6195–214.
- (3) Rieth, S., Baddeley, C. & Badjic, J. D. *Soft Matter*, **2007**, 3 (4), 137.
- (4) Krieg, E., Bastings, M. M. C., Besenius, P. & Rybtchinski, B. *Chem. Rev.*, **2016**, 116 (4), 2414–2477.
- (5) de Greef, T. F. A. & Meijer, E. W. *Nature*, **2008**, 453 (7192), 171–173.
- (6) Thiele, J., Ma, Y., Bruekers, S. M. C., Ma, S. & Huck, W. T. S. *Adv. Mater.*, **2014**, 26 (1), 125–148.
- (7) Webber, M. J., Appel, E. A., Meijer, E. W. & Langer, R. Supramolecular biomaterials. *Nat. Mater.*, **2015**, 15 (1), 13–26.
- (8) Fernandez-Castano Romera, M., Lafleur, R. P. M., Guibert, C., Voets, I. K., Storm, C. & Sijbesma, R. P. *Angew. Chemie. Int. Ed.*, **2017**, 56 (30), 8771–8775.
- (9) Obert, E., Bellot, M., Bouteiller, L., Andrioletti, F., Lehen-Ferrenbach, C. & Boué, F. *J. Am. Chem. Soc.*, **2007**, 129 (50), 15601–15605.
- (10) Park, T. & Zimmerman, S. C. *J. Am. Chem. Soc.*, **2006**, 128 (35), 11582–11590.
- (11) Wilson, A. J. *Soft Matter*, **2007**, 3 (4), 409.
- (12) Shen, Z., Wang, T. & Liu, M. *Chem. Commun.*, **2014**, 50 (17), 2096–9.

Chapter 3

- (13) Leenders, C. M. A., Baker, M. B., Pijpers, I. A. B., Lafleur, R. P. M., Albertazzi, L., Palmans, A. R. A. & Meijer, E. W. *Soft Matter*, **2016**, *12* (11), 2887–2893.
- (14) Baram, J., Weissman, H., Tidhar, Y., Pinkas, I. & Rybtchinski, B. *Angew. Chem. Int. Ed.*, **2014**, *53* (16), 4123–6.
- (15) Nakano, Y., Markvoort, A. J., Cantekin, S., Filot, I. A. W., Ten Eikelder, H. M. M., Meijer, E. W. & Palmans, A. R. A. *J. Am. Chem. Soc.*, **2013**, *135*, 16497–16506.
- (16) Lloyd, G. O. & Steed, J. W. *Nat. Chem.*, **2009**, *1*, 437–442.
- (17) Siddiqui, S. & Spano, F. *Chem. Phys. Lett.*, **1999**, *308*, 99–105.
- (18) Rybtchinski, B. *ACS Nano*, **2011**, *5*, 6791–818.
- (19) Rudolph, T., Kumar Allampally, N., Fernández, G. & Schacher, F. H. *Chem. Eur. J.*, **2014**, *20*, 13871–13875.
- (20) Jalani, K., Dhiman, S., Jain, A. & George, S. J. *Chem. Sci.*, **2017**, *8*, 6030–6036.
- (21) Wu, J. I., Jackson, J. E. & Schleyer, P. V. R. *J. Am. Chem. Soc.*, **2014**, *136*, 13526–13529.
- (22) Kakeshpour, T., Wu, J. I. & Jackson, J. E. *J. Am. Chem. Soc.*, **2016**, *138*, 3427–3432.
- (23) Anand, M., Fernández, I., Schaefer, H. F. & Wu, J. I. *J. Comput. Chem.*, **2016**, *37*, 59–63.
- (24) Kakeshpour, T., Bailey, J. P., Jenner, M. R., Howell, D. E., Staples, R. J., Holmes, D., Wu, J. I., Jackson, J. E. *Angew. Chem. Int. Ed.*, **2017**, *56*, 9842.
- (25) Saez Talens, V., Englebienne, P., Trinh, T. T., Noteborn, W. E. M., Voets, I. K. & Kieltyka, R. E. *Angew. Chemie. Int. Ed.*, **2015**, *54* (36), 10502–10506.

- (26) Soberats, B., Martínez, L., Sanna, E., Sampedro, A., Rotger, C. & Costa. *Chem. Eur. J.*, **2012**, *18*, 7533–7542.
- (27) López, C., Ximenis, M., Orvay, F., Rotger, C. & Costa, A. *Chem. Eur. J.*, **2017**, *23*, 7590–7597.
- (28) Ian Storer, R., Aciro, C. & Jones, L. H. *Chem. Soc. Rev.*, **2011**, *40*, 2330.
- (29) Alemán, J., Parra, A., Jiang, H. & Jørgensen, K. A. *Chem. Eur. J.*, **2011**, *17*, 6890–6899.
- (30) Quiñonero, D., Prohens, R., Garau, C., Frontera, A., Ballester, P., Costa, A. & Deyà, P. M. *Chem. Phys. Lett.*, **2002**, *351*, 115–120.
- (31) Busschaert, N., Elmes, R. B. P., Czech, D. D., Wu, X., Kirby, I. L., Peck, E. M., Hendzel, K. D., Shaw, S. K., Chan, B., Smith, B. D., Jolliffe, K. A. & Gale, P. A. *Chem. Sci.*, **2014**, *5*, 3617–3626.
- (32) Lee, H. J., Choi, Y. S., Lee, K. B., Park, J. & Yoon, C. J. *J. Phys. Chem. A.*, **2002**, *106*, 7010–7017.
- (33) Lenthall, J. T., Foster, J. A., Anderson, K. M., Probert, M. R., Howard, J. A. K. & Steed, J. W. *CrystEngComm*, **2011**, *13*, 3202–3212.
- (34) Custelcean, R., Engle, N. L. & Bonnesen, P. V. *CrystEngComm*, **2007**, *9*, 452.
- (35) Allen, F. H., Bird, C. M., Rowland, R. S. & Raithby, P. R. *Acta Crystallogr. Sect. B Struct. Sci.*, **1997**, *53*, 680–695.
- (36) Bergman, J., Pettersson, B., Hasimbegovic, V. & Svensson, P. H. *J. Org. Chem.*, **2011**, *76*, 1546–1553.
- (37) Lamour, G., Kirkegaard, J. B., Li, H., Knowles, T. P. & Gsponer, J. *Source Code Biol. Med.*, **2014**, *9*, 16.
- (38) Makky, A., Bousset, L., Polesel-Maris, J. & Melki, R. *Sci. Rep.*, **2016**, *6*, 37970.

- (39) Leenders, C. M. A., Albertazzi, L., Mes, T., Koenigs, M. M. E., Palmans, A. R. A., Meijer, E. W. *Chem. Commun.*, **2013**, 49, 1963–1965.
- (40) Korevaar, P. A., Newcomb, C. J., Meijer, E. W., & Stupp, S. I. *J. Am. Chem. Soc.*, **2014**, 136, 8540–8543.
- (41) Boekhoven, J., Brizard, A. M., van Rijn, P., Stuart, M. C. A., Eelkema, R., & van Esch, J. H. *Angew. Chemie. Int. Ed.*, **2011**, 50, 12285–12289.
- (42) Raczyńska, E. D., Hallman, M., Kolczyńska, K. & Stępniewski, T. M. *Symmetry (Basel)*, **2010**, 2, 1485–1509.
- (43) Chen, Z., Wannere, C. S., Corminboeuf, C., Puchta, R. & Schleyer, P. von R. *Chem. Rev.*, **2005**, 105, 3842–3888.
- (44) Schleyer, P. V. R., Maerker, C., Dransfeld, A., Jiao, H. & Van Eikema Hommes, N. J. R. *J. Am. Chem. Soc.*, **1996**, 118, 6317–6318.
- (45) Mo, Y., Song, L. & Lin, Y. *J. Phys. Chem. A.*, **2007**, 111, 8291–8301.
- (46) Frisch, M. J., Trucks, G. W., Schlegel, H. B., Scuseria, G. E., Robb, M. A., Cheeseman, J. R., Scalmani, G., Barone, V., Mennucci, B., Petersson, G. A., Nakatsuji, H., Caricato, M., Li, X., Hratchian, H. P., Izmaylov, A. F., Bloino, J., Zheng, G., Sonnenberg, J. L., Hada, M., Ehara, M., Toyota, K., Fukuda, R., Hasegawa, J., Ishida, M., Nakajima, T., Honda, Y., Kitao, O., Nakai, H., Vreven, T., Montgomery, J. A., Jr., Peralta, J. E., Ogliaro, F., Bearpark, M., Heyd, J. J., Brothers, E., Kudin, K. N., Staroverov, V. N., Keith, T., Kobayashi, R., Normand, J., Raghavachari, K., Rendell, A., Burant, J. C., Iyengar, S. S., Tomasi, J., Cossi, M., Rega, N., Millam, J. M., Klene, M., Knox, J. E., Cross, J. B., Bakken, V., Adamo, C., Jaramillo, J., Gomperts, R., Stratmann, R. E., Yazyev, O., Austin, A. J., Cammi, R., Pomelli, C., Ochterski, J. W., Martin, R. L., Morokuma, K., Zakrzewski, V. G., Voth, G. A., Salvador, P., Dannenberg, J. J., Dapprich, S., Daniels, A. D., Farkas, Ö., Foresman, J. B., Ortiz, J. V., Cioslowski, J., Fox, D. J. *Gaussian 09, revision D.01*, Gaussian, Inc., Wallingford, CT, **2013**.

- (47) Schmidt, M. W., Baldrige, K. K., Boatz, J. A., Elbert, S.T., Gordon, M. S., Jensen, J. H., Koseki, S., Matsunaga, N., Nguyen, K. A., Su, S., Windus, T. L., Dupuis, M., Montgomery J. A. *J. Comput. Chem.*, **1993**, *14*, 1347–1363.

3.6 Supporting Information

3.6.1 Materials

All reagents and chemicals were obtained from commercial sources at the highest purity available and used without further purification. O-methylundecaethylene glycol was obtained from Polypure and Broadpharm. Palladium on matrix activated carbon, triethylsilane and all other commercially available chemicals were purchased from Sigma Aldrich. Deuterated chloroform was purchased from Euriso-top and Milli-Q water was employed for all the experiments.

3.6.2 General methods

Cryo transmission electron microscopy (Cryo-TEM). Cryogenic TEM (cryo-TEM) samples were imaged with a Tecnai F20 equipped with a field emission gun (FEI company) at 200 keV using a Gatan UltraScan camera (Gatan company) with a defocus between -4 and -10 μm . Samples were prepared by applying a 3 μL sample of **1(a/b)** or **2(a/b)** in water to a glow-discharged Quantifoil R2/2 holey carbon film or 300 mesh copper grid with a lacey-carbon support film (Supplier-Electron Microscopy Sciences). Excess liquid was blotted off for 1 second and plunge-frozen in liquid ethane using a Leica EMGP. The length and width of the aggregates were measured using Fiji software (<https://fiji.sc/> - TIA reader plugin). The size distribution was obtained by measuring the length and the width of 50 fibers per sample. Details on the calculation of the persistence length (P_i) and bending rigidity (κ) are given in Supplementary Note 2. The resulting assemblies of **1a** and **2a** were tracked by using the Easyworm software.³⁷

Small angle X-ray scattering (SAXS). Small angle X-ray scattering measurements (SAXS) were carried out on a SAXSLAB GANESHA 300 XL SAXS system equipped with a GeniX 3D Cu Ultra Low Divergence micro focus sealed tube source producing X-rays with a wavelength $\lambda = 1.54 \text{ \AA}$ at a flux of $1 \times 10^8 \text{ ph/s}$ and a Pilatus 300K silicon pixel detector with 487×619 pixels of $172 \mu\text{m} \times 172 \mu\text{m}$ in size, which is placed at two sample-to-detector distances of 713 and 1513 mm respectively to access a q -range of $0.06 \leq q \leq 0.44 \text{ \AA}^{-1}$ with $q = 4 \pi/\lambda (\sin\Theta/2)$. Samples of 4 and 5 mg mL^{-1} concentration

were prepared the night before measurement and contained at room temperature in 2 mm quartz capillaries (Hilgenberg GmbH) during the measurements. Further details are described in Supplementary Note 3.

Ultraviolet-visible spectroscopy (UV-Vis). Absorption spectra were acquired using a Cary 300 UV-Vis spectrophotometer. All measurements were performed at room temperature using a quartz cuvette with a path length of 1 cm scanning from 200 to 500 nm. Samples were prepared by dissolving the analyte in the corresponding solvent to reach a final concentration of 30 μM . Samples were left to equilibrate overnight prior measurement.

Infrared spectroscopy (IR). IR spectra in the solid state were recorded on a Perkin Elmer UATR Two FT-IR spectrometer set to a resolution of 4 cm^{-1} . IR spectra in the solution state were recorded using a Bio-Rad Excalibur spectrometer equipped with a nitrogen cooled MCT detector. A liquid transmission cell with CaF_2 windows and a fixed nominal path length of 50 μm was used. Solution phase measurements were performed using D_2O and HFIP- d_2 at room temperature with a final concentration of 5.8 mM for all the samples. After preparation, samples were equilibrated overnight prior to measurement. Spectra were recorded at room temperature, with a resolution of 1 cm^{-1} averaged over 128 scans. The final absorbance spectra was expressed in terms of absorbance and corrected by manual subtraction of a water vapor spectrum. Baseline subtraction was performed using Origin 9.1 software.

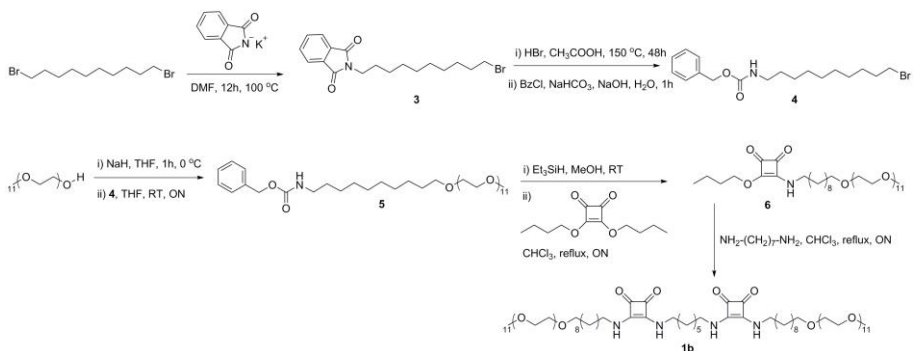
Static light scattering (SLS). SLS experiments were conducted on an ALV/CGS-3 MD-4 compact goniometer system equipped with a multiple Tau digital real time correlator (ALV-7004) and a solid-state laser ($\lambda = 532\text{ nm}$; 40 mW). All samples were prepared at a concentration of 580 μM and equilibrated overnight prior to measurement. Experiments covered scattering angles from 60 to 120°, averaged over 6 runs of 10 s each at room temperature.

Computational methods. Geometries of the **1'** and **2'** monomers, head-to-tail hexamers, and stacked hexamers were optimized in implicit solvation at $\epsilon = 16.7$ at the IEF-PCM-B3LYP-D3/6-31+G(d) level using ultrafine grid employing the Gaussian09 program.⁴⁶ "Head-to-tail" hexamers of **1'** and **2'** were optimized with C_{2v} symmetry constraint, based on an initial geometry where the N-H groups of each unit were hydrogen bonded to the C=O/S groups of a neighboring unit along the squaramide ring plane. "Stacked" hexamers of **1'** and **2'** were optimized with a constrained C_s symmetry, based on an initial geometry where the N-H groups of each unit were stacked above and below the C=O/S groups of a neighboring monomeric unit. Based on geometries optimized at the IEF-PCM-B3LYP-D3/6-31+G(d) level, single point hydrogen bonding interaction energies (ΔE_{HB}) of the "head-to-tail" and "stacked" hexamers of **1'** and **2'** were computed in implicit solvation at $\epsilon = 16.7$ at the IEF-PCM-M06-2X/6-311+G(d,p) level; ΔE_{HB} is the total electronic energy of a hexamer minus six times the total electronic energy of its monomeric units. Electron density difference (EDD) maps for the "head-to-tail" and "stacked" dimers of **1'** and **2'** were computed at the B3LYP-D3/6-31+G(d) level.

Due to the limited selection of dielectric constants available in Gaussian09 for frequency and TD-DFT calculations, computed IR, UV, and NICS analyses for the monomers and hexamers were performed in implicit solvation at $\epsilon = 8.5$ to mimic both the low dielectric environment of the HFIP solvent as well as the hydrophobic environment of the self-assembled polymers in water. IR vibrational frequencies were computed at the IEF-PCM-B3LYP-D3/6-31+G(d) level. TD-DFT calculations were performed at the IEF-PCM-M06-2X/6-311+G(d,p) level known to match well with experimental UV results. Isotropic nucleus independent chemical shifts (NICS)^{43,44} values were computed at 0.6 Å above the squaramide ring centers and at 0.8 Å above the thiosquaramide rings centers, at the IEF-PCM-PW91/IGLOIII level. Block-localized wavefunction (BLW)⁴⁵ computations were performed in implicit solvation at $\epsilon = 8.5$ at the PCM-B3LYP/6-31G(d) level with the GAMESS 2013-R1 program⁴⁷ (see full details for the BLW method in section 3.6.10).

3.6.3 Synthetic routes

3.1 Synthesis of compound 1b



Scheme S3.1. Synthetic route for compound 1b

Synthesis of 3

1,10-dibromodecane (20.0 g, 66.7 mmol) was added to potassium phthalimide (2.5 g, 13.4 mmol) in DMF (20 mL), resulting in a cloudy suspension that was refluxed for 12 h. Once the solvent was removed by evaporation under vacuum, the reaction mixture was purified by column chromatography (ethyl acetate/petroleum ether, 1:40). The resulting product was concentrated in a rotary evaporator, followed by drying with a gentle stream of air overnight to yield a white solid.

Yield: 4.1 g, 83 %. ¹H-NMR (δ_{H} [ppm], CDCl₃, 500 MHz): 7.88-7.84 (m, 2H), 7.75-7.71 (m, 2H), 3.72-3.68 (t, 2H), 3.44-3.40 (t, 2H), 1.90-1.83 (m, 2H), 1.71-1.65 (m, 2H), 1.45-1.29 (m, 12H). ¹³C-NMR (δ_{C} [ppm], CDCl₃, 125 MHz): 168.46, 133.90, 132.20, 123.18, 38.07, 34.13, 32.87, 29.40, 29.38, 29.17, 28.77, 28.63, 28.20, 26.87.

Synthesis of 4

Compound 3 (3.0 g, 8.1 mmol) was dissolved in acetic acid (10 mL), hydrogen bromide (48 %, 4 mL) was added and the mixture was refluxed at 150 °C for 48 h. The brown suspension was evaporated to dryness using a rotary evaporator followed by a gentle stream of air overnight. The deprotection of the phthalimide to yield the primary amine was followed by

Chapter 3

$^1\text{H-NMR}$ and $^{13}\text{C-NMR}$. The reaction was assumed to be quantitative by $^1\text{H-NMR}$ and the product was used without further purification.

$^1\text{H-NMR}$ (δ_{H} [ppm], CDCl_3 , 400 MHz): 8.04 (br s, 3H), 3.46-3.41 (t, 2H), 3.05 (m, 2H), 2.13-1.79 (m, 4H), 1.35-1.32 (m, 4H), 1.09-1.05 (m, 8H). $^{13}\text{C-NMR}$ (δ_{C} [ppm], CDCl_3 , 100 MHz): 40.29, 34.04, 32.88, 29.37, 29.31, 28.97, 28.77, 28.21, 27.53, 26.61.

Sodium bicarbonate (1.0 g, 12.0 mmol) in water (15 mL) was added to the deprotected primary amine, resulting in a foaming solution. The mixture was cooled to 0°C prior to the addition of benzyl chloroformate (2.3 mL, 16.1 mmol). A 1M solution of sodium hydroxide (3.5 mL, 3.5 mmol) was then added dropwise over 20 minutes and stirred overnight. The reaction mixture was extracted from the aqueous layer 5 times with chloroform (20 mL). The product was purified by column chromatography using petroleum ether/ethyl acetate, 9:1, and the solvents were removed using a rotary evaporator yielding a yellow solid.

Yield: 1.9 g, 63 %. $^1\text{H-NMR}$ (δ_{H} [ppm], CDCl_3 , 400 MHz): 7.37-7.28 (m, 5H), 5.11 (s, 2H), 4.88 (br s, 1H), 3.44-3.39 (m, 2H), 3.22-3.13 (m, 2H), 2.05-1.80 (m, 2H), 1.52-1.41 (m, 2H), 1.33-1.30 (m, 10H). $^{13}\text{C-NMR}$ (δ_{C} [ppm], CDCl_3 , 100 MHz): 156.03, 137.29, 128.29, 127.68, 127.64, 65.01, 40.13, 38.73, 29.35, 28.82, 28.72, 28.64, 28.46, 26.92, 26.18, 25.76.

Synthesis of 5

O-methyl-undecaethylene glycol (0.8 g, 1.6 mmol) was dissolved in tetrahydrofuran (5 mL) and cooled to 0°C . Sodium hydride (60 % in mineral oil) (55.7 mg, 2.3 mmol) was then added, resulting in vigorous foaming. The reaction mixture was stirred for one hour; then the ice bath was removed, compound **4** (0.9 g, 2.3 mmol) was added, and stirred overnight at room temperature. Purification of the product was performed by flash column chromatography on a C18 silica column with a gradient of 10-90% $\text{CH}_3\text{CN}/\text{H}_2\text{O}$ over 45 minutes. The purified product was concentrated using a rotary evaporator and lyophilized overnight to yield a white solid.

Yield: 30 %, 0.4 g. ¹H-NMR (δ_{H} [ppm], CDCl₃, 400 MHz): 7.36-7.28 (m, 5H), 5.09 (s, 2H), 4.22-4.20 (m, 1H), 3.64-3.52 (m, 43H), 3.46-3.37 (m, 5H), 3.18-3.13 (m, 2H), 1.63-1.27 (m, 16H). ¹³C-NMR (δ_{C} [ppm], CDCl₃, 100 MHz): 128.56, 128.12, 72.00, 71.59, 70.62, 70.56, 70.11, 69.75, 66.61, 63.84, 59.08, 41.19, 30.02, 29.69, 29.52, 29.31, 26.79, 26.13. LC-MS: t= 8.20 min, m/z: 823.60 [M+H]⁺.

Synthesis of 6

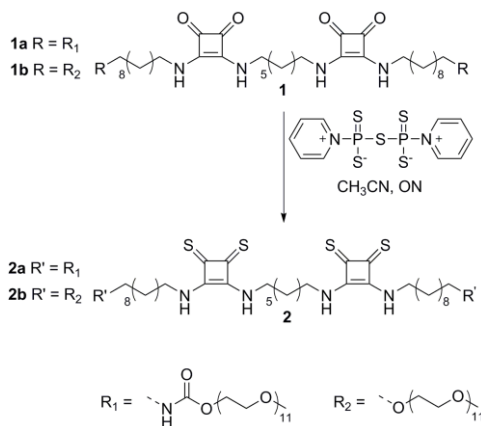
Compound **5** (0.4 g, 0.5 mmol) was dissolved in methanol (5 mL) with a catalytic amount of Pd/C, and degassed briefly with argon gas. Subsequently, triethylsilane (1.5 mL, 9.4 mmol) was added dropwise over 20 minutes resulting in an effervescent solution. Once the catalytic hydrogenation was complete, the reaction mixture was filtered over Celite to remove the remaining Pd/C. The solvent was removed by rotary evaporation followed by a gentle stream of air. The dried product was redissolved in chloroform (10 mL), to which 3,4-dibutoxy-3-cyclobutene-1,2-dione (10 μ L, 0.5 mmol) and DIPEA (121 μ L, 0.9 mmol) were added. Purification of the crude product was performed by flash column chromatography on a C18 silica column with a gradient of 10-90% CH₃CN/H₂O over 40 minutes. The purified product was concentrated using a rotary evaporator and lyophilized overnight to yield a white solid.

Yield: 39 %, 150 mg. ¹H-NMR (δ_{H} [ppm], CDCl₃, 400 MHz): 4.77-4.72 (m, 2H), 4.24-4.21 (m, 1H), 3.70-3.54 (m, 42H), 3.48-3.38 (m, 7H), 3.17-3.13 (m, 1H), 1.82-1.75 (m, 2H), 1.64-1.56 (m, 4H), 1.49-1.40 (m, 4H), 1.33-1.29 (m, 16H), 1.00-0.94 (t, 3H). ¹³C-NMR (δ_{C} [ppm], CDCl₃, 100 MHz): 189.54, 182.93, 177.36, 172.42, 156.43, 74.30, 73.38, 71.89, 71.85, 71.48, 70.53, 70.02, 66.67, 65.54, 63.80, 59.03, 58.98, 55.22, 54.25, 44.86, 41.05, 36.14, 34.09, 32.29, 32.00, 31.77, 30.66, 29.93, 29.58, 29.44, 29.38, 29.21, 29.10, 28.71, 28.13, 26.71, 26.33, 26.03, 18.63, 18.50, 13.68, 13.58. LC-MS: t= 7.75 min, m/z: 824.67 [M+H]⁺

Synthesis of 1b

Compound **6** (150 mg, 0.2 mmol) and DIPEA (5 drops) were added to chloroform (3 mL). Subsequently, 1,7-heptanediamine (41 μ L, 0.3 mmol) was added in 10 μ L aliquots every 2-3 hours to the reaction mixture. After complete addition, the solution was refluxed overnight. Purification of the resulting compound was performed by flash column chromatography on a C18 silica column with a gradient of 30-90% CH₃CN/H₂O over 40 minutes. The collected fractions were combined, concentrated under reduced pressure in a rotary evaporator and lyophilized to yield a white spongy solid.

Yield: 42 %, 62 mg. ¹H-NMR (δ_{H} [ppm], CDCl₃, 600 MHz): 7.77 (br s, 1H), 7.53 (br s, 1H), 4.22 (br s, 1H), 3.77-3.64 (m, 88H), 3.60-3.44 (m, 12H), 3.39 (s, 6H), 1.97-1.55 (m, 10H), 1.41-1.27 (m, 32H). ¹³C-NMR (δ_{C} [ppm], CDCl₃, 150 MHz): 182.80, 181.70, 169.08, 167.22, 72.02, 71.98, 71.67, 71.59, 70.69, 70.65, 70.62, 70.58, 70.56, 70.07, 69.80, 63.89, 62.88, 59.15, 44.84, 43.25, 41.15, 31.32, 30.05, 29.72, 29.65, 29.62, 29.47, 29.41, 26.55, 26.18, 24.82. LC-MS: $t = 7.47$ min, m/z : 1630.27 [M+H]⁺



Scheme S3.2. Synthetic route for compounds **2a-b**.

Synthesis of 2a

Compound **1a** (76 mg, 0.05 mmol) was dissolved in dry acetonitrile (5 mL). Pentathiodiphosphorus(V) acid-P,P'-bis(pyridinium betaine) (340 mg, 0.9 mmol) was added to the reaction mixture and stirred overnight at room temperature. The product was purified by reverse phase high-performance liquid chromatography on a C18 column using a gradient of 10-70% CH₃CN/H₂O over 30 minutes. The product was concentrated by rotary evaporation and lyophilized overnight to obtain a yellow solid.

Yield: 89 %, 70.4 mg. ¹H-NMR (δ_{H} [ppm], CDCl₃, 600 MHz): 8.28 (br s, 2H), 8.42 (br s, 2H), 5.01 (br s, 2H), 4.22-4.19 (m, 4H), 4.12 (m, 8H), 3.67-3.53 (m, 88H), 3.38 (s, 6H), 3.17-3.13 (m, 4H), 1.76-1.63 (m, 12H), 1.52-1.27 (m, 34H). ¹³C-NMR (δ_{C} [ppm], CDCl₃, 150 MHz): 203.92, 203.51, 170.98, 170.92, 156.57, 72.00, 70.58, 69.83, 63.84, 59.14, 58.55, 54.26, 50.99, 44.25, 43.55, 42.62, 41.20, 41.02, 40.53, 31.36, 31.12, 30.03, 29.88, 29.71, 29.53, 29.36, 29.19, 29.03, 27.71, 27.57, 26.85, 26.76, 26.63, 26.51, 26.24, 25.81, 25.55. LC-MS: t = 8.81 min, m/z: 1780.27 [M+H]⁺

Synthesis of 2b

Compound **1b** (10 mg, 6 μ mol) was dissolved in dry acetonitrile (2 mL). Pentathiodiphosphorus(V) acid-P,P'-bis(pyridinium betaine) (100 mg, 0.3 mmol) was added to the reaction mixture and stirred overnight at room temperature. The product was purified by reverse phase high-performance liquid chromatography with a C18 column using a gradient of 10-70% CH₃CN/H₂O over 30 minutes. The product was concentrated by rotary evaporation and lyophilized overnight to obtain compound **4** as a sticky yellow solid.

Yield: 67 %, 6.8 mg. ¹H-NMR (δ_{H} [ppm], CDCl₃, 600 MHz): 4.16-4.13 (m, 4H), 3.68-3.57 (m, 92H), 3.49-3.45 (m, 4H), 3.40 (s, 6H), 1.75-1.74 (m, 6H), 1.60-1.56 (m, 6H), 1.44-1.28 (m, 30 H). ¹³C-NMR (δ_{C} [ppm], CDCl₃, 150 MHz): 203.59, 170.96, 170.91, 71.99, 71.92, 71.67, 71.62, 71.44, 70.78, 70.62, 70.59, 70.56, 70.50, 70.47, 70.18, 70.03, 59.18, 44.24, 43.41, 40.54, 31.07,

Chapter 3

29.70, 29.61, 29.55, 29.51, 29.25, 29.07, 27.54, 26.65, 26.51, 26.14, 26.05.

LC-MS: t= 8.80 min, m/z : 1694.40 [M+H]⁺

3.6.4. Fourier transform infrared (FTIR) spectroscopy

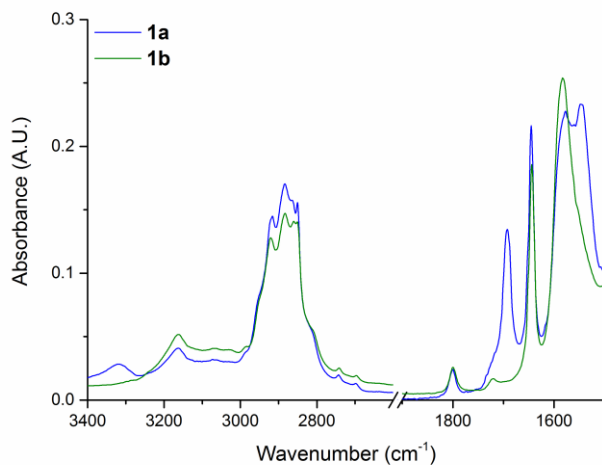


Figure S3.1. Solid FTIR spectra of **1a** and **1b** at room temperature recorded in ATR mode.

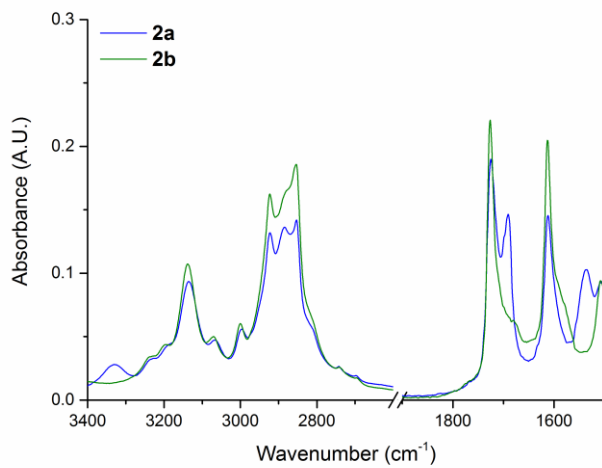


Figure S3.2. Solid FTIR spectra of **2b** and **2b** at room temperature recorded in ATR mode.

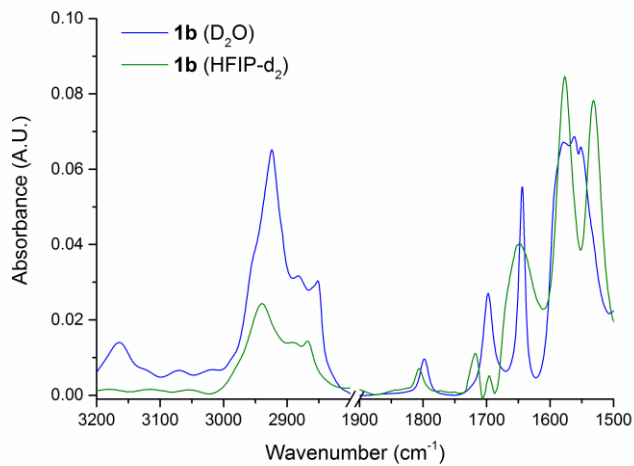


Figure S3.3. FTIR spectra of **1b** in D_2O and HFIP-d_2 .

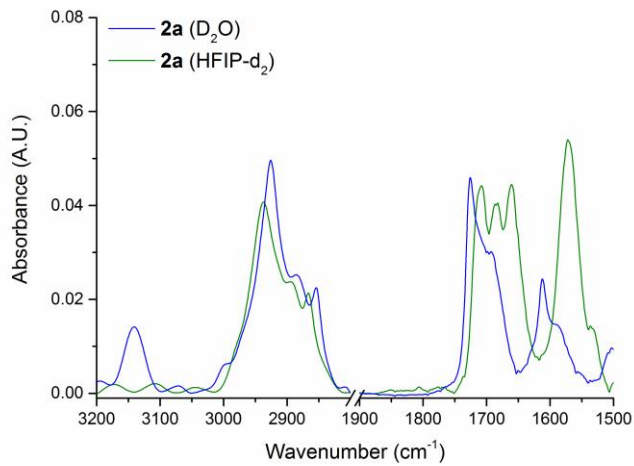


Figure S3.4. FTIR spectra of **2a** in D_2O and HFIP-d_2 .

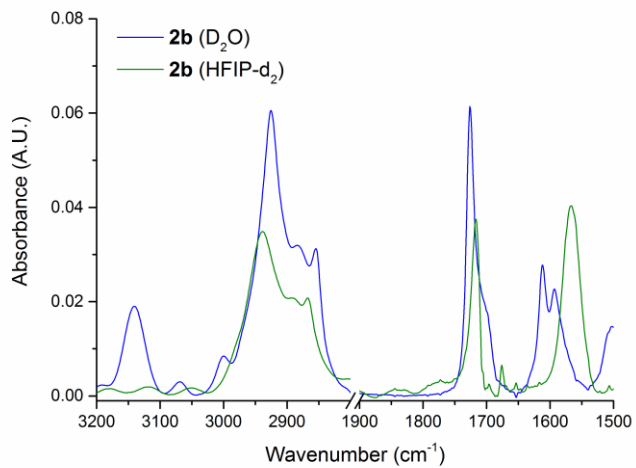


Figure S3.5. FTIR spectra of **2b** in D_2O and HFIP-d_2 .

3.6.5 Cryogenic transmission electron microscopy

Calculation of the persistence length (P_l) and bending rigidity (κ). The cryo-TEM images were converted into text files and imported into the open source software Easyworm developed by Lamour *et al.*¹ We tracked the fiber (**1a**) and rod (**2a**) contour lengths, and then calculated the persistence length and bending rigidity of fibrillar objects above 100 nm for **1a**, and of rod-like objects longer than 20 nm for thionated compounds **2a**. The persistence length was calculated from the mean squared end-to-end distance $\langle R^2 \rangle_{2D}$, which in the worm-like chain (WLC) model for semi-flexible polymers is related to the intercontour length (l) as:

$$\langle R^2 \rangle_{2D} = 4P_l l \left[1 - \frac{2P_l}{l} \left(1 - e^{-\frac{l}{2P_l}} \right) \right]$$

With the P_l , the bending rigidity (κ) of the supramolecular polymers was determined as

$$\kappa = K_b \cdot T \cdot P_l$$

with K_b being the Boltzmann constant, and T the temperature in K.

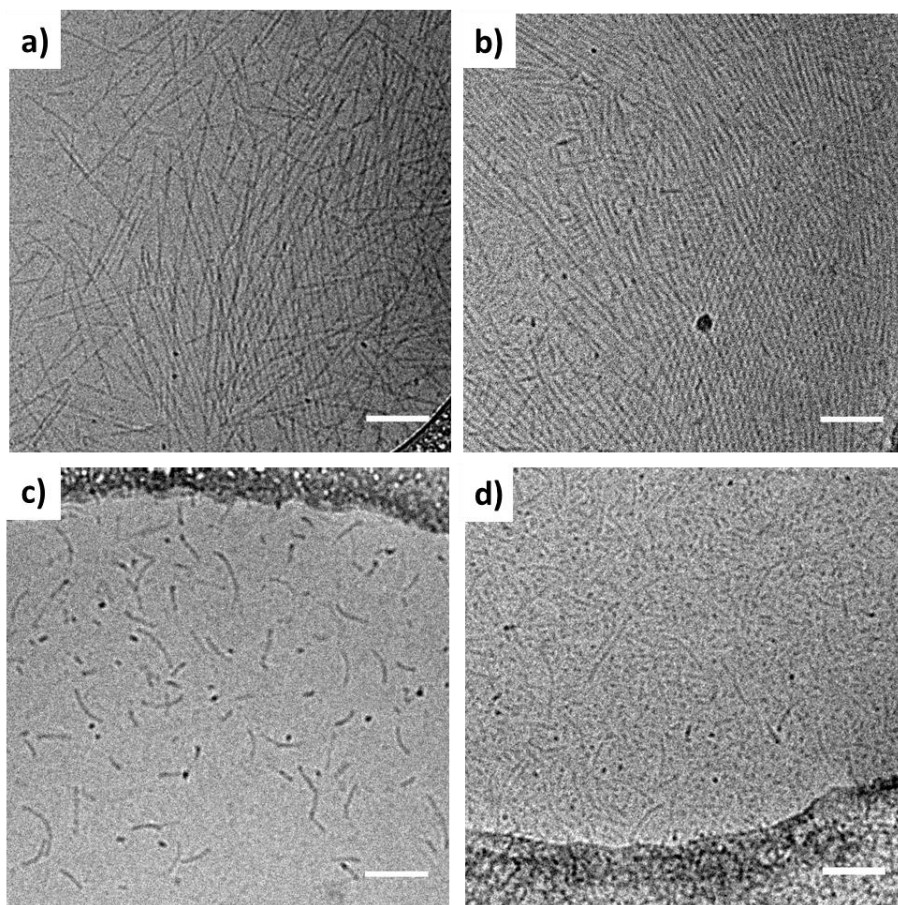


Figure S3.6. CryoTEM images of oxosquaramide-based bolaamphiphiles with carbamate **1a** (a), without carbamate **1b** (b), thiosquaramide-based bolaamphiphiles **2a** with carbamate (c) and without carbamate **2b** (d). Cryo-TEM images of the various squaramide-based monomers were taken at a 10-fold lower concentration (580 μ M) compared to an earlier publication.²

Chapter 3

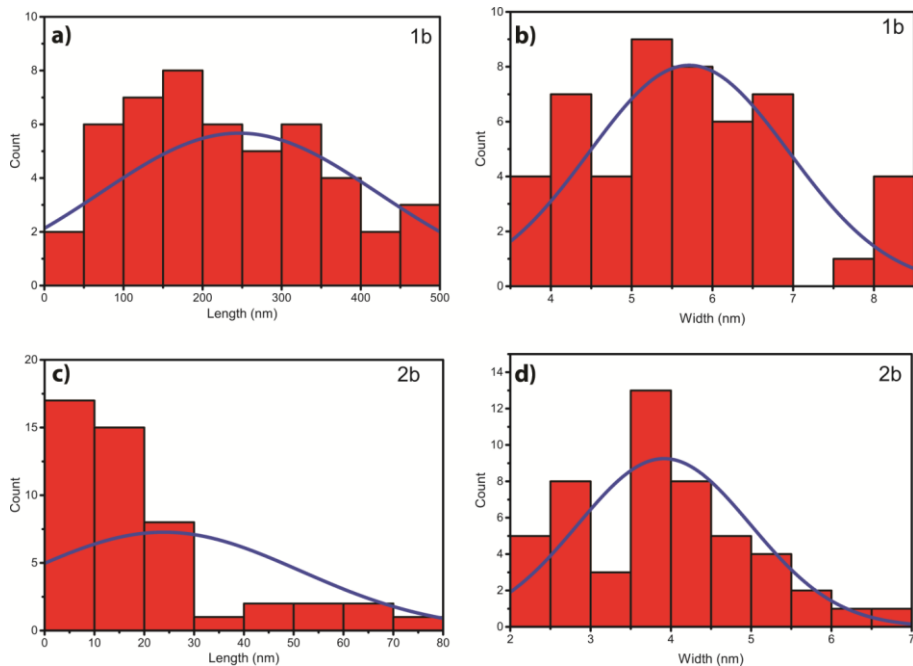


Figure S3.7. Histograms of length and width distributions of **1b** (a, b) and **2b** (c, d) ($N = 50$; average length: 246 ± 176 nm for **1b**, and 24 ± 27 nm for **2b**; average width: 5.7 ± 1.2 nm for **1b**, and 3.9 ± 1.1 nm for **2b**).

3.6.6 Small angle X-ray scattering (SAXS)

The calibration of the beam center and the q -range was achieved by using silver behenate as a standard. The SAXS patterns were brought to an absolute intensity scale using the calibrated detector response function, known sample-to-detector distance, measured incident and transmitted beam intensities, and azimuthally averaged to obtain one dimensional SAXS profiles. The scattering curves of the self-assembled fibers were obtained by subtraction of the scattering contribution of the solvent and quartz cell, by SAXS utilities (<http://www.sztucki.de/SAXSutilities/>). The resulting SAXS profiles were analyzed using the software package SasView (<http://www.sasview.org/>).

SAXS experiments were performed to study the supramolecular polymers constructed from the oxosquaramide and thiosquaramide bolaamphiphiles in water at room temperature. The SAXS profiles of the 4 and 5 mg/mL samples are provided in **Figure S3.8** for the 4 different molecules used in this study. In the low- q regime, the scattering profiles decay with a powerlaw slope of unity for the samples **1a**, **1b** and **2a**. This slope is characteristic for scattering profiles of 1D objects (the length for these structures is beyond the resolution of the experiment ($\sim\pi/q_{\min} = 48$ nm)). Sample **2b** presented a powerlaw slope of 0.72, likely due to the coexistence in solution of two morphologies: rod-like and spherical objects. Upon normalization to 1 mg mL^{-1} , the SAXS profiles taken at 4 and 5 mg mL^{-1} superpose, which means that interfiber interactions can be ignored at these length scales.

The Casassa–Holtzer plot of the data for **1a**, **1b** and **2a** is given in **Figure S3.9**. Similar data treatment was performed for molecule **2b** by using the estimated slope for $I_{cs}(q)$ determination. We extract the cross-sectional mass per unit length, M_L , from the height of the resulting plateau according to

$$\frac{d\Sigma(q)}{d\Omega} = I(q) = \frac{\pi}{q} I_{cs}(q)$$

$$M_L = \frac{I_{cs}(0)}{c\Delta\rho_M^2}$$

with $\Delta\rho_M$ being the electron length density difference per mass, extracted from the fitting curves in SasView.

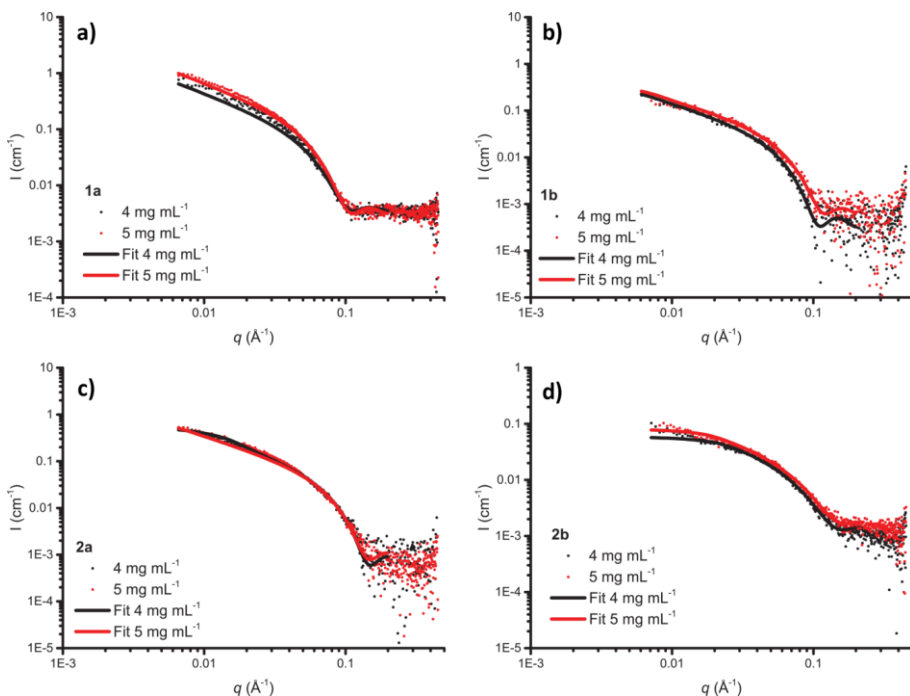


Figure S3.8. SAXS profiles of supramolecular polymers of **1a** (a), **1b** (b), **2a** (c) and **2b** (d), collected at a concentration of 4 and 5 mg mL⁻¹ (the symbols correspond to experimental data (I vs. q) and the lines represent the form factor employed (homogeneous cylinders for **1a** and **1b**, and flexible cylinders for **2a** and **2b**).

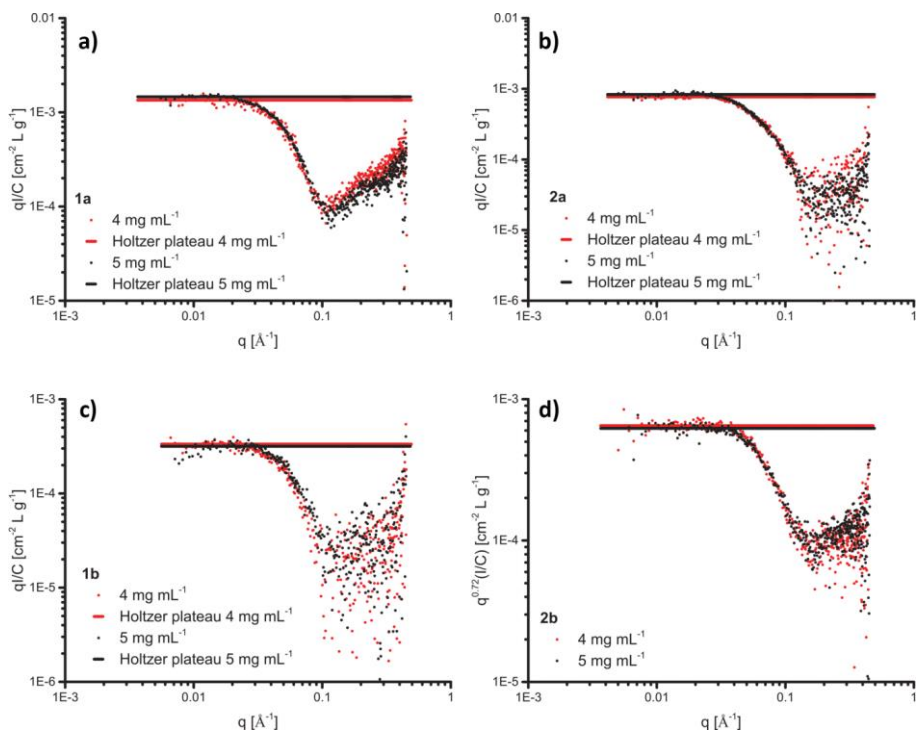


Figure S3.9. Casassa–Holtzer plot of the scattering profiles for monomers **1a**, **1b** and **2a**, and the $I_{CS}(q)$ plateau for **2b**. The plateaus ($0.0066 \leq q \leq 0.0282 \text{ \AA}^{-1}$) are indicated by dashed red and black lines.

Table S3.1. Structural parameters extracted from the SAXS profiles of the oxo- and thiosquaramide-based bolaamphiphiles.

Sample	$\Delta\rho_{\text{cyl}} (\text{\AA}^{-2})$	$\Delta\rho_{\text{M}} (\text{cm g}^{-1})$	$I (\text{cm}^{-2} \text{L g}^{-1})$	$I_{\text{cs}} (0) (\text{cm}^{-2})$	$M_{\text{f}} (\text{g nm}^{-1})$	molec/nm	$r_{\text{cs}} (\text{nm})$	Kuhn length (nm)
1a (4 mg/mL)	10.44×10^6	8.91×10^9	1.35×10^5	1.72×10^5	5.41×10^{20}	19	3.4	
1a (5 mg/mL)	10.46×10^6	9.07×10^9	1.46×10^5	2.32×10^5	5.65×10^{20}	20	3.4	
1b (4 mg/mL)	9.94×10^6	4.72×10^9	3.33×10^4	4.25×10^4	4.78×10^{20}	18	3.4	
1b (5 mg/mL)	9.99×10^6	5.12×10^9	3.17×10^4	5.05×10^4	3.86×10^{20}	14	3.2	
2a (4 mg/mL)	10.44×10^6	8.64×10^9	9.45×10^4	1.20×10^5	4.03×10^{20}	14	2.3	4.5
2a (5 mg/mL)	10.50×10^6	9.42×10^9	8.30×10^4	1.32×10^5	2.98×10^{20}	10	2.3	14.1
2b (4 mg/mL)	10.10×10^6	6.03×10^9	6.49×10^4	8.27×10^4	5.68×10^{20}	20	2.3	17.1
2b (5 mg/mL)	10.10×10^6	6.02×10^9	6.21×10^4	9.89×10^4	5.46×10^{20}	19	2.2	21.0

Finally, we model the experimental data using a form factor developed for homogeneous (**1a** and **1b**) and flexible cylinders (**2a** and **2b**) (Figure S3.8). Since all samples are dissolved in water, we fix $\rho_{\text{solvent}} = 9.37 \cdot 10^6 \text{ \AA}^{-2}$. From the modeled form factors, we obtain values for the cross-sectional radius of the fibers, r_{cs} , and their electron length density, ρ_{cyl} (see Table S3.1).

3.6.7 UV-Vis spectroscopy

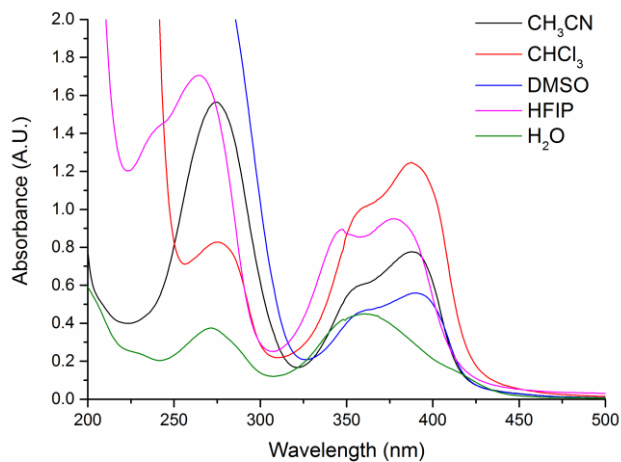


Figure S3.10. UV-Vis spectra of **2a** (30 μM) in various solvents at room temperature.

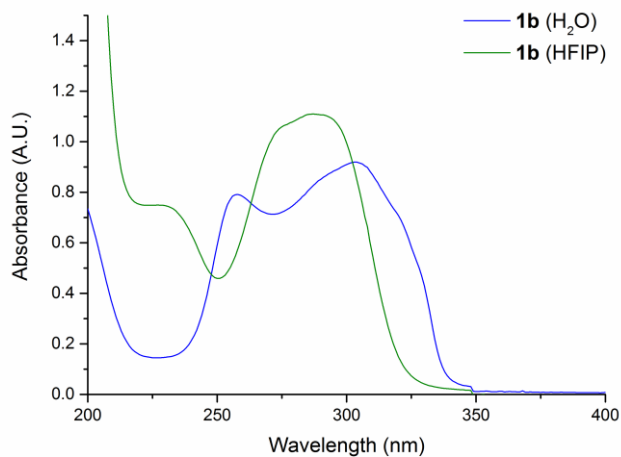


Figure S3.11. UV-Vis spectra of **1b** (30 μM) in water and HFIP.

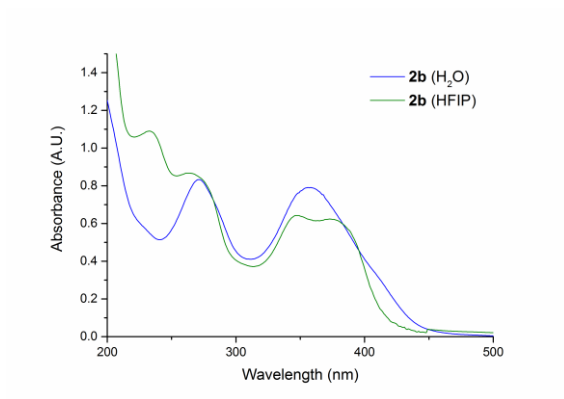


Figure S3.12. UV-Vis spectra of **2b** (30 μM) in water and HFIP.

3.6.8 Comparison of computed “head-to-tail” vs. “stacked” geometries in implicit solvation

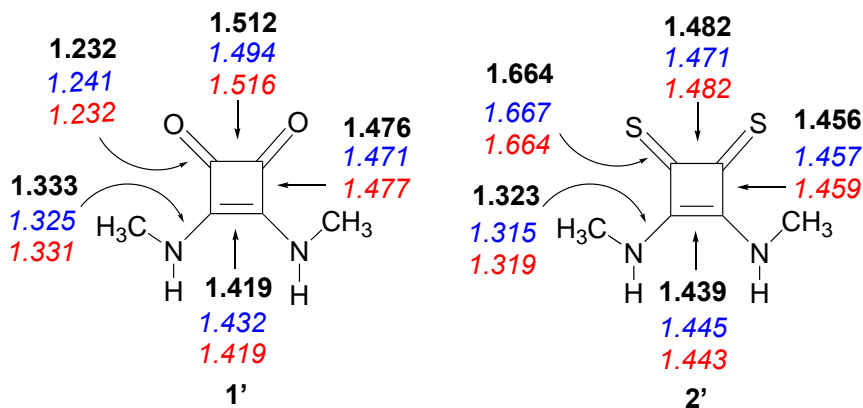


Figure S3.13. Computed geometries in implicit solvation (at $\epsilon = 16.7$) at IEF-PCM-B3LYP-D3/6-31+G(d) for the isolated monomers (bond distances in Å, values in bold font), “head-to-tail” hexamers (values in italics font, in blue), and “stacked” hexamers (values in italics, in red) of **1'** and **2'**. For hexamer structures, the bond distances shown above are based on the average of each monomeric unit.

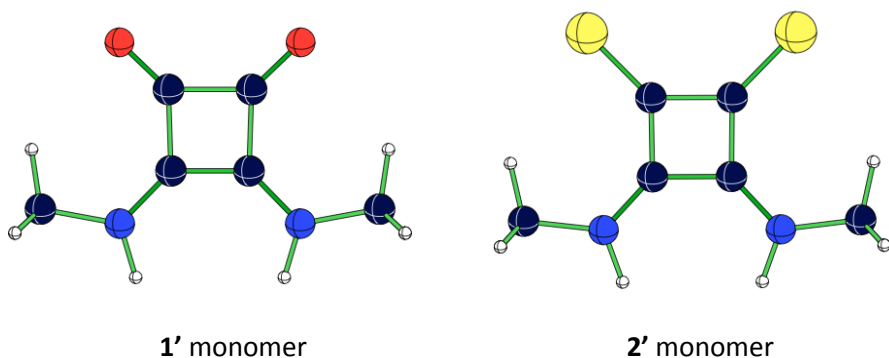


Figure S3.14. Computed structure in implicit solvation (at $\epsilon = 16.7$) at IEF-PCM-B3LYP-D3/6-31+G(d) for the monomers of **1'** and **2'** (see optimized Cartesian coordinates in Table S3.8).

Chapter 3

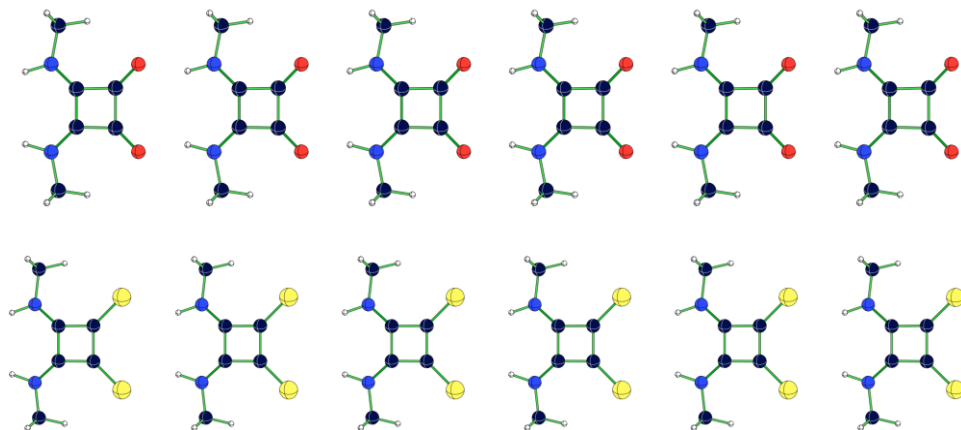


Figure S3.15. Top view of computed structure in implicit solvation (at $\epsilon = 16.7$) at IEF-PCM-B3LYP-D3/6-31+G(d) for the “head-to-tail” hexamers of **1'** (top) and **2'** (bottom) (see optimized Cartesian coordinates in Table S3.8).

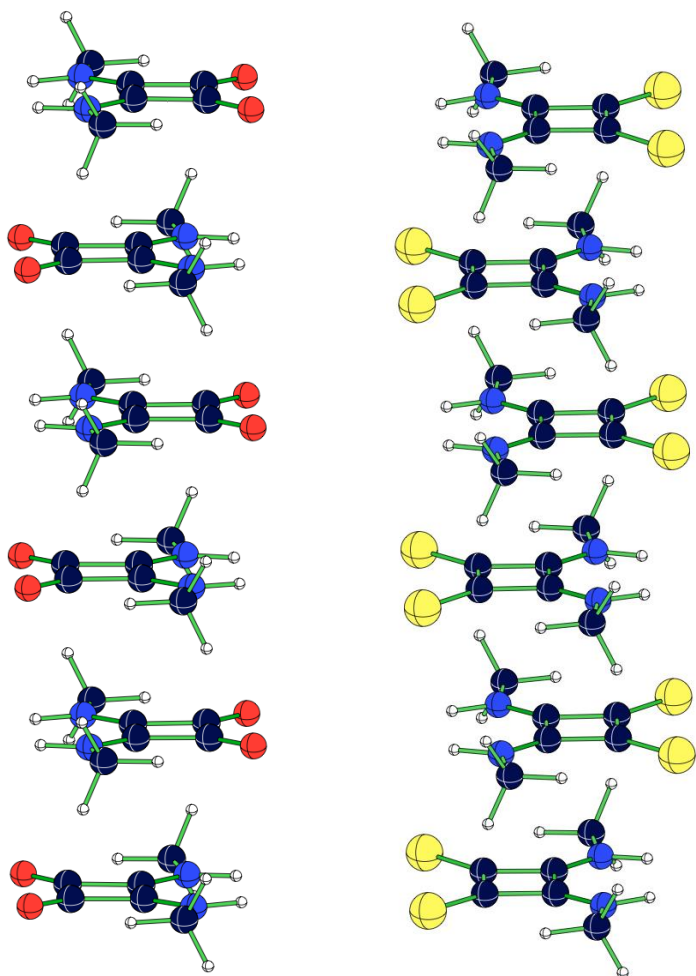


Figure S3.16. Side view of computed structure in implicit solvation (at $\epsilon = 16.7$) at IEF-PCM-B3LYP-D3/6-31+G(d) for the “stacked” hexamers of **1'** (left) and **2'** (right) (see optimized Cartesian coordinates in Supplementary Table 8).

3.6.9 Block-Localized Wave function (BLW) method

Block-Localized Wavefunction (BLW) computations, the most efficient variant of *ab initio* valence bond theory, quantified the π -electron delocalization energies (DE_{π}) of the isolated N-methyl thiosquaramide monomers (**1'** and **2'**) and of the individual monomer units in the “head-to-tail” and “stacked” hexamers of **1'** and **2'**. The DE_{π} values for each of the monomer rings were computed by comparing the energy of the fully delocalized wavefunction (ψ_{deloc}) of the monomer to that of its hypothetical π -electron localized wavefunction (ψ_{loc}), in which the expansion of molecular orbitals over basis functions were restricted to a selected subspace in the molecule [$DE_{\pi} = E(\psi_{\text{deloc}}) - E(\psi_{\text{loc}})$]. For **1'** and **2'**, ψ_{loc} was constructed by partitioning the electrons and basis functions of the molecule into six subspaces (“blocks”); two blocks for the two nitrogen π -lone pairs, two blocks for the C=X π -bonds (X = O or S), one block for the C=C π -bond, and one block for the remaining sigma electrons (see scheme below). Each π -block included two π -electrons (four for the C=S π -bonds) and the p_z , d_{xz} , d_{yz} basis functions belonging to the heavy atoms in the blocks. The computed DE_{π} values of the isolated **1'** and **2'** monomers were compared to those of the monomer units in the “head-to-tail” and “stacked” hexamers, and the resulting ΔDE_{π} difference provided a measure of the extra “gain” in π -electron delocalization in **1'** or **2'** upon self-assembly through noncovalent interactions [$\Delta DE_{\pi} = \Sigma DE_{\pi}$ (“head-to-tail” or “stacked” monomers) – DE_{π} (monomer)]. All BLW computations were performed in implicit solvation (at $\epsilon = 8.5$) at the B3LYP/6-31G(d)//IEF-PCM-B3LYP-D3//6-31+G(d) level, employing GAMESS 2013-R1.

Table S3.2. Computed BLW- ΔDE_{π} values (in kcal/mol) for each of the monomer rings in the “head-to-tail” and “stacked” hexamers of **1'** and **2'** in implicit solvation. More negative ΔDE_{π} values indicate greater cyclic π -electron delocalization gain in the monomers upon self-assembly.

Ring	1'		2'	
	“head-to-tail”	“stacked”	“head-to-tail”	“stacked”
A	-14.87	-8.77	-15.15	-12.41
B	-31.06	-17.11	-29.87	-25.58
C	-34.49	-15.73	-33.08	-22.55
D	-34.55	-15.74	-33.13	-22.55
E	-31.82	-17.11	-30.12	-25.58
F	-17.90	-8.77	-16.67	-12.41

3.6.10 Harmonic Oscillator Model of Electron Delocalization (HOMED) index

HOMED is a geometric criterion for evaluating the aromaticity of heterocycles:

$$\text{HOMED} = 1 - \frac{1}{n} \left\{ \alpha_{CC} \sum [R_o(\text{CC}) - R_i(\text{CC})]^2 + \alpha_{CX} \sum [R_o(\text{CX}) - R_i(\text{CX})]^2 \right\} \quad (1)$$

where α_{CC} and α_{CX} are calculated as

$$\alpha_{2i} = 2 \{ (R_o - R_s)^2 + (R_o - R_d)^2 \}^{-1} \quad \text{for an even number of bonds} \quad (2)$$

$$\alpha_{2i+1} = (2i+1) \{ (i+1)(R_o - R_s)^2 + i(R_o - R_d)^2 \}^{-1} \quad \text{for an odd number of bonds}$$

R_s (single bond length), R_d (double bond length) and R_o (optimal bond length) are the computed reference bond lengths for CC, CN, CO and CS bonds based on the reference molecules shown on the right. All reference bond lengths and HOMED parameters were computed based on geometries optimized in implicit solvation (at $\epsilon = 16.7$) at IEF-PCM-B3LYP-D3/6-31+G(d) (see Table S3.3).

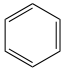
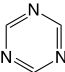
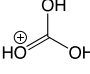
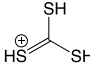
Bond	R_s	R_d	R_o
C-C	<chem>H3C-CH3</chem>	<chem>H2C=CH2</chem>	
C-N	<chem>H3C-NH2</chem>	<chem>H2C=NH</chem>	
C-O	<chem>H3C-OH</chem>	<chem>H2C=O</chem>	
C-S	<chem>H3C-SH</chem>	<chem>H2C=S</chem>	

Table S3.3. Computed parameters for HOMED analysis.

Bond	R_s	R_d	R_o	α_{2i}
CC	1.533 Å	1.336 Å	1.400 Å	91.630
CN	1.446 Å	1.275 Å	1.338 Å	128.070
CO	1.433 Å	1.215 Å	1.285 Å	74.870
CS	1.841 Å	1.624 Å	1.723 Å	84.553

Table S3.4. Computed HOMED values for squaramide units in the “head-to-tail” and “stacked” hexamers of **1'** and **2'** based on geometries optimized in implicit solvation.

Ring	1'		2'	
	“head-to-tail”	“stacked”	“head-to-tail”	“stacked”
A	0.361	0.328	0.447	0.444
B	0.392	0.330	0.454	0.442
C	0.394	0.330	0.454	0.447
D	0.394	0.330	0.455	0.448
E	0.392	0.332	0.455	0.442
F	0.367	0.328	0.456	0.444
Isolated monomer	0.329		0.447	

3.6.11 Nucleus-Independent Chemical Shifts (NICS) analysis

Table S3.5. Computed isotropic NICS values (in ppm) for the “head-to-tail” and “stacked” hexamers of **1'** (computed at 0.6 Å above the ring center of each monomer) and **2'** (computed at 0.8 Å above the ring center of each monomer) in implicit solvation (at $\epsilon = 8.5$) at PW91/IGLOIII//IEF-PCM-B3LYP-D3/6-31+G(d).

Ring	1'		2'	
	“head-to-tail”	“stacked”	“head-to-tail”	“stacked”
A	-6.69	-6.52	-3.65	-3.22
B	-7.07	-7.09	-3.72	-3.64
C	-7.13	-7.88	-3.73	-4.22
D	-7.16	-7.95	-3.75	-4.40
E	-7.19	-7.60	-3.78	-4.56
F	-7.25	-6.95	-3.85	-3.90
Isolated Monomer	-6.95 ppm		-3.73 ppm	

3.6.12 Computed IR frequencies and intensities

Table S3.6. Computed infrared (IR) stretching frequencies (values in cm^{-1}) for the monomer, “head-to-tail” hexamer, and “stacked” hexamer of **1'** in implicit solvation (at $\epsilon = 8.5$) at IEF-PCM-B3LYP-D3/6-31+G(d).

Mode	monomer	head-to-tail	stacked
C=O sym. stretching	1654	1547-1667	1547-1652
C=O antisym. stretching	1580	1579-1698	1581-1718
Ring breathing	1851	1847-1859	1851-1866
N–H sym. stretching	3592	3320-3369	3585-3589
N–H antisym. stretching	3577	3307-3573	3570-3573

Table S3.7. Computed infrared (IR) stretching frequencies (values in cm^{-1}) and intensities (italicized, in parenthesis) for the monomer, “head-to-tail” hexamer, and “stacked” hexamer of **2'** in implicit solvation (at $\epsilon = 8.5$) at IEF-PCM-B3LYP-D3/6-31+G(d).

Mode	monomer	head-to-tail	stacked
C=S sym. stretching	1324	1226-1330	1230-1330
C=S antisym. stretching	1164	1154-1272	1174-1274
Ring breathing	1757	1764-1774	1761-1774
N–H sym. stretching	3579	3349-3577	3574-3576
N–H antisym. stretching	3564	3342-3561	3561-3564

3.6.13 Cartesian coordinates of optimized geometries

Table S3.8. Optimized Cartesian coordinates (in Å) and computed total electronic energies for the isolated monomers (constrained to C_{2v}), “head-to-tail” hexamers (constrained to C_{2v}), and “stacked” hexamers (constrained to C_s) of **1'** and **2'** in implicit solvation (at $\epsilon = 16.7$) at IEF-PCM-B3LYP-D3/6-31+G(d).

1' monomer (C_{2v})

	X	Y	Z
C	-1.46569	-1.47504	0.00000
C	-0.04627	-1.47504	0.00000
C	-1.51196	0.00000	0.00000
C	0.00000	0.00000	0.00000
N	-2.39609	-2.43032	0.00000
N	0.88413	-2.43032	0.00000
C	-3.83615	-2.16669	0.00000
C	2.32419	-2.16669	0.00000
O	-2.40268	0.85105	0.00000
O	0.89072	0.85105	0.00000
H	-4.29981	-2.60020	-0.89210
H	-4.29981	-2.60020	0.89210
H	2.78785	-2.60020	-0.89210
H	2.78785	-2.60020	0.89210
H	-3.99798	-1.08827	0.00000
H	2.48602	-1.08827	0.00000
H	0.59429	-3.40114	0.00000
H	-2.10624	-3.40114	0.00000

Total electronic energy = -493.4185755 a.u.

1' “head-to-tail” hexamer (C_{2v})

	X	Y	Z
C	0.25080	0.74470	0.00000
C	0.25080	-0.74470	0.00000
O	1.11927	1.63393	0.00000
O	1.11927	-1.63393	0.00000
C	-1.21865	0.71732	0.00000
C	-1.21865	-0.71732	0.00000
N	-2.16569	1.64074	0.00000

Chapter 3

N	-2.16569	-1.64074	0.00000
H	-3.16100	1.38125	0.00000
H	-3.16100	-1.38125	0.00000
C	-1.88891	3.07761	0.00000
C	-1.88891	-3.07761	0.00000
H	-0.81078	3.24296	0.00000
H	-0.81078	-3.24296	0.00000
H	-2.32661	3.54120	-0.89018
H	-2.32661	-3.54120	0.89018
H	-2.32661	-3.54120	-0.89018
H	-2.32661	3.54120	0.89018
N	-14.38430	-1.64113	0.00000
N	-14.38430	1.64113	0.00000
C	-13.43725	-0.71697	0.00000
C	-13.43725	0.71697	0.00000
C	-11.96780	-0.74503	0.00000
C	-11.96780	0.74503	0.00000
O	-11.09995	-1.63406	0.00000
O	-11.09995	1.63406	0.00000
C	-14.10864	-3.07842	0.00000
C	-14.10864	3.07842	0.00000
N	-8.27422	-1.64078	0.00000
N	-8.27422	1.64078	0.00000
C	-7.32723	-0.71732	0.00000
C	-7.32723	0.71732	0.00000
C	-5.85782	-0.74465	0.00000
C	-5.85782	0.74465	0.00000
O	-4.98933	-1.63387	0.00000
O	-4.98933	1.63387	0.00000
C	-7.99759	-3.07771	0.00000
C	-7.99759	3.07771	0.00000
C	-19.56333	0.71355	0.00000
C	-19.56333	-0.71355	0.00000
C	-18.09328	-0.74838	0.00000
C	-18.09328	0.74838	0.00000
O	-17.23072	1.63572	0.00000

O	-17.23072	-1.63572	0.00000
N	-20.51151	1.64342	0.00000
N	-20.51151	-1.64342	0.00000
H	-21.48361	1.35617	0.00000
H	-21.48361	-1.35617	0.00000
C	-20.24356	-3.08403	0.00000
C	-20.24356	3.08403	0.00000
H	-19.16501	-3.24387	0.00000
H	-19.16501	3.24387	0.00000
H	-20.67776	-3.54529	0.89235
H	-20.67776	3.54529	-0.89235
H	-20.67776	3.54529	0.89235
H	-20.67776	-3.54529	-0.89235
H	-15.37684	1.37966	0.00000
H	-15.37684	-1.37966	0.00000
H	-13.03054	-3.24357	0.00000
H	-13.03054	3.24357	0.00000
H	-14.54617	-3.54165	0.89038
H	-14.54617	3.54165	-0.89038
H	-14.54617	3.54165	0.89038
H	-14.54617	-3.54165	-0.89038
H	-9.26926	1.38108	0.00000
H	-9.26926	-1.38108	0.00000
H	-6.91948	-3.24309	0.00000
H	-6.91948	3.24309	0.00000
H	-8.43532	-3.54121	0.89020
H	-8.43532	3.54121	-0.89020
H	-8.43532	3.54121	0.89020
H	-8.43532	-3.54121	-0.89020
C	4.89249	0.71694	0.00000
C	4.89249	-0.71694	0.00000
C	6.36237	-0.74536	0.00000
C	6.36237	0.74536	0.00000
O	7.23010	1.63444	0.00000
O	7.23010	-1.63444	0.00000
N	3.94482	1.64052	0.00000

Chapter 3

N	3.94482	-1.64052	0.00000
H	2.94979	1.38082	0.00000
H	2.94979	-1.38082	0.00000
C	4.22149	-3.07729	0.00000
C	4.22149	3.07729	0.00000
H	5.29964	-3.24258	0.00000
H	5.29964	3.24258	0.00000
H	3.78400	-3.54122	0.89017
H	3.78400	3.54122	-0.89017
H	3.78400	3.54122	0.89017
H	3.78400	-3.54122	-0.89017
C	11.03011	0.71326	0.00000
C	11.03011	-0.71326	0.00000
C	12.50424	-0.75246	0.00000
C	12.50424	0.75246	0.00000
O	13.36200	1.64390	0.00000
O	13.36200	-1.64390	0.00000
N	10.07537	1.63700	0.00000
N	10.07537	-1.63700	0.00000
H	9.08340	1.37341	0.00000
H	9.08340	-1.37341	0.00000
C	10.34712	-3.07361	0.00000
C	10.34712	3.07361	0.00000
H	11.42509	-3.24086	0.00000
H	11.42509	3.24086	0.00000
H	9.91023	-3.53949	0.89005
H	9.91023	3.53949	-0.89005
H	9.91023	3.53949	0.89005
H	9.91023	-3.53949	-0.89005

Total electronic energy = -2960.6149774a.u.

1' "stacked" hexamer (C_s)

	X	Y	Z
C	-6.40975	1.79408	-0.70977
C	-6.40975	1.79408	0.70977
C	-5.83035	3.15135	-0.75734

C	-5.83035	3.15135	0.75734
N	-6.76142	0.90141	-1.63391
N	-6.76142	0.90141	1.63391
C	-6.63408	1.11828	-3.07487
C	-6.63408	1.11828	3.07487
O	-5.47877	3.92455	-1.64922
O	-5.47877	3.92455	1.64922
H	-7.10092	-0.00654	1.33841
H	-7.10092	-0.00654	-1.33841
H	-5.94373	0.38497	-3.50343
H	-5.94373	0.38497	3.50343
H	-6.24839	2.12322	-3.24862
H	-6.24839	2.12322	3.24862
H	-7.61097	1.01844	-3.55844
H	-7.61097	1.01844	3.55844
C	-3.28468	0.69424	0.70972
C	-3.28468	0.69424	-0.70972
C	-3.84072	-0.67277	0.75854
C	-3.84072	-0.67277	-0.75854
N	-2.91597	1.58607	1.62551
N	-2.91597	1.58607	-1.62551
C	-3.00055	1.37233	3.06853
C	-3.00055	1.37233	-3.06853
O	-4.15977	-1.45820	1.65214
O	-4.15977	-1.45820	-1.65214
H	-2.56201	2.48573	-1.32157
H	-2.56201	2.48573	1.32157
H	-2.00624	1.46242	3.51648
H	-2.00624	1.46242	-3.51648
H	-3.39227	0.37234	3.25575
H	-3.39227	0.37234	-3.25575
H	-3.66821	2.11421	3.51718
H	-3.66821	2.11421	-3.51718
C	-0.29946	-0.65756	-0.70946
C	-0.29946	-0.65756	0.70946
C	0.26239	0.70717	-0.75890

Chapter 3

C	0.26239	0.70717	0.75890
N	-0.66649	-1.55032	-1.62550
N	-0.66649	-1.55032	1.62550
C	-0.57420	-1.33935	-3.06847
C	-0.57420	-1.33935	3.06847
O	0.58611	1.48972	-1.65284
O	0.58611	1.48972	1.65284
H	-1.03150	-2.44550	1.32144
H	-1.03150	-2.44550	-1.32144
H	0.09077	-2.08621	-3.51305
H	0.09077	-2.08621	3.51305
H	-0.17506	-0.34222	-3.25544
H	-0.17506	-0.34222	3.25544
H	-1.56676	-1.42401	-3.52131
H	-1.56676	-1.42401	3.52131
C	2.78162	-1.77984	0.70946
C	2.78162	-1.77984	-0.70946
C	2.21977	-3.14456	0.75890
C	2.21977	-3.14456	-0.75890
N	3.14864	-0.88707	1.62550
N	3.14864	-0.88707	-1.62550
C	3.05635	-1.09804	3.06847
C	3.05635	-1.09804	-3.06847
O	1.89604	-3.92711	1.65284
O	1.89604	-3.92711	-1.65284
H	3.51366	0.00811	-1.32144
H	3.51366	0.00811	1.32144
H	4.04891	-1.01338	3.52131
H	4.04891	-1.01338	-3.52131
H	2.65722	-2.09517	3.25545
H	2.65722	-2.09517	-3.25545
H	2.39138	-0.35118	3.51305
H	2.39138	-0.35118	-3.51305
C	5.76683	-3.13163	-0.70972
C	5.76683	-3.13163	0.70972
C	6.32287	-1.76462	-0.75854

C	6.32287	-1.76462	0.75854
N	5.39813	-4.02346	-1.62551
N	5.39813	-4.02346	1.62551
C	5.48271	-3.80972	-3.06853
C	5.48271	-3.80972	3.06853
O	6.64192	-0.97919	-1.65214
O	6.64192	-0.97919	1.65214
H	5.04417	-4.92313	1.32157
H	5.04417	-4.92313	-1.32157
H	6.15038	-4.55160	-3.51717
H	6.15038	-4.55160	3.51717
H	5.87443	-2.80973	-3.25575
H	5.87443	-2.80973	3.25575
H	4.48840	-3.89982	-3.51648
H	4.48840	-3.89982	3.51648
C	8.89191	-4.23146	0.70977
C	8.89191	-4.23146	-0.70977
C	8.31251	-5.58873	0.75734
C	8.31251	-5.58873	-0.75734
N	9.24359	-3.33880	1.63391
N	9.24359	-3.33880	-1.63391
C	9.11624	-3.55566	3.07487
C	9.11624	-3.55566	-3.07487
O	7.96093	-6.36193	1.64922
O	7.96093	-6.36193	-1.64922
H	9.58310	-2.43085	-1.33841
H	9.58310	-2.43085	1.33841
H	10.09313	-3.45582	3.55845
H	10.09313	-3.45582	-3.55845
H	8.73055	-4.56060	3.24863
H	8.73055	-4.56060	-3.24863
H	8.42588	-2.82236	3.50342
H	8.42588	-2.82236	-3.50342

Total electronic energy = -2960.5861726 a.u.

2' monomer (C_{2v})

Chapter 3

	X	Y	Z
C	-0.02112	-1.43894	0.00000
C	0.00000	0.00000	0.00000
C	1.43442	-1.48168	0.00000
C	1.45617	0.00000	0.00000
N	-1.00832	-2.31907	0.00000
N	-0.96093	0.90873	0.00000
C	-0.86004	-3.77702	0.00000
C	-0.76992	2.36170	0.00000
S	2.60713	-2.66232	0.00000
S	2.66303	1.14571	0.00000
H	-1.92125	0.58154	0.00000
H	-1.95861	-1.96383	0.00000
H	-1.33599	-4.19361	0.89268
H	-1.23344	2.79208	0.89268
H	0.19996	-4.02789	0.00000
H	0.29699	2.58135	0.00000
H	-1.33599	-4.19361	-0.89268
H	-1.23344	2.79208	-0.89268

Total electronic energy = -1139.3393076 a.u.

2' "head-to-tail" hexamer (C_{2v})

	X	Y	Z
C	0.71525	0.73462	0.00000
C	0.71525	-0.73462	0.00000
S	1.89509	1.91855	0.00000
S	1.89509	-1.91855	0.00000
C	-0.74136	0.72364	0.00000
C	-0.74136	-0.72364	0.00000
N	-1.71175	1.60931	0.00000
N	-1.71175	-1.60931	0.00000
H	-2.68530	1.28371	0.00000
H	-2.68530	-1.28371	0.00000
C	-1.54716	3.06459	0.00000
C	-1.54716	-3.06459	0.00000
H	-0.48689	3.31356	0.00000

H	-0.48689	-3.31356	0.00000
H	-2.02482	3.48221	-0.89124
H	-2.02482	-3.48221	0.89124
H	-2.02482	-3.48221	-0.89124
H	-2.02482	3.48221	0.89124
N	-15.54516	-1.60857	0.00000
N	-15.54516	1.60857	0.00000
C	-14.57384	-0.72333	0.00000
C	-14.57384	0.72333	0.00000
C	-13.11739	-0.73493	0.00000
C	-13.11739	0.73493	0.00000
S	-11.93824	-1.91883	0.00000
S	-11.93824	1.91883	0.00000
C	-15.38219	-3.06409	0.00000
C	-15.38219	3.06409	0.00000
N	-8.62763	-1.60928	0.00000
N	-8.62763	1.60928	0.00000
C	-7.65722	-0.72363	0.00000
C	-7.65722	0.72363	0.00000
C	-6.20062	-0.73462	0.00000
C	-6.20062	0.73462	0.00000
S	-5.02087	-1.91860	0.00000
S	-5.02087	1.91860	0.00000
C	-8.46314	-3.06459	0.00000
C	-8.46314	3.06459	0.00000
C	-21.50091	0.72143	0.00000
C	-21.50091	-0.72143	0.00000
C	-20.04544	-0.73741	0.00000
C	-20.04544	0.73741	0.00000
S	-18.86877	1.91731	0.00000
S	-18.86877	-1.91731	0.00000
N	-22.47165	1.61457	0.00000
N	-22.47165	-1.61457	0.00000
H	-23.42735	1.27299	0.00000
H	-23.42735	-1.27299	0.00000
C	-22.30583	-3.07152	0.00000

Chapter 3

C	-22.30583	3.07152	0.00000
H	-21.24375	-3.31196	0.00000
H	-21.24375	3.31196	0.00000
H	-22.77837	-3.49091	0.89278
H	-22.77837	3.49091	-0.89278
H	-22.77837	3.49091	0.89278
H	-22.77837	-3.49091	-0.89278
H	-16.51678	1.28026	0.00000
H	-16.51678	-1.28026	0.00000
H	-14.32203	-3.31355	0.00000
H	-14.32203	3.31355	0.00000
H	-15.85973	-3.48149	0.89139
H	-15.85973	3.48149	-0.89139
H	-15.85973	3.48149	0.89139
H	-15.85973	-3.48149	-0.89139
H	-9.60103	1.28348	0.00000
H	-9.60103	-1.28348	0.00000
H	-7.40286	-3.31356	0.00000
H	-7.40286	3.31356	0.00000
H	-8.94077	-3.48219	0.89125
H	-8.94077	3.48219	-0.89125
H	-8.94077	3.48219	0.89125
H	-8.94077	-3.48219	-0.89125
C	6.17620	0.72346	0.00000
C	6.17620	-0.72346	0.00000
C	7.63282	-0.73494	0.00000
C	7.63282	0.73494	0.00000
S	8.81331	1.91790	0.00000
S	8.81331	-1.91790	0.00000
N	5.20546	1.60920	0.00000
N	5.20546	-1.60920	0.00000
H	4.23209	1.28344	0.00000
H	4.23209	-1.28344	0.00000
C	5.37013	-3.06440	0.00000
C	5.37013	3.06440	0.00000
H	6.43049	-3.31311	0.00000

H	6.43049	3.31311	0.00000
H	4.89264	-3.48228	0.89124
H	4.89264	3.48228	-0.89124
H	4.89264	3.48228	0.89124
H	4.89264	-3.48228	-0.89124
C	13.11343	0.72168	0.00000
C	13.11343	-0.72168	0.00000
C	14.57030	-0.73835	0.00000
C	14.57030	0.73835	0.00000
S	15.76263	1.90651	0.00000
S	15.76263	-1.90651	0.00000
N	12.13866	1.60775	0.00000
N	12.13866	-1.60775	0.00000
H	11.16726	1.28006	0.00000
H	11.16726	-1.28006	0.00000
C	12.30442	-3.06206	0.00000
C	12.30442	3.06206	0.00000
H	13.36586	-3.30748	0.00000
H	13.36586	3.30748	0.00000
H	11.82879	-3.48289	0.89119
H	11.82879	3.48289	-0.89119
H	11.82879	3.48289	0.89119
H	11.82879	-3.48289	-0.89119

Total electronic energy = -6836.1167066 a.u.

2' "stacked" hexamer (C_s)

	X	Y	Z
C	0.10182	-0.75181	-0.72066
C	0.10182	-0.75181	0.72066
C	-0.44249	0.60065	-0.74122
C	-0.44249	0.60065	0.74122
N	0.48305	-1.64773	-1.61282
N	0.48305	-1.64773	1.61282
C	0.44278	-1.48739	-3.06826
C	0.44278	-1.48739	3.06826
S	-0.86016	1.71484	-1.90389

Chapter 3

S	-0.86016	1.71484	1.90389
H	0.88599	-2.51438	1.27107
H	0.88599	-2.51438	-1.27107
H	1.46260	-1.53409	-3.46210
H	1.46260	-1.53409	3.46210
H	-0.00493	-0.52422	-3.30960
H	-0.00493	-0.52422	3.30960
H	-0.15524	-2.29180	-3.50580
H	-0.15524	-2.29180	3.50580
C	3.13322	0.63802	0.72178
C	3.13322	0.63802	-0.72178
C	3.69382	-0.70945	0.74110
C	3.69382	-0.70945	-0.74110
N	2.76238	1.53746	1.61066
N	2.76238	1.53746	-1.61066
C	2.82148	1.39468	3.06636
C	2.82148	1.39468	-3.06636
S	4.14999	-1.80696	1.90578
S	4.14999	-1.80696	-1.90578
H	2.38949	2.41712	-1.26732
H	2.38949	2.41712	1.26732
H	3.45510	2.18729	3.47446
H	3.45510	2.18729	-3.47446
H	3.23884	0.41974	3.31390
H	3.23884	0.41974	-3.31390
H	1.81002	1.48263	3.47312
H	1.81002	1.48263	-3.47312
C	6.20596	1.80764	-0.72147
C	6.20596	1.80764	0.72147
C	5.64816	3.15627	-0.74162
C	5.64816	3.15627	0.74162
N	6.57733	0.90775	-1.61049
N	6.57733	0.90775	1.61049
C	6.52313	1.05203	-3.06620
C	6.52313	1.05203	3.06620
S	5.19399	4.25330	-1.90642

S	5.19399	4.25330	1.90642
H	6.94180	0.02484	1.26665
H	6.94180	0.02484	-1.26665
H	7.53575	0.96337	-3.47035
H	7.53575	0.96337	3.47035
H	6.10787	2.02780	-3.31415
H	6.10787	2.02780	3.31415
H	5.89005	0.26066	-3.47750
H	5.89005	0.26066	3.47750
C	9.21057	3.18894	0.72147
C	9.21057	3.18894	-0.72147
C	9.76835	1.84030	0.74162
C	9.76835	1.84030	-0.74162
N	8.83920	4.08884	1.61049
N	8.83920	4.08884	-1.61049
C	8.89340	3.94455	3.06619
C	8.89340	3.94455	-3.06619
S	10.22251	0.74326	1.90641
S	10.22251	0.74326	-1.90641
H	8.47474	4.97174	-1.26664
H	8.47474	4.97174	1.26664
H	9.52650	4.73592	3.47750
H	9.52650	4.73592	-3.47750
H	9.30864	2.96878	3.31415
H	9.30864	2.96878	-3.31415
H	7.88079	4.03324	3.47035
H	7.88079	4.03324	-3.47035
C	12.28335	4.35847	-0.72178
C	12.28335	4.35847	0.72178
C	11.72280	5.70596	-0.74110
C	11.72280	5.70596	0.74110
N	12.65416	3.45901	-1.61066
N	12.65416	3.45901	1.61066
C	12.59506	3.60179	-3.06636
C	12.59506	3.60179	3.06636
S	11.26665	6.80348	-1.90578

Chapter 3

S	11.26665	6.80348	1.90578
H	13.02701	2.57934	1.26732
H	13.02701	2.57934	-1.26732
H	13.60652	3.51381	-3.47312
H	13.60652	3.51381	3.47312
H	12.17773	4.57675	-3.31390
H	12.17773	4.57675	3.31390
H	11.96141	2.80921	-3.47446
H	11.96141	2.80921	3.47446
C	15.31479	5.74819	0.72066
C	15.31479	5.74819	-0.72066
C	15.85905	4.39571	0.74122
C	15.85905	4.39571	-0.74122
N	14.93359	6.64413	1.61282
N	14.93359	6.64413	-1.61282
C	14.97385	6.48379	3.06826
C	14.97385	6.48379	-3.06826
S	16.27669	3.28151	1.90389
S	16.27669	3.28151	-1.90389
H	14.53068	7.51079	-1.27107
H	14.53068	7.51079	1.27107
H	15.57189	7.28817	3.50581
H	15.57189	7.28817	-3.50581
H	15.42152	5.52060	3.30960
H	15.42152	5.52060	-3.30960
H	13.95403	6.53052	3.46209
H	13.95403	6.53052	-3.46209

Total electronic energy = -6836.139497a.u.

Table S3.9. Optimized Cartesian coordinates (in Å) and computed total electronic energies for the isolated monomers (constrained to C_{2v}), “head-to-tail” hexamers (constrained to C_{2v}), and “stacked” hexamers (constrained to C_s) of **1'** and **2'** at ω B97X-D/6-311+G(d,p) in the gas-phase.

1' monomer (C_{2v})

	X	Y	Z
C	0.97683	-0.98889	0.00000
C	0.00000	0.00000	0.00000

C	2.07670	0.00000	0.00000
C	1.00230	1.08766	0.00000
N	0.95696	-2.33029	0.00000
N	-1.34154	-0.00342	0.00000
C	2.16439	-3.14273	0.00000
C	-2.13911	1.21389	0.00000
O	3.27969	-0.06223	0.00000
O	0.95484	2.29132	0.00000
H	2.20638	-3.77483	0.89068
H	2.20638	-3.77483	-0.89068
H	-2.77066	1.26363	0.89068
H	-2.77066	1.26363	-0.89068
H	3.02967	-2.48088	0.00000
H	-1.46670	2.07098	0.00000
H	-1.82866	-0.88377	0.00000
H	0.07069	-2.80657	0.00000

Total electronic energy = -493.3397188 a.u.

ZPE = 0.140953 a.u.

NIm = 2 (65.65 icm^{-1} , 39.67 icm^{-1})

1' "head-to-tail" hexamer (C_{2v})

	X	Y	Z
C	0.22323	0.74547	0.00000
C	0.22323	-0.74547	0.00000
O	1.07506	1.62327	0.00000
O	1.07506	-1.62327	0.00000
C	-1.23989	0.70836	0.00000
C	-1.23989	-0.70836	0.00000
N	-2.18175	1.63633	0.00000
N	-2.18175	-1.63633	0.00000
H	-3.17226	1.38688	0.00000
H	-3.17226	-1.38688	0.00000
C	-1.88313	3.05988	0.00000
C	-1.88313	-3.05988	0.00000
H	-0.80349	3.20525	0.00000
H	-0.80349	-3.20525	0.00000

Chapter 3

H	-2.30926	3.53340	-0.88752
H	-2.30926	-3.53340	0.88752
H	-2.30926	-3.53340	-0.88752
H	-2.30926	3.53340	0.88752
N	-14.37701	-1.63812	0.00000
N	-14.37701	1.63812	0.00000
C	-13.43530	-0.70730	0.00000
C	-13.43530	0.70730	0.00000
C	-11.97178	-0.74643	0.00000
C	-11.97178	0.74643	0.00000
O	-11.12124	-1.62303	0.00000
O	-11.12124	1.62303	0.00000
C	-14.07865	-3.06282	0.00000
C	-14.07865	3.06282	0.00000
N	-8.27429	-1.63677	0.00000
N	-8.27429	1.63677	0.00000
C	-7.33285	-0.70847	0.00000
C	-7.33285	0.70847	0.00000
C	-5.87000	-0.74516	0.00000
C	-5.87000	0.74516	0.00000
O	-5.01734	-1.62230	0.00000
O	-5.01734	1.62230	0.00000
C	-7.97606	-3.06079	0.00000
C	-7.97606	3.06079	0.00000
C	-19.58365	0.70243	0.00000
C	-19.58365	-0.70243	0.00000
C	-18.11691	-0.75176	0.00000
C	-18.11691	0.75176	0.00000
O	-17.27488	1.62692	0.00000
O	-17.27488	-1.62692	0.00000
N	-20.53190	1.63712	0.00000
N	-20.53190	-1.63712	0.00000
H	-21.49827	1.35379	0.00000
H	-21.49827	-1.35379	0.00000
C	-20.24768	-3.06779	0.00000
C	-20.24768	3.06779	0.00000

H	-19.16815	-3.21075	0.00000
H	-19.16815	3.21075	0.00000
H	-20.66709	-3.53941	0.89085
H	-20.66709	3.53941	-0.89085
H	-20.66709	3.53941	0.89085
H	-20.66709	-3.53941	-0.89085
H	-15.36206	1.38473	0.00000
H	-15.36206	-1.38473	0.00000
H	-12.99891	-3.20609	0.00000
H	-12.99891	3.20609	0.00000
H	-14.50212	-3.53671	0.88834
H	-14.50212	3.53671	-0.88834
H	-14.50212	3.53671	0.88834
H	-14.50212	-3.53671	-0.88834
H	-9.26365	1.38642	0.00000
H	-9.26365	-1.38642	0.00000
H	-6.89647	-3.20609	0.00000
H	-6.89647	3.20609	0.00000
H	-8.40185	-3.53400	0.88771
H	-8.40185	3.53400	-0.88771
H	-8.40185	3.53400	0.88771
H	-8.40185	-3.53400	-0.88771
C	4.86554	0.70679	0.00000
C	4.86554	-0.70679	0.00000
C	6.33026	-0.74780	0.00000
C	6.33026	0.74780	0.00000
O	7.17735	1.62710	0.00000
O	7.17735	-1.62710	0.00000
N	3.92182	1.63602	0.00000
N	3.92182	-1.63602	0.00000
H	2.93238	1.38594	0.00000
H	2.93238	-1.38594	0.00000
C	4.22133	-3.05874	0.00000
C	4.22133	3.05874	0.00000
H	5.30126	-3.20275	0.00000
H	5.30126	3.20275	0.00000

Chapter 3

H	3.79634	-3.53389	0.88753
H	3.79634	3.53389	-0.88753
H	3.79634	3.53389	0.88753
H	3.79634	-3.53389	-0.88753
C	11.02811	0.70047	0.00000
C	11.02811	-0.70047	0.00000
C	12.50110	-0.75901	0.00000
C	12.50110	0.75901	0.00000
O	13.32512	1.64846	0.00000
O	13.32512	-1.64846	0.00000
N	10.07464	1.63249	0.00000
N	10.07464	-1.63249	0.00000
H	9.09026	1.37673	0.00000
H	9.09026	-1.37673	0.00000
C	10.37044	-3.05366	0.00000
C	10.37044	3.05366	0.00000
H	11.45078	-3.19680	0.00000
H	11.45078	3.19680	0.00000
H	9.94769	-3.53326	0.88749
H	9.94769	3.53326	-0.88749
H	9.94769	3.53326	0.88749
H	9.94769	-3.53326	-0.88749

Total electronic energy = -2960.1976596 a.u.

ZPE = 0.858612 a.u.

NIm = 1 (6.63 i cm⁻¹)

1' "stacked" hexamer (C_s)

	X	Y	Z
C	9.70850	0.69718	0.26029
C	9.70850	-0.69718	0.26029
C	9.53235	0.76232	-1.20170
C	9.53235	-0.76232	-1.20170
N	9.78361	1.61684	1.22926
N	9.78361	-1.61684	1.22926
C	9.51627	3.02829	0.99213
C	9.51627	-3.02829	0.99213

O	9.37440	1.64780	-2.01036
O	9.37440	-1.64780	-2.01036
H	9.67787	-1.30193	2.18132
H	9.67787	1.30193	2.18132
H	8.50185	3.28306	1.31131
H	8.50185	-3.28306	1.31131
H	9.62572	3.23229	-0.07230
H	9.62572	-3.23229	-0.07230
H	10.23378	3.63803	1.54399
H	10.23378	-3.63803	1.54399
C	6.38080	-0.69982	-0.14557
C	-6.42173	-0.69718	-0.13587
C	6.38080	0.69982	-0.14557
C	-6.42173	0.69718	-0.13587
C	6.53097	-0.75901	1.31460
C	-6.24555	-0.76232	1.32612
C	6.53097	0.75901	1.31460
C	-6.24555	0.76232	1.32612
N	6.24919	-1.60541	-1.11002
N	-6.49684	-1.61684	-1.10483
N	6.24919	1.60541	-1.11002
N	-6.49684	1.61684	-1.10483
C	6.39968	-3.03463	-0.90035
C	-6.22952	-3.02829	-0.86770
C	6.39968	3.03463	-0.90035
C	-6.22952	3.02829	-0.86770
O	6.61597	-1.64573	2.14045
O	-6.08758	-1.64780	2.13478
O	6.61597	1.64573	2.14045
O	-6.08758	1.64780	2.13478
H	6.23455	1.29059	-2.06761
H	-6.39115	1.30193	-2.05689
H	6.23455	-1.29059	-2.06761
H	-6.39115	-1.30193	-2.05689
H	5.59552	-3.56465	-1.41403
H	-5.21511	-3.28307	-1.18689

Chapter 3

H	5.59552	3.56465	-1.41403
H	-5.21511	3.28307	-1.18689
H	6.33824	-3.23992	0.16782
H	-6.33897	-3.23229	0.19673
H	6.33824	3.23992	0.16782
H	-6.33897	3.23229	0.19673
H	7.36677	-3.37361	-1.28172
H	-6.94704	-3.63803	-1.41957
H	7.36677	3.37361	-1.28172
H	-6.94704	3.63803	-1.41957
C	3.25957	0.69855	0.12005
C	-3.09401	0.69982	0.27000
C	3.25957	-0.69855	0.12005
C	-3.09401	-0.69982	0.27000
C	3.09527	0.76088	-1.33914
C	-3.24419	0.75901	-1.19017
C	3.09527	-0.76088	-1.33914
C	-3.24419	-0.75901	-1.19017
N	3.38064	1.60469	1.08702
N	-2.96237	1.60541	1.23444
N	3.38064	-1.60469	1.08702
N	-2.96237	-1.60541	1.23444
C	3.25928	3.03589	0.87582
C	-3.11289	3.03463	1.02477
C	3.25928	-3.03589	0.87582
C	-3.11289	-3.03463	1.02477
O	2.99856	1.65032	-2.15851
O	-3.32920	1.64573	-2.01602
O	2.99856	-1.65032	-2.15851
O	-3.32920	-1.64573	-2.01602
H	3.42952	-1.29087	2.04365
H	-2.94778	-1.29059	2.19203
H	3.42952	1.29087	2.04365
H	-2.94778	1.29059	2.19203
H	2.32798	3.40506	1.31388
H	-2.30875	3.56466	1.53846

H	2.32798	-3.40506	1.31388
H	-2.30875	-3.56466	1.53846
H	3.25963	3.23298	-0.19577
H	-3.05144	3.23992	-0.04339
H	3.25963	-3.23298	-0.19577
H	-3.05144	-3.23992	-0.04339
H	4.10604	3.54916	1.33615
H	-4.07998	3.37360	1.40612
H	4.10604	-3.54916	1.33615
H	-4.07998	-3.37360	1.40612
C	0.02722	-0.69855	0.00435
C	0.02722	0.69855	0.00435
C	0.19154	-0.76088	1.46353
C	0.19154	0.76088	1.46353
N	-0.09385	-1.60469	-0.96263
N	-0.09385	1.60469	-0.96263
C	0.02752	-3.03589	-0.75142
C	0.02752	3.03589	-0.75142
O	0.28827	-1.65032	2.28291
O	0.28827	1.65032	2.28291
H	-0.81923	-3.54916	-1.21177
H	0.95883	-3.40505	-1.18949
H	-0.81923	3.54916	-1.21177
H	0.95883	3.40505	-1.18949
H	0.02718	-3.23298	0.32016
H	0.02718	3.23298	0.32016
H	-0.14276	1.29087	-1.91925
H	-0.14276	-1.29087	-1.91925

Total electronic energy = -2960.1844542 a.u.

ZPE = 0.859890 a.u.

NIm = 7 (32.95*i* cm⁻¹, 31.18*i* cm⁻¹, 28.55*i* cm⁻¹, 22.79*i* cm⁻¹, 21.35*i* cm⁻¹, 20.04*i* cm⁻¹, 17.92*i* cm⁻¹)

2' monomer (C_{2v})

	X	Y	Z
C	-0.04232	-1.40693	0.00000

Chapter 3

C	0.00000	0.00000	0.00000
C	1.40770	-1.49423	0.00000
C	1.45265	0.00000	0.00000
N	-1.04412	-2.28918	0.00000
N	-0.94697	0.94087	0.00000
C	-0.87735	-3.73616	0.00000
C	-0.69353	2.37521	0.00000
S	2.53441	-2.67520	0.00000
S	2.64829	1.11112	0.00000
H	-1.33456	-4.17163	0.89148
H	-1.33456	-4.17163	-0.89148
H	-1.12375	2.83737	0.89148
H	-1.12375	2.83737	-0.89148
H	0.18758	-3.96475	0.00000
H	0.38321	2.53938	0.00000
H	-1.90884	0.64332	0.00000
H	-1.98638	-1.93436	0.00000

Total electronic energy = -1139.267555 a.u.

ZPE = 0.136849 a.u.

NIm = 1 (12.92i cm⁻¹)

2' "head-to-tail" hexamer (C_{2v})

	X	Y	Z
C	0.66300	0.73442	0.00000
C	0.66300	-0.73442	0.00000
S	1.82073	1.91247	0.00000
S	1.82073	-1.91247	0.00000
C	-0.78430	0.71449	0.00000
C	-0.78430	-0.71449	0.00000
N	-1.75333	1.60101	0.00000
N	-1.75333	-1.60101	0.00000
H	-2.72309	1.28094	0.00000
H	-2.72309	-1.28094	0.00000
C	-1.56687	3.04519	0.00000
C	-1.56687	-3.04519	0.00000
H	-0.50250	3.27356	0.00000

H	-0.50250	-3.27356	0.00000
H	-2.03238	3.47521	-0.88911
H	-2.03238	-3.47521	0.88911
H	-2.03238	-3.47521	-0.88911
H	-2.03238	3.47521	0.88911
N	-15.47992	-1.60213	0.00000
N	-15.47992	1.60213	0.00000
C	-14.50982	-0.71330	0.00000
C	-14.50982	0.71330	0.00000
C	-13.06267	-0.73566	0.00000
C	-13.06267	0.73566	0.00000
S	-11.90712	-1.91232	0.00000
S	-11.90712	1.91232	0.00000
C	-15.29343	-3.04697	0.00000
C	-15.29343	3.04697	0.00000
N	-8.61219	-1.60143	0.00000
N	-8.61219	1.60143	0.00000
C	-7.64342	-0.71451	0.00000
C	-7.64342	0.71451	0.00000
C	-6.19622	-0.73432	0.00000
C	-6.19622	0.73432	0.00000
S	-5.03908	-1.91274	0.00000
S	-5.03908	1.91274	0.00000
C	-8.42584	-3.04591	0.00000
C	-8.42584	3.04591	0.00000
C	-21.42288	0.70968	0.00000
C	-21.42288	-0.70968	0.00000
C	-19.97467	-0.74009	0.00000
C	-19.97467	0.74009	0.00000
S	-18.82087	1.90649	0.00000
S	-18.82087	-1.90649	0.00000
N	-22.38984	1.61593	0.00000
N	-22.38984	-1.61593	0.00000
H	-23.34326	1.28894	0.00000
H	-23.34326	-1.28894	0.00000
C	-22.19070	-3.06224	0.00000

Chapter 3

C	-22.19070	3.06224	0.00000
H	-21.12283	-3.27202	0.00000
H	-21.12283	3.27202	0.00000
H	-22.64226	-3.50081	0.89154
H	-22.64226	3.50081	-0.89154
H	-22.64226	3.50081	0.89154
H	-22.64226	-3.50081	-0.89154
H	-16.44482	1.27732	0.00000
H	-16.44482	-1.27732	0.00000
H	-14.22877	-3.27373	0.00000
H	-14.22877	3.27373	0.00000
H	-15.75577	-3.47859	0.88995
H	-15.75577	3.47859	-0.88995
H	-15.75577	3.47859	0.88995
H	-15.75577	-3.47859	-0.88995
H	-9.58112	1.28060	0.00000
H	-9.58112	-1.28060	0.00000
H	-7.36152	-3.27425	0.00000
H	-7.36152	3.27425	0.00000
H	-8.89084	-3.47595	0.88930
H	-8.89084	3.47595	-0.88930
H	-8.89084	3.47595	0.88930
H	-8.89084	-3.47595	-0.88930
C	6.08825	0.71323	0.00000
C	6.08825	-0.71323	0.00000
C	7.53586	-0.73606	0.00000
C	7.53586	0.73606	0.00000
S	8.69415	1.91091	0.00000
S	8.69415	-1.91091	0.00000
N	5.11728	1.60068	0.00000
N	5.11728	-1.60068	0.00000
H	4.14865	1.27985	0.00000
H	4.14865	-1.27985	0.00000
C	5.30494	-3.04410	0.00000
C	5.30494	3.04410	0.00000
H	6.36988	-3.27059	0.00000

H	6.36988	3.27059	0.00000
H	4.84060	-3.47590	0.88911
H	4.84060	3.47590	-0.88911
H	4.84060	3.47590	0.88911
H	4.84060	-3.47590	-0.88911
C	13.02007	0.70865	0.00000
C	13.02007	-0.70865	0.00000
C	14.46978	-0.74262	0.00000
C	14.46978	0.74262	0.00000
S	15.63563	1.90051	0.00000
S	15.63563	-1.90051	0.00000
N	12.04132	1.59932	0.00000
N	12.04132	-1.59932	0.00000
H	11.07730	1.27481	0.00000
H	11.07730	-1.27481	0.00000
C	12.23284	-3.04013	0.00000
C	12.23284	3.04013	0.00000
H	13.30004	-3.25891	0.00000
H	13.30004	3.25891	0.00000
H	11.77319	-3.47879	0.88917
H	11.77319	3.47879	-0.88917
H	11.77319	3.47879	0.88917
H	11.77319	-3.47879	-0.88917

Total electronic energy = -6835.7542175 a.u.

ZPE = 0.831786 a.u.

NIm = 7 (19.29 icm^{-1} , 17.05 icm^{-1} , 14.19 icm^{-1} , 10.98 icm^{-1} , 7.87 icm^{-1} , 2.09 icm^{-1} , 1.33 icm^{-1})

2' "stacked" hexamer (C_s)

	X	Y	Z
C	9.70112	0.70895	0.11128
C	9.70112	-0.70895	0.11128
C	9.72480	0.74293	-1.33885
C	9.72480	-0.74293	-1.33885
N	9.66146	1.60739	1.08405
N	9.66146	-1.60739	1.08405

Chapter 3

C	9.64445	3.05070	0.89082
C	9.64445	-3.05070	0.89082
S	9.69034	1.88980	-2.51254
S	9.69034	-1.88980	-2.51254
H	9.49358	-1.27932	2.02396
H	9.49358	1.27932	2.02396
H	8.71412	3.46087	1.29034
H	8.71412	-3.46087	1.29034
H	9.71891	3.26464	-0.17435
H	9.71891	-3.26464	-0.17435
H	10.49204	3.50474	1.40805
H	10.49204	-3.50474	1.40805
C	6.47513	-0.71450	0.01264
C	-6.41433	-0.70895	0.01307
C	6.47513	0.71450	0.01264
C	-6.41433	0.70895	0.01307
C	6.46287	-0.73677	1.46176
C	-6.43806	-0.74293	1.46321
C	6.46287	0.73677	1.46176
C	-6.43806	0.74293	1.46321
N	6.48137	-1.60208	-0.95525
N	-6.37464	-1.60739	-0.95969
N	6.48137	1.60208	-0.95525
N	-6.37464	1.60739	-0.95969
C	6.46660	-3.04724	-0.78264
C	-6.35766	-3.05070	-0.76647
C	6.46660	3.04724	-0.78264
C	-6.35766	3.05070	-0.76647
S	6.45734	-1.88628	2.64870
S	-6.40363	-1.88980	2.63689
S	6.45734	1.88628	2.64870
S	-6.40363	1.88980	2.63689
H	6.50976	1.26863	-1.90899
H	-6.20669	1.27932	-1.89959
H	6.50976	-1.26863	-1.90899
H	-6.20669	-1.27932	-1.89959

H	5.57991	-3.45477	-1.27290
H	-5.42732	-3.46088	-1.16595
H	5.57991	3.45477	-1.27290
H	-5.42732	3.46088	-1.16595
H	6.44036	-3.27454	0.28178
H	-6.43217	-3.26464	0.29870
H	6.44036	3.27454	0.28178
H	-6.43217	3.26464	0.29870
H	7.36678	-3.47004	-1.23355
H	-7.20524	-3.50473	-1.28373
H	7.36678	3.47004	-1.23355
H	-7.20524	3.50473	-1.28373
C	3.25006	0.71323	0.10602
C	-3.18835	0.71450	0.11181
C	3.25006	-0.71323	0.10602
C	-3.18835	-0.71450	0.11181
C	3.25561	0.73837	-1.34315
C	-3.17607	0.73677	-1.33731
C	3.25561	-0.73837	-1.34315
C	-3.17607	-0.73677	-1.33731
N	3.24379	1.60308	1.07469
N	-3.19460	1.60208	1.07970
N	3.24379	-1.60308	1.07469
N	-3.19460	-1.60208	1.07970
C	3.24625	3.04769	0.89892
C	-3.17984	3.04723	0.90709
C	3.24625	-3.04769	0.89892
C	-3.17984	-3.04723	0.90709
S	3.25602	1.88845	-2.52560
S	-3.17052	1.88628	-2.52426
S	3.25602	-1.88845	-2.52560
S	-3.17052	-1.88628	-2.52426
H	3.23552	-1.27058	2.02888
H	-3.22300	-1.26863	2.03344
H	3.23552	1.27058	2.02888
H	-3.22300	1.26863	2.03344

Chapter 3

H	2.35196	3.46629	1.36559
H	-2.29315	3.45477	1.39736
H	2.35196	-3.46629	1.36559
H	-2.29315	-3.45477	1.39736
H	3.25048	3.27294	-0.16640
H	-3.15357	3.27454	-0.15734
H	3.25048	-3.27294	-0.16640
H	-3.15357	-3.27454	-0.15734
H	4.13821	3.46425	1.37184
H	-4.08002	3.47004	1.35798
H	4.13821	-3.46425	1.37184
H	-4.08002	-3.47004	1.35798
C	0.03672	-0.71323	0.01847
C	0.03672	0.71323	0.01847
C	0.03116	-0.73837	1.46764
C	0.03116	0.73837	1.46764
N	0.04299	-1.60308	-0.95020
N	0.04299	1.60308	-0.95020
C	0.04054	-3.04769	-0.77443
C	0.04054	3.04769	-0.77443
S	0.03074	-1.88846	2.65009
S	0.03074	1.88846	2.65009
H	-0.85142	-3.46426	-1.24735
H	0.93483	-3.46629	-1.24109
H	-0.85142	3.46426	-1.24735
H	0.93483	3.46629	-1.24109
H	0.03629	-3.27294	0.29089
H	0.03629	3.27294	0.29089
H	0.05127	1.27058	-1.90439
H	0.05127	-1.27058	-1.90439

Total electronic energy = -6835.8024592 a.u.

ZPE = 0.837358 a.u.

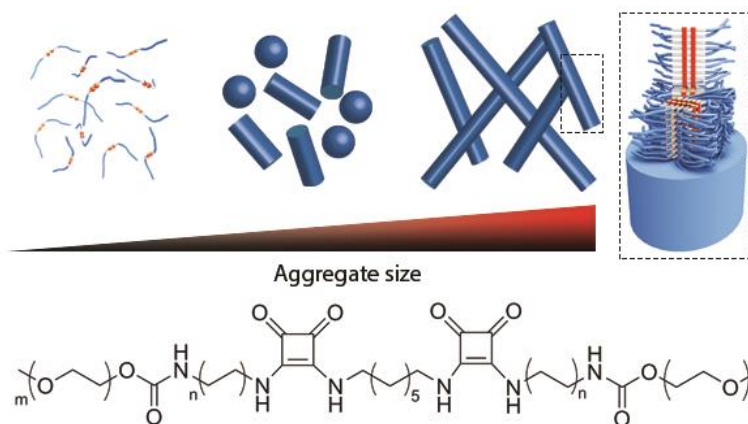
NIm = 3 (19.63 icm^{-1} , 15.84 icm^{-1} , 7.12 icm^{-1})

REFERENCES

- (1) Lamour, G.; Kirkegaard, J. B.; Li, H.; Knowles, T. P.; Gsponer, J. *Source Code Biol. Med.* **2014**, *9* (1), 16.
- (2) Saez Talens, V.; Englebienne, P.; Trinh, T. T.; Noteborn, W. E. M.; Voets, I. K.; Kieltyka, R. E. *Angew. Chemie - Int. Ed.* **2015**, *54* (36), 10502.

CHAPTER 4

Morphological transitions of a squaramide-based supramolecular polymer nanoparticle in water by modulating its monomer structure



This chapter was prepared as an original research paper: Victorio Saez Talens, D. M. M. Makurat, Tingxian Liu, Willem E. M. Noteborn, Wei Dai, Clément L. Guibert, Ilja K. Voets and Roxanne E. Kieltyka.

4.1 Abstract

We report the synthesis of a library of squaramide-based bolaamphiphiles with variable hydrophobic and hydrophilic domain sizes, consisting of varied aliphatic chains ($n = 2$ to 12 methylene repeat units) and linear oligo(ethylene glycol) ($m = 11$ to 36 repeat units), to probe their self-assembly into supramolecular polymer nanoparticles in water. Systematic variation of the hydrophobic chain length show that a minimum hydrophobic domain is required to shield the squaramide units from water when a constant hydrophilic domain is maintained for self-assembly. By contrast, an increase in the hydrophilic chain length of the bolaamphiphile, keeping the hydrophobic domain constant, results in a gradual transition from fibrillar to spherical nanoscale objects with an alteration in the aggregation mode of the monomers. By understanding the self-assembly space achievable for this bolaamphiphilic monomer through modulating its chemical structure, we show that supramolecular polymer nanoparticles of variable shape and size can be easily prepared.

4.2 Introduction

Supramolecular self-assembly has garnered much interest for the preparation of functional nanostructures due to its modular and expeditious nature. Anisotropic, shape-persistent nanostructures can be achieved through the supramolecular polymerization of designed monomer units by non-covalent interactions such as hydrogen-bonding, ionic, π - π and hydrophobic effects.^{1–10} This approach can be especially useful in the development of therapeutic nanoparticle libraries for drug delivery, where size and shape among other physicochemical properties can be used to guide their biodistribution, uptake and clearance *in vivo*.^{11–17} However, control over nanoparticle shape and size still remains non-trivial, especially in aqueous media where the use of strong non-covalent interactions within the monomer are necessary to drive self-assembly, but can also result in kinetically trapped aggregates.^{18–22} This challenge highlights that more insight into the monomer features that drive supramolecular polymerization is required to be able to exploit such nanostructures for future biomedical applications.

Bolaamphiphiles are highly attractive self-assembling modules because of their capacity to access a range of well-defined nanostructures in solution, such as micelles, vesicles and high aspect ratio assemblies, such as rods, helices or ribbons.^{23–27} They consist of two hydrophilic domains with a central hydrophobic core to facilitate self-assembly in water. When rigid chains or hydrogen bonds are introduced into their structure, a transition from vesicular aggregates to elongated rod-like micelles or supramolecular polymers is observed.^{23,24} To this end, hydrogen-bonding units, such as amides²⁸ or ureas^{27,29} are commonly incorporated into the hydrophobic domain, and recently, our group demonstrated the use of squaramides^{30,31} to elicit such morphological transitions.

Squaramides^{32–35} are minimalistic ditopic hydrogen bonding units that provide unique opportunities for supramolecular polymer construction^{30,31,36,37} with two N-H hydrogen bond donors opposite two C=O hydrogen bond acceptors on a cyclobutenedione ring. Their high synthetic accessibility starting from commercially available squaric esters permits their facile incorporation into a wide range of synthetic scaffolds.^{31,38–40} Previously, our group reported the incorporation of two squaramide synthons into an aliphatic core flanked by two undeca(ethylene glycol) chains to prepare supramolecular polymers in water (Figure 4.1, **1**).^{30,31} I herein probe the self-assembly scope of this squaramide-based bolaamphiphile by modulating the size of the hydrophilic and hydrophobic

domains and examine their self-assembly into supramolecular polymers from the molecular to the nanoscale (Figure 4.1).

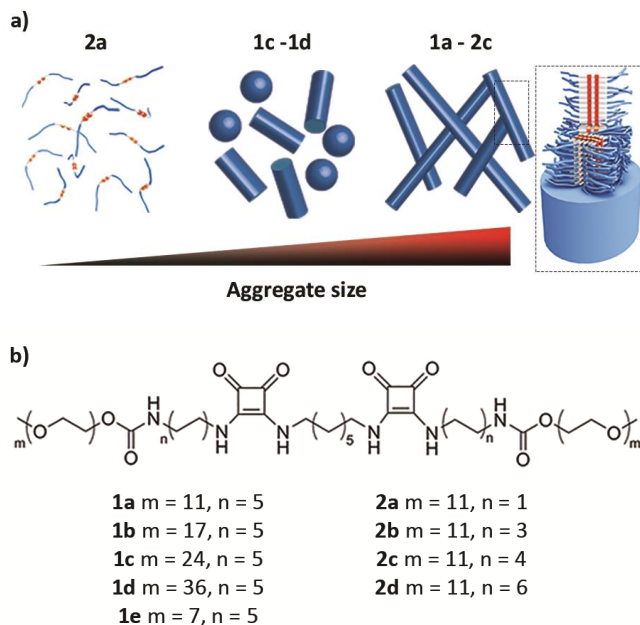


Figure 4.1. (a) Schematic representation of morphologies achievable by modulation of the squaramide-based monomers. (b) Chemical structures of the squaramide-based bolaamphiphiles examined in this study.

4.3 Results and discussion

The influence of the hydrophilic chains on the self-assembly of squaramide-based bolaamphiphiles was examined by synthesizing derivatives with 17 (**1b**), 24 (**1c**), and 36 (**1d**) and 7 (**1e**) oligo(ethylene glycol) repeat units while maintaining the aliphatic chain length constant ($n=5$) between this domain and the squaramide units (Figure 4.1). Secondly, the contribution of the hydrophobic domain of the bolaamphiphile was studied by modifying the aliphatic spacer between the hydrophilic chain and the squaramide motifs with 2 (**2a**), 6 (**2b**), 8 (**2c**) and 12 (**2d**) methylene repeat units, while keeping the remainder of the hydrophobic and hydrophilic undeca(ethylene glycol) chains lengths constant. An analogous synthetic approach to **1a** was used to prepare the squaramide-based bolaamphiphile library with moderate yields over the various steps (see supporting information, section 4.6.3). Optically clear solutions ($c = 580 \mu\text{M}$) of

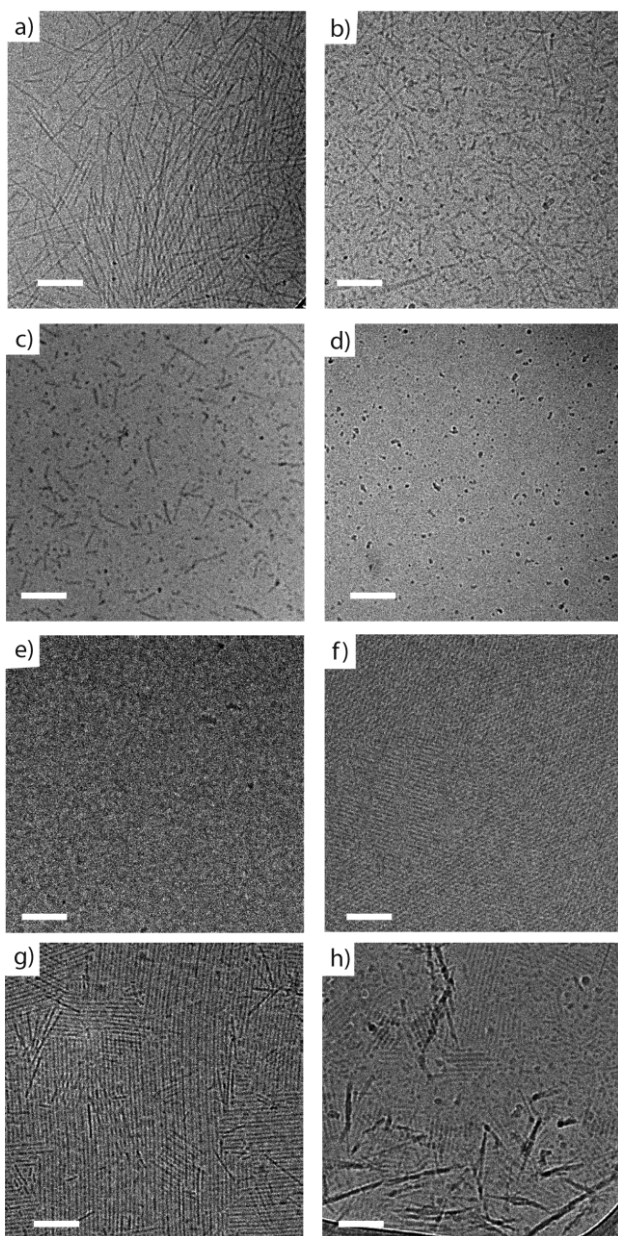


Figure 4.2. Cryo-TEM images of **1a** (a), **1b** (b), **1c** (c), **1d** (d), **2a** (e), **2b** (f), **2c** (g) and **2d** (h) in water (580 μ M). Scale bar: 100 nm.

the various bolaamphiphiles were obtained when the compounds were dissolved in water, except for **1e** that required sonication. This compound was abandoned

for further study and the remaining samples were left to stand 24 hours prior to measurement.

Cryogenic transmission electron microscopy (cryo-TEM) was used as a first approach to probe the effect of modulating the hydrophobic and hydrophilic domains of the bolaamphiphiles on the supramolecular polymer structure (Figure 4.2, see supporting information, section 4.6.4). Morphologically distinct self-assembled structures were obtained with systematic modification of the hydrophilic chain length. Samples of **1a** displayed almost exclusively stiff high aspect ratio fibers, while **1b** predominantly displayed elongated fibrillar constructs with a smaller population of shorter, sometimes spherical objects (Figure 4.2a and 4.2b). The fiber lengths were 234 ± 108 nm and 109 ± 44 nm for **1a** and **1b**, respectively. However, due to the high dispersity of these samples, fiber-like domains of up to a micron in length could be observed for **1a** and half of this value for **1b**, with comparable diameters of 6-7 nm. Self-assembly of **1c** (Figure 4.2c) showed a mixture of spherical aggregates with a diameter of 6 ± 1 nm and rod-like aggregates with a length of 57 ± 24 nm, and is suggestive of kinetic trapping of the bolaamphiphile. For **1d**, only spherical aggregates were found with a diameter of 9 ± 4 nm (Figure 4.2d). These results suggest that the steric bulk provided by the longer oligo(ethylene glycol) chain lengths drives the formation of spherical structures.

Subsequently, the effect of modulating the aliphatic chain length on the self-assembly of **2a-d** was studied. No aggregates in solution were observed for **2a** (Figure 4.2e). Alternatively, **2b** (Figure 4.2f) displayed thin filamentous structures difficult to distinguish from the background, and **2c** (Figure 4.2g) exhibited fibrillar objects on the order of 200 ± 93 nm and disperse in length with thickness of 5-6 nm. A combination of short rod-like objects and bundles thereof were found for **2d** (Figure 4.2h). Thus, bolaamphiphile self-assembly into supramolecular polymers is observed when the aliphatic chains separating the hydrophilic side chains and the squaramide units have at least 8 to 10 methylene repeat units with a fixed undeca(ethylene glycol) chain length.

Small angle X-ray scattering (SAXS) experiments were performed to further characterize the differences in morphology between the various supramolecular polymers prepared from **1a-d**, namely with respect to their size and shape (Figure 4.3a and supporting information). For **1a**, we previously reported a SAXS profile

characteristic of rod-like structures with a length L outside the accessible q -range. It displays a $I \propto q^{-1}$ powerlaw regime at low q values, followed by a $I \propto q^{-4}$ regime at high q values.³¹ The experimental data was described with a form factor for rigid, homogenous cylinders yielding a cross-sectional radius of ~ 3.5 nm, which is comparable to the diameter measured by cryo-TEM. We further obtained a cross-sectional mass per unit length (M_L) of $\sim 5.3 \times 10^{20} \pm 0.6 \times 10^{20}$ g nm⁻¹ from the form factor modeling, which suggests approximately 18 - 21 squaramide bolaamphiphiles per nm along the fiber. The same model was applied to describe the SAXS profiles of **1b**, providing an r_{cs} of ~ 3.7 nm and a M_L of $\sim 5.9 \times 10^{20} \pm 0.5 \times 10^{20}$ g nm⁻¹ that translates into a value of roughly 16 - 20 bolaamphiphiles per nm. In contrast, **1c** could not be modeled satisfactorily in the same manner. Instead, two form factors (for homogeneous cylinders and spheres) were employed to take the coexistence between fibrils and spherical objects as revealed by cryo-TEM into account. Finally, the sample containing the longest hydrophilic chain, **1d**, gave rise to scattering profiles characteristic of objects with a low aspect ratio. A plateau is found at low q values followed by an $I \propto q^{-4}$ powerlaw regime at high q -values. This data set was best modeled with form factors derived for homogeneous and fuzzy spheres,^{41,42} yielding comparable quality of fit and radii of ~ 5.5 nm, providing an estimated overall aggregation number of 31-63 molecules. The small angle X-ray scattering experiments confirm the transition from predominantly fibrillar towards spherical morphologies upon increasing oligo(ethylene glycol) length as seen in the cryo-TEM images.

The self-assembly of the various squaramide-based bolaamphiphiles was further probed at the molecular level by ultraviolet-visible spectroscopy (UV-Vis), fluorescence and IR spectroscopy. Earlier, we reported that self-assemblies of **1a** in water showed UV-Vis maxima at 255 and 329 nm, corresponding to the HOMO-(LUMO+1) and HOMO-LUMO transitions of the squaramide synthon, respectively.³¹ These maxima were largely insensitive to changes in concentration, meanwhile heating of the bolaamphiphiles up to 85°C resulted in perturbation of these bands, thus suggestive of strong aggregation in water. Even with a slightly longer oligo(ethylene glycol) (OEG) chain, **1b** showed a comparable absorption

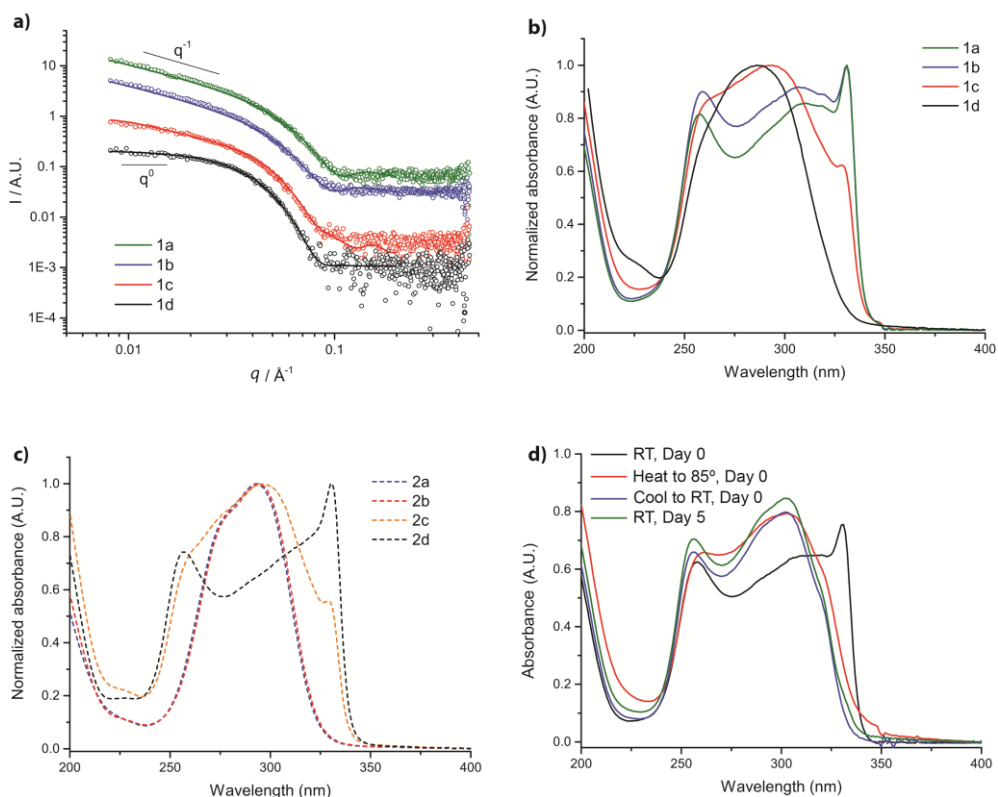


Figure 4.3. (a) SAXS profiles for 4 mg/mL samples of **1a**, **1b**, **1c** and **1d** in water (circular dots) modeled with a form factor describing a rigid homogenous cylinder for **1a** and **1b** (green and blue line), two form factors of a describing a homogenous cylinder and a homogenous sphere for **1c** (red line) and a form factor of a fuzzy sphere for **1d** (black line). The scattering profiles have been shifted vertically by multiplying by a factor of 2 (red line), 7 (blue line) and 20 (green line). (b, c) Normalized UV-Vis absorption traces of (b) **1a-d** and (c) **2a-d** ($c = 30 \mu\text{M}$) in water at room temperature after 24 hours of sample equilibration. d) UV-Vis spectrum of **1a** at different temperatures: RT, Day 0 (black line), Heat to 85 °C, Day 0 (red line), Cool to RT, Day 0 (blue line) and RT, Day 5 (green line).

spectrum in water, whereas in spectra of **1c** and **1d** the sharp bands at 255 and 329 nm were of decreased intensity with red and blue-shifts of these maxima, respectively, consistent with a lower degree of polymerization (Figure 4.3b). Conversely, decreasing the length of the aliphatic spacer between the squaramide motifs and the hydrophilic oligo(ethylene glycol) chains resulted in even more pronounced differences in the UV-Vis spectra (Figure 4.3c). The UV-Vis spectra for **1a-d** and **2a-d** corroborate the morphologies observed at the nanoscale by cryo-TEM and SAXS.

Temperature-dependent UV-Vis measurements (Figure 4.3d) were carried out to gain insight into supramolecular polymerization of **1a**. Heating the fibrillar sample from 25 to 85 °C resulted in spectra consistent with depolymerization of the bolaamphiphiles. The absorbance at 329 nm, a maxima consistent with the aggregated state, as a function of increasing temperature showed an abrupt decrease in intensity around 60 °C. Upon cooling, this peak showed strong hysteresis and did not return after five days, suggesting the formation of a kinetically trapped aggregate distinct from the initial supramolecular polymer. However, it is unclear how much more time is required to return to the initial fibrillar aggregate state.

UV-Vis spectra of **2a** and **2b** bearing 2 and 6 methylenes, respectively, lacked features of squaramide self-assembly in water, consistent with cryo-TEM imaging. When the length of the aliphatic spacer is further increased to 8 methylene units, as in **2c**, the onset of a spectral profile similar to that of **1a** is observed. In the case of **2d**, the spectral profile resembled that of **1a** with peaks at 329 and 255 nm, on par with earlier findings of squaramide self-assembly. Thus, self-assembly of squaramide-based bolaamphiphiles is readily probed by UV-Vis spectroscopy, revealing distinct regimes of polymerization consistent with their molecular structure.

Aggregation of the squaramide-based bolaamphiphiles was further supported by fluorescence measurements using the Nile red dye (NR, see supporting information, section 4.6.8). NR is a hydrophobic dye that undergoes a blue shift in its emission maximum at 650 nm and an increase in fluorescence intensity when encapsulated in a hydrophobic environment. This shift thus provides a view into the contribution of the hydrophobic effect to the self-assembly process.⁴³ A blue-shift of the emission wavelength and 4 to 5-fold increase in the peak intensity of

NR were recorded for **1a-d** when compared against the dye in water as a control (Figure 4.4a). The same shift was observed for **1a** and **1b**, $\Delta\lambda_{\max} = -35$ nm, while **1c** presented a $\Delta\lambda_{\max} = -26$ nm and **1d** a $\Delta\lambda_{\max} = -21$ nm, consistent with a decrease in the hydrophobic character of the bolaamphiphile with increasing oligo(ethylene glycol) length.

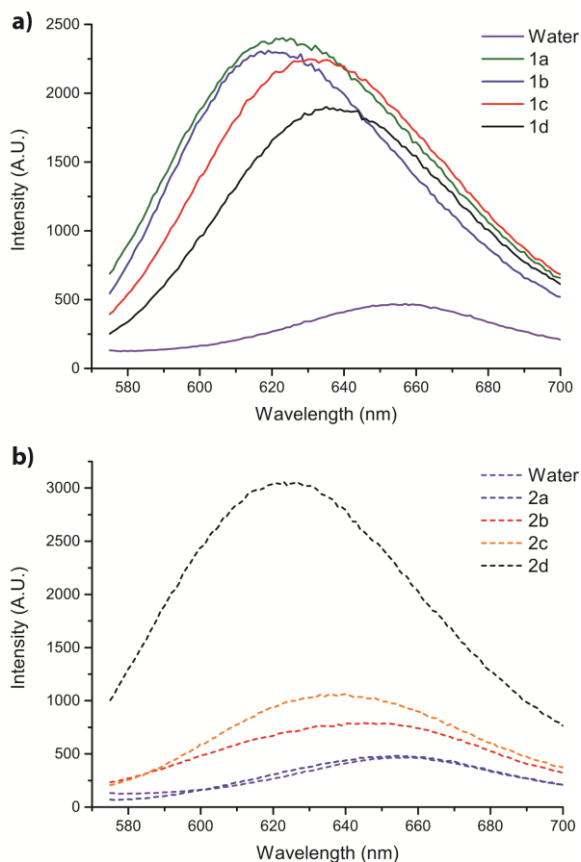


Figure 4.4. Fluorescence spectra of NR (ex. = 550 nm) with **1a-e** (a) and **2a-d** (b) in aqueous solution ($c = 30 \mu\text{M}$).

Conversely, for **2a-d** a gradual increase in the fluorescence intensity is measured with the increased length of the aliphatic spacer, as expected (Figure 4.4b). An emission peak was recorded for **2a** on par with that of the NR dye in water, whereas shifts of $\Delta\lambda_{\max}$ of -10, -18 and -38 nm were measured for **2b**, **2c** and **2d**, respectively, with a 6-fold increase in the intensity for the latter. The fluorescence

results support the UV-Vis measurements and trends when altering the hydrophobic and hydrophilic domains of the squaramide-based bolaamphiphile.

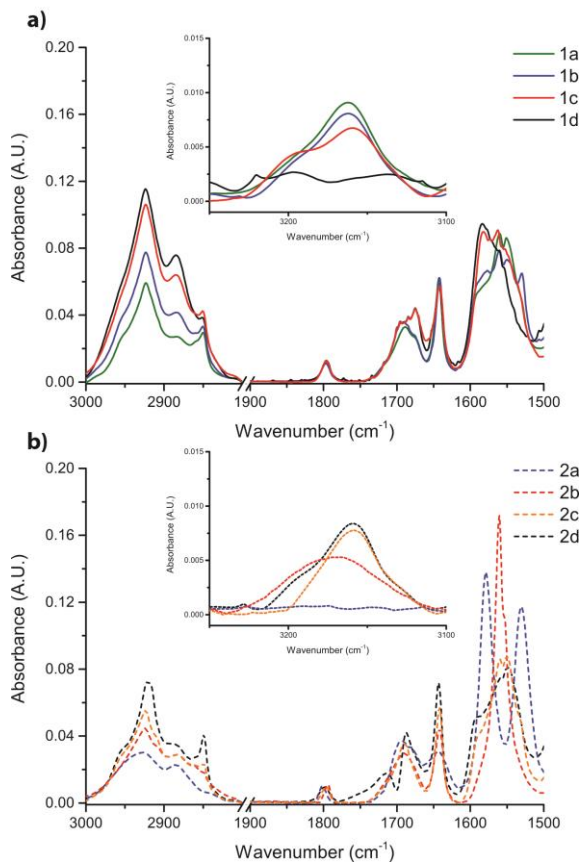


Figure 4.5. FTIR spectra of **1a-d** (a) and **2a-d** (b) in D₂O (*c* = 5.8 mM). N-H (inset), amide I and amide II regions are plotted.

Fourier transform infrared (FTIR) spectroscopy was used to investigate the hydrogen bonding in the various squaramide-based supramolecular polymer nanoparticles. For compound **1a**, we earlier reported the N-H stretch at 3162 cm⁻¹ and C=O stretches at 1687, 1676 and 1642 cm⁻¹ for the squaramide and carbamate moieties of the squaramide-based bolaamphiphile when self-assembled in water, while a small broad peak at 1796 cm⁻¹ was assigned to the ring breathing of the squaramide moiety.³¹ The features of the IR spectrum were largely unchanged with decreasing concentration, except for its intensity. When the temperature was increased from 25 to 65 °C (Figure S4.13) in water, a shift to higher

wavenumbers of the N-H peak of **1a** of 3 cm^{-1} with a decrease in its intensity with concomitant changes in the carbonyl region were observed, indicative of hydrogen-bonding between bolaamphiphiles. Through increasing the oligo(ethylene glycol) chain length (**1b** to **1d**), the N-H stretch peak becomes bimodal and decreases in intensity towards the baseline. In the carbonyl region, similar patterns of bands are observed for **1a** and **1b**, and **1c** and **1d** (Figure 4.5a). The spectral differences between these two sets of bolaamphiphiles in the C=O and N-H regions are thus suggestive of a distinct mode of aggregation between both pairs. Subsequently, we measured samples **1b-d** in HFIP- d_2 (see supporting information, section 4.6.7). As expected, loss of the N-H stretch peak was observed for **1b-d** due its likely superposition with the O-H stretch. The ring breathing peak and the C=O stretches of the squaramide synthon in the amide I region were shifted to higher wavenumbers by $10\text{-}15\text{ cm}^{-1}$ and decreased in intensity with the addition of HFIP- d_2 , consistent with disassembly of the supramolecular polymer. The IR results suggest a distinct aggregation mode between **1a** and **1b**, and **1c** and **1d** due to the increased length of the oligo(ethylene glycol) chains that imposed sterically on the formation of supramolecular polymers.

IR studies were also carried out on **2a-d** where the eventual formation of fibrillar aggregates in water was observed. The gradual appearance of a vibration at 3162 cm^{-1} was observed when comparing the N-H stretches (inset Figure 4.5b) of **2a** and **2d**. This result is consistent with the increased hydrophobic shielding of the squaramide units from their aqueous surroundings with lengthening of the aliphatic spacer. In the amide II region, **2a** showed two sharp peaks at 1578 cm^{-1} and 1530 cm^{-1} , similar to those found for **2a** when dissolved in HFIP- d_2 and absent in **2b-d**. Moreover, a gradual increase in intensity was observed for the carbonyl stretch of the squaramide at 1643 cm^{-1} and the ring breathing peak moved to lower wavenumbers (from 1801 cm^{-1} for **2a** to 1797 cm^{-1} for **2d**), consistent with their polymerization upon increasing aliphatic chain length. Thus, lesser degree of aggregation is observed when increasing the length of the hydrophilic oligo(ethylene glycol) chains from 11 to 36 repeat units, while 8 methylene repeat units are optimal in the aliphatic spacer within the bolaamphiphile to facilitate the interaction between the squaramides by hydrogen bonding.

4.4 Conclusions

In conclusion, I have synthesized a library of squaramide-based bolaamphiphiles where we systematically modify the hydrophilic side chains (**1a-e**) and the hydrophobic core (**2a-d**) independently to study their consequence on self-assembly of the supramolecular polymers. A minimum hydrophobic chain length of 8 carbons between the squaramide and a fixed undeca(ethylene glycol) chain length was required to ensure the formation of fibrillar aggregates. On the other hand, further increasing the oligo(ethylene glycol) chain length (up to $m=36$), while maintaining the same aliphatic chain length constant of 10 carbons, was found to provide a handle to guide their morphological transition from fibrillar to spherical aggregates due to increasing steric demand of the hydrophilic domains. Moreover, spectroscopic studies propose a distinct mode of bolaamphiphile self-assembly when spherical aggregates are formed; changes to the hydrogen-bonding configuration observed in comparison to the fiber structures. However, the precise nature of their self-assembly in these spherical aggregates is unknown, namely whether they occupy a bent or straight configuration²⁴ and if they are being encountered during thermal depolymerization of the supramolecular polymer fibers. Thus, studies are underway to further characterize their nature and whether the various morphologies are kinetically trapped or thermodynamic assemblies, and the potential to control their supramolecular polymerization.

4.5 References

- (1) Aida, T.; Meijer, E. W.; Stupp, S. I. *Science* **2012**, *335* (6070), 813–817.
- (2) Krieg, E.; Bastings, M. M. C.; Besenius, P.; Rybtchinski, B. *Chem. Rev.* **2016**, *16*, 2414–2477.
- (3) Schmuck, C. *Nat. Nanotechnol.* **2011**, *6* (3), 136–137.
- (4) Schmidt, H.-W. *Angew. Chemie Int. Ed.* **2012**, *51* (44), 10933–10933.
- (5) Chierotti, M. R.; Gobetto, R. *Supramol. Chem. From Mol. to Nanomater.* **2012**, 4014.
- (6) Buerkle, L. E.; Rowan, S. J. *Chem. Soc. Rev.* **2012**, *41*, 6089.
- (7) Lehn, J. -M. *Angew. Chemie Int. Ed. English* **1990**, *29* (11), 1304–1319.
- (8) Boekhoven, J.; Stupp, S. I. *Adv. Mater.* **2014**, *26* (11), 1642–1659.
- (9) de Greef, T. F. A.; Meijer, E. W. *Nature* **2008**, *453* (7192), 171–173.

Chapter 4

- (10) De Greef, T. F.; Smulders, M. M. J.; Wolffs, M.; Schenning, A. P. H. J.; Sijbesma, R. P.; Meijer, E. W. *Chem. Rev.* **2009**, *109* (11), 5687–5754.
- (11) Hoffman, A. S. *J. Control. Release* **2008**, *132* (3), 153–163.
- (12) Venkataraman, S.; Hedrick, J. L.; Ong, Z. Y.; Yang, C.; Ee, P. L. R.; Hammond, P. T.; Yang, Y. Y. *Adv. Drug Deliv. Rev.* **2011**, *63* (14–15), 1228–1246.
- (13) Webber, M. J.; Langer, R. *Chem. Soc. Rev.* **2017**, *46*, 6600–6620.
- (14) Simone, E. A.; Dziubla, T. D.; Muzykantov, V. R. *Expert Opin. Drug Deliv.* **2008**, *5* (12), 1283–1300.
- (15) Webber, M. J.; Appel, E. A.; Meijer, E. W.; Langer, R. *Nat. Mater.* **2015**, *15* (1), 13–26.
- (16) Bachmann, M. F.; Jennings, G. T. *Nat. Rev. Immunol.* **2010**, *10* (11), 787–796.
- (17) Petros, R. A.; DeSimone, J. M. *Nat. Rev. Drug Discov.* **2010**, *9* (8), 615–627.
- (18) Yan, Y.; Huang, J.; Tang, B. Z. *Chem. Commun.* **2016**, *52*, 11870–11884.
- (19) Denkova, A. G.; Mendes, E.; Coppens, M.-O. *Soft Matter* **2010**, *6* (11), 2351.
- (20) Baram, J.; Weissman, H.; Rybtchinski, B. *J. Phys. Chem. B* **2014**, *118* (41), 12068–12073.
- (21) Miti, T.; Mulaj, M.; Schmit, J. D.; Muschol, M. *Biomacromolecules* **2015**, *16* (1), 326–335.
- (22) Leenders, C. M. A.; Baker, M. B.; Pijpers, I. A. B.; Lafleur, R. P. M.; Albertazzi, L.; Palmans, A. R. A.; Meijer, E. W. *Soft Matter* **2016**, *12* (11), 2887–2893.
- (23) Nuraje, N.; Bai, H.; Su, K. *Prog. Polym. Sci.* **2013**, *38* (2), 302–343.
- (24) Fuhrhop, J.-H.; Wang, T. *Chem. Rev.* **2004**, *104*, 2901–2937.
- (25) Pal, A.; Karthikeyan, S.; Sijbesma, R. *J. Am. Chem. Soc.* **2010**, *132* (23), 7842–7843.
- (26) Rudolph, T.; Kumar Allampally, N.; Fernández, G.; Schacher, F. H. *Chem. Eur. J.* **2014**, *20* (43), 13871–13875.

- (27) Obert, E.; Bellot, M.; Bouteiller, L.; Andrioletti, F.; Lehen-Ferrenbach, C.; Boué, F. *J. Am. Chem. Soc.* **2007**, *129* (50), 15601–15605.
- (28) Shimizu, T.; Iwaura, R.; Masuda, M.; Hanada, T.; Yase, K. *J. Am. Chem. Soc.* **2001**, *123* (25), 5947–5955.
- (29) Fernandez-Castano Romera, M.; Lafleur, R. P. M.; Guibert, C.; Voets, I. K.; Storm, C.; Sijbesma, R. P. *Angew. Chemie - Int. Ed.* **2017**, *56* (30), 8771–8775.
- (30) Noteborn, W. E. M.; Saez Talens, V.; Kieltyka, R. E. *ChemBioChem* **2017**, 1995–1999.
- (31) Saez Talens, V.; Englebienne, P.; Trinh, T. T.; Noteborn, W. E. M.; Voets, I. K.; Kieltyka, R. E. *Angew. Chemie - Int. Ed.* **2015**, *54* (36), 10502–10506.
- (32) Ian Storer, R.; Aciro, C.; Jones, L. H. *Chem. Soc. Rev.* **2011**, *40* (5), 2330.
- (33) Alemán, J.; Parra, A.; Jiang, H.; Jørgensen, K. A. *Chem. Eur. J.* **2011**, *17* (25), 6890–6899.
- (34) Quiñonero, D.; Frontera, A.; Ballester, P.; Deyà, P. M. *Tetrahedron Lett.* **2000**, *41* (12), 2001–2005.
- (35) Quiñonero, D.; Prohens, R.; Garau, C.; Frontera, A.; Ballester, P.; Costa, A.; Deyà, P. M. *Chem. Phys. Lett.* **2002**, *351* (1–2), 115–120.
- (36) López, C.; Ximenis, M.; Orvay, F.; Rotger, C.; Costa, A. *Chem. Eur. J.* **2017**, *23* (31), 7590–7594.
- (37) Tong, C.; Liu, T.; Saez Talens, V.; Noteborn, W. E. M.; Sharp, T. H.; Hendrix, M. M. R. M.; Voets, I. K.; Mummery, C. L.; Orlova, V. V.; Kieltyka, R. E. *Biomacromolecules* **2018**, acs.biomac.7b01614.
- (38) Wurm, F. R.; Klok, H.-A. *Chem. Soc. Rev* **2013**, *42* (42), 8179–8574.
- (39) Martínez, L.; Martorell, G.; Sampedro, Á.; Ballester, P.; Costa, A.; Rotger, C. *Org. Lett.* **2015**, *17* (12), 2980–2983.
- (40) Schiller, J.; Alegre-Requena, J. V; Marqués-López, E.; Herrera, R. P.; Casanovas, J.; Alemán, C.; Díaz Díaz, D. *Soft Matter* **2016**, 4361–4374.

Chapter 4

- (41) Rathgeber, S.; Monkenbusch, M.; Kreitschmann, M.; Urban, V.; Brulet, A. *J. Chem. Phys.* **2002**, *117* (8), 4047–4062.
- (42) Stieger, M.; Pedersen, J. S.; Lindner, P.; Richtering, W. *Langmuir* **2004**, *20* (17), 7283–7292.
- (43) Stuart, M. C. A.; Van De Pas, J. C.; Engberts, J. B. F. N. *J. Phys. Org. Chem.* **2005**, *18* (9), 929–934.

4.6 Supporting Information

4.6.1 Materials

All solvents and reagents were obtained from commercial suppliers and were used without further purification. The oligo(ethylene glycol) methyl ether (s) were obtained from Polypure and Broadpharm. Deuterated dimethyl sulfoxide and chloroform were purchased from Euriso-top. Palladium on matrix activated carbon, triethylsilane, deuterium oxide, hexafluoroisopropanol and all other commercial grade reagents and chemicals were purchased from Sigma Aldrich and used as received. Milli-Q water was used for all the studies.

4.6.2 General methods

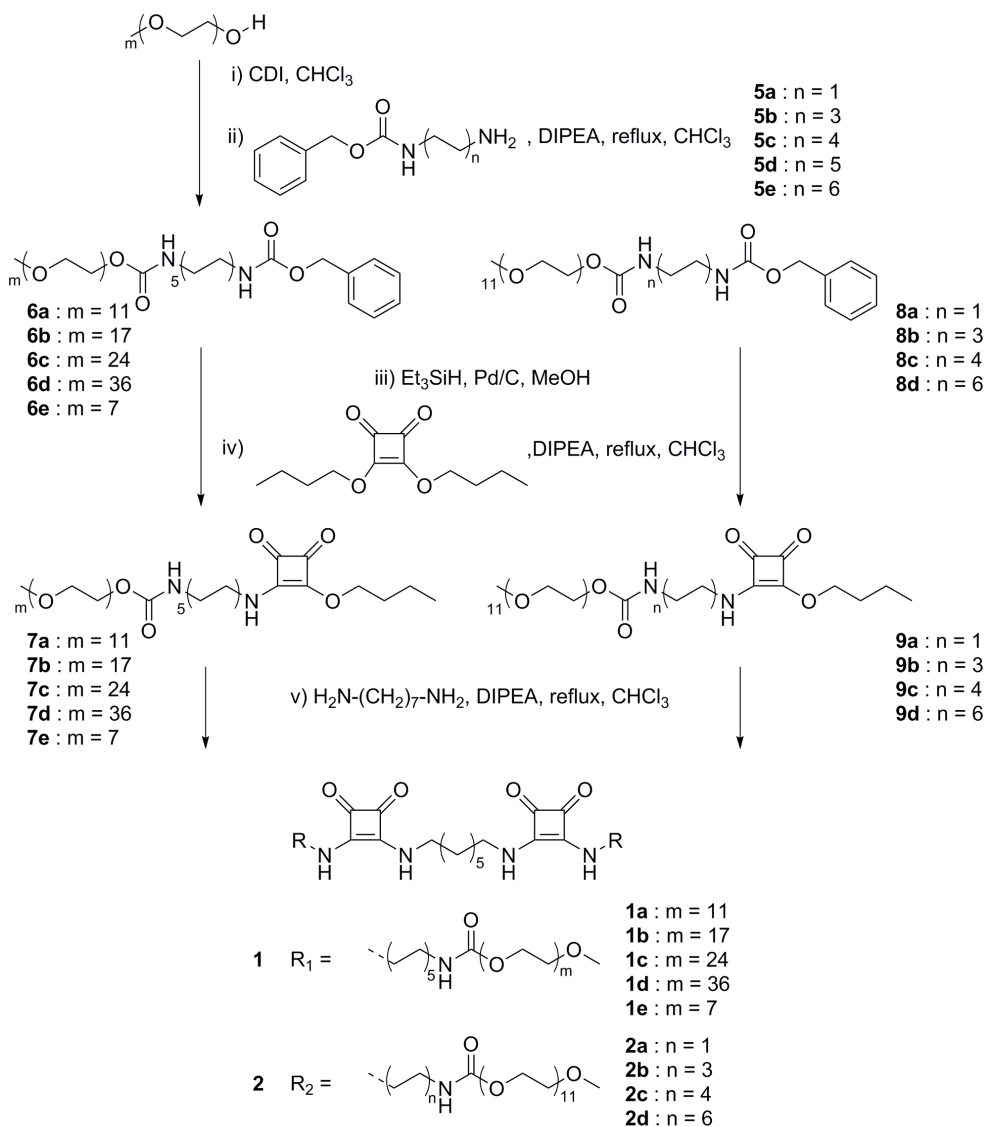
The squaramide-based bolaamphiphiles were purified using a Grace Reveleris X1 flash chromatography system equipped with a C18 column. ^1H NMR and ^{13}C NMR spectra were acquired on a Bruker Ascend 850, a Bruker DMX-400, a Bruker AV-III-600 MHz and a Bruker DPX-300 MHz at 298K. LC-MS analysis was performed on a Finnigan Surveyor HPLC system equipped with a Gemini C18 50 \times 4.60 mm column (UV detection at 200-600 nm), coupled to a Finnigan LCQ Advantage Max mass spectrometer with ESI, or with a TSQ Quantum Access MAX system equipped with a Gemini 3 μm C18 110 \AA 50 \times 4.60 mm column (UV detection at 214 nm and 254 nm). The mobile phase consisted of a gradient of 10-90% of H_2O - CH_3CN with 0.1% trifluoroacetic acid over 13.5 minutes. MALDI-TOF-MS (Matrix-assisted laser desorption ionization–time-of-flight) spectra were recorded on a Bruker microflex LRF mass spectrometer in reflection positive-ion mode using α -cyano-4-hydroxycinnamic acid as a matrix on a ground steel target plate. Cryogenic transmission electron microscopy (cryo-TEM) samples were applied to freshly glow-discharged Lacey Carbon Film (300 mesh Cu grids) and plunge-frozen in liquid ethane using a Leica EM GP. Images were recorded with a Tecnai F20 FEG (FEI company, The Netherlands), equipped with a field emission gun at 200 keV using a Gatan UltraScan camera (Gatan company, Germany). Small angle X-ray scattering (SAXS) measurements were carried on a SAXSLAB GANESHA 300 XL SAXS system equipped with a GeniX 3D Cu Ultra Low Divergence micro focus sealed tube source producing X-rays with a wavelength $\lambda = 1.54 \text{ \AA}$ at a flux of 1×10^8 ph/s and a Pilatus 300K silicon pixel detector with 487 \times 619 pixels of 172 μm \times 172 μm in size placed at two sample-to-detector distances of 713 and 1513 mm respectively to access a q -range of $0.006 \leq q \leq 0.44 \text{ \AA}^{-1}$ with $q = 4 \pi/\lambda(\sin\theta/2)$.

Chapter 4

Silver behenate was used for calibration of the beam center and the q range. Samples were contained at room temperature in 2 mm quartz capillaries (Hilgenberg GmbH, Germany). The two-dimensional SAXS patterns were brought to an absolute intensity scale using the calibrated detector response function, known sample-to-detector distance, measured incident and transmitted beam intensities, and azimuthally averaged to obtain one dimensional SAXS profiles. The scattering curves of the self-assembled structures were obtained by subtraction of the scattering contribution of the solvent and quartz capillary. The small angle X-ray scattering profiles were analyzed using the software package SasView (<http://www.sasview.org/>). Absorption spectra were obtained on a Cary 300 UV-Vis spectrophotometer. All measurements were carried out using a quartz cuvette with a 1 cm path length. Fluorescence spectra were acquired on a Tecan Plate Reader Infinite M1000 using 96 well plates (PP Microplate, solid F-bottom (flat), chimney well). Transmission FTIR spectra were measured using a Bio-Rad Excalibur spectrometer equipped with a nitrogen cooled MCT detector. A liquid transmission cell with CaF_2 windows and a fixed nominal path length of 50 mm was used. Sample spectra were recorded in deuterated solvents at room temperature, with a resolution of 1 cm^{-1} . For each spectrum 128 scans were averaged. The final absorbance spectra was expressed in terms of absorbance and corrected by manual subtraction of a water vapor spectrum. Baseline was subtracted and brought to a zero value by using Origin 9.1 software.

4.6.3 Synthetic routes

Synthesis of squaramide-based bolaamphiphiles



Scheme S4.1. Synthetic route of **1a-e** and **2a-d**.

The synthesis of **5d**, **6a**, **7a** and **1a** were reported in chapter 2.¹ A similar synthetic approach was followed for the synthesis of the rest of the monomers, which is reported below.

Synthesis of 5a

1,n-alkyldiamine (**a**: n=2, 1.8 g, 30 mmol) was dissolved in 50 mL CH₂Cl₂ and cooled to 0°C. Benzyl chloroformate (2.6 g, 15 mmol) was dissolved in 75 mL CH₂Cl₂ and added dropwise over 1 hour to a solution while stirring. The reaction was allowed to reach room temperature and allowed to stir overnight. After completion, the solution was washed 3x with brine, dried with MgSO₄, and the CH₂Cl₂ was evaporated under reduced pressure. The crude product was purified by normal phase chromatography by using CH₂Cl₂/CH₃OH/Et₃N (99/0/1-75/24/1 v/v/v).

5a: Yield: 2.47 g, 85.0 % ¹H-NMR (δ_H[ppm], DMSO-d₆, 300 MHz): 7.38-7.27 (m, 5H), 5.00 (s, 2H), 3.08-3.02 (m, 2H), 2.66-2.61 (t, 2H). ¹³C-NMR (δ_C[ppm], DMSO-d₆, 75 MHz) 156.71, 137.56, 128.78, 128.20, 128.16, 65.72, 42.79, 41.11.

Synthesis of 5b-5e

A similar synthetic approach to **5d** was carried out for the synthesis of **5b**, **5c** and **5e**. N-(Benzyloxycarbonyloxy)succinimide (**b**: 2.2 g, 8.8 mmol, **c**: 0.9 g, 3.6 mmol, **e**: 1.8 g, 7.2 mmol) was dissolved in 150 mL chloroform and added dropwise over 1 hour to a cooled (0°C), stirring solution of 1,n-alkyldiamine (**b**: n=6; 5.0 g, 43.0 mmol, **c**: n=8; 2.5 g, 17.3 mmol, **e**: n=12; 8.6 g, 43.0 mmol) dissolved in 150 mL chloroform. Afterwards, the reaction was allowed to reach room temperature and stirred for an additional 18 hours. At the end of the reaction, the solution of **5b** was evaporated to dryness, dissolved in ethyl acetate and washed 3x with water. Subsequently, the aqueous layers were combined and adjusted to pH 12 with NaOH and saturated with NaCl. This solution was extracted 3x with ethyl acetate and the combined organic layers were washed 3x with brine, dried over MgSO₄ and evaporated to yield compound **5b** as a white crystalline solid.

For **5c** and **5e**, the respective solutions were evaporated to dryness and 200 mL of ethyl acetate was added. Subsequently, 200 mL of a 1M HCl solution were added to these solutions resulting in a precipitate in the organic layer. The precipitates were collected by filtration and washed with ethyl acetate to obtain the final compounds as white crystalline solids.

5b: Yield: 1.69 g, 76.5 % ¹H-NMR (δ_H[ppm], DMSO-d₆, 400 MHz): 7.41-7.26 (m, 5H), 5.05 (s, 2H), 3.55-3.48 (m, 2H), 3.02-2.96 (q, 2H), 1.49-1.22 (m, 8H). ¹³C-NMR

(δ_c [ppm], DMSO- d_6 , 100 MHz): 156.61, 137.86, 128.88, 128.27, 65.60, 51.08, 41.70, 32.93, 30.97, 30.18, 29.96, 27.30, 26.67, 26.56.

5c: Yield: 0.68 g, 67.6 % $^1\text{H-NMR}$ (δ_H [ppm], DMSO- d_6 , 400 MHz): 8.12 (s, 3H), 7.38-7.23 (m, 5H), 5.00 (s, 2H), 3.00-2.95 (q, 2H), 2.74-2.70 (t, 2H), 1.59-1.54 (m, 2H), 1.41-1.36 (m, 2H), 1.30-1.22 (m, 8H) $^{13}\text{C-NMR}$ (δ_c [ppm], DMSO- d_6 , 100 MHz): 156.55, 137.79, 129.55, 128.15, 127.47, 65.51, 40.70, 40.62, 40.41, 29.82, 28.95, 28.93, 27.34, 26.57, 26.28.

5e: Yield: 1.73 g, 71.7 % $^1\text{H-NMR}$ (δ_H [ppm], DMSO- d_6 , 400 MHz): 8.07 (s, 3H), 7.35-7.23 (m, 5H), 4.98 (s, 2H), 2.96-2.93 (q, 2H), 2.71-2.69 (t, 2H), 1.55-1.50 (m, 2H), 1.37-1.35 (m, 2H), 1.26-1.21 (m, 16H) $^{13}\text{C-NMR}$ (δ_c [ppm], DMSO- d_6 , 100 MHz): 156.66, 137.91, 129.02, 128.81, 128.18, 65.62, 40.88, 39.09, 29.99, 29.54, 29.46, 29.33, 29.16, 27.51, 26.83, 26.47.

Synthesis of 6b-e

Oligo(ethylene glycol) methyl ether with various repetition units (**b**: $n=17$, 0.5 g, 0.64 mmol, **c**: $n=24$, 0.3 g, 0.27 mmol, **d**: $n=36$, 0.3 g, 0.19 mmol, and **e**: $n=7$, 0.5 g, 1.47 mmol) were activated with 1,1'-carbonyldiimidazole (CDI) (**b**: $n=17$, 0.18 g, 1.10 mmol, **c**: $n=24$, 0.07 g, 0.40 mmol, **d**: $n=36$, 45 mg, 0.30 mmol, and **e**: $n=7$, 0.36 g, 2.21 mmol) in a minimal amount of chloroform (~1 mL). The solution was stirred until complete conversion was observed by LC-MS. To the resulting solution, **5d** (**b**: $n=17$, 0.29 g, 1 mmol, **c**: $n=24$, 0.13 g, 0.43 mmol, **d**: $n=36$, 0.12 g, 0.39 mmol, and **e**: $n=7$, 0.9 g, 2.94 mmol,) a few drops of DIPEA, and chloroform (up to 10 mL) were added and refluxed overnight. The product was purified by flash column chromatography using an $\text{CH}_3\text{CN}/\text{H}_2\text{O}$ gradient from 10-90% over 30-45 minutes on a C18 silica column. The product was concentrated by evaporation and lyophilized to obtain a white solid.

6b: Yield: 0.35 g, 49.1 % $^1\text{H-NMR}$ (δ_H [ppm], CDCl_3 , 600 MHz): 7.35-7.29 (m, 5H), 5.08 (s, 2H), 4.20-4.19 (t, 2H), 3.75-3.62 (m, 64H), 3.55-3.53 (t, 2H), 3.37 (s, 3H), 3.18-3.12 (m, 4H), 2.09 (br s, 2H), 1.47-1.46 (m, 4H), 1.27-1.25 (m, 12H). $^{13}\text{C-NMR}$ (δ_c [ppm], CDCl_3 , 150 MHz): 156.53, 136.80, 128.63, 128.24, 128.20, 72.05, 70.72, 70.68, 70.64, 69.82, 66.67, 63.91, 59.17, 41.23, 41.15, 30.06, 29.53, 29.33, 26.83. LC-MS: 7.53 min, m/z : 1113.20 $[\text{M}+\text{H}]^+$. MALDI-TOF-MS: m/z calc: 1112.68; found: 1136.19 $[\text{M}+\text{Na}]^+$.

Chapter 4

6c: Yield: 0.30 g, 76.6 % ¹H-NMR (δ_{H} [ppm], CDCl₃, 600 MHz): 7.37-7.31 (m, 5H), 5.10 (s, 2H), 4.23-4.21 (t, 2H), 3.79-3.65 (m, 92H), 3.57-3.55 (t, 2H), 3.39 (s, 3H), 3.21-3.16 (m, 4H), 1.50-1.47 (m, 4H), 1.28 (m, 12H). ¹³C-NMR (δ_{C} [ppm], CDCl₃, 150 MHz): 156.43, 136.77, 128.57, 128.13, 72.02, 70.69, 70.65, 70.60, 69.77, 66.63, 63.88, 59.10, 41.11, 30.01, 29.47, 29.27, 26.77. LC-MS: 6.79 min, *m/z*: 1421.93 [M+H]⁺. MALDI-TOF-MS: *m/z* calc: 1420.87; found: 1444.08 [M+Na]⁺.

6d: Yield: 0.26 g, 71.9 % ¹H-NMR (δ_{H} [ppm], CDCl₃, 600 MHz): 7.29-7.23 (m, 5H), 5.02 (s, 2H), 4.89 (s, 1H), 4.14-4.12 (t, 2H), 3.59-3.46 (m, 142H), 3.31 (s, 3H), 3.12-3.06 (m, 4H), 1.41-1.40 (m, 4H), 1.20-1.19 (m, 12H). ¹³C-NMR (δ_{C} [ppm], CDCl₃, 150 MHz): 156.33, 136.65, 128.40, 128.00, 127.65, 71.85, 70.52, 70.48, 70.42, 69.59, 66.39, 63.68, 58.95, 41.00, 40.93, 29.84, 29.31, 29.11, 26.61. LC-MS: 6.61min, *m/z*: 1950.47 [M+H]⁺. MALDI-TOF-MS: *m/z* calc: 1949.18; found: 1972.32 [M+Na]⁺.

6e: Yield: 0.62 g, 62.7 % ¹H-NMR (δ_{H} [ppm], CDCl₃, 400 MHz): 7.29-7.23 (m, 5H), 5.03 (s, 2H), 4.15-4.12 (t, 2H), 3.67-3.54 (m, 24H), 3.50-3.47 (t, 2H), 3.31 (s, 3H), 3.13-3.05 (m, 4H), 1.44-1.39 (m, 4H), 1.26-1.21 (m, 12H). ¹³C-NMR (δ_{C} [ppm], CDCl₃, 100 MHz): 156.43, 136.69, 128.44, 128.02, 127.98, 71.86, 70.58, 70.56, 70.53, 70.50, 70.47, 70.43, 69.63, 66.44, 63.71, 60.51, 58.95, 41.05, 40.98, 40.90, 29.95, 29.89, 29.36, 29.17, 26.66. LC-MS: 7.81 min, *m/z*: 673.20[M+H]⁺.MALDI-TOF-MS: *m/z* calc: 672.42; found: 694.93 [M+Na]⁺, 710.94 [M+K]⁺.

Synthesis of 7b-e

Compound **6** (**b**: 0.24 g, 0.22 mmol, **c**: 0.30 g, 0.21 mmol, **d**: 0.26 g, 0.13 mmol, **e**: 0.20 g, 0.30 mmol,) was dissolved in 1-3 mL methanol, and a catalytic amount of Pd/C was added. Subsequently, triethylsilane (**b**: 0.41 mL, 2.6 mmol, **c**: 0.43 mL, 2.7 mmol, **d**: 0.18 mL, 1.1 mmol, **e**: 0.41 mL, 2.6 mmol) was added dropwise to the reaction mixture. The solution became effervescent due to the *in situ* formation of H₂(g). Complete deprotection was confirmed by TLC-MS (additional Et₃SiH was added in case the deprotection was incomplete) and the solution was filtered over Celite in order to remove Pd/C. The filtrate was concentrated by rotary evaporation and a gentle stream of air was used to dry the product. The white solid was redissolved in chloroform (~10 mL), and 3,4-dibutoxy-3-cyclobutene-1,2-dione was added (**b**: 50 μ L, 0.23 mmol, **c**: 55 μ L, 0.25 mmol, **d**: 28 μ L, 0.13 mmol, **e**: 85 μ L, 0.39 mmol,) with a few drops of DIPEA. The reaction mixture was stirred and refluxed overnight. The crude product was purified by flash column chromatography using a gradient of 10-90% CH₃CN/H₂O over 30-45 minutes on a

C18 silica column. The product was concentrated by evaporation and lyophilized overnight to obtain compound **7b-e** as a white solid.

7b: Yield: 143 mg, 58.6 % ¹H-NMR (δ_{H} [ppm], CDCl₃, 600 MHz): 4.90 (br s, 1H), 4.74-4.69 (t, 2H), 4.21-4.20 (t, 2H), 3.75-3.72 (t, 2H), 3.67-3.63 (m, 64H), 3.55-3.54 (t, 2H), 3.42-3.40 (m, 2H), 3.37 (s, 3H), 3.16-3.13 (t, 2H), 1.89-1.77 (m, 2H), 1.60-1.58 (m, 2H), 1.48-1.43 (m, 4H), 1.28-1.24 (m, 12H), 0.98-0.95 (t, 3H). ¹³C-NMR (δ_{C} [ppm], CDCl₃, 150 MHz): 189.19, 183.01, 177.49, 172.56, 156.56, 73.53, 72.03, 70.70, 70.65, 70.62, 70.61, 69.80, 68.11, 63.93, 59.18, 45.00, 41.10, 32.14, 30.75, 30.00, 29.42, 29.25, 29.15, 26.76, 26.40, 25.73, 18.78, 13.81. LC-MS: 7.17 min, *m/z*: 1131.33 [M+H]⁺. MALDI-TOF-MS: *m/z* calc: 1130.69; found: 1153.99 [M+Na]⁺.

7c: Yield: 164 mg, 54.0 % ¹H-NMR (δ_{H} [ppm], CDCl₃, 600 MHz): 4.91 (br s, 1H), 4.76-4.74 (t, 2H), 4.24-4.23 (t, 2H), 3.76-3.66 (m, 90H), 3.58-3.57 (m, 4H), 3.45-3.44 (m, 2H), 3.40 (s, 3H), 3.19-3.16 (t, 2H), 1.82-1.81 (m, 2H), 1.63-1.61 (m, 2H), 1.51-1.43 (m, 4H), 1.36-1.26 (m, 12H), 1.01-0.96 (t, 3H). ¹³C-NMR (δ_{C} [ppm], CDCl₃, 150 MHz): 189.02, 183.19, 177.34, 172.49, 156.44, 73.40, 71.94, 70.60, 70.56, 70.52, 69.69, 63.82, 59.04, 44.87, 40.99, 32.03, 30.64, 29.89, 29.28, 29.11, 29.02, 26.63, 26.28, 18.66, 13.68. LC-MS: 6.42 min, *m/z*: 1439.74 [M+2H]²⁺. MALDI-TOF-MS: *m/z* calc: 1438.88; found: 1462.09 [M+Na]⁺.

7d: Yield: 160 mg, 61.0 % ¹H-NMR (δ_{H} [ppm], CDCl₃, 600 MHz): 6.59 (br s, 1H), 4.90 (br s, 1H), 4.72-4.70 (t, 2H), 4.18-4.16 (t, 2H), 3.73-3.48 (m, 142H), 3.39-3.35 (m, 5H), 3.13-3.10 (m, 2H), 1.77-1.75 (m, 2H), 1.60-1.55 (m, 2H), 1.46-1.41 (m, 4H), 1.28-1.25 (m, 12H), 0.95-0.93 (t, 3H). ¹³C-NMR (δ_{C} [ppm], CDCl₃, 150 MHz): 177.34, 156.44, 73.40, 71.94, 70.60, 70.56, 70.52, 69.69, 63.82, 59.04, 44.87, 40.99, 32.03, 30.64, 29.89, 29.28, 29.11, 29.02, 26.63, 26.28, 18.66, 13.68. LC-MS: 7.28 min, *m/z*: 1968.20 [M+H]⁺. MALDI-TOF-MS: *m/z* calc: 1967.19; found: 1990.30 [M+Na]⁺.

7e: Yield: 179 mg, 87.1 % ¹H-NMR (δ_{H} [ppm], CDCl₃, 400 MHz): 7.20 (br s, 1H), 5.03 (br s, 1H), 4.70-4.67 (t, 2H), 4.16-4.15 (t, 2H), 3.63-3.58 (m, 24H), 3.51-3.49 (m, 2H), 3.37-3.34 (m, 2H), 3.32 (s, 3H), 3.11-3.09 (t, 2H), 1.76-1.72 (m, 2H), 1.58-1.54 (m, 2H), 1.45-1.40 (m, 4H), 1.30-1.22 (m, 12H), 0.94-0.90 (t, 3H). ¹³C-NMR (δ_{C} [ppm], CDCl₃, 100 MHz): 189.56, 182.73, 177.31, 172.48, 156.46, 73.27, 71.86, 70.49, 69.60, 68.51, 63.74, 58.93, 44.81, 40.96, 31.98, 30.99, 30.59, 29.86, 29.32, 29.13, 29.03, 26.63, 26.30, 18.61, 13.63. LC-MS: 7.33 min, *m/z*: 691.07[M+H]⁺. MALDI-TOF-MS: *m/z* calc: 690.43; found: 694.93 [M+Na]⁺, 710.94 [M+K]⁺.

Synthesis of 8a-d

Undeca(ethylene glycol) methyl ether (**a**: 0.51 g, 1 mmol, **b**: 0.5 g, 1 mmol, **c**: 0.5 g, 1 mmol, **d**: 0.53 g, 1.02 mmol) was activated with 1,1'-carbonyldiimidazole (**a**: 0.19 g, 1.19 mmol, **b**: 0.25 g, 1.5 mmol, **c**: 0.25 g, 1.5 mmol, **d**: 0.20 g, 1.22 mmol) in chloroform (~1 mL) and was reacted until complete conversion was confirmed by LC-MS. To the resulting solution containing the activated undeca(ethylene glycol) methyl ether, **5a** (0.23 g, 1.18 mmol), **5b** (0.5 g, 2 mmol), **5c** (0.56 g, 2 mmol) and **5e** (0.41 g, 1.22 mmol) were added respectively, followed by the addition of few drops of DIPEA and left to reflux overnight. The product was purified by flash column chromatography using a gradient of 10-90% CH₃CN/H₂O over 30-45 minutes on a C18 silica column. The product was concentrated by evaporation and lyophilized overnight to obtain a white solid.

8a: Yield: 0.56 g, 77 % ¹H-NMR (δ_{H} [ppm], CDCl₃, 400 MHz): 7.33-7.28 (m, 5H), 5.53 (s, 1H), 5.07 (s, 2H), 4.18-4.17 (m, 2H), 3.72-3.70 (m, 42H), 3.35 (s, 3H), 3.28 (m, 4H). ¹³C-NMR (δ_{C} [ppm], CDCl₃, 100 MHz): 156.95, 156.88, 136.60, 128.55, 128.18, 128.15, 71.97, 70.64, 70.60, 70.59, 70.55, 69.56, 66.73, 64.07, 59.09, 41.32, 41.40, 29.75. LC-MS: 5.20 min, m/z: 759.22 [M+Na]⁺. MALDI-TOF-MS: m/z calc: 736.85; found: 759.65 [M+Na]⁺.

8b: Yield: 0.43 g, 54.3 % ¹³C-NMR (δ_{C} [ppm], CDCl₃, 100 MHz): 156.46, 136.64, 128.51, 128.23, 128.08, 71.93, 70.60, 70.56, 70.51, 69.71, 66.61, 63.84, 60.71, 59.04, 40.85, 29.93, 29.89, 29.84, 26.25, 26.23. LC-MS: 6.51 min, m/z: 793.27[M+H]⁺.MALDI-TOF-MS: m/z calc: 792.46; found: 815.20 [M+Na]⁺, 831.20 [M+K]⁺.

8c: Yield: 0.52 g, 63.3 % ¹H-NMR (δ_{H} [ppm], CDCl₃, 400 MHz): 7.37-7.31 (m, 5H), 5.10 (s, 2H), 4.23-4.20 (m, 2H), 3.69-3.64 (m, 42H), 3.57-3.54 (m, 2H), 3.38 (s, 3H), 3.20-3.13(m, 4H), 1.51-1.46 (m, 4H), 1.31-1.30 (m, 8H). ¹³C-NMR (δ_{C} [ppm], CDCl₃, 100 MHz): 156.66, 136.68, 128.50, 128.15, 128.06, 71.93, 70.60, 70.56, 70.54, 70.51, 69.69, 66.56, 63.80, 59.03, 41.00, 29.93, 29.90, 29.11, 26.61. LC-MS: 7.06 min, m/z: 821.40[M+H]⁺. MALDI-TOF-MS: m/z calc: 820.49; found: 843.38 [M+Na]⁺, 859.38 [M+K]⁺.

8d: Yield: 0.45 g, 64.3 % ¹H-NMR (δ_{H} [ppm], CDCl₃, 400 MHz): 7.38-7.31 (m, 5H), 5.11 (s, 2H), 4.24-4.21 (t, 2H), 3.71-3.55 (m, 44H), 3.40 (s, 3H), 3.23-3.17 (m, 4H), 1.84 (s, 2H), 1.50-1.49 (m, 4H), 1.20 (m, 16H). ¹³C-NMR (δ_{C} [ppm], CDCl₃, 100 MHz):

156.25, 136.51, 128.50, 128.06, 71.94, 70.57, 70.52, 69.69, 66.56, 63.80, 59.03. LC-MS: 7.82 min, m/z : 876.76 $[M+H]^+$. MALDI-TOF-MS: m/z calc: 876.56; found: 899.60 $[M+Na]^+$.

Synthesis of 9a-d

Compound **8** (**a**: 0.55 g, 0.74 mmol, **b**: 0.30 g, 0.38 mmol, **c**: 0.075 g, 0.09 mmol, **d**: 0.44 g, 0.51 mmol) was dissolved in 1-3 mL methanol, and a catalytic amount of Pd/C was added, as described previously for compound **7**. The Cbz-deprotection of the amine moiety was achieved by the dropwise addition of Et_3SiH to provide an effervescent solution (**a**: 1.19 mL, 7.45 mmol, **b**: 0.6 mL, 3.8 mmol, **c**: 0.14 mL, 0.9 mmol, **d**: 0.81 mL, 5.1 mmol). Complete deprotection was confirmed by TLC-MS and the solution was filtered over Celite to remove the Pd/C. The filtrate was concentrated by rotary evaporation and a gentle stream of air to dry the product. The white solid was redissolved in chloroform (~ 10 mL) and 3,4-dibutoxy-3-cyclobutene-1,2-dione was added (**a**: 208 μ L, 0.96 mmol, **b**: 106 μ L, 0.49 mmol, **c**: 26 μ L, 0.117 mmol, **d**: 142 μ L, 0.66 mmol) with few drops of DIPEA. The reaction mixture was stirred and refluxed overnight. The crude product was purified by flash column chromatography using a gradient of 10-90% CH_3CN/H_2O over 30-45 minutes on a C18 silica column. The product was concentrated by evaporation and lyophilized overnight to obtain compound **9a-d** as a white solid.

9a: Yield: 240 mg, 42.6 % 1H -NMR (δ_H [ppm], $CDCl_3$, 400 MHz): 4.72-4.69 (m, 2H), 4.21-4.19 (t, 2H), 3.76-3.63 (m, 40H), 3.55-3.53 (m, 2H), 3.37 (s, 3H), 1.78-1.76 (m, 2H), 1.45-1.41 (m, 2H), 0.97-0.95 (t, 3H). ^{13}C -NMR (δ_C [ppm], $CDCl_3$, 100 MHz): 188.96, 183.45, 177.34, 172.98, 156.86, 73.41, 71.90, 71.85, 70.56, 70.52, 70.51, 70.48, 70.44, 70.40, 70.30, 70.28, 69.37, 64.04,, 59.04, 44.79, 41.76, 41.70, 41.24, 32.03, 29.71, 18.66, 13.72. LC-MS: 4.82 min, m/z : 754.54 $[M+H]^+$. MALDI-TOF-MS: m/z calc: 754.44; found: 777.33 $[M+Na]^+$.

9b: Yield: 200 mg, 65.2 % 1H -NMR (δ_H [ppm], $CDCl_3$, 400 MHz): 6.70 (br s, 1H), 5.01 (br s, 1H), 4.77-4.72 (t, 2H), 4.22-4.20 (t, 2H), 3.75-3.63 (m, 42H), 3.58-3.54 (m, 2H), 3.38 (s, 3H), 3.21-3.16 (t, 2H), 1.81-1.77 (m, 2H), 1.66-1.60 (m, 2H), 1.59-1.36 (m, 8H), 0.99-0.95 (t, 3H). ^{13}C -NMR (δ_C [ppm], $CDCl_3$, 100 MHz): 177.39, 172.47, 156.54, 73.39, 71.92, 70.58, 70.54, 70.49, 69.64, 63.87, 59.00, 44.62, 40.67, 32.02, 30.48, 29.81, 26.06, 25.87, 18.63, 13.66. LC-MS: 6.09 min, m/z : 811.33 $[M+H]^+$. MALDI-TOF-MS: m/z calc: 810.47; found: 833.23 $[M+Na]^+$, 849.22 $[M+K]^+$.

9c: Yield: 48.33 mg, 63.1 % ¹H-NMR (δ_{H} [ppm], CDCl₃, 400 MHz): 5.14(br s, 1H), 4.69-4.66 (t, 2H), 4.15-4.13 (t, 2H), 3.63-3.57 (m, 42H), 3.50-3.48 (m, 2H), 3.32 (s, 3H), 3.18 (t, 2H), 2.80 (s, 2H), 1.75-1.71 (m, 2H), 1.55-1.53 (m, 2H), 1.44-1.37 (m, 4H), 1.25 (m, 8H), 0.93-0.90 (t, 3H). ¹³C-NMR (δ_{C} [ppm], CDCl₃, 100 MHz): 177.22, 172.35, 156.38, 73.26, 71.82, 70.44, 70.37, 69.56, 63.69, 58.92, 44.73, 40.86, 31.95, 30.51, 29.79, 28.98, 26.50, 26.21, 18.59, 13.62. LC-MS: 6.67 min, m/z: 839.33 [M+H]⁺. MALDI-TOF-MS: *m/z* calc: 838.50; found: 861.32 [M+Na]⁺, 877.27 [M+K]⁺.

9d: Yield: 310 mg, 69% ¹H-NMR (δ_{H} [ppm], CDCl₃, 400 MHz): 4.75-4.74 (m, 2H), 4.23-4.21 (t, 2H), 3.68-3.56 (m, 44H), 3.40 (s, 3H), 3.18-3.14 (t, 2H), 1.80-1.78 (m, 2H), 1.63-1.60 (m, 2H), 1.48-1.46 (m, 4H), 1.28 (m, 16H), 1.02-0.97 (t, 3H). ¹³C-NMR (δ_{C} [ppm], CDCl₃, 100 MHz): 189.53, 182.93, 177.52, 172.47, 156.51, 73.47, 71.98, 70.65, 70.61, 70.56, 69.75, 63.86, 59.11, 44.96, 41.10, 32.09, 31.16, 30.74, 30.00, 29.54, 29.29, 29.18, 26.79, 26.41, 18.73, 13.76. LC-MS: 7.39 min, m/z: 894.81 [M+H]⁺. MALDI-TOF-MS: *m/z* calc: 894.57; found: 917.44 [M+Na]⁺.

Synthesis of 1b-e

Compound **7** (**b**: 98 mg, 0.086 mmol, **c**: 80 mg, 0.056 mmol, **d**: 128 mg, 0.066 mmol, **e**: 180 mg, 0.26 mmol,) was dissolved in 10 mL chloroform with a few drops of DIPEA. 1,7-heptanediamine (**b**: 6.5 μ L, 0.043 mmol, **c**: 4.23 μ L, 0.028 mmol, **d**: 5 μ L, 0.033 mmol, **e**: 20 μ L, 0.13 mmol,) was added to the reaction mixture and refluxed overnight. If necessary, an additional amount of 1,7-heptanediamine (up to a maximum of 2 equivalents) were added until the starting material **7** disappeared. The completion of the reaction was verified by LC-MS, and purified by flash column chromatography using a gradient of 10-90% CH₃CN/H₂O over 30-45 minutes on a C18 silica column. The product was concentrated down by evaporation and lyophilized overnight to obtain a white solid.

1b: Yield: 53.2 mg, 54.7 % ¹H-NMR (δ_{H} [ppm], CDCl₃, 400 MHz): 5.05 (br s, 1H), 4.21-4.20 (m, 4H), 3.73-3.65 (m, 136 H), 3.56-3.55 (t, 4H), 3.39 (s, 6H), 3.15-3.13 (m, 4H), 2.85-1.65-1.63 (m, 8H), 1.48-1.26 (m, 34H). ¹³C-NMR (δ_{C} [ppm], CDCl₃, 100 MHz): 182.62, 181.55, 168.97, 167.13, 156.53, 71.90, 70.56, 70.52, 70.50, 70.49, 70.46, 69.67, 63.77, 59.05, 44.75, 43.22, 41.06, 31.16, 29.95, 29.47, 29.27, 29.24, 26.75, 26.42, 24.80. LC-MS: 6.83 min, m/z: 1153.47 [M+H+Na]²⁺ MALDI-TOF-MS: *m/z* calc: 2243.39; found: 2266.66 [M+Na]⁺.

1c: Yield: 38.5 mg, 48.4 % $^1\text{H-NMR}$ (δ_{H} [ppm], CDCl_3 , 850 MHz): 4.22 (m, 4H), 3.75-3.56 (m, 196H), 3.40 (s, 6H), 3.16-3.15 (m, 4H), 1.92 (br s, 10H), 1.65-1.64 (m, 8H), 1.50-1.27 (m, 36H). $^{13}\text{C-NMR}$ (δ_{C} [ppm], CDCl_3 , 212.5 MHz): 182.26, 182.13, 168.80, 167.78, 156.53, 71.92, 71.89, 70.54, 70.52, 70.49, 70.44, 70.38, 70.34, 70.31, 69.81, 69.72, 63.66, 59.05, 44.60, 43.27, 41.08, 31.03, 29.86, 29.70, 29.42, 29.31, 29.18, 29.11, 26.68, 26.36, 24.86. LC-MS: 6.60 min, m/z : 1431.60 $[\text{M}+2\text{H}]^{2+}$. MALDI-TOF-MS: m/z calc: 2859.75; found: 2883.15 $[\text{M}+\text{Na}]^+$.

1d: Yield: 59.0 mg, 46.3 % $^1\text{H-NMR}$ (δ_{H} [ppm], CDCl_3 , 850 MHz): 5.07 (br s, 1H), 4.21 (m, 4H), 3.74-3.55 (m, 286 H), 3.38 (s, 6H), 3.14-3.13 (m, 4H), 1.63 (m, 8H), 1.47-1.25 (m, 34H). $^{13}\text{C-NMR}$ (δ_{C} [ppm], CDCl_3 , 212.5 MHz): 71.90, 70.67, 70.56, 70.52, 70.51, 70.48, 70.45, 70.42, 69.70, 63.72, 59.07, 44.65, 43.21, 41.07, 41.05. LC-MS: 6.91 min, m/z : 1968.33 $[\text{M}+2\text{H}]^{2+}$, 985.80 $[\text{M}+4\text{H}]^{4+}$. MALDI-TOF-MS: m/z calc: 3916.38; found: 3939.67 $[\text{M}+\text{Na}]^+$.

1e: Yield: 76.2 mg, 42.9 % $^1\text{H-NMR}$ (δ_{H} [ppm], CDCl_3 , 400 MHz): 4.23 (m, 4H), 3.68-3.66 (m, 52H), 3.59-3.56 (t, 4H), 3.40 (s, 6H), 3.18-3.15 (m, 4H), 2.96-2.86 (br s, 6H), 1.71-1.64 (m, 6H), 1.52-1.27 (m, 36H). $^{13}\text{C-NMR}$ (δ_{C} [ppm], CDCl_3 , 100 MHz): 181.61, 168.71, 157.55, 72.90, 72.79, 71.53, 71.44, 70.74, 64.68, 60.04, 45.87, 42.08, 31.35, 30.90, 30.81, 30.39, 30.23, 30.15, 30.04, 27.73, 27.41, 27.73 LC-MS: 7.64 min, m/z : 1363.60 $[\text{M}+\text{H}]^+$. MALDI-TOF-MS: m/z calc: 1362.86; found: 1385.91 $[\text{M}+\text{Na}]^+$.

Synthesis of 2a-d

Compound **9** (**a**: 118 mg, 0.16 mmol, **b**: 200 mg, 0.25 mmol, **c**: 40 mg, 0.05 mmol, **d**: 106 mg, 0.11 mmol) was dissolved in 10 mL chloroform with a few drops of DIPEA. 1,7-heptanediamine (**a**: 11.8 μL , 0.078 mmol, **b**: 18.9 μL , 0.125 mmol, **c**: 3.8 μL , 0.025 mmol, **d**: 8.9 μL , 0.059 mmol) was added to the mixture and refluxed overnight. If necessary, an additional amount of 1,7-heptanediamine (up to a maximum of 2 equivalents) were added until the starting material **7** disappeared. The product was purified by flash column chromatography using a gradient of 10-90% $\text{CH}_3\text{CN}/\text{H}_2\text{O}$ over 30-45 minutes on a C18 silica column. The product was concentrated by evaporation and lyophilized overnight to obtain a white solid.

2a: Yield: 66.0 mg, 56.6 % $^1\text{H-NMR}$ (δ_{H} [ppm], CDCl_3 , 850 MHz): 7.41 (s, 1H), 6.21 (s, 1H) 4.21-4.17 (m, 4H), 3.76-3.53 (m, 92H), 3.41 (s, 4H), 3.37 (s, 6H), 1.66-1.65 (m, 4H), 1.44-1.40 (m, 6H). $^{13}\text{C-NMR}$ (δ_{C} [ppm], CDCl_3 , 212.5 MHz): 182.87, 182.05,

Chapter 4

168.80, 167.67, 156.78, 71.91, 71.89, 70.61, 70.60, 70.58, 70.55, 70.52, 70.50, 70.48, 70.44, 70.43, 70.40, 70.38, 69.70, 69.39, 68.93, 68.86, 67.03, 66.81, 63.81, 59.05, 43.79, 43.06, 42.14, 29.81, 24.43. LC-MS: 4.56 min, m/z : 1491.17 [M+H]⁺. MALDI-TOF-MS: m/z calc: 1490.82; found: 1513.927 [M+Na]⁺.

2b: Yield: 90.1 mg, 45.5 % ¹H-NMR (δ_{H} [ppm], CDCl₃, 850 MHz): 8.45 (s, 2H), 5.36 (s, 2H), 4.24-4.21 (m, 4H), 3.73-3.66 (m, 84H), 3.58-3.56 (t, 4H), 3.40 (s, 6H), 3.20-3.16 (m, 4H), 2.87 (s, 4H), 1.69-1.65 (m, 8H), 1.55-1.36 (m, 18H). ¹³C-NMR (δ_{C} [ppm], CDCl₃, 212.5 MHz): 192.44, 186.56, 181.92, 169.17, 157.75, 72.91, 72.87, 71.57, 71.56, 71.53, 71.50, 71.47, 71.45, 71.43, 71.41, 71.39, 71.37, 71.34, 71.31, 70.76, 70.68, 64.89, 64.68, 60.11, 45.38, 44.77, 41.83, 31.69, 30.75, 30.61, 27.05, 26.83. LC-MS: 5.85 min, m/z : 1604.67 [M+H]⁺. MALDI-TOF-MS: m/z calc: 1602.95; found: 1603.97 [M+H]⁺, 1625.93 [M+Na]⁺, 1641.87 [M+K]⁺.

2c: Yield: 19.4 mg, 48 % ¹H-NMR (δ_{H} [ppm], CDCl₃, 400 MHz): 8.38 (s, 2H), 5.20 (s, 2H), 4.23 (m, 4H), 3.70-3.66 (m, 84H), 3.57-3.56 (t, 4H), 3.39 (s, 6H), 3.16-3.14 (m, 4H), 1.49-1.43 (m, 12H), 1.37-1.26 (m, 22H). ¹³C-NMR (δ_{C} [ppm], CDCl₃, 100 MHz): 181.50, 169.10, 168.55, 157.48, 72.92, 72.88, 72.86, 72.83, 71.57, 71.54, 71.52, 71.51, 71.48, 71.46, 71.44, 71.42, 71.41, 71.39, 71.37, 71.34, 70.75, 70.71, 64.83, 64.70, 60.06, 45.77, 45.60, 44.85, 42.03, 41.34, 31.86, 30.85, 30.77, 30.74, 30.07, 30.01, 29.78, 27.64, 27.31, 26.15. LC-MS: 6.38 min, m/z : 1659.73 [M+H]⁺. MALDI-TOF-MS: m/z calc: 1659.01; found: 1660.14 [M+H]⁺, 1682.07 [M+Na]⁺, 1698.02 [M+K]⁺.

2d: Yield: 53 mg, 50.5 % ¹H-NMR (δ_{H} [ppm], CDCl₃, 400 MHz): 7.85 (s, 2H), 7.56 (s, 2H), 5.20 (s, 2H), 4.23-4.20 (m, 4H), 3.70-3.55 (m, 92H), 3.39 (s, 6H), 3.17-3.13 (m, 4H), 2.20 (s, 4H), 1.66 (m, 8H), 1.49-1.26 (m, 42H). ¹³C-NMR (δ_{C} [ppm], CDCl₃, 100 MHz): 182.21, 168.91, 167.05, 156.50, 71.91, 70.57, 70.53, 70.49, 69.66, 63.81, 59.03, 44.84, 43.11, 41.09, 31.19, 29.97, 29.57, 29.29, 26.77, 26.47, 24.66. LC-MS: 7.10 min, m/z : 1773.11 [M+H]⁺. MALDI-TOF-MS: m/z calc: 1771.13; found: 1794.886 [M+Na]⁺.

4.6.4 Cryogenic transmission electron microscopy (cryo-TEM)

Cryogenic transmission electron microscopy (cryo-TEM) samples were prepared by applying three microliters of sample solution (580 μM) to a freshly glow-discharged Lacey Carbon Film (300 mesh Cu grids). The excess of liquid was blotted away for 1 second (95% humidity, RT, Whatman No.4 filter paper) and plunge-frozen in liquid ethane at $-183\text{ }^\circ\text{C}$ using a Leica EM GP. Images of the vitrified samples were recorded with a Tecnai F20 FEG (FEI company, The Netherlands), equipped with a field emission gun at 200 keV using a Gatan UltraScan camera (Gatan company, Germany) with a defocus between -3 and $-9\text{ }\mu\text{m}$. The obtained cryo-TEM images were analyzed using the "Fiji" image processing software. Samples **1a**, **1b**, **1c**, **1d** and **2c** were analyzed. The length and width of 50 aggregates were measured per sample. Values are expressed as the average \pm their standard deviation.

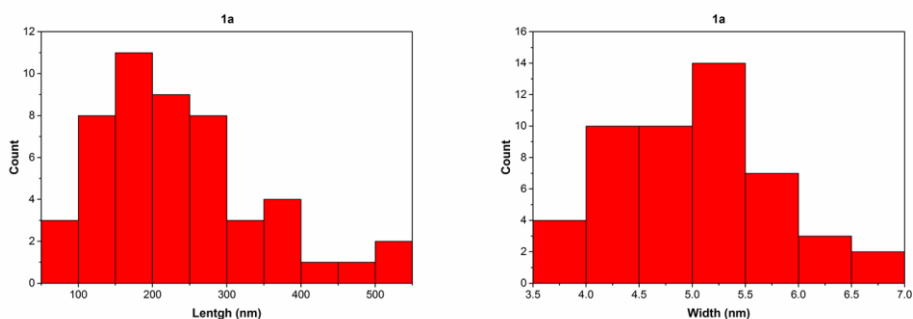


Figure S4.1. Histograms of length ($234 \pm 108\text{ nm}$) and width ($5 \pm 1\text{ nm}$) distributions measured for **1a**.

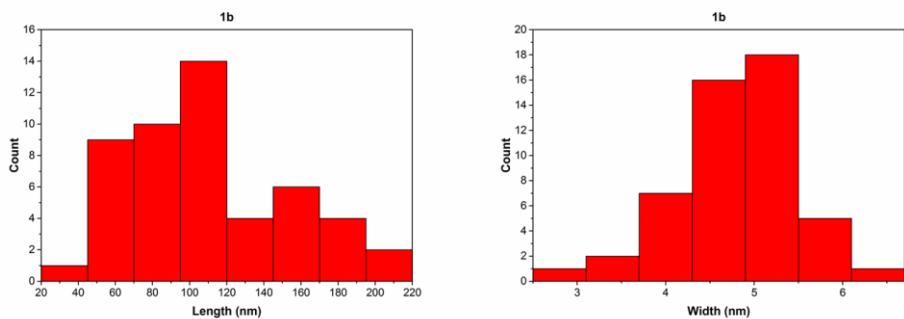


Figure S4.2. Histograms of length (109 ± 44 nm) and width (5 ± 1 nm) distributions measured for **1b**.

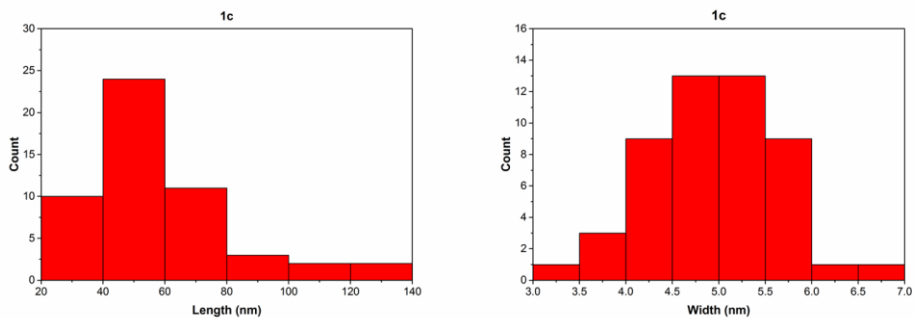


Figure S4.3. Histograms of length (57 ± 24 nm) and width (5 ± 1 nm) distributions measured for **1c**.

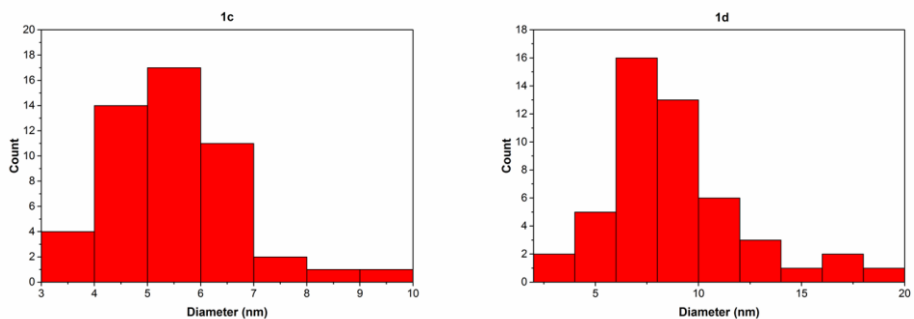


Figure S4.4. Histograms of diameter distributions measured for spherical aggregates of **1c** (6 ± 1 nm) (left) and **1d** (9 ± 4 nm) (right).

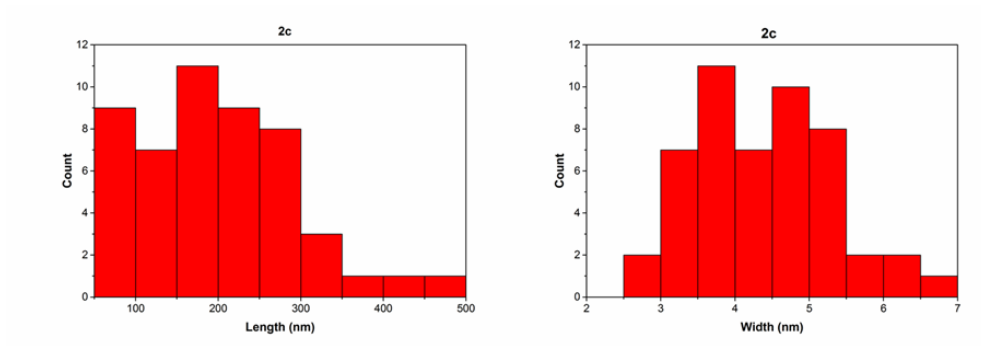


Figure S4.5. Histograms of length (200 ± 93 nm) and width (4 ± 1 nm) distributions measured for **2c**.

4.6.5 Small angle X-ray scattering (SAXS)

Small angle X-ray scattering (SAXS) experiments were performed on aqueous solutions of the monomers **1a**, **1b**, **1c** and **1d** to study their progressive transition from fiber-like to spherical aggregates upon increasing the length of the hydrophilic segment. All SAXS measurements were carried out in MQ water at room temperature. The SAXS profiles of the 4 and 5 mg/mL samples are given in Figure S4.7 for the molecules above. In the low- q regime, the scattering profiles in log-log representation of **1a** and **1b** exhibited a powerlaw slope of -1, which is typical for cylindrical objects. A low- q plateau followed by a steep powerlaw decay with a slope of approximately -4 in the high- q regime is observed for sample **1d** with the longest oligo(ethylene glycol) chain, which is typical for low aspect ratio aggregates, such as spherical objects. Sample **1c** displays a profile where a moderate slope between 0 and -1 is observed in the low-to-intermediate q regime due to the coexistence of fibrillar and spherical aggregates. Upon normalization to 1 mg mL^{-1} (Figure S4.6) the SAXS profiles collected at 4 and 5 mg mL^{-1} superpose for monomers **1a**, **1b** and **1d**. We can safely neglect interspecies interactions and model these data sets exclusively using a form factor model. However, the 4 and 5 mg mL^{-1} spectra of **1c** do not superpose, as the coexistence is concentration-dependent, favoring a different equilibrium between fibrillar and spherical aggregates at 4 versus 5 mg mL^{-1} .

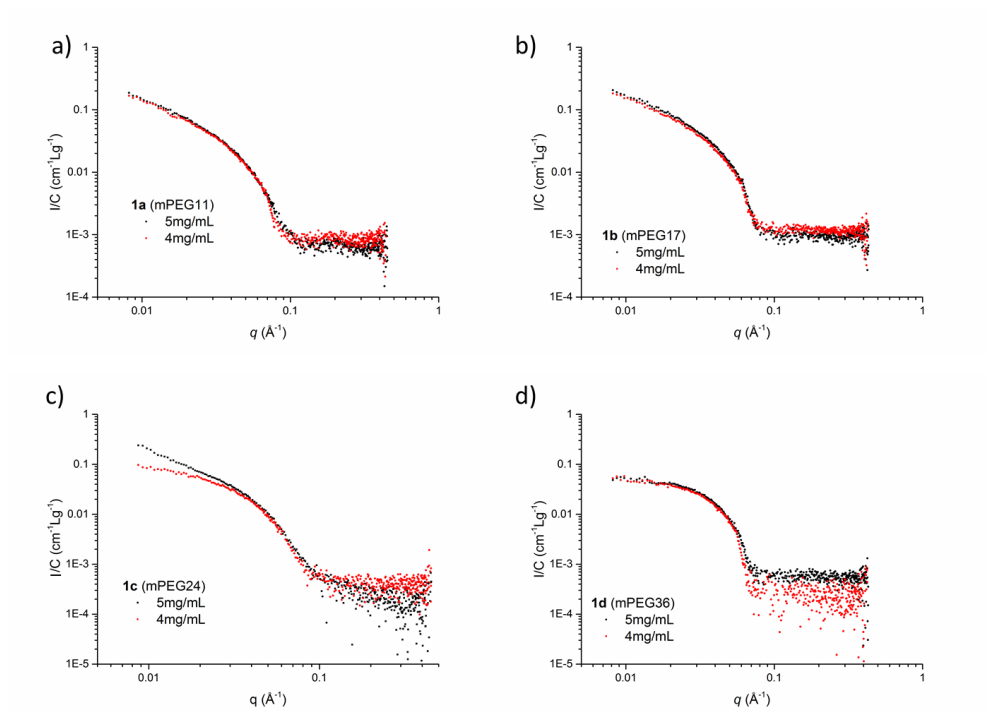


Figure S4.6. SAXS profiles of squaramide-based supramolecular polymers collected at a concentration of 4 and 5 mg mL^{-1} normalized by weight concentration for a) **1a**, b) **1b**, c) **1c**, and d) **1d** (i.e., the symbols correspond to experimental data (I/c vs. q)).

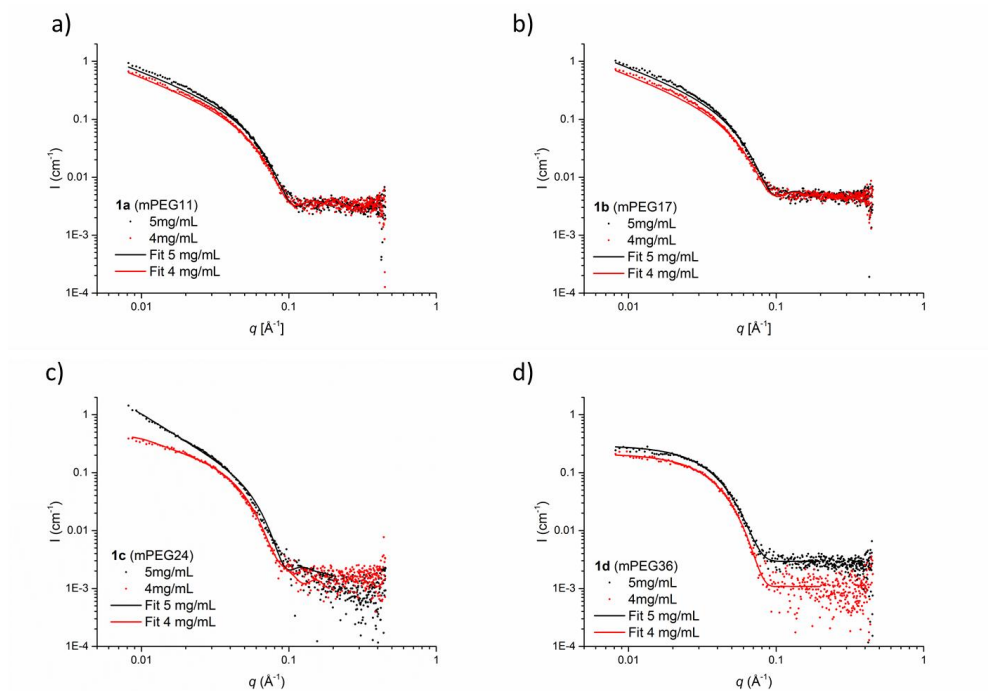


Figure S4.7. SAXS profiles of a) **1a**, b) **1b**, c) **1c**, and d) **1d**. Symbols represent experimental data; lines represent data modeled with a form factor for rigid homogeneous cylinder form molecules **1a** (a) and **1b** (b), two form factors describing a homogenous cylinder and a homogeneous sphere for **1c** (c) and fuzzy spheres for monomer **1d** (d).

Appropriate form factors were selected to model the SAXS profiles in Figure S4.7. The SAXS profiles of **1a** and **1b** were modeled with a form factor of homogeneous cylinders, **1d** with a form factor for fuzzy spherical objects, while for **1c**, two form factors describing a homogenous cylinder and a homogeneous sphere were utilized to model the data. Other form factors such as flexible or core shell homogeneous cylinders were tested for the monomers **1a** and **1b**, while a homogeneous sphere form factor was also tested for **1d**, resulting in modeling with a lower level of accuracy. In all cases, a fixed $\rho_{\text{solvent}} = 9.37 \times 10^6 \text{ \AA}^{-2}$ was used. The values obtained from modeling the various curves are reported in table S4.1.

To extract the cross-sectional mass per unit length, M_L , from the scattering profiles for **1a** and **1b**, two equations were used:

$$I(q) = \frac{\pi}{q} I_{cs}(q) \quad (1)$$

$$M_L = \frac{I_{cs}(0)}{c\Delta\rho_M^2} \quad (2)$$

The electron length density difference per mass, $\Delta\rho_M$ was extracted from modeling of the curves and the height of the Holtzer plateau, I_{cs} , which is indicated by the solid lines in Figure S4.8 (a and b). For all samples, the specific volume, $\nu = 0.83 \text{ cm}^3 \text{ g}^{-1}$, was estimated based on the reciprocal density of oligo(ethylene glycol) ($M_w > 600 \text{ g mol}^{-1}$, $\rho = 1.2 \text{ g cm}^{-3}$),² on par with an earlier publication.¹

In order to estimate the number of monomers in spherical aggregates of **1d**, we used:

$$I(0) = N(\Delta\rho V)^2 = \frac{C\Delta\rho^2\nu^2 MW}{N_A} \quad (3)$$

$I(0)$ was obtained from equation (2). The molecular weight of the aggregate (M_w) was calculated from the mass per unit volume (C), contrast ($\Delta\rho_M$), specific volume (ν) of **1d**, and Avogadro's number (N_A).³

Table S4.1. Structural parameters extracted from the SAXS profiles of the squaramide-based bolaamphiphiles **1a**, **1b** and **1d**.

Sample	$\Delta\rho_{cvl} (\text{Å}^{-2})$	$\Delta\rho_M (\text{cm g}^{-1})$	$I (\text{cm}^2 \text{ L g}^{-1})$	$I_{cs}(0) (\text{cm}^2)$	$M_L (\text{g nm}^{-1})$	$M_w (\text{g mol}^{-1})$	molec/nm	$r_{cs} (\text{nm})$
1a (4 mg/mL)	10.44×10^6	8.91×10^9	1.48×10^5	1.88×10^5	5.93×10^{20}	-	21	3.4
1a (5 mg/mL)	10.46×10^6	9.07×10^9	1.37×10^5	2.18×10^5	5.30×10^{20}	-	18	3.5
1b (4 mg/mL)	10.40×10^6	8.54×10^9	1.70×10^5	2.17×10^5	7.44×10^{20}	-	20	3.8
1b (5 mg/mL)	10.46×10^6	9.06×10^9	1.53×10^5	2.44×10^5	5.95×10^{20}	-	16	3.8
1d (4 mg/mL)	10.44×10^6	1.37×10^{10}	8.09×10^5	1.03×10^6	-	1.20×10^{12}	31*	3.6
1d (5 mg/mL)	10.55×10^6	9.77×10^9	8.49×10^5	1.35×10^6	-	2.48×10^{12}	63*	4.5

* Estimated overall aggregation number.

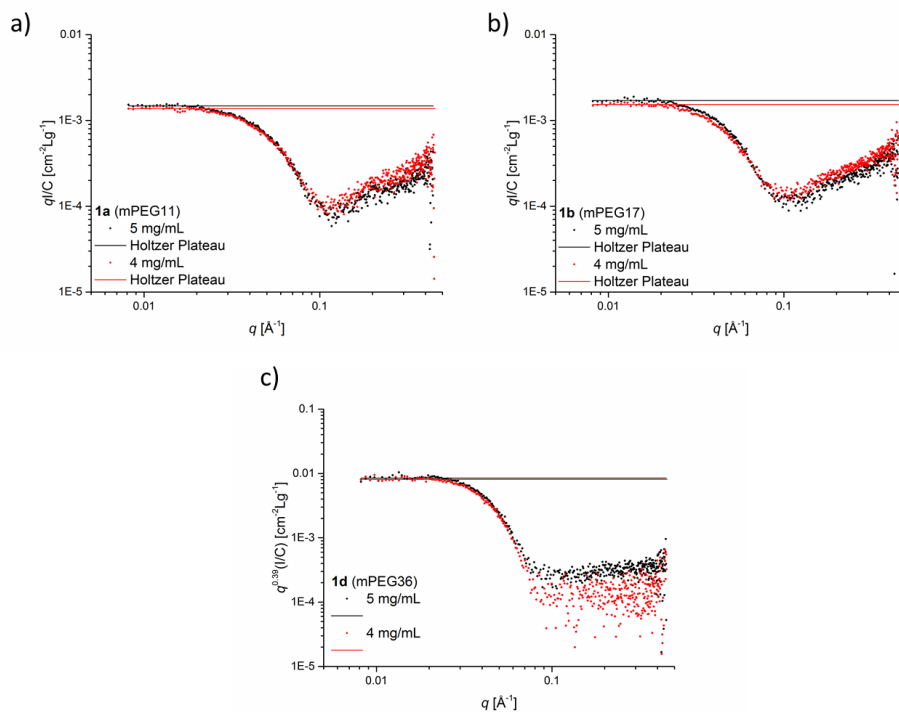


Figure S4.8: Casassa–Holtzer plot of the scattering profiles in Figure S4.7 for **1a** (a) and **1b** (b). The Holtzer plateaus ($0.0065 \leq q \leq 0.0197 \text{ \AA}^{-1}$) are indicated by solid red and black lines. $I_{cs}(q)$ determination plot of the scattering profile for **1d** (c). The $I_{cs}(q)$ plateau ($0.0086 \leq q \leq 0.0245 \text{ \AA}^{-1}$) is indicated by the red and black lines.

4.6.6. UV-vis spectroscopy

UV-Vis samples were prepared from stock solutions of the various squaramide-based bolaamphiphiles **1a-d** and **2a-d** (5.8 mM) equilibrated overnight prior to their dilution at the measuring concentration (30 μ M).

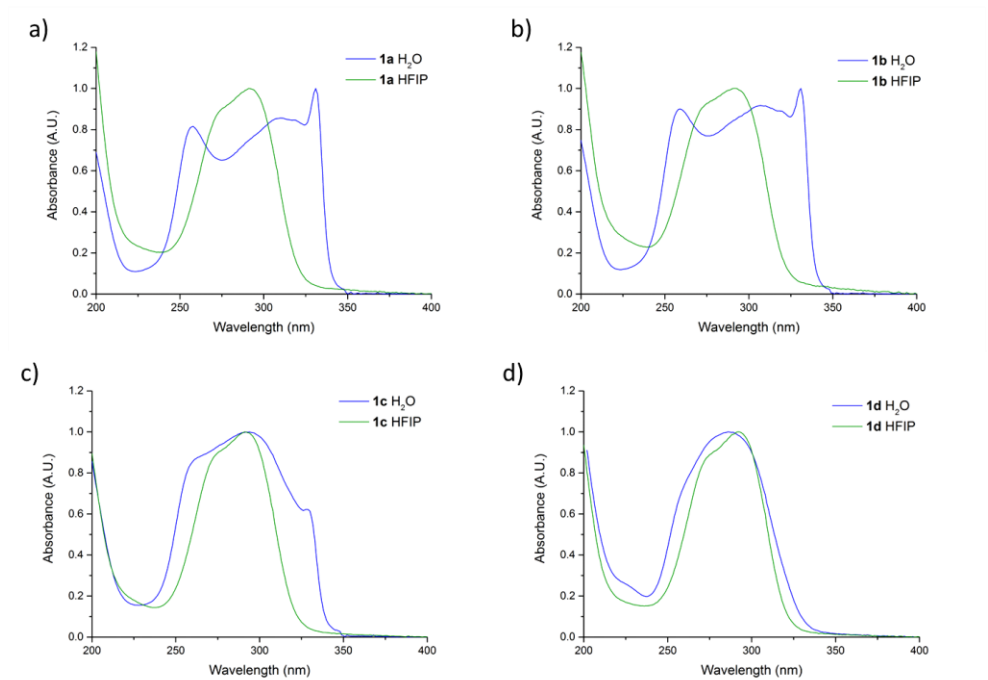


Figure S4.9. Normalized UV-Vis spectra of **1a** (a), **1b** (b), **1c** (c) and **1d** (d) in water (blue) and HFIP (green) at 30 μ M.

Chapter 4

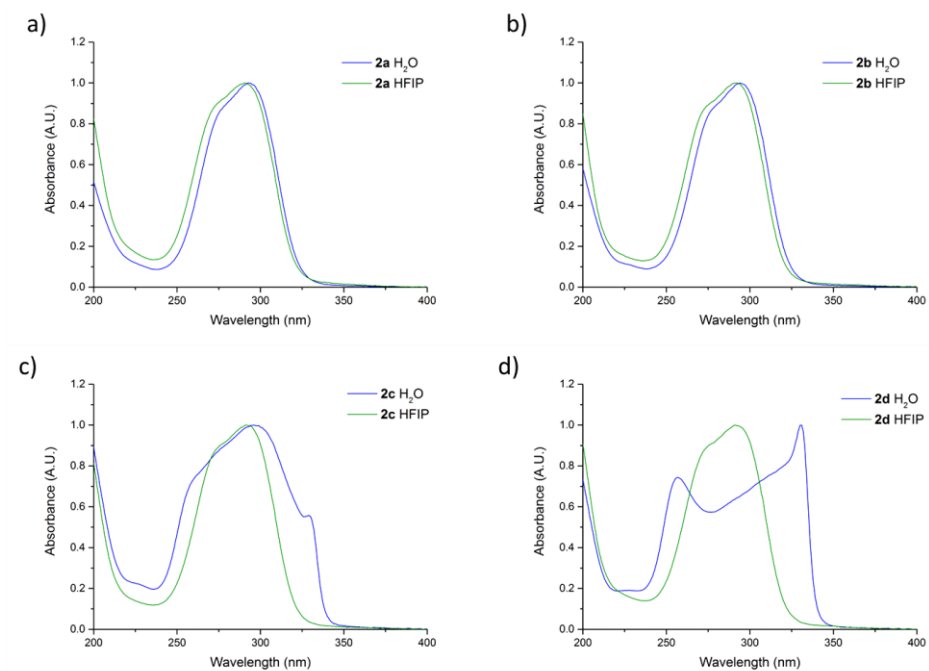


Figure S4.10. Normalized UV-Vis spectra of **2a** (a), **2b** (b), **2c** (c) and **2d** (d) in water (blue) and HFIP (green) at 30 μ M.

4.6.7. Fourier transform infrared (FTIR)

Solutions of the various squaramide-based bolaamphiphiles (5.8 mM) were prepared in D_2O and HFIP- d_2 and left to equilibrate overnight before measurement.

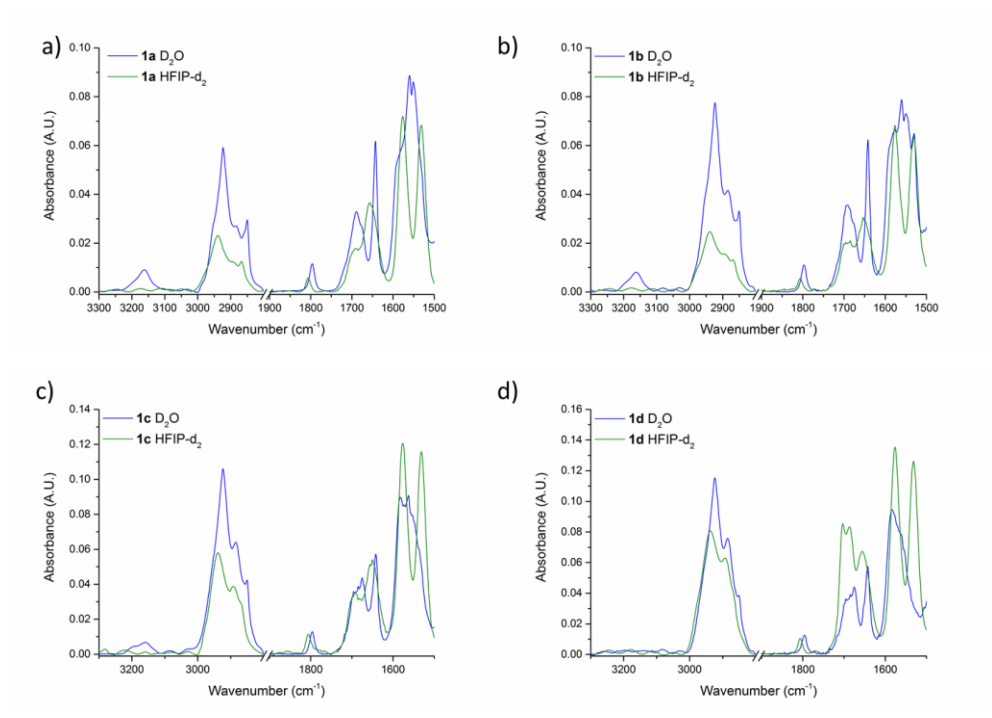


Figure S4.11. FTIR spectra recorded for **1a** (a), **1b** (b), **1c** (c) and **1d** (d) in D_2O and HFIP- d_2 in N-H and C-H stretch regions above 2800 cm^{-1} , and the amide I and amide II region between $1900\text{-}1500\text{ cm}^{-1}$.

Chapter 4

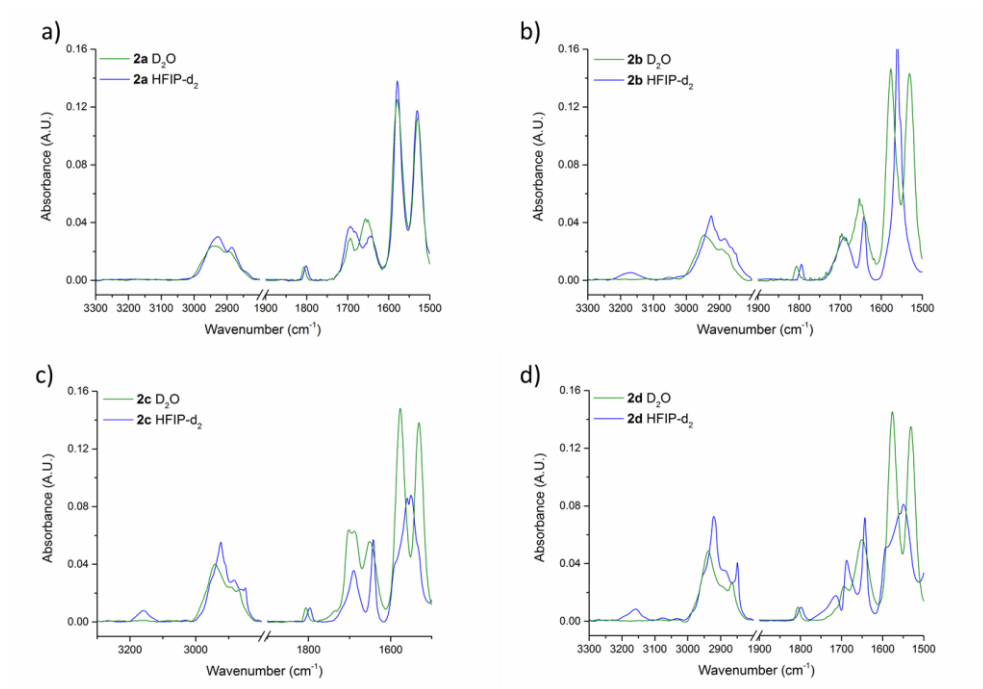


Figure S4.12. FTIR spectra for **2a** (a), **2b** (b), **2c** (c) and **2d** (d) in D_2O and HFIP- d_2 in N-H and C-H stretch regions above 2800 cm^{-1} , and the amide I and amide II regions between 1900-1500 cm^{-1} .

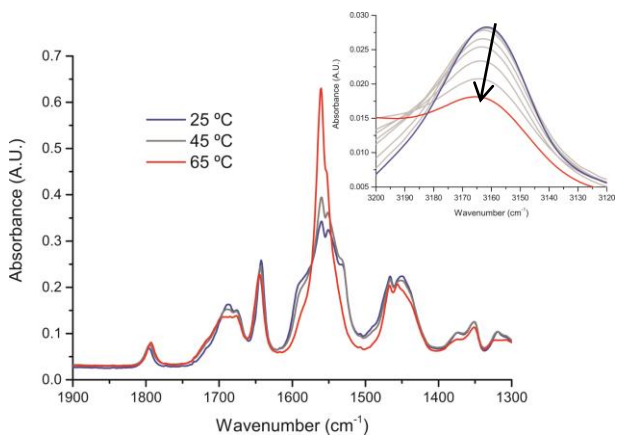


Figure S4.13. FTIR spectrum of **1a** in D_2O with increasing temperature from 25 °C (blue line) to 65 °C (red line). Inset: NH region (3200-3120 cm^{-1}).

4.6.8. Fluorescence spectroscopy

Examination of hydrophobic domains: 7 μL of a 15 μM (0.005 mg/mL) stock solution of Nile Red in CH_3OH was spotted in the wells of a 96-well plate (PP Microplate, solid F-bottom (flat), chimney well) and was placed under vacuum for at least four hours. Once the solvent was completely removed, 100 μL of the various squaramide-based bolaamphiphiles (stock solution: 30 μM) were added to the wells pre-spotted with Nile Red. The solutions were shaken vigorously in the Tecan plate reader (300 seconds, 654 rpm, linear mode) and then allowed to equilibrate overnight at room temperature. Fluorescence measurements were collected at excitation wavelength of 550 nm and an emission wavelength from 570 to 700 nm.

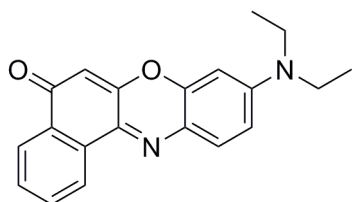


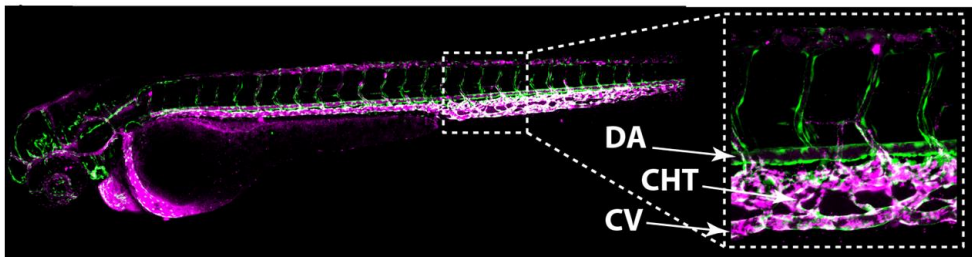
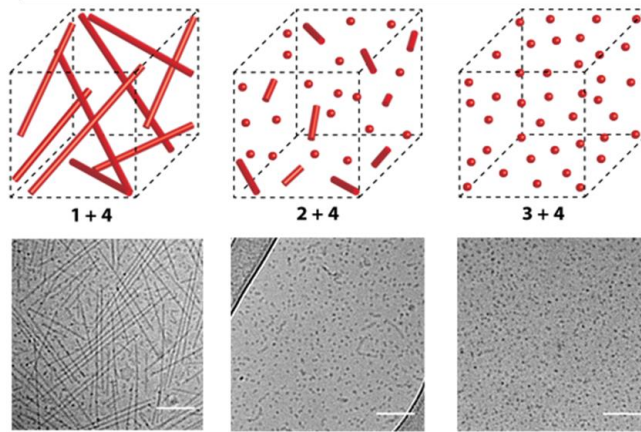
Figure S4.14. Molecular structure of Nile Red (NR).

4.6.9. References

- (1) Saez Talens, V.; Englebienne, P.; Trinh, T. T.; Noteborn, W. E. M.; Voets, I. K.; Kieltyka, R. E. *Angew. Chemie - Int. Ed.* **2015**, *54* (36), 10502–10506.
- (2) Lewalter, J.; Skarping, G.; Ellrich, D.; Schoen, U. *MAK Collect. Occup. Heal. Saf.* **2012**, *10*, 248–270.
- (3) Jacques, D. A.; Trehwella, J. *Protein Sci.* **2010**, *19* (4), 642–657.

CHAPTER 5

Biodistribution of squaramide-based supramolecular polymer nanoparticles in zebrafish embryos



This chapter was prepared as an original research paper: Victorio Saez Talens, Gabriela Arias Alpizar, Jeroen Bussmann, Alexander Kros, Roxanne E. Kieltyka

5.1 Abstract

Supramolecular polymer biomaterials are attractive scaffolds to prepare nanoparticles for drug delivery due to their easy fabrication, and tunable shape and size. However, their exploitation as therapeutic nanocarriers until now has been limited, and a clear *in vivo* picture of their biodistribution and uptake remains challenging due to the opacity of the mammalian models used to study these processes. Here, I prepare fluorescently-labeled squaramide-based supramolecular polymer nanoparticles of varied shape, from fibrillar to spherical aggregates, and size, from hundreds to tens of nanometers, and tracking their *in vivo* biodistribution and uptake behavior once injected intravenously in a zebrafish embryo model. In all cases, the supramolecular polymer nanoparticles evaded macrophages, however they display distinct biodistribution consistent with particle type: spherical aggregates tens of nanometers in diameter circulate freely throughout the blood vessel lumen, whereas fibrillar aggregates several hundred nanometers in length were found to associate with scavenger endothelial cells that are functionally homologous to mammalian liver. Moreover, endothelial scavenging of the high aspect ratio self-assemblies was mediated largely through the Stabilin-2 transmembrane receptor as demonstrated previously for isotropic anionic nanoparticles. By applying a supramolecular approach based on squaramides for nanoparticle construction in combination with the transparent zebrafish embryo model, I show a facile means to generate cargo-loaded nanoparticles of various size and shape to establish such models as a first-line approach to probe biodistribution and mechanistic aspects of cellular uptake in the drug delivery community.

5.2 Introduction

Much effort has been dedicated to design and synthesize nanoparticulate (less than 500 nm in any dimension) carriers with precisely engineered physicochemical properties for the targeted delivery of therapeutics. To this end, particles of varied features including size, shape, surface charge, functionality, and elasticity have been prepared.¹⁻⁹ Irrespective of their designs it has been demonstrated that >99% of such particles are cleared by the liver, yet the cellular mechanisms by which these processes occur remain unclear due to the inherent difficulty to visualize them in mammalian models. A promising alternative to gain insight into the routing of such particles *in vivo* at the cellular level is the zebrafish (*Danio rerio*) embryo model system. This model system provides unparalleled opportunities in comparison to first-line mouse models used to assess the nanoparticle fate *in vivo* due their optical transparency, homology with 70% of human disease genes, easy manipulation with its fast development and external fertilization.¹⁰⁻¹² Recently, we have demonstrated the use of the zebrafish caudal vein to study processes related to nanoparticle uptake in the mammalian liver at the molecular level.¹³ The sequestration and uptake of isotropic anionic nanoparticles was highly reliant on Stabilin-2, a transmembrane receptor on scavenger endothelial cells resident in the caudal vein, using *stab2* knockouts we validated the importance of this receptor for nanoparticle clearance in the liver.

Supramolecular self-assembly can provide access to a wide range of soft nanostructures, including those that are filamentous, through the polymerization of designed monomers using non-covalent interactions, such as hydrogen-bonding, aromatic interactions, electrostatic and/or hydrophobic effects.^{5,14-21} This approach is of interest for applications in drug delivery because of its facile and modular character, where functional monomers can be combined in a mix-and-match fashion to prepare designed nanocarriers of varied physicochemical properties against a specific therapeutic target.²²⁻²⁶ Although most studies involving supramolecular nanoparticles that are spherical or filamentous take place *in vitro*,^{5,22,27,28} a number of *in vivo* studies have been executed in mouse models.^{6,23,29-35} When their biodistribution is characterized, significant localization of the carrier is observed in the liver³⁶⁻⁴⁰ as previously observed for inorganic nanoparticles.^{7,42} However, it still remains unclear what physicochemical parameters are necessary to reduce their clearance by the liver. By combining a supramolecular approach to nanoparticle construction with the zebrafish embryo

Chapter 5

model system, the door is opened to rapidly generate nanoparticle libraries to visually screen the nanoparticle-biological interface *in vivo* to unveil new opportunities to improve the systemic delivery of therapeutic payloads to their intended target.

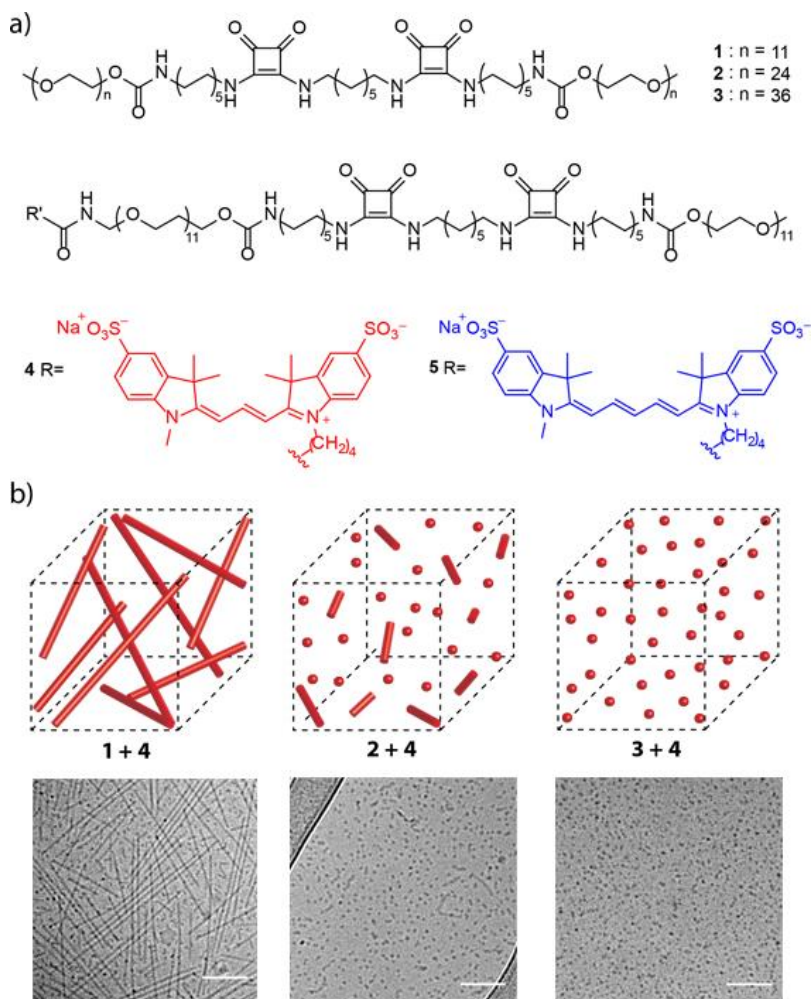


Figure 5.1. Squaramide-based bolaamphiphiles used to prepare supramolecular polymer nanoparticles for *in vivo* biodistribution studies. (a) Chemical structure of bolaamphiphile monomers **1**, **2** and **3** employed in the study to form fibrillar (**1**), mixed rod and spherical (**2**) or spherical (**3**) nanoparticles, respectively, upon self-assembly. The fluorescently-labeled squaramide-based monomer with a Sulfo-Cy3 dye (**4**) is used for tracking of the various supramolecular polymer nanostructures, while the Sulfo-Cy5 dye (**5**) is used in combination for fluorescence resonance energy transfer (FRET) experiments. (b) Schematic representation of the morphology of the co-assembled native (**1**, **2** or **3**) with dye-labeled monomer **4** (2 mol%) into fluorescently-labeled squaramide-based supramolecular polymer nanoparticles prior to injection into a zebrafish embryo model. Representative cryo-TEM images of co-assembled squaramide-based supramolecular polymer nanoparticles from native monomers ($c = 2\text{mM}$) **1**, **2** and **3** with **4** in water. Samples were prepared using the native squaramide-based bolaamphiphile monomer co-assembled with 2 mol% of Sulfo-Cy3 labeled squaramide-based bolaamphiphile **4**, displaying fiber-like structures for **1**, a mixture of spherical and rod-like structures for **2** and spherical aggregates for **3**. The scale bars represent 100 nm.

Earlier in our research group, we reported the self-assembly of a squaramide-based bolaamphiphile, consisting of monomer **1** (Figure 5.1a) into a supramolecular polymer nanoparticles in water.^{42,43} Squaramides are ditopic hydrogen-bonding synthons that consist of a cyclobutenedione ring with two NH hydrogen bond donors opposite two carbonyl hydrogen bond acceptors⁴⁴ that benefit energetically from a gain in aromatic character upon self-assembly through hydrogen-bonding and hydrophobic interactions.^{42,45,46} Classically, squaramides have been used in areas such as medicinal chemistry^{47,48} catalysis^{49,50} and bioconjugation,^{51,52} however their application in polymers is underexplored. Recently, I have demonstrated the ability to tune the morphology of these squaramide-based supramolecular polymer nanoparticles from fibrillar to spherical by modulating the length of the oligo(ethylene glycol) (OEG) hydrophilic domain of the monomer: from $n = 11$ resulting in fiber-like objects, to spherical aggregates with $n = 36$ (Figure 5.1a).⁵³ I herein report, the preparation of fluorescently-labeled squaramide-based supramolecular polymer nanoparticles with distinct shapes and sizes in aqueous media in order to tag and visually track their *in vivo* biodistribution and clearance by the Stabilin-2 receptor in a zebrafish embryo model to understand the range of this receptor in the clearance of nanoparticulate carriers for future drug delivery applications.

5.3 Results and discussion

Synthesis and co-assembly of fluorescently-labeled supramolecular polymer nanoparticles. The general molecular structure of the squaramide-based bolaamphiphile consists of two squaramides located within the center of its hydrophobic core surrounded by two hydrophilic oligo(ethylene glycol) oligomers at its opposite ends (**1**, **2** and **3**, Figure 5.1a). The two squaramide synthons are separated by an alkyl chain of seven methylene units, while an additional chain of ten methylene units are at the outer peripheries of the squaramide moieties. In this work, hydrophilic oligo(ethylene glycol) oligomers (OEG) of increasing chain length ((**1**) MW = 517 Da ($n=11$), (**2**) MW = 1089 Da ($n=24$) and (**3**) MW = 1617 Da ($n=36$)) were used to flank the hydrophobic core to drive the formation of supramolecular polymer nanoparticles of distinct shapes and sizes while providing a means to maintain the same surface chemistry. To be able to tag and track the various supramolecular polymer nanoparticles for their facile visualization in the transparent zebrafish embryo model system, an asymmetrically labeled squaramide-based bolaamphiphile, similar in molecular structure to **1**, with either

a fluorescent Sulfo-Cy3 (**4**) or a Sulfo-Cy5 (**5**) dye were synthesized. These molecules are predicted to co-assemble the fluorescently-labeled squaramide-based bolaamphiphiles because of their equally sized hydrophobic domains compared to the various supramolecular polymer nanoparticles containing distinct hydrophilic domains. Therefore, a single reporter monomer could be used for the labeling of the various structures under study.

Sulfonated variants of cyanine dyes were coupled to the monomers because of their increased solubility and introduced asymmetrically into the bolaamphiphile to reduce the potential for disruption of the formed supramolecular polymers or aggregation. The synthesis of the asymmetrically fluorescently-labeled squaramide-based bolaamphiphile was performed in a convergent manner, starting with the catalytic hydrogenation of O-(2-azidoethyl)undecaethylene glycol followed by Boc protection of the resulting amine group *in situ* using Boc-anhydride (see supporting information, section 5.6.4). Subsequently, the hydroxyl group of the heterobifunctional oligo(ethylene glycol) was activated using 1,1'-carbonyldiimidazole (CDI) and further reacted with N-Cbz-1,10-decanediamine and purified by reverse phase chromatography with a yield of 51%. Subsequently, catalytic hydrogenation of the Cbz protecting group led to the coupling of the amphiphile to 3,4-dibutoxy-3-cyclobutene-1,2-dione to provide a monosubstituted squaramide with a yield of 61% after purification by reverse-phase chromatography. The squaramide-based amphiphile with a Boc-protected amine at the OEG terminus was coupled to a second squaramide-based amphiphile with an internal C7-alkyl mono-Boc protected diamine chain and methoxy group at the OEG terminus on its periphery. The internal C7-alkyl mono-Boc protected diamine was deprotected under acidic conditions and then ligated to the squaramide-based amphiphiles with a Boc-protected amine under basic conditions with heating and purified by reverse-phase chromatography to yield the heterobifunctional squaramide-based bolaamphiphile in 36% yield. The sulfonated dyes were subsequently coupled to the squaramide-based bolaamphiphiles by Boc-deprotection of the terminal amine group and its reaction with the corresponding Sulfo-Cy3 or Sulfo-Cy5 NHS ester under basic conditions to yield **4** or **5** after HPLC, in a yield of 40-45%.

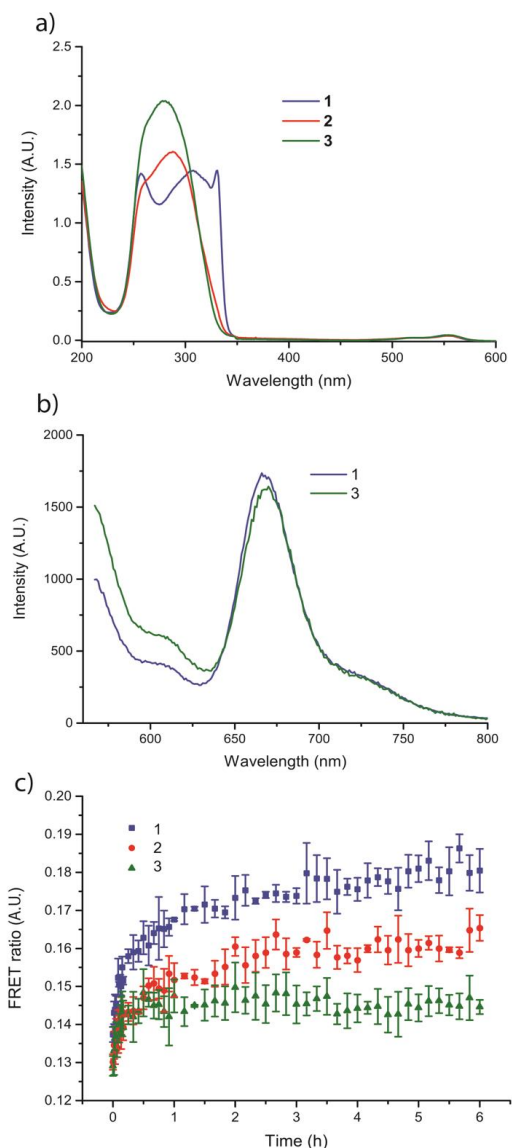


Figure 5.2. Spectroscopic studies of the self-assembled squaramide-based supramolecular polymer nanoparticles ($c = 30 \mu\text{M}$). (a) UV-Vis spectra of **1** (blue line), **2** (red line), and **3** (green line) co-assembled with **4** (2 mol%). (b) Static measurements of **1** and **3** with an equimolar amount of **4** and **5** (2 mol% total of the dye-labeled monomers); FRET signal observed at 670 nm (c) Dynamic measurements of **1**, **2** and **3** co-assembled with **4** or **5** (2 mol% of each dye labeled monomer) independently and then mixed together in an equimolar ratio. FRET ratios are compared over time (6 h) for **1** (blue line), **2** (red line), and **3** (green line).

The fluorescently-labeled supramolecular polymer nanoparticles were prepared through co-dissolution of native squaramide-based bolaamphiphile (**1**, **2** or **3**) co-assembled with the Sulfo-Cy3 or Sulfo-Cy5 dye labeled squaramide-based bolaamphiphile (**4** or **5**, 2 mol%) in DMSO at experiment-specific concentrations. The samples were then lyophilized, reconstituted in water at room temperature and left to stand 24 hours prior to subsequent measurements. This facile mix-and-match preparation protocol involving monomer co-assembly can be used to prepare a library of supramolecular polymer nanoparticles with various physicochemical properties for applications in drug delivery.

Using a combination of microscopic and spectroscopic techniques, we first examined the potential of using a single, fluorescently-labeled monomer **4** for tagging of self-assemblies **1-3** with identical hydrophobic core lengths, but distinctly sized hydrophilic domains. In cryo-TEM measurements, highly disperse, fibrillar objects on the order of 282 ± 85 nm in length with a diameter of 6 ± 1 nm were observed for the co-assembly of **1** and **4** (Figure 5.1b, and Figure S5.7). The co-assembly of monomer **2** and **4** displayed a mixture of sphere and rod-like aggregate structures, similar to self-assembly of **2** on its own, with a diameter of 6 ± 1 nm, and comparable to the co-assembly of monomers **1** and **4** (Figure 5.1b and Figure S5.9). Conversely, supramolecular polymer nanoparticles of **3** and **4** displayed spherical objects in solution with a diameter of 9 ± 2 nm (Figure 5.1b and Figure S5.10). Surprisingly, monomer **4** also self-assembled on its own at the concentration used for co-assembly with **1**, **2**, or **3**, forming fibrillar aggregates with a length of 387 ± 194 nm. Remarkably, these fibrillar structures are not observed when monomer **4** is co-assembled with compounds **2** or **3**, suggesting that the dye-labeled monomers are likely inserted into the various self-assemblies. Moreover, the measured dimensions of the supramolecular polymer nanoparticles with the dye-labeled monomers are on par with cryo-TEM measurements of the self-assembled native monomers **1**, **2**, and **3**, indicating that they are unaffected by the incorporation of the dye-labeled monomer.⁵³

UV-Vis spectroscopy measurements further supported the lack of disruption of the supramolecular polymer architecture at the molecular level upon co-assembly of **4** with the various native monomers (Figure 5.2a). Co-assembly of **1** and **4**, showed UV-Vis spectra comparable to native fibrillar self-assemblies of **1** with bands at 255 and 329 nm corresponding to the HOMO \rightarrow (LUMO+1) and HOMO \rightarrow LUMO transitions of the squaramide,⁴² respectively (Figure 5.1a, and Figures

S5.2 and S5.3). Similar spectral traces were recorded for molecules **2** with **4** and **3** with **4** at the same molar ratio, with a lesser degree of blue- and red-shifting of the HOMO \rightarrow (LUMO+1) and HOMO \rightarrow LUMO bands when compared against **1** with **4**. This result highlights a likely difference in packing of the squaramide-based monomers within the self-assembled structures with increasing oligo(ethylene glycol) length. The spectral data for **2** and **3** with **4** are on par with those obtained for the native monomers that showed a decrease or absence of the band at 329 nm and a shoulder at 255 nm, yet self-assembly was observed.⁵³ Collectively, these results suggest that introduction of the fluorescent monomer into the prepared supramolecular polymer nanoparticles do not interfere with self-assembly of the native monomer.

Fluorescence resonance energy transfer (FRET) measurements were used to study incorporation of dye-labeled monomers into the supramolecular polymer nanoparticles (static measurements) and the rate of monomer exchange between nanoparticles (dynamic measurements). Static measurements were performed to measure the co-localization of monomers labeled with a Sulfo-Cy3 dye (molecule **4**, FRET donor) and those with a Sulfo-Cy5 dye (molecule **5**, FRET acceptor) at 1 mol% each with native monomers **1** or **3**. The co-assembly of monomers **1** or **3** with **4** and **5** resulted in an intermediate degree of FRET efficiency in comparison to other supramolecular polymers^{27,54} by examining the acceptor emission at $\lambda_{em} \approx 670$ nm (Figure 5.2b) against the fluorescence intensity of the donor emission $\lambda_{em} \approx 570$ nm. However, a slightly higher degree of FRET efficiency was found for fibers of **1** in comparison to spherical aggregates of **3** and is consistent with their morphological differences. Overall, these results indicate that incorporation of both dye-labeled molecules into the supramolecular polymer nanoparticles occurs despite the distinct size of the hydrophobic domains presented by **1** or **3**.

Dynamic experiments were subsequently performed to understand the rate of monomer exchange between the supramolecular polymer nanoparticles. In these experiments, fluorescently-labeled supramolecular polymer nanoparticles were first prepared by the co-assembly of the native monomers **1**, **2** or **3** with 2 mol% of **4** or **5**. Subsequently, the distinctly labeled fluorescent nanoparticles with Sulfo-Cy3 or Sulfo-Cy5 were mixed and monomer co-localization within the fibers was measured by the evolution in FRET intensity over time. Monomer exchange between assemblies of **1**, **2** or **3** with **4** (Sulfo-Cy3) and assemblies (**1**, **2** or **3**) labeled with reporter molecule **5** (Sulfo-Cy5) were observed with different kinetic

profiles. Assemblies of **3** appeared to reach a plateau after 1 hour suggesting that the sample attained an equilibrium state in its exchange, whereas for **1** a plateau was still not reached after 6 hours. (Figure 5.2c) Qualitatively, the curves show a faster exchange of monomers in the case of the spherical aggregates (*green line*) composed of **3** compared to the fibrillar objects composed of **1** (*blue line*) (Figure 5.1c). However, in all cases the significantly lower FRET ratios observed in dynamic compared to the static measurements suggest that slow dynamics or a partial exchange of monomers⁵⁵ occurs within the fibers, but FRET experiments show the effective labeling of the supramolecular polymer nanoparticles by the Sulfo-Cy monomers.

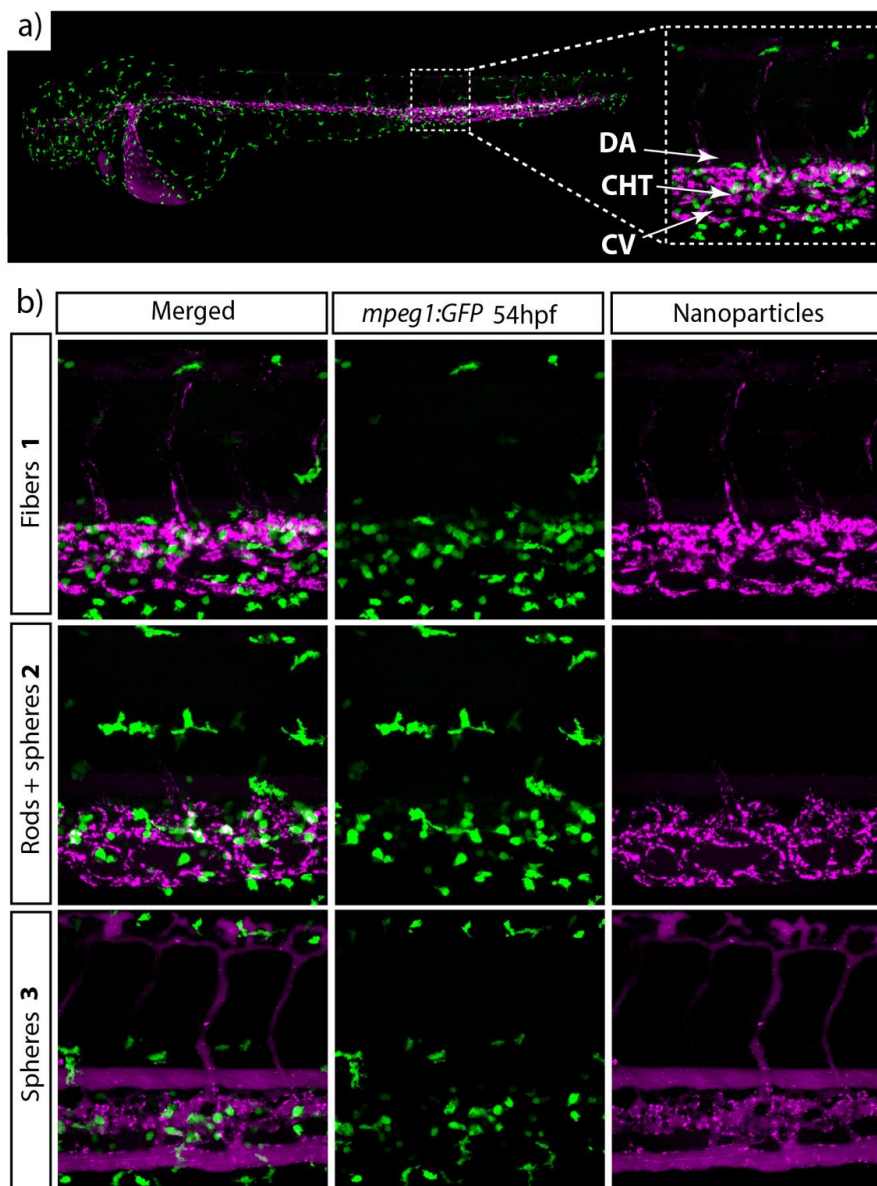


Figure 3. Colocalization studies of the fluorescently-labeled squaramide-based supramolecular polymer nanoparticles with macrophages in the zebrafish. a) Whole-embryo view after 1 hour injection in the Duct of Cuvier of **1** ($c = 2 \text{ mM}$) co-assembled with **4** (2 mol%) in an embryonic zebrafish (*mpeg1:GFP*) at 54 hpf. In the boxed region, a zoom in of the caudal vein showing the dorsal aorta (DA), caudal hematopoietic tissue (CHT) and the caudal veins (CV). b) Fluorescently-labeled squaramide-based supramolecular polymer nanoparticles 1 hour post-injection in a transgenic zebrafish co-expressing GFP in macrophages. On the left panel, schematic representation of **1** (top), **2** (middle) and **3** (bottom) ($c = 2 \text{ mM}$) with **4** (2 mol%). On the right panel, images of the CV area showing the in vivo distribution of each fluorescently-labeled squaramide-based supramolecular polymer nanoparticle tested.

Because the sulfonated-cyanine dyes used to fluorescently tag and track the supramolecular polymer nanoparticles bear a -1 formal charge, ζ -potential measurements were performed to estimate their surface charge in water. Negative ζ -potential values of -32.1 ± 7.1 mV were recorded for **4** that showed a fibrillar morphology ($c = 40 \mu\text{M}$) in cryo-TEM measurements on its own and used at this concentration for co-assembly experiments. Conversely, the co-assembly of native monomers **1**, **2**, or **3** with **4** (2 mol%), resulted in near-neutral ζ -potential values of -4.9 ± 5.2 mV, -12.3 ± 4.7 mV and -11.1 ± 4.5 mV, respectively. As a control, the native monomer **1** ($c = 2$ mM) on its own showed similar ζ -potential values of -7.32 ± 5.5 mV and thus indicated that its co-assembly with monomer **4** was comparable in surface charge from the native self-assembled constructs. Hence, all investigated supramolecular polymer nanoparticles co-assembled with an anionic dye-labeled monomer were near-neutral in surface charge in comparison to **4** on its own that was negative.

Cumulatively, we demonstrate the co-assembly between a single sulfonated-cyanine (3 or 5) labeled fluorescent bolaamphiphile (**4**) and various squaramide-based bolaamphiphiles of increasing OEG hydrophilic side chain lengths (**1**, $n = 11$; **2**, $n = 24$; and **3**, $n = 36$) to prepare fluorescently tagged supramolecular polymer nanoparticle self-assemblies. This mix-and-match strategy considerably reduces the synthetic effort to obtain libraries of functional assemblies by using a single cargo-loaded molecule that co-assembles with a variety of monomers.

***In vivo* evaluation of squaramide-based supramolecular polymer nanoparticles.**

To establish the squaramide-based nanoparticles as potential drug carriers *in vivo*, zebrafish embryos were used between 52-56 hpf (hours post-injection). At this stage, blood circulation is robust and most organs, including liver and kidney have emerged. The stability of the supramolecular polymer nanoparticles was first assessed in biological media by monitoring their morphology in the presence of increasing concentration of carp serum (CS) concentration. Carp serum was used as the closest practical approximation to zebrafish serum. Diluted concentrations of CS, ranging from 1 to 25 v/v%, were probed to enable differentiation of the supramolecular polymer nanoparticles from the high background imposed by the serum components in cryo-TEM (Figure S5.7) measurements. Even in the presence of increasing CS concentrations, the supramolecular polymer nanoparticles consisting of **1** and **4** retained their respective morphologies and sizes relative to

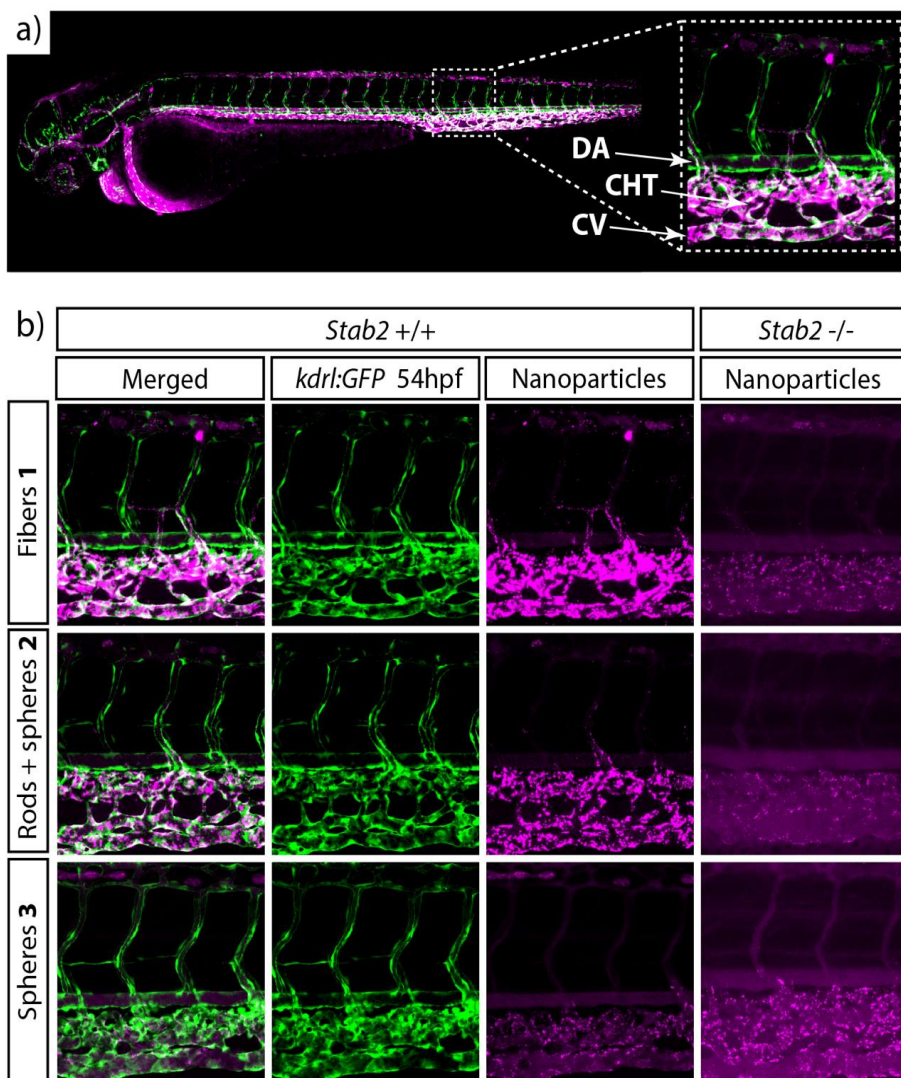


Figure 5.4. Biodistribution of the fluorescently-labeled squaramide-based supramolecular polymer nanoparticles in the zebrafish. a) Whole-embryo view 1 hour post-injection in the Duct of Cuvier of **1** ($c = 2$ mM) with **4** (2 mol%) in an embryonic zebrafish (*kdr1*:GFP) at 54 hpf. In the boxed region, the caudal vein showing the dorsal aorta (DA), caudal hematopoietic tissue (CHT) and the caudal veins (CV), zoomed in. b) Biodistribution of the three different fluorescently-labeled squaramide-based supramolecular polymer nanoparticles 1 hour post-injection. On the left panel, schematic representation of **1** (top) **2** (middle) and **3** (bottom) ($c = 2$ mM) with **4** (2 mol%). On the right panel, images of the CV area showing the distribution of each fluorescently-labeled squaramide-based supramolecular polymer nanoparticles. c) Biodistribution of **1** (top) **2** (middle) and **3** (bottom) ($c = 2$ mM) with **4** (2 mol%) in the zebrafish embryos lacking the *stab2* receptor (*stab2*^{-/-}).

self-assemblies of the native monomer **1** (around several hundreds of nanometers in fiber length and a width between 5-6 nm by cryo-TEM), indicating that the serum components do not affect the formed co-assemblies (see Figure S5.11-S5.14). This result can be expected due to the high density of oligo(ethylene glycol)s on the periphery of the supramolecular polymer nanoparticles and the known use of such polymers to increase circulation time by reducing the interaction of nanoparticles with blood proteins.⁵⁶⁻⁵⁸ However, samples of **2** or **3** with carp serum solutions of varied concentration could not be discriminated from the serum background due to their similar size and contrast.

Zebrafish embryos were first used to study macrophage uptake, since it is well established that this cell type plays an important role processing nanoparticles in an *in vivo* environment often hindering drug delivery through particle clearance.^{13,41,59} Thus, transgenic zebrafish *Tg(mpeg:EGFP)^{gl22}* embryos in which GFP is expressed in macrophages were used, where colocalization indicates uptake of or binding to macrophages of the squaramide-based supramolecular polymer nanoparticles after intravenous injection. Remarkably, no significant colocalization of the supramolecular polymer nanoparticles and macrophages in the injected zebrafish was observed. This result can be explained by the dense presentation of oligo(ethylene glycol)s (MW ranging from 517 to 1617 Da) on the nanoparticle surface that may decrease protein absorption (Figure 5.3 and Figure S5.16). Hence, low protein absorption results in the evasion of macrophages by the squaramide-based supramolecular polymer nanoparticles.

Still, most of the supramolecular assemblies were rapidly removed from circulation (Figure 5.4). Most strikingly, the elongated fibrillar objects composed of the co-assembly of **1** and **4** showed limited free circulation with a preference for accumulation in a subset of venous endothelial cells (Figure 5.4a, 5.4b and Figure S5.15). Recently, we have shown that these cells in the zebrafish embryo are functionally homologous to the liver sinusoidal endothelial cells in mammals. In both zebrafish and mammals, these cells are specialized in endocytosis of macromolecular and nanoparticulate waste from circulation. Within these cells, the transmembrane scavenger receptor Stabilin-2 (*stab2*) plays a major role in mediating nanoparticle uptake from circulation.^{13,60,61}

When we analyzed the nanoparticle distribution of the co-assembled supramolecular polymer nanoparticles composed of **1** and **4** in embryos lacking

the *stab2* receptor (*stab2*^{-/-}), their uptake by scavenger endothelial cells was largely abrogated. Similar results were observed for supramolecular polymer nanoparticles consisting of **2** and **4**, although this structure already displayed reduced uptake and increased circulation time relative to a co-assembly of **1** and **4** in control embryos. Interestingly, for the co-assembly of **3** and **4** only a slight accumulation in scavenger endothelial cells was observed in the knockout embryos, and uptake therefore appeared independent of *stab2* function (Figure 5.4b). Taken together, these results show that *stab2*-mediated nanoparticle uptake by scavenger endothelial cells is highly influenced by nanoparticle shape and/or size. Previously, shape-dependent circulation and distribution were reported for several nanoparticles,^{6,35} but were mainly ascribed to differences in their hydrodynamic properties. By simultaneously exploiting the fluorescent labeling of the squaramide-based supramolecular polymer nanoparticles and the transparency of the zebrafish embryo model, we explore a mechanism for uptake of supramolecular polymer nanoparticles and show a major role for the sinusoidal scavenger receptor *stab2* that can be found analogously in the mammalian liver. This study shows for the first time the potential to track various supramolecular polymer architectures within the zebrafish embryo model to gain understanding of the molecular mechanisms governing the clearance of the nanoparticulate carriers of varied size and shape by liver sinusoidal endothelial cells.

5.4 Conclusions

In conclusion, a mix-and-match approach was used between native squaramide-based bolaamphiphiles of increasing hydrophilic chain lengths and a single asymmetrically-labeled fluorescent bolaamphiphile to prepare fluorescently tagged supramolecular polymer nanoparticles of distinct size and shape for their visual tracking *in vivo* in a zebrafish embryo model. These supramolecular polymer nanoparticles retained their shape and size after co-assembly with the fluorescent monomer in comparison to their native monomers, showed dynamic monomer exchange in FRET experiments, had near-neutral surface charge, and remained self-assembled in the presence of complex biological media such as carp serum. Additionally, the unique *in vivo* biodistribution of these variable aspect ratio squaramide-based supramolecular polymer nanoparticles were demonstrated in zebrafish embryos. Fibrillar morphologies displayed a low circulation time with rapid venous attachment, whereas spherical morphologies demonstrated significantly greater mobility with longer circulation times and improved distribution over the zebrafish. These observations were rationalized by the

clearance of the particles by the scavenger endothelial cells through interaction with stabilin-2. Additionally, it was found that these supramolecular polymer nanoparticles also evaded macrophages. These results demonstrated that the nanocarrier shape and size, even at very high aspect ratios, plays an important role in nanoparticle clearance by scavenger endothelial cells through the Stabilin-2 receptor. The *in vivo* biodistribution behavior could be readily visualized in a zebrafish embryo model for the first time by simple fluorescent tagging using a co-assembly approach of functional monomers providing a synthetically efficient approach. It is anticipated that by understanding the *in vivo* routing of such fibrillar nanoparticles at the cellular level new chemical and/or biological strategies can be developed to improve payload delivery to a particular target.

5.5 References

- (1) Nel, A. E.; Mädler, L.; Velegol, D.; Xia, T.; Hoek, E. M. V.; Somasundaran, P.; Klaessig, F.; Castranova, V.; Thompson, M. *Nat. Mater.* **2009**, *8* (7), 543–557.
- (2) Bao, G.; Bazilevs, Y.; Chung, J.-H.; Decuzzi, P.; Espinosa, H. D.; Ferrari, M.; Gao, H.; Hossain, S. S.; Hughes, T. J. R.; Kamm, R. D.; Liu, W. K.; Marsden, A.; Schrefler, B. *J. R. Soc. Interface* **2014**, *11* (97), 20140301.
- (3) Bozzuto, G.; Molinari, A. *Int. J. Nanomedicine* **2015**, *10*, 975–999.
- (4) Simone, E. A.; Dziubla, T. D.; Muzykantov, V. R. *Expert Opin. Drug Deliv.* **2008**, *5* (12), 1283–1300.
- (5) Webber, M. J.; Langer, R. *Chem. Soc. Rev.* **2017**, *46*, 6600–6620.
- (6) Kinnear, C.; Moore, T. L.; Rodriguez-Lorenzo, L.; Rothen-Rutishauser, B.; Petri-Fink, A. *Chem. Rev.* **2017**, *117* (17), 11476–11521.
- (7) Wilhelm, S.; Tavares, A. J.; Dai, Q.; Ohta, S.; Audet, J.; Dvorak, H. F.; Chan, W. C. W. *Nat. Rev. Mater.* **2016**, *1* (5), 16014.
- (8) Wicki, A.; Witzigmann, D.; Balasubramanian, V.; Huwyler, J. *J. Control. Release* **2015**, *200*, 138–157.
- (9) Petros, R. A.; DeSimone, J. M. *Nat. Rev. Drug Discov.* **2010**, *9* (8), 615–627.
- (10) Lee, K. Y.; Jang, G. H.; Byun, C. H.; Jeun, M.; Searson, P. C.; Lee, K. H. *Biosci. Rep.* **2017**, *37* (3), BSR20170199.

Chapter 5

- (11) Chakraborty, C.; Sharma, A. R.; Sharma, G.; Lee, S.-S. *J. Nanobiotechnology* **2016**, *14* (1), 65.
- (12) Santoriello, C.; Zon, L. I. *J. Clin. Invest.* **2012**, *122* (7), 2337–2343.
- (13) Campbell, F.; Bos, F. L.; Sieber, S.; Arias-Alpizar, G.; Koch, B. E.; Huwyler, J.; Kros, A.; Busmann, J. *ACS Nano* **2018**, *12* (3), 2138–2150.
- (14) Krieg, E.; Bastings, M. M. C.; Besenius, P.; Rybtchinski, B. *Chem. Rev.* **2016**, *16*, 2414–2477.
- (15) Boekhoven, J.; Stupp, S. I. *Adv. Mater.* **2014**, *26* (11), 1642–1659.
- (16) Aida, T.; Meijer, E. W.; Stupp, S. I. *Science* **2012**, *335* (6070), 813–817.
- (17) Webber, M. J.; Appel, E. A.; Meijer, E. W.; Langer, R. *Nat. Mater.* **2015**, *15* (1), 13–26.
- (18) Appel, E. A.; del Barrio, J.; Loh, X. J.; Scherman, O. A. *Chem. Soc. Rev.* **2012**, *41* (18), 6195–6214.
- (19) Leenders, C. M. A.; Baker, M. B.; Pijpers, I. A. B.; Lafleur, R. P. M.; Albertazzi, L.; Palmans, A. R. A.; Meijer, E. W. *Soft Matter* **2016**, *12* (11), 2887–2893.
- (20) Busseron, E.; Ruff, Y.; Moulin, E.; Giuseppone, N. *Nanoscale* **2013**, *5* (16), 7098.
- (21) Fernandez-Castano Romera, M.; Lafleur, R. P. M.; Guibert, C.; Voets, I. K.; Storm, C.; Sijbesma, R. P. *Angew. Chemie - Int. Ed.* **2017**, *56* (30), 8771–8775.
- (22) Bakker, M. H.; Lee, C. C.; Meijer, E. W.; Dankers, P. Y. W.; Albertazzi, L. *ACS Nano* **2016**, *10* (2), 1845–1852.
- (23) Soukasene, S.; Toft, D. J.; Moyer, T. J.; Lu, H.; Lee, H. K.; Standley, S. M.; Cryns, V. L.; Stupp, S. I. *ACS Nano* **2011**, *5* (11), 9113–9121.
- (24) Straßburger, D.; Stergiou, N.; Urschbach, M.; Yurugi, H.; Spitzer, D.; Schollmeyer, D.; Schmitt, E.; Besenius, P. *ChemBioChem* **2018**, 10–15.
- (25) Su, H.; Koo, J. M.; Cui, H. *J. Control. Release* **2015**, *219*, 383–395.
- (26) Shamay, Y.; Shah, J.; Işık, M.; Mizrachi, A.; Leibold, J.; Tschaharganeh, D. F.; Roxbury, D.; Budhathoki-Uprety, J.; Nawaly, K.; Sugarman, J. L.; Baut, E.; Neiman, M. R.; Dacek, M.; Ganesh, K. S.; Johnson, D. C.; Sridharan, R.; Chu,

- K. L.; Rajasekhar, V. K.; Lowe, S. W.; Chodera, J. D.; Heller, D. A. *Nat. Mater.* **2018**, *17* (4), 361–368.
- (27) Rho, J. Y.; Brendel, J. C.; Macfarlane, L. R.; Mansfield, E. D. H.; Peltier, R.; Rogers, S.; Hartlieb, M.; Perrier, S. *Adv. Funct. Mater.* **2017**, *1704569*, 1–11.
- (28) Hinde, E.; Thammasiraphop, K.; Duong, H. T. T.; Yeow, J.; Karagoz, B.; Boyer, C.; Gooding, J. J. and Katharina Gaus, K. *Nat. Nanot.* **2017**, *12*, 81–91.
- (29) Liu, J.; Liu, J.; Chu, L.; Zhang, Y.; Xu, H.; Kong, D.; Yang, Z.; Yang, C.; Ding, D. *ACS Appl. Mater. Interfaces* **2014**, *6* (8), 5558–5565.
- (30) Webber, M. J.; Matson, J. B.; Tamboli, V. K.; Stupp, S. I. *Biomaterials* **2012**, *33* (28), 6823–6832.
- (31) Toft, D. J.; Moyer, T. J.; Standley, S. M.; Ruff, Y.; Ugolkov, A.; Stupp, S. I.; Cryns, V. L. *ACS Nano* **2012**, *6* (9), 7956–7965.
- (32) Dhandhukia, J. P.; Shi, P.; Peddi, S.; Li, Z.; Aluri, S.; Ju, Y.; Brill, D.; Wang, W.; Janib, S. M.; Lin, Y. A.; Liu, S.; Cui, H.; Mackay, J. A. *Bioconjug. Chem.* **2017**, *28* (11), 2715–2728.
- (33) Moyer, T. J.; Kassam, H. A.; Bahnson, E. S. M.; Morgan, C. E.; Tantakitti, F., Chew, T. L., Kibbe, T. L. and Stupp, S. I. *Small* **2015**, *11* (23), 2750–2755.
- (34) Bahnson, E. S. M.; Kassam, H. A.; Moyer, T.J.; Jiang, W.; Morgan, C. E.; Vercammen, J. M.; Jiang, Q.; Flynn, M. E.; Stupp, S. I. and Kibbe, M. R. *Antiox. and redox sign.* **2016**, *24* (8), 401–418.
- (35) Geng, Y.; Dalhaimer, P.; Cai, S.; Tsai, R.; Tewari, M.; Minko, T.; Discher, D. E. *Nat. Nanotechnol.* **2007**, *2* (4), 249–255.
- (36) Morgan, C.E.; Dombrowski, A.W.; Rubert Pérez, C.M.; Bahnson, E.S.; Tsihlis, N.D.; Jiang, W.; Jiang, Q.; Vercammen, J.M.; Prakash, V.S.; Pritts, T.A.; Stupp, S.I.; Kibbe, M.R. *ACS Nano*. **2016**, *10*, (1), 899–909.
- (37) Yang, C.; Chu, L.; Zhang, Y.; Shi, Y.; Liu, J.; Liu, Q.; Fan, S.; Yang, Z.; Ding, D.; Kong, D.; Liu, J. *ACS Appl. Mater. Interfaces* **2015**, *7* (4), 2735–2744.
- (38) Zhang, S.; Zheng, Y.; Fu, D.; Li, W. Wu, Y. Li, B. and Wua, L. *J. Mater. Chem. B*, **2017**, *5*, 4035–4043.
- (39) Chen, D. and Sun J. *Polym. Chem.*, **2015**, *6*, 998–1004
- (40) Zhou, Z.; Xinpeng, M., Jin, E., Tang, J.; Sui, M.; Shen, Y.; Van Kirk, E. A.;

- Murdoch, W. J. and Radosz, M. *Biomaterials* **2013**, *34*, 5722-5735.
- (41) Tsoi, K. M.; Macparland, S. A.; Ma, X. Z.; Spetzler, V. N.; Echeverri, J.; Ouyang, B.; Fadel, S. M.; Sykes, E. A.; Goldaracena, N.; Kathis, J. M.; Conneely, J. B.; Alman, B. A.; Selzner, M.; Ostrowski, M. A.; Adeyi, O. A.; Zilman, A.; McGilvray, I. D.; Chan, W. C. W. *Nat. Mater.* **2016**, *15* (11), 1212–1221.
- (42) Saez Talens, V.; Englebienne, P.; Trinh, T. T.; Noteborn, W. E. M.; Voets, I. K.; Kieltyka, R. E. *Angew. Chemie - Int. Ed.* **2015**, *54* (36), 10502–10506.
- (43) Noteborn, W. E. M.; Saez Talens, V.; Kieltyka, R. E. *ChemBioChem* **2017**, 1995–1999.
- (44) Ian Storer, R.; Aciro, C.; Jones, L. H. *Chem. Soc. Rev.* **2011**, *40* (5), 2330.
- (45) Quiñonero, D.; Frontera, A.; Ballester, P.; Deyà, P. M. *Tetrahedron Lett.* **2000**, *41* (12), 2001–2005.
- (46) Quiñonero, D.; Prohens, R.; Garau, C.; Frontera, A.; Ballester, P.; Costa, A.; Deyà, P. M. *Chem. Phys. Lett.* **2002**, *351* (1–2), 115–120.
- (47) Ribeiro, C. J. A.; Espadinha, M.; Machado, M.; Gut, J.; Gonçalves, L. M.; Rosenthal, P. J.; Prudêncio, M.; Moreira, R.; Santos, M. M. M. *Bioorganic Med. Chem.* **2016**, *24* (8), 1786–1792.
- (48) Olmo, F.; Rotger, C.; Ramírez-Macías, I.; Martínez, L.; Marín, C.; Carreras, L.; Urbanová, K.; Vega, M.; Chaves-Lemaur, G.; Sampedro, A.; Rosales, M. J.; Sánchez-Moreno, M.; Costa, A. *J. Med. Chem.* **2014**, *57* (3), 987–999.
- (49) Malerich, J. P.; Hagihara, K.; Rawal, V. H. *J. Am. Chem. Soc.* **2008**, *130* (44), 14416–14417.
- (50) Konishi, H.; Lam, T. Y.; Malerich, J. P.; Rawal, V. H. *Org. Lett.* **2010**, *12* (9), 2028–2031.
- (51) Martínez, L.; Martorell, G.; Sampedro, Á.; Ballester, P.; Costa, A.; Rotger, C. *Org. Lett.* **2015**, *17* (12), 2980–2983.
- (52) Owen, R. M.; Carlson, C. B.; Xu, J.; Mowery, P.; Fasella, E.; Kiessling, L. L. *ChemBioChem* **2007**, *8* (1), 68–82.
- (53) Saez Talens, V.; Makurat, D. M. M.; Liu, T.; Noteborn, W. E. M.; Dai, W.; Guibert, C. L.; Voets, I. K.; Kieltyka, R. E. *Manuscr. Prep.*

- (54) Baker, M. B.; Gosens, R. P. J.; Albertazzi, L.; Matsumoto, N. M.; Palmans, A. R. A.; Meijer, E. W. *ChemBioChem* **2016**, *17* (3), 207–213.
- (55) da Silva, R. M. P.; van der Zwaag, D.; Albertazzi, L.; Lee, S. S.; Meijer, E. W.; Stupp, S. I. *Nat. Commun.* **2016**, *7*, 10.1038/ncomms11561.
- (56) Knop, K.; Hoogenboom, R.; Fischer, D.; Schubert, U. S. *Angew. Chemie - Int. Ed.* **2010**, *49* (36), 6288–6308.
- (57) Owens, D. E.; Peppas, N. A. *Int. J. Pharm.* **2006**, *307* (1), 93–102.
- (58) Perry, J. L.; Reuter, K. G.; Kai, M. P.; Herlihy, K. P.; Jones, S. W.; Luft, J. C.; Napier, M.; Bear, J. E.; Desimone, J. M. *Nano Lett.* **2012**, *12* (10), 5304–5310.
- (59) Bertrand, N.; Leroux, J. C. *J. Control. Release* **2012**, *161* (2), 152–163.
- (60) Alidori, S.; Bowman, R. L.; Yarin, D.; Romin, Y.; Barlas, A.; Mulvey, J. J.; Fujisawa, S.; Xu, K.; Ruggiero, A.; Riabov, V.; Thorek, D. L. J.; Ulmert, H. D. S.; Brea, E. J.; Behling, K.; Kzhyshkowska, J.; Manova-Todorova, K.; Scheinberg, D. A.; McDevitt, M. R. *Nat. Commun.* **2016**, *7*, 1–11.
- (61) Miller, C. M.; Donner, A. J.; Blank, E. E.; Egger, A. W.; Kellar, B. M.; Østergaard, M. E.; Seth, P. P.; Harris, E. N. *Nucleic Acids Res.* **2016**, *44* (6), 2782–2794.

5.6 Supporting Information

5.6.1 Materials and methods

All reagents and chemicals were purchased from commercial sources and used without further purification. Sulfo-Cy3 and Sulfo-Cy5 dyes were obtained from Lumiprobe, while oligo(ethylene glycols) of various chain lengths ($n = 11, 24, 36$) were purchased from Broadpharm. Monomers **1**, **2** and **3** were synthesized as previously reported.⁵³ The synthetic protocol for the Sulfo-Cy3 and Sulfo-Cy5 squaramide-based bolaamphiphiles **4** and **5**, respectively, can be found in the Supporting Information. MilliQ water was used for all experiments. ζ -potential measurements were performed on a Zetasizer Nano ZS (Malvern). UV-Vis measurements were carried out on a Cary 300 UV-Vis spectrophotometer using a quartz cuvette with a path length of 1 cm. Fluorescence experiments were executed on an Infinite M1000 Pro Tecan plate reader using 96-well plate with a black background.

Preparation protocol of co-assembled sulfonated cyanine-labeled squaramide-based supramolecular polymer nanoparticles. Stock solutions of **1**, **2** or **3** were prepared at a concentration of 5.8 mM in DMSO, while stock solutions of **4** or **5** were prepared at a concentration of 0.2 mM in the same solvent. The native (**1**, **2** or **3**) and dye-labeled monomers (**4** or **5**) were mixed in a glass vial at the appropriate mol ratios (1 or 2 mol%). The solvent was lyophilized and the bolaamphiphile mixture was reconstituted in water at the desired concentration. The resulting clear solutions were left to stand for 24 hours prior to any measurement.

Cryogenic transmission electron microscopy (Cryo-TEM). Samples in water consisting of **1**, **2** or **3** ($c = 2$ mM) co-assembled with reporter molecule **4** (2 mol%), were prepared according to the co-assembly protocol above. The samples were left to stand for 24 hours before deposition on a glow discharged grid. Samples of **1** co-assembled with **4** (2 mol%) with increasing concentration of carp serum were prepared following a similar protocol. Instead of adding fresh water after removal of DMSO by lyophilization, a freshly prepared carp serum solution in water was added in the desired v/v% (ranging from 1 to 25 v/v%) to provide a final concentration of 2 mM of the fluorescently-labeled supramolecular polymer nanoparticle and left to stand 24 hours before deposition on a glow discharged grid. Cryo-TEM samples were prepared by depositing the sample (3 μ L) on a glow

discharged Lacey Carbon Film (300 mesh Cu grids). The excess sample was removed by blotting for 1 second at room temperature with 95 % humidity (Whatman No.4 filter paper) and the resulting films were vitrified at -183 °C using a Leica EMGP. Imaging of the samples was recorded with a Tecnai F20 FEG (FEI), equipped with a field emission gun at 200 kEV using a Gatan UltraScan camera with a defocus between -3 and -10 μm .

UV-Vis spectroscopy. UV-Vis samples in water consisting of **1**, **2** or **3** ($c = 30 \mu\text{M}$) co-assembled with **4** (2 mol%) were prepared according to the co-assembly protocol described above. The samples were left to stand for 24 hours before UV-Vis measurements.

Fluorescence spectroscopy (FRET measurements). The dye-labeled supramolecular polymers nanoparticles were prepared according to the co-assembly protocol mixing **1**, **2** or **3** ($c = 30 \mu\text{M}$) with **4** and/or **5** in different concentrations depending on the experiment. For static measurements: **4** and **5** (300 nM each) were mixed together in an equimolar ratio with native monomer (**1** or **3**) to obtain a total of 2 mol% of the fluorescently-labeled molecules in DMSO prior to lyophilization. After the reconstituted samples in water were left to stand overnight, they were loaded in a fluorimeter and excited at 550 nm (Sulfo-Cy3) and their fluorescence emission was measured from 570 to 800 nm (Sulfo-Cy5) at room temperature. Samples were measured in triplicate. For dynamic measurements: **4** or **5** (600 nM each) were mixed individually with the native monomer (**1**, **2** or **3**) to obtain mixtures of 2 mol% of the fluorescently-labeled molecule in DMSO prior to lyophilization. The equilibrated samples of the Sulfo-Cy3 and Sulfo-Cy5-labeled squaramide-based supramolecular polymer nanoparticles were mixed in a 1:1 ratio (100 μL each) in a 96-well plate by pipetting (2–3 x) with the acquisition of fluorescence data immediately after mixing at room temperature using excitation at 550 nm (Sulfo-Cy3) and measuring fluorescence emission from 570 to 800 nm (Sulfo-Cy5). The FRET ratio is the relative fluorescence intensity of the peaks at 670/570 nm. Experiments were run in triplicate to ensure reproducibility. Raw fluorescence data is provided in Figures S5.4 and S5.5 in the Supplementary Information.

ζ -potential measurements. Samples for electrophoretic mobility experiments were prepared from **1** or **1**, **2** or **3** ($c = 2 \text{ mM}$) co-assembled with **4** (2 mol%) as outlined in the co-assembly protocol above. The samples were then transferred to

a reusable ζ -potential dip cell prior to measurement. The samples were left to stand for 24 hours before ζ -potential measurements.

Zebrafish husbandry and injections. Zebrafish (*Danio rerio*) were maintained and handled according to the guidelines from the Zebrafish Model Organism Database (<http://zfin.org>) and in compliance with the directives of the local animal welfare committee of Leiden University. Transgenic *Tg(kdrl:EGFP)^{s843}*,¹³ *Tg(mpeg:EGFP)^{g122}*¹³ and *stab2^{ib12}* zebrafish¹³ were used. Fertilization was performed by natural spawning at the beginning of the light period and eggs were collected and raised at 28.5 °C in egg water (60 μ g/mL Instant Ocean sea salts). Pigment cell formation was suppressed by adding 1-phenyl-2-thiourea (PTU) to the egg water in 1-day old zebrafish (24-28 hpf).

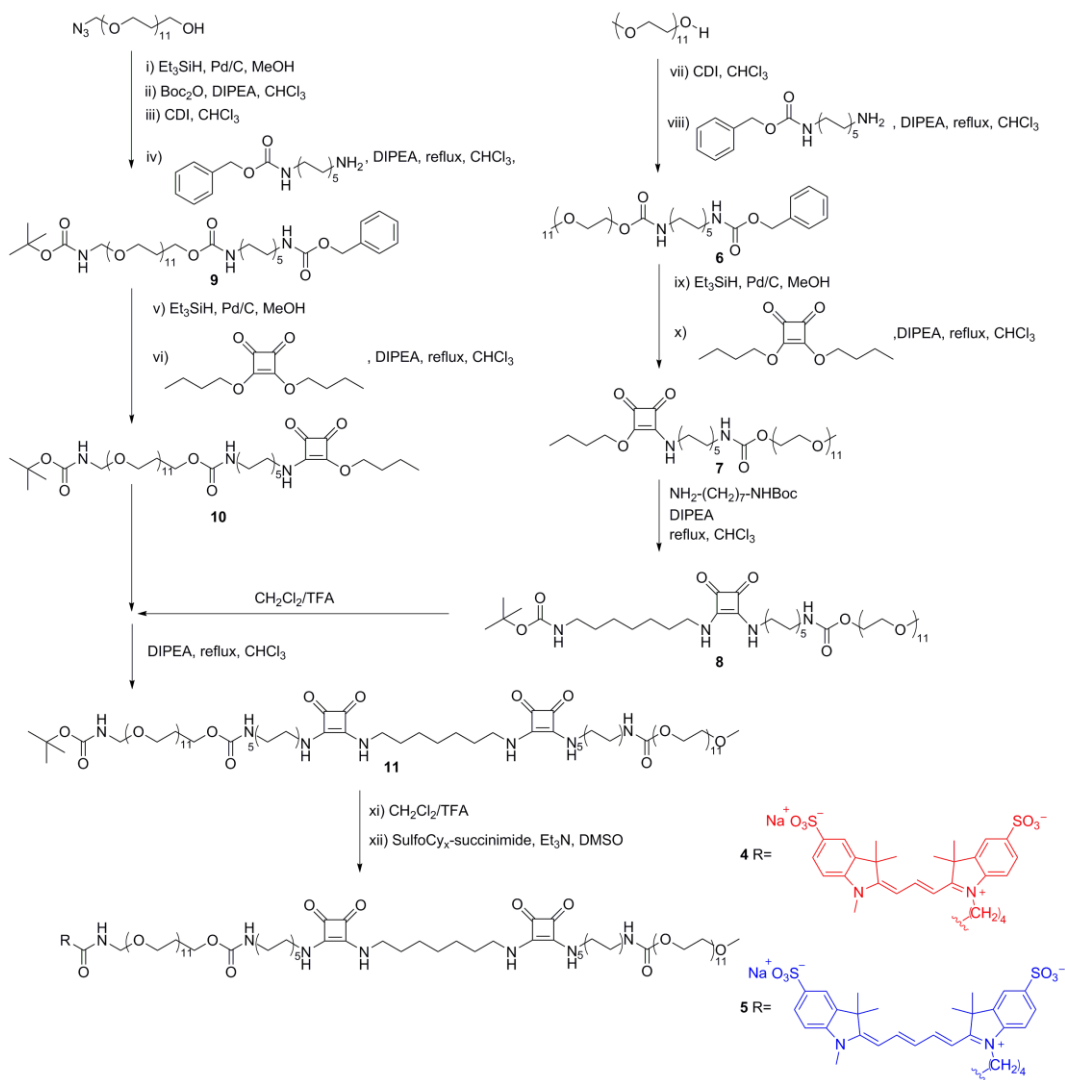
Fluorescently-labeled squaramide-based supramolecular polymer nanoparticles were injected into 2-day old zebrafish embryos (52-56 hpf) using a modified microangiography protocol described previously.¹³ Embryos were anesthetized in 0.01% tricaine and embedded in 0.4% agarose containing tricaine before injection. Calibrated 1 nL volumes of squaramide-based supramolecular polymer nanoparticles consisting of native monomer **1**, **2** or **3** (c = 2 mM) co-assembled with **4** (2 mol%) were injected with a microneedle into the Duct of Cuvier. Successfully injected embryos were identified (damaged-yolk ball embryo excluded) and imaged using a Leica TCS SPE confocal microscope. Confocal micrographs (Z-stacks) for the whole embryo were generated using the 10x air objective (HCX PL FLUOTAR) and overlapping 3 images to cover the complete embryo, or a caudal vein by using 40x water-immersion objective (HCX APO L) to compare distribution of injected molecules. Images were processed using the Fiji, Image J Software and brightness/contrast adjusted.

5.6.2 Characterization methods

The reaction intermediates obtained in the synthesis of the squaramide-based bolaamphiphiles were purified using a Grace Reveleris X1 flash chromatography system equipped with a C18 column, while the final sulfonated cyanine-labeled squaramide-based bolaamphiphiles (**4** and **5**) were purified by RP-HPLC with a Vydac C18 reversed phase column. ¹H NMR and ¹³C NMR spectra were acquired on a Bruker AV-III-600 MHz at 298K. LC-MS analysis was performed with a TSQ Quantum Access MAX system equipped with a Gemini 3 μ m C18 110 Å 50×4.60 mm column (UV detection at 214 nm and 254 nm).

5.6.3 Synthetic route

The synthetic procedure for the sulfonated cyanine-labeled squaramide-based bolaamphiphiles is shown below. Squaramide-based bolaamphiphiles **1**, **2** and **3**, and intermediates **6** and **7** were reported elsewhere.¹



Scheme S5.1. Synthetic route for sulfonated cyanine-labeled monomers **4** and **5**.

Synthesis of 8

N-Boc-1,7-diaminoheptane (41.4 mg, 0.18 mmol) (synthesis reported elsewhere²) was added to a stirred mixture of **7** (106.0 mg, 0.12 mmol) and DIPEA (105.0 μ L, 0.60mmol) in CHCl_3 (10 mL) refluxed overnight. The resulting compound was purified by reversed-phase C18 silica column using a gradient of 10-90% $\text{CH}_3\text{CN}/\text{H}_2\text{O}$ over 45 minutes. The product was concentrated by evaporation and lyophilized to obtain a white solid.

Yield: 70.1 mg, 56.0% ¹H-NMR (δ_{H} [ppm], CDCl_3 , 600 MHz): 7.46 (br s, 1H), 5.09 (br s, 1H), 4.83 (br s, 1H), 4.20-4.19 (m, 2H), 3.84-3.65 (m, 44H), 3.56-3.52 (m, 2H), 3.38 (s, 3H), 3.15-3.06 (m, 4H), 1.64-1.17 (m, 35H). ¹³C-NMR (δ_{C} [ppm], CDCl_3 , 150 MHz): 183.43, 183.40, 169.02, 168.98, 157.58, 157.54, 80.10, 72.90, 72.82, 71.56, 71.53, 71.52, 71.49, 71.27, 70.99, 70.65, 64.81, 45.79, 45.60, 45.53, 42.04, 41.47, 32.19, 31.99, 30.94, 30.53, 30.46, 30.44, 30.31, 30.25, 30.23, 29.83, 29.47, 27.71, 27.58, 27.47, 27.37. LC-MS: t = 6.67 min, m/z: 922.80 [M+H-Boc]⁺.

Synthesis of 9

O-(2-Azidoethyl)undecaethylene glycol (0.6 g, 1.05 mmol) was dissolved in 5 mL MeOH and Pd/C (55.0 mg, 0.52 mmol) was added followed by briefly degassing the reaction mixture with argon. Triethylsilane (1.7 mL, 10.50 mmol) was added dropwise to the reaction mixture resulting in an effervescent solution, and was left stirring at room temperature for two hours. After deprotection, the intermediate was confirmed by LC-MS (t = 3.65 min, m/z: 546.13 [M+H]⁺). Pd/C was removed by filtration over Celite, the reaction mixture was concentrated by rotary evaporation and dried with gentle stream of compressed air. Subsequently, O-(2-aminoethyl)undecaethylene glycol was Boc-protected using Boc-anhydride (0.3 g, 1.37mmol) and DIPEA (0.55 mL, 3.15mmol) in CHCl_3 (10 mL) upon stirring for 2 hours. The intermediate formation was verified by LC-MS (t = 4.73 min, m/z: 545.78 [M+H-Boc]⁺). Next, 1,1'-carbonyldiimidazole (0.29 g, 1.79 mmol) was added to the reaction mixture with stirring for an additional 2-3 hours to activate the hydroxyl group of the oligo(ethylene glycol) and verified by LC-MS (t = 7.57 min, m/z: 639.17 [M+H-Boc]⁺). N-Cbz-1,10-decanediamine (0.42 g, 1.37 mmol) and DIPEA (0.37 mL, 2.10mmol) was added to the reaction mixture and refluxed overnight. The reaction mixture was purified by reversed-phase column chromatography using a 10-90% $\text{CH}_3\text{CN}/\text{H}_2\text{O}$ gradient over 40 minutes. The final

product was concentrated by evaporation of CH₃CN followed by lyophilization of water to obtain compound **9** as a white solid.

Yield: 0.52 g, 50.6% ¹H-NMR (δ_H[ppm], CDCl₃, 600 MHz): 7.28-7.22 (m, 5H), 5.16 (br s, 1H), 5.07-5.05 (br s, 1H), 5.01 (s, 2H), 4.12 (t, 2H), 3.68-3.54 (m, 42H), 3.46-3.44 (t, 2H), 3.23-3.22 (m, 2H), 3.11-3.04 (m, 4H), 1.41-1.37 (m, 13H), 1.26-1.20 (m, 12H). ¹³C-NMR (δ_C[ppm], CDCl₃, 150 MHz): 156.53, 156.09, 136.86, 128.50, 128.09, 128.04, 79.45, 72.72, 70.60, 70.55, 70.27, 69.70, 66.47, 63.78, 41.14, 41.06, 40.43, 29.97, 29.44, 29.25, 28.51, 26.75. LC-MS: t = 8.26min, m/z: 878.33[M+H-Boc]⁺.

Synthesis of **10**

Compound **9** (0.52 g, 0.53 mmol) was dissolved in MeOH (5 mL) and Pd/C (28.0 mg, 0.27 mmol) was added followed by briefly degassing the reaction mixture with argon. Triethylsilane (0.85 mL, 5.32 mmol) was added dropwise to the reaction mixture resulting in an effervescent solution, and was left stirring at room temperature for two hours. After Cbz-deprotection, the intermediate was confirmed by TLC-MS (m/z: 746.13 [M+H-Boc]⁺), Pd/C was removed by filtration over Celite, concentrated by rotary evaporation and dried with gentle stream of compressed air. The crude product was redissolved in CHCl₃ (10 mL) and 3,4-dibutoxy-3-cyclobutene-1,2-dione (149.0 μL, 0.69 mmol) and DIPEA (185.0 μL, 1.06 mmol) were added. The reaction mixture was refluxed overnight and subsequently, purified by C18 silica column using a gradient of 10-90% CH₃CN/H₂O over 40 minutes. The final product was concentrated by evaporation of CH₃CN followed by lyophilization of water to obtain a compound **10** as a white solid.

Yield: 0.42 g, 61.1% ¹H-NMR (δ_H[ppm], CDCl₃, 600 MHz): 5.18 (br s, 1H), 5.05 (br s, 1H), 4.75-4.73 (t, 2H), 4.21-4.20 (t, 2H), 3.76-3.61 (m, 42H), 3.56-3.53 (m, 2H), 3.42-3.37 (m, 2H), 3.31 (br s, 2H), 3.16-3.13 (m, 2H), 1.80-1.77 (m, 2H), 1.62-1.59 (m, 4H), 1.48-1.44 (m, 15H), 1.31-1.28 (m, 12H), 0.99-0.96 (t, 3H). ¹³C-NMR (δ_C[ppm], CDCl₃, 150 MHz): 190.45, 183.89, 178.41, 173.44, 157.47, 157.10, 80.17, 74.40, 72.88, 72.81, 72.64, 72.27, 71.48, 71.37, 71.35, 71.32, 71.25, 71.18, 71.08, 70.98, 70.83, 70.69, 67.91, 64.76, 64.66, 45.88, 45.42, 42.00, 41.34, 41.04, 40.90, 33.03, 32.06, 31.83, 31.63, 30.88, 30.33, 30.16, 30.05, 29.45, 27.66, 27.32, 19.67, 14.70. LC-MS: t = 7.38 min, m/z: 995.30 [M+H-Boc]⁺.

Synthesis of **11**

Trifluoroacetic acid (2 mL) was added to facilitate deprotection of the Boc-protecting group of **8** (31.8 mg, 0.031 mmol) for 20 minutes, and verified by LC-MS ($t = 6.67$ min, m/z : 922.80 [M+H-Boc]⁺). Afterwards, the solvent was evaporated by using a gentle stream of compressed air and the compound was redissolved in CHCl₃ (5 mL) with DIPEA (0.5 mL), and **10** (40.1 mg, 0.041 mmol) was added prior to refluxing the reaction mixture overnight. The compound was purified by C18 column chromatography using a gradient of 10-90% CH₃CN/H₂O over 25 minutes. The final product was concentrated by evaporation of CH₃CN followed by lyophilization of water to obtain a compound **11** as a white solid.

Yield: 20.4 mg, 35.6% ¹H-NMR (δ_H [ppm], CDCl₃, 600 MHz): 7.76 (br s, 1H), 7.52 (br s, 1H), 5.04 (br s, 1H), 4.21-4.20 (m, 4H), 3.69-3.54 (m, 94H), 3.39 (s, 3H), 3.32 (br s, 1H), 3.15 (m, 4H), 1.67-1.64 (m, 8H), 1.48-1.27 (m, 45H). ¹³C-NMR (δ_C [ppm], CDCl₃, 150 MHz): 183.62, 182.51, 170.00, 168.11, 157.54, 80.19, 72.92, 71.57, 71.54, 71.53, 71.49, 71.25, 70.68, 64.81, 60.04, 45.80, 44.21, 42.08, 41.39, 32.17, 30.98, 30.47, 30.27, 30.25, 29.46, 27.76, 27.43, 25.72. LC-MS: $t = 6.73$ min, 1745.55 m/z : [M+H-Boc]⁺.

Synthesis of **4**

Compound **11** (4.5 mg, 0.0024 mmol) was deprotected using a mixture of trifluoroacetic acid (1 mL) for 20 minutes. Deprotection of the Boc-group was confirmed by LC-MS ($t = 5.77$ min, m/z : 1745.27 [M+H]⁺) and the solvents were evaporated by a gentle stream of compressed air before being redissolved in DMSO (1.5 mL). Triethylamine (250 μ L) was added to the stirring solution along with Sulfo-Cy3 NHS ester (2.12 mg, 0.0036 mmol). MilliQ water (3.5 mL) was added to the reaction mixture and dialyzed against water using a dialysis bag with a molecular weight cut off (MWCO) = 1000 Da. The compound was purified by reversed-phase HPLC using a C18 column and a gradient of 10-90% CH₃CN/H₂O over 25 minutes. The product fractions were collected and lyophilized to yield compound **4** as a sticky pink material.

Yield: 2.36 mg, 45.01%. LC-MS: $t = 5.83$ min, m/z : 2345.1 [M+H]⁺.

Synthesis of 5

Compound **11** (4.5 mg, 0.0024 mmol) was Boc-protected with a mixture of trifluoroacetic acid (1 mL) for 20 minutes. Deprotection of the Boc-group was confirmed by LC-MS ($t = 5.77$ min, m/z : 1745.27 $[M+H]^+$) and the solvents were evaporated by a gentle stream of compressed air before being redissolved in DMSO (1.5 mL). Triethylamine (250 μ L) was added to the stirring solution along with Sulfo-Cy5 NHS ester (2.2 mg, 0.0036 mmol). MilliQ-water was added to the reaction mixture and dialyzed against water using a dialysis bag with a molecular weight cut off (MWCO)= 1000 Da. The compound was purified by reversed-phase HPLC using a C18 column and a gradient of 10-90% $\text{CH}_3\text{CN}/\text{H}_2\text{O}$ over 25 minutes. The product fractions were collected and lyophilized to yield compound **4** as a sticky dark blue material.

Yield: 2.13 mg, 40.14%. LC-MS: $t = 5.87$ min, m/z : 2372.03 $[M+H]^+$.

5.6.4. Cryo-TEM of 4

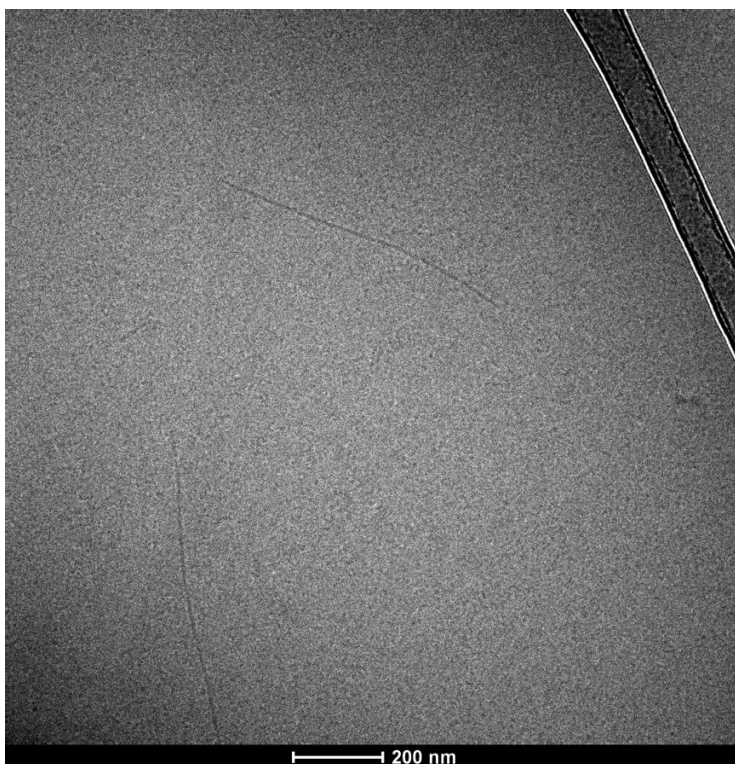


Figure S5.1. Cryogenic transmission electron microscopy (cryo-TEM) of **4** ($c = 40 \mu\text{M}$) on its own in water, as a control. Fibrillar aggregates are observed.

5.6.5 UV-Vis spectra

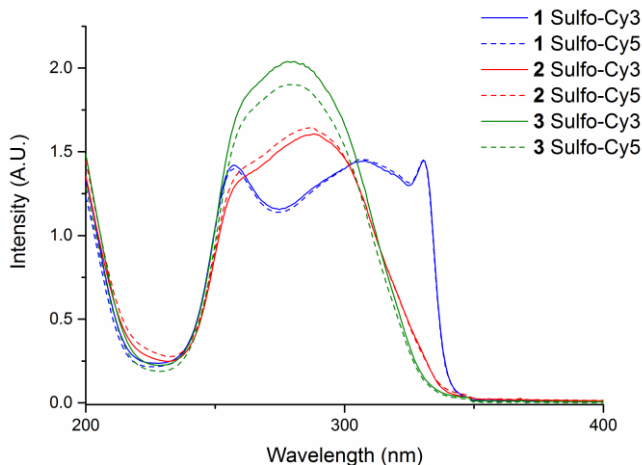


Figure S5.2. UV-Vis spectrum (200-400 nm) of **1**, **2** and **3** ($c = 30\mu\text{M}$) with 2 mol% **4** (solid line) and **5** (dashed line).

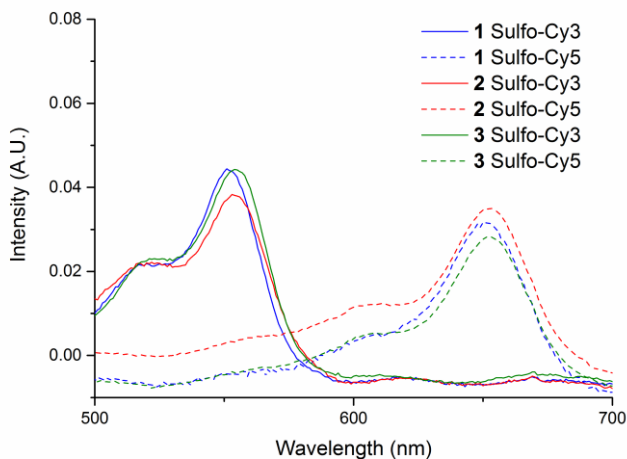


Figure S5.3. UV-Vis spectrum (500-700 nm) of **1**, **2** and **3** ($c = 30 \mu\text{M}$) with 2 mol% **4** (solid line) and **5** (dashed line).

5.6.6. Fluorescence spectra

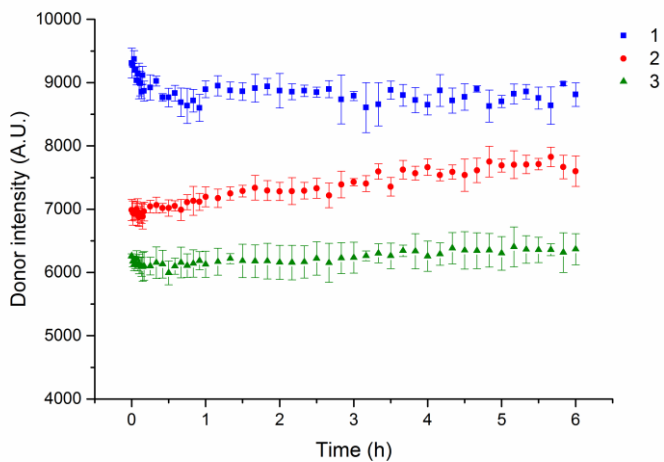


Figure S5.4. Raw fluorescent data from the donor ($\lambda_{\text{exc}}= 550 \text{ nm}$ $\lambda_{\text{em}}= 570 \text{ nm}$) channel from FRET dynamic experiments where solutions containing **1** (blue), **2** (red) and **3** (green) labeled with **4** or **5** (2 mol%) are mixed in an equimolar ratio at room temperature.

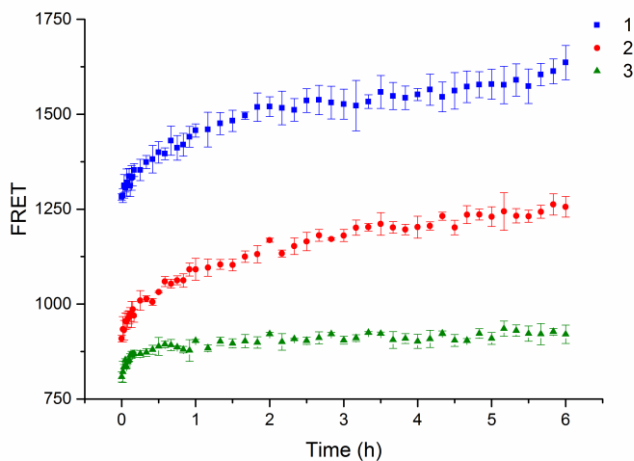


Figure S5.5. Raw fluorescence data ($\lambda_{\text{exc}}= 550 \text{ nm}$ $\lambda_{\text{em}}= 670 \text{ nm}$) measuring the FRET channel in dynamic experiments where solutions of **1** (blue), **2** (red) and **3** (green) labeled with **4** or **5** (2 mol%) are mixed in an equimolar ratio at room temperature.

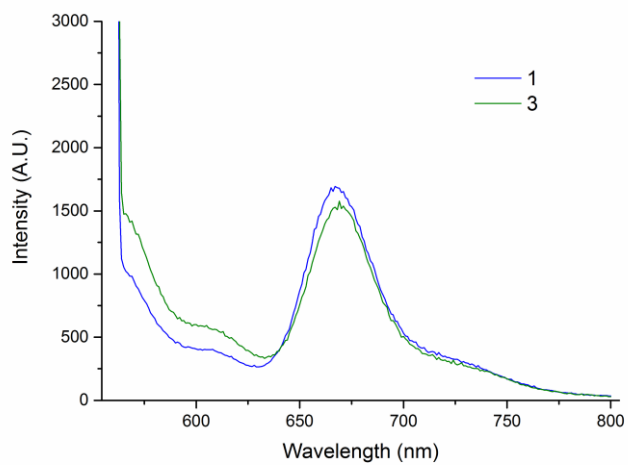


Figure S5.6. Static FRET measurements (zoom in, from 560 to 800 nm) of **1** and **3** with an equimolar amount of **4** and **5** (2 mol% total of the dye-labeled monomers); FRET signal observed at 670 nm.

3.5.7 Cryo-TEM of **1** with carp serum

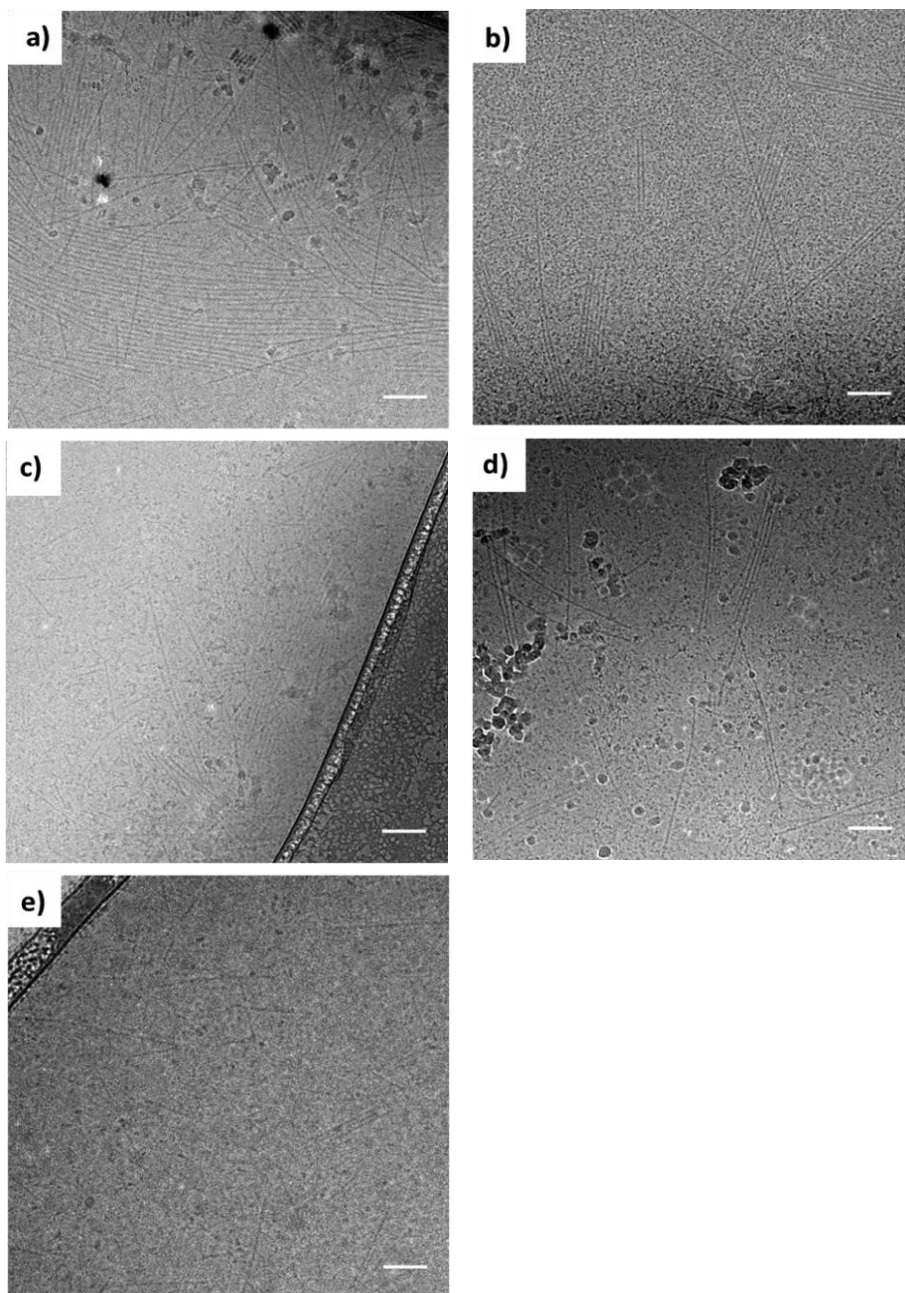


Figure S5.7. Cryo-TEM images of squaramide-based supramolecular polymer nanoparticles of **1** ($c = 2$ mM) with 2 mol% **4** in a solution with increasing carp serum from 1-25 v/v%: 1% (a), 2.5% (b), 5% (c), 10% (d) and 25% (e). Fibrillar structures are retained with increasing carp serum concentration. Scale bar: 100 nm.

3.5.8 Supramolecular polymer nanoparticles length and width distributions

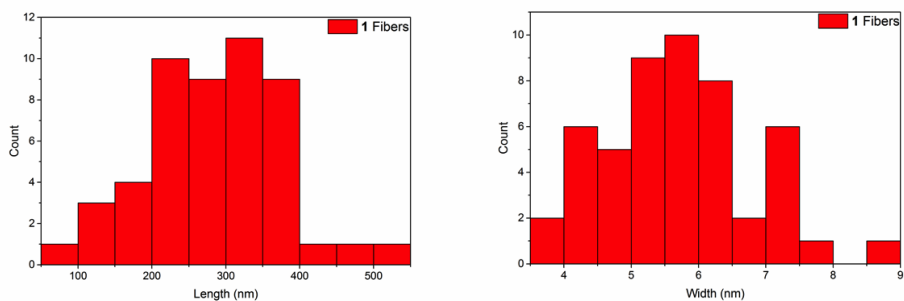


Figure S5.8. Histograms of length (282 ± 84 nm) and width (6 ± 1 nm) distributions measured for **1** ($N = 50$).

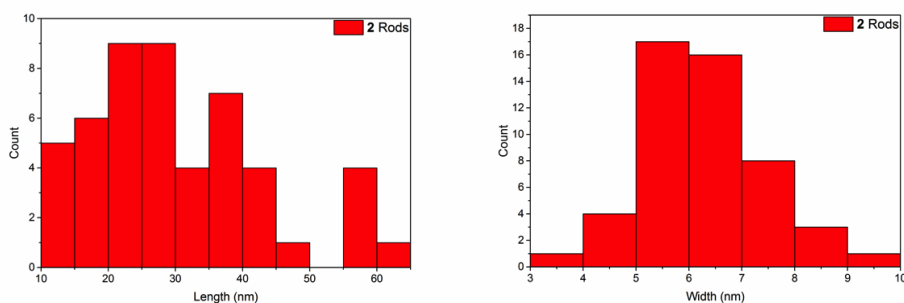


Figure S5.9. Histograms of length (31 ± 13 nm) and width (6 ± 1 nm) distributions measured for **2** ($N = 50$).

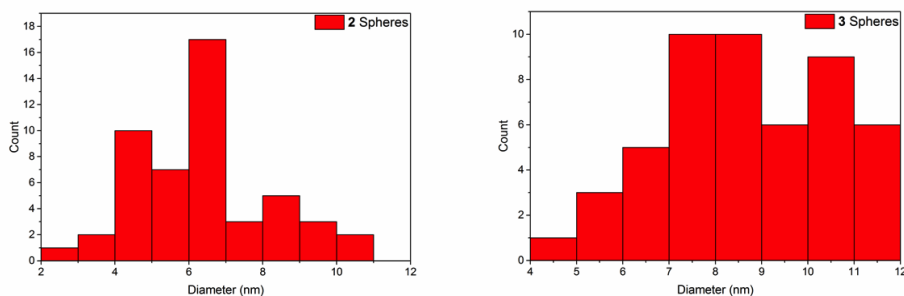


Figure S5.10. Histograms of diameter distributions measured for spherical aggregates of **2** (6 ± 2 nm)(left) and **3** (9 ± 2 nm) (right) ($N = 50$).

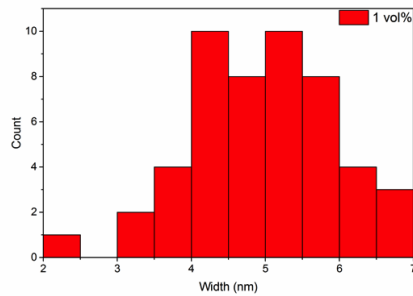
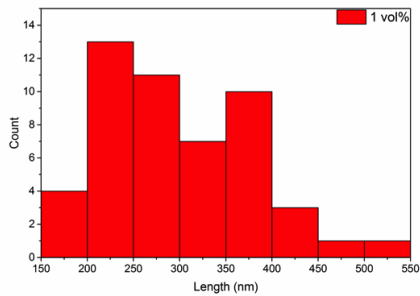


Figure S5.11. Histograms of length (299 ± 78 nm) and width (5 ± 1 nm) distributions measured for **1** at 1 v/v% of carp serum (N = 50).

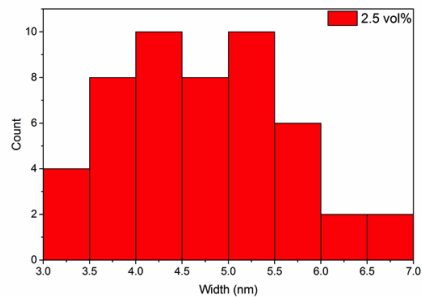
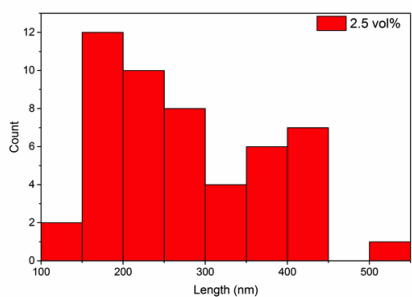


Figure S5.12. Histograms of length (277 ± 103 nm) and width (5 ± 1 nm) distributions measured for **1** at 2.5 v/v% of carp serum (N = 50).

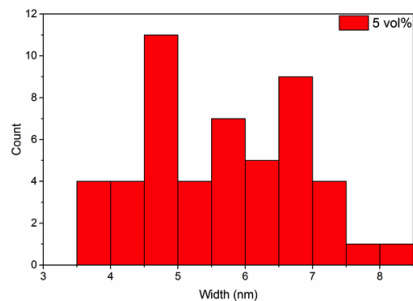
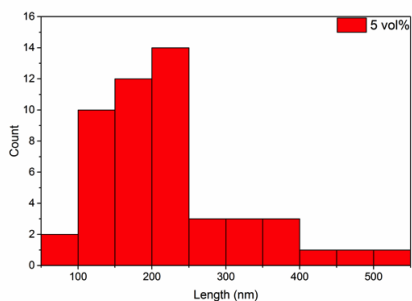


Figure S5.13. Histograms of length (218 ± 96 nm) and width (6 ± 1 nm) distributions measured for **1** at 5 v/v% of carp serum (N = 50).

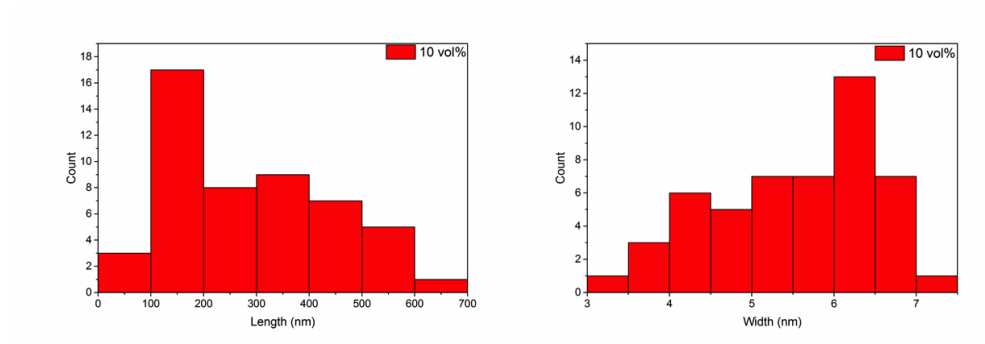
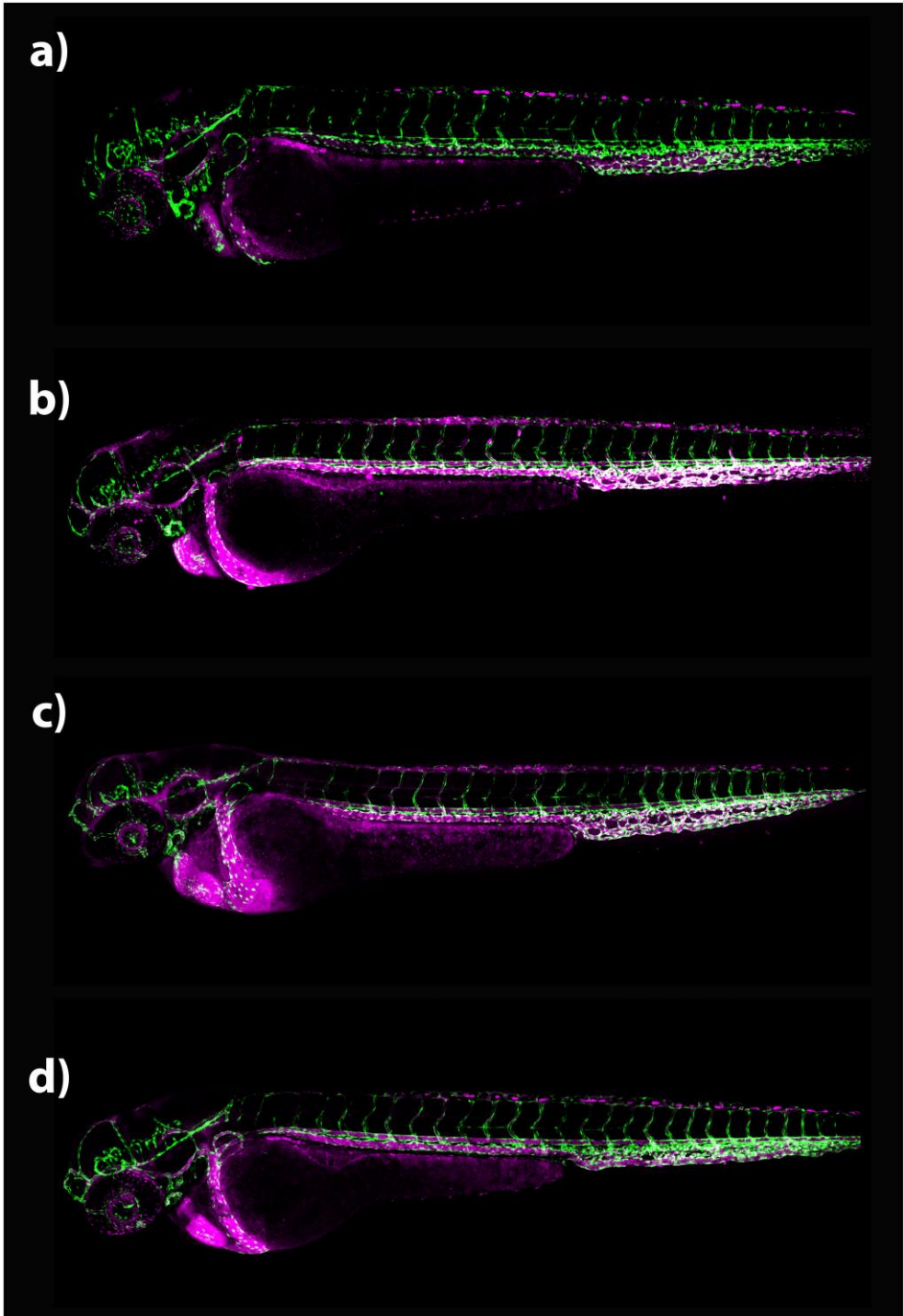


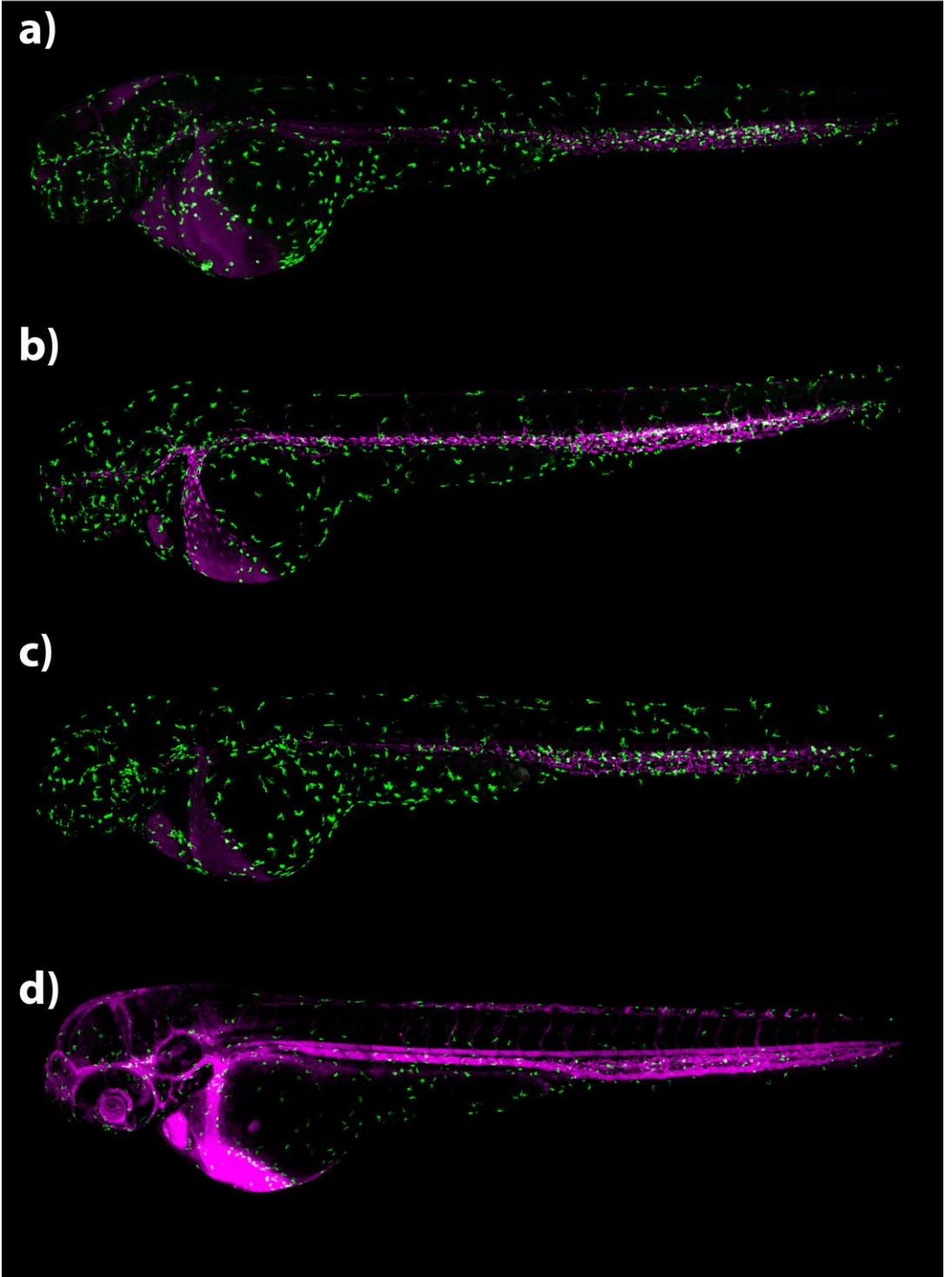
Figure S5.14. Histograms of length (288 ± 142 nm) and width (6 ± 1 nm) distributions measured for **1** at 10 v/v% of carp serum (N = 50).

5.6.9 Whole embryo zebrafish imaging



Chapter 5

Figure S5.15. Biodistribution of the fluorescently-labeled squaramide-based supramolecular polymer nanoparticles in the zebrafish. Whole-embryo view 1 hour post-injection in the Duct of Cuvier with **1** (a), **2** (b) and **3** (c) ($c = 2 \text{ mM}$) co-assembled with 2 mol% **4** in an embryonic zebrafish (*kdr1:GFP*) at 54 hpf. (d) Whole-embryo view after 1 hour injection in the Duct of Cuvier with **4** ($c = 40 \text{ }\mu\text{M}$) on its own in an embryonic zebrafish (*kdr1:GFP*) at 54 hpf. This control experiment is carried out to track the biodistribution of the negatively charged monomer itself.



Chapter 5

Figure S5.16. Uptake studies of the fluorescently-labeled squaramide-based supramolecular polymer nanoparticles by macrophages in the zebrafish. Whole-embryo view 1 hour post-injection in the Duct of Cuvier with **1** (a), **2** (b) and **3** (c) ($c = 2 \text{ mM}$) and 2 mol% of **4** in an embryonic zebrafish (mpeg1:GFP) at 54 hpf. (d) Whole-embryo view after 1 hour injection in the Duct of Cuvier with **4** ($c = 40 \text{ }\mu\text{M}$) on its own in an embryonic zebrafish at 54 hpf. This control experiment is carried out to track the uptake of the negatively charged particles of **4** by macrophages studies in zebrafish.

5.6.10 References

- (1) Saez Talens, V.; Englebienne, P.; Trinh, T. T.; Noteborn, W. E. M.; Voets, I. K.; Kieltyka, R. E. *Angew. Chemie - Int. Ed.* **2015**, *54* (36), 10502–10506.
- (2) Dardonville, C.; Fernandez-Fernandez, C.; Gibbons, S. L.; Ryan, G. J.; Jagerovic, N.; Gabilondo, A. M.; Meana, J. J.; Callado, L. F. *Bioorganic Med. Chem.* **2006**, *14* (19), 6570–6580.

CHAPTER 6

Summary and perspectives

The self-assembly of molecular building blocks into well-defined supramolecular structures through non-covalent forces is a powerful approach for the construction of materials. Inspired by Nature that takes advantage of these reversible bonding forces to elicit numerous processes at various length scales, the field of supramolecular materials strives to develop scaffolds that are adaptable, reversible and functional for a broad range of applications from biomedicine to electronics. In order to truly exploit these synthetic polymer assemblies in areas such as regenerative medicine or drug delivery, their self-assembly under biological conditions needs to be well-understood. In aqueous media, the hydrophobic effect is often the dominant driving force in promoting monomer aggregation, while other non-covalent interactions such as hydrogen-bonding and aromatic interactions promote their aggregation into organized fibrillar architectures. Although cyclic π -conjugated molecules are often employed in such monomers, the consequence of the aromatic character on self-assembly is often overlooked despite the frequent use of aromaticity to explain the stability of such molecules and the unexpected efficiencies of certain reactions involving π -conjugated rings. In this thesis, I examined the interplay of aromaticity and hydrogen bonding on the self-assembly of a squaramide-based supramolecular polymer in water. Squaramide derivatives were employed as ditopic hydrogen-bonding synthons that benefit from their partial aromatic character to modulate their hydrogen-bond strength upon self-assembly. Systematic variations of the various hydrophobic and hydrophilic domains of the monomer enabled the generation of a small library to probe the contribution of the various monomer domains to the resultant structure. Preliminary *in vivo* studies in zebrafish embryos revealed their potential to evade macrophages, however they are still removed from circulation by the stabilin-2 receptor when as a rod-like or fibrillar aggregate.

In **chapter 2**, the synergistic contribution of hydrogen-bonding and aromaticity as driving forces to trigger one-dimensional self-assembly of supramolecular polymers in water is explored. Two squaramide synthons are embedded within the hydrophobic core of a bolaamphiphile to promote supramolecular polymer self-assembly. Microscopy studies (cryo-TEM and AFM) show the formation of high-aspect-ratio fibers up to a micron in length and are supported by scattering (DLS and SAXS) techniques that reveal the presence of 10-30 squaramide-based bolaamphiphiles per cross section. UV-Vis spectroscopy studies reveal the influence of the self-assembly on the electronic properties of the squaramide

synthon, while IR provides insight into their geometric changes in this process; namely, a decrease in bond length alternation of the squaramide units upon self-assembly. These observations are further explained by the application of density functional theory to measure magnetic, geometric and energetic properties of the self-assembled monomers, supporting the hypothesis of hydrogen-bonding reinforcement through a gain in aromaticity. In this study, I show that squaramides are excellent directional units to promote the self-assembly of supramolecular polymers and that a gain in aromaticity through hydrogen bonding can contribute significantly (30%) to the overall interaction energy of the monomer units. By merging computation and experiment, this seminal study opens the door to exploring if this effect occurs in a wider range of organic synthons used to construct supramolecular polymers and its consequence on the resultant assemblies.

Chapter 3 demonstrates the potential of aromatic gain to switch the self-assembly mode of a squaramide unit in a one-dimensional shape persistent aggregate by O → S substitution. First, I have shown the synthesis of a thiosquaramide-based bolaamphiphile derivative by using a zwitterionic P₄S₁₀-pyridine thionating agent, replacing selectively the oxygen atoms with sulfur atoms on the squaramide carbonyls. Next, their self-assembly into short flexible rod-like structures was observed by cryo-TEM and supported by SAXS. Through a combination of experiment, using UV-Vis and IR spectroscopy, and computation, by estimating NICS, HOMA and ASE values, I demonstrate that oxosquaramides prefer a head-to-tail hydrogen-bonding arrangement promoted by aromatic gain, while thiosquaramides prefer π -stacked arrangement to enhance their aromatic character. These studies highlight the potential of coupling of aromatic character and non-covalent forces in these systems, opening a new door in the rational design of new supramolecular motifs.

Further insight into the growth mechanism of these squaramide-based (oxo and thio) supramolecular polymers is required. The self-assembly of these systems can be followed by various spectroscopic techniques, such as UV-Vis where the proper fitting to either isodesmic or cooperative models in a heating-cooling curve would provide clues into their growth mechanism in water. However, one limitation in probing such assemblies resides in the large hydrophobic domain provided by the bolaamphiphile, which can result in the formation of kinetically trapped states during the heating-cooling cycles. A plausible solution would be to find a miscible

Chapter 6

co-solvent to decrease the kinetic barrier promoted by the hydrophobic effects of the amphiphiles, while avoiding complete disruption of the supramolecular aggregate.

In **chapter 4**, systematic variations of the ethylene glycol side chains ($n = 7$ to 36) and outer aliphatic spacers ($m = 2$ to 12) of the aforementioned squaramide-based bolaamphiphile monomers were prepared and characterized. First, a monomer library is prepared following the synthetic approach developed in chapter 2. Subsequently, the morphologies of the resulting aggregates from the monomer library were probed. Systematic modification of the ethylene glycol hydrophilic side chains resulted in a gradual morphological transition from fibrillar-like domains ($n = 11$) to spherical objects ($n = 36$) as observed in cryo-TEM and SAXS experiments. On the other hand, an aliphatic spacer of eight methylene units was necessary to shield the squaramide units at the concentrations studied by the same analysis methods. These observations are further supported at the molecular level by UV-Vis and IR spectroscopic measurements. The potential for using these systems as drug carrier vehicles is examined by performing encapsulation experiments using Nile Red as hydrophobic cargo. To better tailor the prepared nanoparticles for various applications, such as drug delivery, length control ($\text{Đ} \sim 1.0$) over the formed self-assemblies through controlled supramolecular polymerization is very much necessary. In order to achieve this goal, it is critical to understand the growth mechanism of these squaramide-based polymers and to explore the effect of various self-assembly pathways on the formed products.

In **chapter 5**, I follow the distribution and circulation behavior of fluorescently tagged squaramide-based supramolecular structures of various morphologies, as described in chapter 4, in a zebrafish embryo model *in vivo*. The design and synthesis of the unsymmetrically labeled cyanine-3 squaramide-based bolaamphiphile is reported. The co-assembly of this reporter molecule with the native squaramide monomers is followed by zeta-potential and fluorescence measurements, and their morphologies are examined by cryo-TEM microscopy on their own and in the presence of increasing carp serum, where a retention of the aggregate morphology is observed. Additionally, injection of the premade fluorescent aggregates of various shapes into zebrafish embryos was performed to track the biodistribution and circulation of the three architectures *in vivo*. Here, all structures were found to evade macrophages, making them good candidates as

drug delivery nanocarriers. Finally, it was found that the nanocarrier shape and size plays an important role in nanoparticle clearance by scavenger endothelial cells by the Stabilin-2 receptor.

The use of supramolecular polymers as biocompatible drug carriers is an exciting area that requires further research because of its promise to expeditiously prepare highly functionalized carriers for targeted drug delivery applications. Here, I show how these nanoparticles behave once injected into an *in vivo* model. At this point, many possibilities can follow these studies. A possible step would involve conjugating drugs to the supramolecular monomers for self-assembly to prolong or decrease their circulation time. Furthermore, the decoration of these systems by employing cell targeting peptides or aptamers could promote their specific delivery to a given cellular target. This is not a straightforward aim since many parameters have to be taken in consideration simultaneously, but such materials would advance the knowledge in effective drug carrier design.

Samenvatting

De zelfassemblage van moleculaire bouwstenen in goed vormgegeven supramoleculaire structuren door non-covalente krachten is een krachtige aanpak voor de constructie van materialen. In een natuurlijke omgeving profiteren processen van deze omkeerbare bindende krachten, om verscheidene processen bij verschillende lengtematen uit te lokken. Met deze natuurlijke omgeving als inspiratiebron streeft het wetenschappelijke veld van supramoleculaire materialen ernaar om materialen te ontwikkelen die aanpasbaar, omkeerbaar en functioneel zijn voor een breed spectrum aan applicaties, van medische biologie tot elektronica. Om deze synthetische polymeer assemblage ten volle uit te kunnen buiten in onderzoeksgebieden zoals regeneratieve geneeskunde of medicijn aflevering, moet de zelfassemblage onder biologische condities tot in detail begrepen worden. In waterige media is het hydrofobe effect vaak de dominante drijvingskracht bij het verwekken van monomeer aggregatie. Andere non-covalente interacties, zoals waterstofbrug formatie en π -interacties, bevorderen hun aggregatie in georganiseerde fibrillaire architecturen. π -Geconjugeerde moleculen zijn vaak ingezet in dergelijke monomeren. Het effect van het aromatische karakter op zelf-assemblage wordt vaak over het hoofd gezien, ondanks het regelmatige gebruik van aromaticiteit bij het verklaren van de stabiliteit van vele moleculen en de onverwachte effectiviteit van bepaalde reacties. In deze dissertatie hebben we het aromatische effect op de sterkte van de waterstofbrug in waterstofbrug-formatie van een gedeeltelijk aromatische monomeer in een zelf-geassembleerd aggregaat in water. We hebben afgeleiden van squaramiden ingezet als ditopische waterstofbrug synthonen die baat hebben bij hun gedeeltelijk aromatische karakter om de sterkte van hun waterstofbrug te moduleren bij zelf-assemblage. We hebben deze synthonen ingebed in een bolaamfifiel om de monomeer unit te synthetiseren, die zichzelf verder assembleert in water. Systematische variaties van de verscheidene moleculaire domeinen van de monomeer maken de creatie van een veelvoud aan moleculen mogelijk, zodat de contributie van de verschillende monomeer domeinen aan de uiteindelijke structuur getest kan worden. Voorafgaande *in vivo* onderzoeken in zebravissen hebben hun potentieel als biocompatibele nanovoertuigen voor medicijnaflevering die macrofage kunnen ontwijken laten zien.

In hoofdstuk twee worden de synergistische bijdragen van waterstofbrugformatie en aromaticiteit als drijvende krachten bij eendimensionale zelfassemblage van supramoleculaire polymeren in water onderzocht. Twee squaramide synthonen zijn ingebed in de hydrofobe kern van een bolaamfifiel om een supramoleculaire zelf-geassembleerde polymeer te bevorderen. Microscopische onderzoeken (cryo-TEM en AFM) laten de formatie zien van vezels met een hoge aspectverhouding met een maximale lengte van een micron. Dit wordt ondersteund door verstrooiingstechnieken (DLS en SAXS), die de aanwezigheid van 10-30 bolaamfifielen gebaseerd in squaramiden per kruissectie laten zien. Onderzoeken die gebruik maken van UV-Vis spectroscopie laten de invloed van zelf-assemblage op de elektronische eigenschappen van de squaramide synthon zien. IR Technieken leveren inzicht in de geometrische veranderingen in dit proces, namelijk een afname in afwisseling van de lengte van de binding van de squaramide eenheden bij zelf-assemblage. Deze observaties worden verder uitgelegd door de applicatie van dichtheidsfunctionaaltheorieberekeningen om magnetische, geometrische en energetische eigenschappen van de zelf-geassembleerde monomeren te meten. Dit ondersteunt de hypothese van de versterking van de waterstofbruggen, door een toename in aromaticiteit. In dit onderzoek laten we zien dat squaramiden uitmuntende directionele zelf-geassembleerende eenheden zijn om de zelf-assemblage van supramoleculaire polymeren te bevorderen en dat een toename in aromaticiteit door waterstofbrug-formatie significant kan bijdragen aan de algemene interactie energie van de monomeer eenheden.

Hoofdstuk drie laat het potentieel van aromatische toename om de zelf-assemblage modus van een squaramide eenheid te veranderen in een eendimensioneel vormvast aggregaat door O → S vervanging. Allereerst hebben we de synthese van een op thiosquaramide bolaamfifiele afgeleid product laten zien, door gebruik te maken van een zwitterionische P₄S₁₀-pyridine thionatische reactant. Deze reactant stelt ons in staat om zeer selectief de zuurstofatomen te vervangen door zwavelatomen op de squaramide carbonyl groepen. Daarna werd de zelf-assemblage van de bolamfifiel in korte flexibele staafvormige structuren geobserveerd met behulp van cryoTEM en SAXS. Door een combinatie van experimenten waarbij we gebruik maakten van UV-Vis, IR spectroscopie en schattingen van NICS, HOMA en ASE waarden op basis van computatie laten we zien dat oxosquaramides een arrangement van kop-staart waterstofbrug-formatie versterkt door aromatische toename prefereren. Daarentegen prefereren

thiosquaramiden π -interacties zodat zij hun aromatische karakter optimaal kunnen verbeteren. Deze onderzoeken belichten het potentieel van het koppelen van een aromatisch karakter met non-covalente krachten in deze systemen, waarmee zij een nieuw licht schijnen op het rationele ontwerp van nieuwe supramoleculaire motieven.

Verder begrip van hoe het groeimechanisme van deze supramoleculaire polymeren werkt is noodzakelijk. De zelf-assemblage van deze systemen kan bekeken worden met verschillende spectroscopische technieken. Bijvoorbeeld met UV-Vis, waarbij de juiste inpassing in isodesmische of coöperatieve modellen in een verhitting-afkoeling curve verder inzicht kunnen bieden over de zelf-assemblage van deze systemen in water. Een beperking van het testen van dergelijke assemblages ligt in het grote hydrofobe domein, dat veroorzaakt wordt door de bolaamfifiel, die kan resulteren in de formatie van kinetisch gevangen toestand tijdens de cycli van verhitting en afkoeling. Een co-solvent die de kinetische barriere, die versterkt wordt door de hydrofobe effecten van de amfifielen, verzwakt en tegelijkertijd complete verstoring van het supramoleculaire aggregaat ontwijkt, zou een plausibele oplossing kunnen vormen voor dit probleem.

In hoofdstuk vier hebben we systematische variaties van de ethyleenglycol zijketens ($n = 7$ to 36) en de buitenste alifatische spacers ($m = 2$ to 12) van de eerdergenoemde squaramide bolaamfifiele monomeren, gesynthetiseerd en gekarakteriseerd. Eerst hebben we een verzameling monomeren voorbereid volgens de synthetische aanpak die we ontworpen hebben in hoofdstuk twee. Daarna hebben we de vormen van de verzamelde monomeer aggregaten getest. Systematische modificatie van de ethyleenglycol hydrofiele zijketens resulteerden in een geleidelijke overgang van fibrilar-achtige domeinen ($n = 11$) naar bolvormige objecten ($n = 36$), zoals we geobserveerd hebben in cryoTEM en SAXS experimenten. Aan de andere kant was een alifatische spacer van acht methyleen eenheden nodig om de squaramide eenheden af te schermen bij de bestudeerde concentraties met dezelfde analyse methoden. Deze bevindingen worden verder ondersteund op moleculair niveau met behulp van UV-Vis en IR spectroscopische metingen. Het potentieel van deze systemen als medicijn dragende voertuigen hebben we onderzocht met Nile-Red als hydrofobe lading.

In hoofdstuk vijf onderzoeken we de verdeling en circulatiegedrag van fluorescent gelabelde supramoleculaire structuren gebaseerd op squaramides, op basis van de verschillende vormen die we in hoofdstuk vier beschreven hebben, in het *in vivo* zebravis model. Het ontwerp en de synthese van de asymmetrisch gelabelde cyanine-3 squaramide bolaamfifiel wordt beschreven. De assemblage van deze reporter-molecuul met de oorspronkelijke squaramide monomeren wordt opgevolgd door zeta-potentieel en fluorescentie metingen en de vormen zijn onderzocht door middel van cryoTEM microscopie, zowel onafhankelijk en in aanwezigheid van een toenemend percentage carp serum, waarbij een vormvastheid van het aggregaat zichtbaar is. Tot slot zijn de zebravis embryo's geïnjecteerd met de geprepareerde fluorescente aggregaten met verschillende vormen, zodat het gedrag en de circulatie van de drie architecturen geobserveerd kon worden *in vivo*. De fibrillaire aggregaten circuleerden vaker een kortere periode ten opzichte van de bolvormige structuren. Alle structuren bleken de macrofagen en de scavenger receptor stabilin 2 te ontwijken, waardoor ze ideale nanodragers zijn voor medicijn aflevering.

Het gebruik van supramoleculaire polymeren als biocompatibele medicijndragers is een opwindend onderwerp dat verder onderzocht moet worden vanwege de immense belofte om relatief snel kwalitatieve functionele dragers voor specifieke doeleinden te ontwikkelen. Wij hebben laten zien hoe deze nanodeeltjes zich gedragen wanneer ze geïnjecteerd zijn in een *in vivo* model. Op dit moment zijn er vele opvolgmogelijkheden voor deze onderzoeken. Een logische stap zou het samenvoegen van medicijnen met supramoleculaire monomeren voor zelf-assemblage zijn, zodat de circulatietijd verlengd of verkort kan worden. De functionalisering van deze systemen door het gebruik van peptiden die zich op specifieke cellen richten of het gebruik van aptameren zou de aflevering naar een specifieke cel kunnen bevorderen. Dit is geen makkelijk doel, omdat er met vele parameters tegelijkertijd rekening gehouden moet worden, maar het gebruik van deze materialen zou de kennis over het ontwerpen van effectieve medicijnaflevering grote stappen laten nemen.

Curriculum Vitae

Victorio Saez Talens was born on September 6, 1990 in Carcaixent, País Valencià (Spain). He graduated from the Institut Arabista Ribera Carcaixent in 2008, where he became interested in chemistry and other science related subjects. Thereafter, he started his BSc studies in Chemistry at the University of Valencia. In 2012 he moved to Leiden University within the Erasmus Exchange Program to perform his Master thesis under the supervision of prof. dr. Alexander Kros with the title "*Synthesis and characterization of gold bioconjugates*". In 2013, he received the *Licenciatura* degree (equivalent to MSc) in Chemistry at the University of Valencia.

In August 2013, he started his PhD studies in the group of Supramolecular and Biomaterials Chemistry, Leiden Institute of Chemistry, under the supervision of dr. Roxanne E. Kieltyka and prof. dr. Alexander Kros. During his PhD studies, he collaborated with prof. dr. Ilja K. Voets (Technische Universiteit Eindhoven), dr. Judy I. Wu (Houston University) and dr. Sylvestre Bonnet (Universiteit Leiden). Since February 2018 he is working as project manager in ITENE (Packaging, Transport and Logistics Research Center) at the technological group of Advanced Materials, located in Valencia, Spain.

The results reported in this dissertation were presented at the following meetings and conferences:

1. "Aromatic gain as driving force for supramolecular polymerization in water" Jan Reedijk Symposium, Leiden, The Netherlands, October 2014 (*Poster Presentation*).
2. "Aromatic gain as driving force for supramolecular polymerization in water" Chemistry as Innovative Science (CHAINS), Veldhoven, The Netherlands, December 2014 (*Poster Presentation*).
3. "Aromatic gain in a supramolecular polymer" Dutch Polymer Days, Lunteren, The Netherlands, March 2015 (Winner of the first prize *poster presentation* in the Chemistry and Biomedical section).
4. "Aromatic gain in a supramolecular polymer" Chemistry as Innovative Science (CHAINS), Veldhoven, The Netherlands, November 2015 (*Oral Presentation*).
5. "Squaramide-based supramolecular building blocks for supramolecular polymerization" Dutch Polymer Days, Lunteren, The Netherlands, March 2016 (*Poster Presentation*).
6. "Understanding self-assembly in supramolecular polymers" NVvM cryo workgroup spring meeting 2016, NeCEN, Leiden, The Netherlands, April 2016 (*Oral Presentation*).
7. "Modulation of hydrogen-bond strength in a squaramide-based supramolecular polymer" Jan Reedijk Symposium, Leiden, The Netherlands, October 2016 (*Poster Presentation*).
8. "Modulation of the hydrogen-bond strength in a supramolecular polymer" Chemistry as Innovative Science (CHAINS), Veldhoven, The Netherlands, December 2016 (*Poster Presentation*).
9. "Squaramide-based supramolecular polymers: influence of aromaticity on the strength of hydrogen-bond interaction" Dutch Polymer Days, Lunteren, The Netherlands, March 2017 (Winner of the first prize *oral presentation* in the Chemistry section).

10. "Modulation of hydrogen-bond strength in a squaramide-based supramolecular polymer" Advanced Polymers via Macromolecular Engineering (APME), Ghent, Belgium, May 2017 (*Poster Presentation*).
11. "Aromaticity-Modulated Non-Covalent Interactions: A Self-Assembly Mode "Tug-of-War" in Squaramide-Based Supramolecular Polymers" Jan Reedijk Symposium, Leiden, The Netherlands, October 2017 (*Poster Presentation*).

List of publications

1. **V. Saez Talens**, P. Englebienne, T.T. Trinh, W.E.M. Noteborn, I.K. Voets, R.E. KIELTYKA. "Aromatic gain in a supramolecular polymer." *Angewandte Chemie International Edition* **2015**, 54, 10502.
2. W.E.M Noteborn, D.N.H. Zwagerman, **V. Saez Talens**, C. Maity, L. van der Mee, J.M. Poolman, S. Mytnyk, J.H. van Esch, A. Kros, R. Eelkema, R.E. KIELTYKA. "Crosslinker-Induced Effects on the Gelation Pathway of a Low Molecular Weight Hydrogel." *Advanced materials*, **2017**, 29, 1603769.
3. B. Siewert, M. Langerman, Y. Hontani, J.T.M. Kennis, V.H.S. van Rixel, B. Limburg, M.A. Siegler, **V. Saez Talens**, R.E. KIELTYKA and S. Bonnet. "Turning on the red phosphorescence of a [Ru(tpy)(bpy)(Cl)]Cl complex by amide substitution: self-aggregation, toxicity, and cellular localization of an emissive ruthenium-based amphiphile." *Chemical Communications*, **2017**, 53, 11126
4. W.E.M. Noteborn, **V. Saez Talens** and R.E. KIELTYKA. "Reversible Loading of Nanoscale Elements on a Multicomponent Supramolecular Polymer System by Using DNA Strand Displacement." *ChemBioChem*, **2017**, 18, 1995
5. C. Tong; T. Liu; **V. Saez Talens**; W.E.M. Noteborn; T.H. Sharp; M. Hendrix; I.K. Voets; C.L. Mummery; V.V. Orlova; R.E. KIELTYKA. "Squaramide-based supramolecular materials for 3D cell culture of human induced pluripotent stem cells and their derivatives." *Biomacromolecules*, **2018**, 19, 1091.
6. S.H.C. Askes, N. Bossert, J. Bussmann, **V. Saez Talens**, R.E. KIELTYKA, A. Kros, S. Bonnet, and D. Heinrich. "Dynamics of dual-fluorescent polymersomes with durable integrity in living cancer cells and zebrafish embryos". *Biomaterials*, **2018**, 168, 54.
7. **V. Saez Talens**, M. Boraghi, R. Rudge, C.H. Wu, T.T. Trinh, P. Englebienne, I.K. Voets, J.I. Wu, R.E. KIELTYKA. "A Self-Assembly Mode "Tug-of-War" in Squaramide-Based Supramolecular Polymers Driven by Aromaticity-Modulated Hydrogen Bonding" *Manuscript in preparation*.
8. **V. Saez Talens**, D.M.M. Makurat, T. Liu, W.E.M. Noteborn, W. Dai, C.L. Guibert, I.K. Voets and R.E. KIELTYKA. "Morphological transitions of a squaramide-based

supramolecular polymer nanoparticle in water by modulating its monomer structure." *Manuscript in preparation.*

9. **V. Saez Talens**, G. Arias Alpizar, J. Bussmann, A. Kros, R.E. Kieltyka. "Biodistribution of squaramide-based supramolecular polymer nanoparticles in zebrafish embryos." *Manuscript in preparation.*